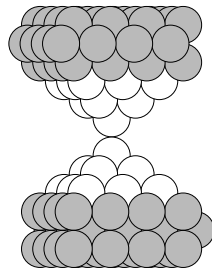


---

# Current-Voltage Behavior of Atomic-Sized Transition Metal Contacts

---



Søren Kynde Nielsen

PhD thesis



# Preface

This thesis is submitted to the Faculty of Science at the University of Aarhus, Århus, Denmark, in order to fulfill the requirements for obtaining the PhD degree in physics. The studies have been carried out under the supervision of Flemming Besenbacher in the scanning tunneling microscopy (STM) laboratory at the Center for Atomic-Scale Materials Physics (CAMP) at the Department of Physics and Astronomy from August 1998 to July 2002. CAMP is sponsored by the Danish National Research Foundation.

Many of the experimental results were obtained during two visits to the Solid State Physics Group (VSM) at the Kamerlingh Onnes Laboratory, University of Leiden, Leiden, The Netherlands in the autumn and winter of 2000 and the summer of 2001.

**Søren Kynde Nielsen**

Department of Physics and Astronomy  
Center for Atomic-scale Materials Physics  
University of Aarhus, Denmark

**PhD thesis**  
September 2002

# Acknowledgments

First of all I would like to thank my supervisor Flemming Besenbacher for his enthusiastic approach and his motivating behavior concerning getting the job done! His greatest influence on my life came about when he encouraged me to go abroad, resulting in my two visits at the Kamerlingh Onnes Laboratory at the University of Leiden in Holland. This turned out to be a great learning experience, and it must have strengthened my character tremendously.

Fellow CAMP member Kim Hansen acted as my co-supervisor for the first three years of my PhD. During the last year, he has been available for correspondence offering continued support and guidance. Kim's enthusiasm for physics in general and nano-science in particular has been a great inspiration and help to me. I have on numerous occasions benefitted from his huge knowledge on subjects related to our work, and his corrections, comments and suggestions on the chapters of this thesis are invaluable. For all this I am *very* grateful.

I would also like to thank the other two senior members of CAMP, Erik Lægsgaard for his technical support and Ivan Stensgaard for his guidance in the early stages of my PhD. They both have an always present and warm, but very dry humour, which I have enjoyed at several occasions after I finally learned to appreciate it.

I am grateful to professor Jan M. van Ruitenbeek for welcoming me into the VSM group in Leiden. His calm presence in the lab was a great help, providing a pleasant working environment. Through interesting discussions and comments on my work he has contributed to the writing of several chapters. I was especially pleased on the occasions where he and his wife invited our little group to visit them in their beautiful home.

It was a pleasure to work with Yves Noat in Leiden. While he introduced me to the mechanically controllable break-junction (MCBJ) we performed, in close collaboration, the experiments presented in Chapter 9. His great enthusiasm for the experimental work and especially for infinite discussions had a positive influence on my work in Leiden.

I owe Roel Smit thanks for providing extra data and figures which helped elucidate the experimental results presented in Chapter 9.

In general I extend my thanks to all members of the VSM group for making my stay pleasant, especially Luca Bai, Carlos Untiedt and Roel Smit, for sharing many evenings and cinema experiences, making me feel at home.

I have enjoyed collaborating with Mads Brandbyge at the Microelectronic Center, Technical University of Denmark. Apart from fruitful discussions he contributed with the theoretical input to Chapters 6–8, greatly enhancing their quality. His calculations guided the understanding of our experimental observations and have been vital for the publication of articles in high-impact journals; an outcome which is highly appreciated.

I would furthermore like to thank all the people who have been part of the CAMP group in the past four years, for creating a very interesting research environment which it has been a pleasure to be part of.

Special thanks to both Jeanette Dandanell and Anette Skovgaard for proof reading my manuscript, correcting numerous typos and grammatical errors. If there are some left, they will have entered with later changes.

A thanks also to Marianne Larsen for allowing me to use her drawings for the making of the very first and most amusing figure.

Having finished with all the professional acknowledgments, a few, but to me very important people still remain. To all my friends and family, thanks for being there for me.

I can never thank my parents enough for their continued support through my entire study at the University. They always offered their support both during happy times but more importantly also when I was down.

Finally I extend my deepest gratitude to my girlfriend Line. For the past six months where I have worked almost continuously on this thesis she was always there to cheer me up and help me through the tough times. For this and a multitude of other reasons, I owe her all my love.

Søren Kynde Nielsen  
Århus, September 2002

# List of Publications

In this thesis, the references listed below are referred to with capital Roman numerals, whereas other references are cited using Arabic numerals.

## Publications

- [I] *Fast and accurate current-voltage curves of metallic quantum point contacts*,  
K. Hansen, S. K. Nielsen, E. Lægsgaard, I. Stensgaard, and F. Besenbacher, *Rev. Sci. Instr.* **71**, 1793–1803 (2000).
- [II] *Current-voltage curves of gold quantum point contacts revisited*,  
K. Hansen, S. K. Nielsen, M. Brandbyge, E. Lægsgaard, I. Stensgaard, and F. Besenbacher, *Appl. Phys. Lett.* **77**, 708–710 (2000).
- [III] *Current-Voltage Curves of Atomic-Sized Transition Metal Contacts: An Explanation Why Au is Ohmic and Pt is Not*,  
S. K. Nielsen, M. Brandbyge, K. Hansen, K. Stokbro, J. M. van Ruitenbeek and F. Besenbacher, *Phys. Rev. Lett.* **89**, 066804 (2002).
- [IV] *Current-voltage curves of atomic-sized transition metal contacts*,  
S. K. Nielsen, K. Hansen, M. Brandbyge, J. M. van Ruitenbeek and F. Besenbacher, in preparation (unpublished).
- [V] *Current-induced disruptions of monatomic transition metal contacts*,  
S. K. Nielsen, K. Hansen, M. Brandbyge, J. M. van Ruitenbeek and F. Besenbacher, in preparation (unpublished).
- [VI] *Bias-dependent peak shift in conductance histograms of atomic-sized platinum contacts*,  
S. K. Nielsen, Y. Noat, M. Brandbyge, R. H. M. Smit, K. Hansen, L. Y. Chen, A. I. Yanson, F. Besenbacher and J. M. van Ruitenbeek, in preparation (unpublished).



# Contents

<b>1</b>	<b>Introduction</b>	<b>1</b>
1.1	Why study nano-sized structures? . . . . .	2
1.2	Feynman's bottom! . . . . .	3
1.3	The six metals: Au, Pt, Ag, Cu, Pd and Ni . . . . .	4
1.4	Structure of the thesis . . . . .	6
	References . . . . .	9
<b>2</b>	<b>Theory of Conductance</b>	<b>11</b>
2.1	From macroscopic to atomic-sized contacts . . . . .	11
2.2	The circular orifice . . . . .	15
2.3	The Landauer-Büttiker formalism . . . . .	18
2.4	The adiabatic approximation . . . . .	21
2.5	Quantized conductance . . . . .	22
2.6	Eigenchannels . . . . .	23
	References . . . . .	24
<b>3</b>	<b>Experimental Realization of ASCs</b>	<b>29</b>
3.1	Introduction . . . . .	30
3.2	Scanning tunneling microscope . . . . .	32
3.3	Mechanically controllable break-junction . . . . .	34
	References . . . . .	37
<b>4</b>	<b>Conductance Histograms</b>	<b>41</b>
4.1	Concept . . . . .	42
4.2	Review . . . . .	45
4.3	The noble metals: Au, Ag and Cu . . . . .	48
4.4	The platinum metals: Pt, Pd and Ni . . . . .	51
	References . . . . .	56

<b>5</b>	<b>Fast and Accurate Electronic Setup</b>	<b>61</b>
5.1	Introduction . . . . .	61
5.2	Block diagram of the setup . . . . .	62
5.3	The current-to-voltage converter . . . . .	63
5.4	Model of the circuit . . . . .	68
5.5	Calibration . . . . .	70
5.6	Calculating $G$ , $I$ , and $V$ . . . . .	71
5.7	Timing the burst . . . . .	72
5.8	Performance on resistors . . . . .	76
5.9	Performance on a breaking Au ASC . . . . .	79
5.10	Summary . . . . .	81
	References . . . . .	82
<b>6</b>	<b>Effect of Impurities on <math>I</math>-<math>V</math> Curves of Au</b>	<b>85</b>
6.1	Introduction . . . . .	86
6.2	Experimental details . . . . .	86
6.3	Current-voltage curves . . . . .	88
6.4	Tight-binding calculations . . . . .	90
6.5	Tunneling through a thin insulating film . . . . .	92
6.6	Conclusion . . . . .	94
6.7	Other effects of contamination on ASCs . . . . .	95
6.7.1	Exposing ASCs of Au to ambient conditions . . . . .	95
6.7.2	Monatomic chains with extremely long bond lengths . . . . .	96
6.7.3	Influence of hydrogen on platinum . . . . .	100
6.7.4	Conclusion . . . . .	103
	References . . . . .	104
<b>7</b>	<b>Current-Voltage Curves of ASCs</b>	<b>111</b>
7.1	Experimental details . . . . .	112
7.2	Why gold is Ohmic and platinum is not . . . . .	115
7.2.1	Examples of current-voltage curves . . . . .	115
7.2.2	Fitting to a polynomial . . . . .	116
7.2.3	Density functional theory calculations . . . . .	120
7.2.4	Discussion . . . . .	124
7.2.5	Conclusion . . . . .	126
7.3	Current-voltage curves of noble metals . . . . .	127
7.4	Current-voltage curves of platinum metals . . . . .	131
7.5	Discussion . . . . .	137
7.6	Conclusion . . . . .	140
	References . . . . .	142

<b>8</b>	<b>Current-Induced Disruptions</b>	<b>145</b>
8.1	Motivation . . . . .	145
8.2	Introduction . . . . .	146
8.3	Experimental details . . . . .	147
8.4	Cumulated break probability . . . . .	153
8.5	Dependence on voltage rate . . . . .	155
8.5.1	Cumulated break-current for gold . . . . .	155
8.5.2	Cumulated break-current for copper . . . . .	156
8.5.3	Kolmogorov-Smirnov test and STM experiments . . . . .	159
8.5.4	Cumulated break-current for palladium . . . . .	161
8.6	Comparing the six metals . . . . .	163
8.7	Simple model . . . . .	169
8.7.1	Basic assumptions . . . . .	170
8.7.2	Solution to model . . . . .	172
8.7.3	Fitting to real data . . . . .	173
8.8	Discussion . . . . .	174
8.9	Conclusion . . . . .	177
	References . . . . .	179
<b>9</b>	<b>Bias Dependence of Pt Histograms</b>	<b>181</b>
9.1	Introduction . . . . .	182
9.2	Bias-dependent histograms . . . . .	183
9.3	Comparison with current-voltage curves . . . . .	185
9.4	Plateau-length histograms . . . . .	188
9.5	Return histograms . . . . .	192
9.6	Discussion . . . . .	193
9.7	Conclusion . . . . .	195
	References . . . . .	196
<b>10</b>	<b>Outlook</b>	<b>199</b>
	References . . . . .	202
<b>11</b>	<b>Danish Summary</b>	<b>203</b>
<b>A</b>	<b>Interpretation of Fits to <math>I</math>-<math>V</math> Curves</b>	<b>213</b>
<b>B</b>	<b>Applying Selection Criteria to <math>I</math>-<math>V</math> Curves</b>	<b>217</b>
<b>C</b>	<b>Reliability of the Fitting Procedure</b>	<b>221</b>



# Chapter 1

## Introduction

**Nano!** The buzz word in science today. We hear words like nano-science, nano-technology, nano-machines, nano-structures, nano-wires etc. The word controls the money flow in research, which I find rather amusing, since it originates from Greek: *Nanos*, meaning dwarf. People of this stature were, amongst other, made famous by the well-known fellows presented below [1].

Nano is often used as a prefix for units, as in *nanometer* (nm) — a billionth part of a meter. It is indeed also on the nano-scale that all types of nano-science are practiced. A few nanometers is the typical length-scale for simple molecules and it will already be longer than the interatomic distances in bulk metal. The nano-scale is generally too small to be imaged with the wavelength of visible light ( $\lambda \approx 400\text{--}800\text{ nm}$ ), but methods for imaging these tiny structures exist!

This *thesis* will, however, focus on the electronic properties of nano-wires. But how did these nano-structures become such a hot topic in the first place?



*The Seven Nanos. Is it those from the first paragraph?*

## 1.1 Why study nano-sized structures?

In computer technology the scale of transistors and interconnects on the microchips has already decreased into the sub-micrometer regime. The number of integrated circuits on a chip has doubled approximately every year since the first microprocessor was built in 1971. This tendency is known as Moore's law [2], after the predictions of Gordon Moore, one of the co-founders of Intel [3]. His prediction, from 1975, was based on the development since 1965 and he only expected it to last another ten years out. Notwithstanding, Moore's law still holds today at a point where almost 42 million transistors can be packed onto one single chip.<sup>1</sup> The doubling rate has, however, recently slowed down to "only" once every year and a half.

In the continued development of smaller and faster components, several obstacles had to be overcome. Every time a major problem arose, better methods were invented avoiding any serious slow-down of the miniaturization. In a few years new and serious problems will arise again. One of these seems impossible to avoid, as it is based on a fundamental physical limit: In a transistor, the gate oxide layer insulates the voltage electrode from the current-carrying electrodes. The gate oxide is the narrowest feature of the transistor, and today it is only a few nanometers thick. The problem is based in the fact that the silicon oxide ( $\text{SiO}_2$ ) layer has to be at least five silicon (Si) atoms thick to remain insulating [4]. We are now approaching the "end of the road" for silicon very fast and according to predictions, the limit will already be reached in 2012 [4]. A completely new approach seems to be the only way to bypass the problem.

Another serious factor for the performance of microchips is the interconnects connecting the different components. In the first decades of producing microchips, the wiring was only a small part of the chip and did not affect the overall performance. Today the interconnects have become the largest part of the chip, and the increasing resistance  $R$  gives rise to the main limitation of the speed through the relaxation time  $\tau = RC_p$  [5], with  $C_p$  the parasitic capacitance.

The line width of the finest interconnects is at present only 130 nm [5], and the wires have for long been invisible in light microscopes. They are now so small that half a million of these wires are needed before the bundle is as thick as a hair. Making them even thinner leads to higher resistance and increasing problems with the heat dissipation of the microchip.

While the fundamental research of today might not prevent the "end of the road" for silicon, the methods to be used in future computers must develop from basic investigations like those presented in this thesis.

---

<sup>1</sup>The 2000: Pentium® 4 Processor from Intel [3].

## 1.2 Feynman's bottom!

On the opposite page we found that the physical limit of the gate oxide thickness will soon be reached, but what is the corresponding limit for the dimensions of the interconnects? The answer to this question was given as early as in 1959 when Richard P. Feynman discussed the numerous possibilities of miniaturization in his visionary talk "There's Plenty of Room at the Bottom" [6]. Apart from predicting the development of several techniques in use today, e.g. the design of smaller computer components using evaporating techniques, he mainly focused on the absolute smallest building block: The *atom*. Feynman's bottom is the individual atom, which he proposed should be used directly to build electronic components. From this we find that the smallest possible interconnect consists of a wire of single atoms.

Monatomic wires represent the smallest possible connection between two objects. The electrons carrying a current through these constrictions will be influenced by quantum physics, and the classical laws will no longer apply.

Several fundamental questions comes to mind:

1. Will it ever be possible to achieve long-term stable atomic-sized wires?
2. What is then the definition of long-term; hours, days, weeks, . . . , years?
3. If these wires are ever obtained, will they be of any use in nano-computers?

At the moment none of these question can be answered and it might never be possible to use nano-wires on an industrial scale. If, however, the development of computers continue during this new millennium, the diameter of the interconnects will reach atomic dimensions in a good fifty years. With the increasing interest for using single molecules as functional units [7, 8] performing the task of, for example, a transistor [9, 10], nano-scale interconnects will soon be needed. The importance of this was underlined since, according to Science, the breakthrough of the year 2001 was nanocircuits, with focus on the successful wiring of several molecular devices [11].

With the above considerations in mind, we have gone all the way down to *Feynman's bottom* [6] and investigated monatomic metal contacts, or in general atomic-sized contacts (ASCs). These structures are also often referred to as nano-wires or even quantum point contacts (QPCs). Since we investigate metal contacts with typically only one to ten atoms at the apex, I choose to describe them as *atomic-sized contacts*. This is the most appropriate term since the term nano-wires covers a broader range from much larger contacts ( $\sim 10$  nm) [12–14] down to monatomic chains [15, 16], exotic configurations which we usually

avoid in most of our experiments. The term QPCs is more appropriately used to describe microscopic features fabricated on semiconducting heterostructures [17–19].

Our investigation has mainly focused on increasing the understanding of the electrical properties of ASCs by measuring current-voltage ( $I$ - $V$ ) curves under different conditions. The quantum effects are very important, and several interesting phenomena are discovered. Another subject of this thesis is the investigation of the stability of monatomic metal contacts or chains towards applied current. Both issues are very important when using ASCs as interconnects.

### 1.3 The six metals: Au, Pt, Ag, Cu, Pd and Ni

The noble metal gold (Au) has been the object of our main focus, and it has turned out to be very easy to work with. Also platinum (Pt) — neighbor of Au in the periodic table — has been investigated in detail. The position of Au and Pt and their neighboring metals in the periodic table is depicted in Fig. 1.1. We have also performed experiments using samples of the four transition metals situated above Au and Pt in the periodic table, i.e. the remaining *noble metals* silver (Ag) and copper (Cu) and the two other *platinum metals* palladium (Pd) and nickel (Ni). The noble and the platinum metals are framed in Fig. 1.1.

I am aware that the definitions given here for the noble and especially the platinum metals are not generally accepted [20]. Since Au is the most noble (i.e. inert)<sup>2</sup> of all the metals [21], it makes sense to use the term for Au. Also Ag will only react with very few substances, but Cu might not really qualify as particularly noble. For these three metals the correct term is actually the coinage metals [20] due to their former usage, but within the research field investigating ASCs, it has become widespread practice to use noble metals instead.

The concept of platinum metals usually covers the six transition metals with Pt at one corner and then from there one metal up and two metals to the left in the periodic table [20].<sup>3</sup> However, in this thesis, I stick to the definitions of the noble and the platinum metals as stated in Fig. 1.1.

I will often refer to the relation between two or more of these six metals, and

---

<sup>2</sup>The same property which has provided the name for the noble gases.

<sup>3</sup>This definition of the platinum metals hence include Pt, Pd, iridium (Ir), rhodium (Rh), osmium (Os), and ruthenium (Ru) [20]. It has Pt and Pd in common with our definition but Ni is not included. The six metals studied in this thesis also have Pt in one corner, but from there it is one metal to the right and two metals up instead.

Excerpt from the  
Periodic Table of the Elements

(9)		(10)	(11)	(12)
← VIII →			IB	IIB
Co Cobalt	Platinum metals	Ni Nickel	Cu Copper	Zn Zinc
Rh Rhodium		Pd Palladium	Ag Silver	Cd Cadmium
Ir Iridium		Pt Platinum	Au Gold	Hg Mercury

Noble metals

Figure 1.1: This excerpt from the periodic table of the elements [20], shows a group of transition metals in which the six metals studied in this thesis are framed. The noble metals are Au, Ag and Cu, and the platinum metals are Pt, Pd and Ni. These definitions can be debated. When referring to the relative position of a metal I use the terms neighbor, upper neighbor(s) and group (see text for further details).

several different terms will be used. With Fig. 1.1 as a reference point, it should be possible to avoid any doubt as to the meaning. As an example we find that for Au, the *neighbor* is Pt, the *upper neighbor(s)* is Ag (and Cu), and finally Au belongs to a *group* — the noble metals: Au, Ag and Cu. These concepts will be widely used in chapters, where all six metals are discussed.

The noble metals are iso-electronic and they hence share several properties. The platinum metals *do not* share the same electronic structure, but although distinct differences are found, they *do* behave similarly in many respects.

## 1.4 Structure of the thesis

Most chapters in this thesis are based either on the experimental results obtained during my PhD or on a description of the experimental setups we have used. However, in several chapters I present either data measured or theoretical calculations performed by other scientists. These results contribute with valuable pieces of information to increase the general understanding of our observations. In this context I also mention that several figures have either been provided by others, or re-printed/adapted from earlier publications with the authors' permission. All these contributions are very much appreciated.

Chapter 2 provides a brief introduction to the theory of conductance through ASCs. Here important concepts and units related to the conductance of contacts from macroscopic down to the Ångström<sup>4</sup> length scale will be defined.

In Chapter 3, the two experimental methods used to form ASCs will be discussed. These include the scanning tunneling microscope (STM) and the mechanically controllable break-junction (MCBJ) technique. The STM imaging method is a non-contact scanning of the microscope tip over the surface and it allows us to obtain images like the CAMP logo on the cover of this thesis, and even atomic resolution can be achieved on a daily basis. We have rather used the STM to form ASCs by indenting the tip into the sample followed by a subsequent retraction. The MCBJ method is better suited for the formation of ASCs than the STM, since it is constructed with this as its sole purpose. The ASCs form between the two fractured surfaces of a broken metal wire (the sample). Both methods creates the ASCs under ultra-clean conditions.

In Chapter 4, I follow up on the formation of ASCs with a presentation of the most used method to investigate their properties: The *conductance histogram*. I will often use the term histogram, when there is no risk of confusion (see the description of Chapter 9). By compiling a conductance histogram, the preferred conductance values of ASCs are revealed. Although it is not the main focus of this thesis, it forms an important subset of our experimental results. Together with a discussion of the concept and a detailed review, examples of conductance histograms will be presented for all six metals.

When ASCs are formed with the STM at room temperature (RT) under ultra-high vacuum (UHV) they are very unstable and will diffuse out of contact in milliseconds. To measure  $I$ - $V$  curves on these metastable structures we have developed an ultra-fast and very accurate experimental setup. The development of this setup is the subject of Chapter 5.

---

<sup>4</sup>Ångström is the unit used when measuring atomic distances:  $1 \text{ \AA} = 0.1 \text{ nm} = 10^{-10} \text{ m}$ .

In Chapter 6, we used our fast setup to measure  $I$ - $V$  curves on ASCs for the first time. We formed the contacts at RT in the UHV-STM between the Au tip and the Au sample. The effect of contamination on the  $I$ - $V$  behavior is investigated, and it is found that the  $I$ - $V$  curves are almost linear (Ohmic) when a clean Au contact is formed under UHV. Non-linear  $I$ - $V$  curves are, however, observed if the sample is not cleaned properly under UHV after exposure to air. Tight-binding (TB) calculations confirm the linearity of the clean Au contacts, and a simple barrier model explains the non-linear curves with tunneling through an insulating film formed on the surface of the Au sample. If the tip is only pressed lightly towards the surface (*soft* indentation) the contamination layer will be squeezed between two metal electrodes and no metallic contact will be obtained. This may on the other hand be achieved with the so-called *hard* indentations, where the tip breaks through the surface layer.

An extensive review will be given in the last section of this chapter, presenting a deeper insight into the possible influence of contaminations. Three main issues will be discussed in detail: 1) Experiments with ASCs obtained on Au samples which have been exposed to ambient conditions (RT in air). 2) Experiments where monatomic chains with extremely long bond lengths have been observed. 3) An experiment where ASCs are formed after hydrogen ( $H_2$ ) has been introduced into the vacuum chamber.

In Chapter 7, the MCBJ, which works at liquid helium (He) temperature (4.2 K) under cryogenic vacuum, is used to study  $I$ - $V$  curves on the noble and the platinum metals. Whereas the linearity of  $I$ - $V$  curves on Au is confirmed, we find that the  $I$ - $V$  curves are clearly non-linear for Pt. A density functional theory (DFT) calculation confirms the results, and the differences between Au and Pt are explained by their different outer electronic structures. The other two noble metals, Ag, and Cu, also display very linear  $I$ - $V$  curves. For the remaining platinum metals, Pd and Ni, the  $I$ - $V$  curves are, as for Pt, clearly non-linear but they do not behave exactly like Pt.

In Chapter 8, *current-induced disruptions* of *monatomic* contacts are investigated. By increasing the applied voltage over a monatomic contact until it breaks, the stability towards large currents can be tested. It turns out that Au is by far the most stable of the metals, and the current of 234  $\mu$ A sustained by the single most stable monatomic Au contact resulted in the highest current density ever measured: 3.3 GA/mm<sup>2</sup>! (In a light bulb the current density is only about 1 A/mm<sup>2</sup>). In contrast, ASCs of Ni and Pd are less stable and break at much lower currents than any of the other four metals. Even for these monatomic contacts, the current density will, however, be enormous when compared to macroscopic contacts.

In Chapter 9, the bias dependence of Pt conductance histograms is investigated. For Au, the position of the peaks in the conductance histogram was previously shown to be bias independent. For Pt, however, the first peak clearly shifts to higher conductances when the bias increases past 300 mV. We use three different types of histograms<sup>5</sup> together with  $I$ - $V$  curves to show that this is not related to an electronic effect, but rather to a geometric transition where monatomic chains are replaced by monatomic contacts.

In Chapter 10, a brief outlook on the future possibilities can be found, and a Danish resume will be given in Chapter 11 for the interested non-specialist.<sup>6</sup>

Finally the three appendices will provide a detailed description of the fitting of  $I$ - $V$  curves. The interpretation of the fitting is discussed in Appendix A, and the selection criteria used to sort the  $I$ - $V$  data are described in Appendix B. In the last, Appendix C, we show, by use of different test experiments, that the fitting procedure is reliable.

For the convenience of the reader, I define acronyms like ASC and STM the first time they appear in any chapter, and references can be found at the end of each chapter. In this way it will be possible to read each chapter independently from the others, although several cross referencing between the chapters occur.

---

<sup>5</sup>Apart from the conductance histograms, we also compile plateau length histograms revealing preferred disruption lengths of monatomic chains, and return histograms, which are a type of conductance histograms compiled from *forming* ASCs as opposed to the *breaking* ASCs used for all other conductance histograms presented in this thesis.

<sup>6</sup>It also represents a possibility for anyone, who can read Danish, to find out what I have achieved over the four years of my PhD, by only reading 10 pages instead of flicking through all 224 pages of this bulky thriller.

## References

- [1] In English/Danish: The seven dwarfs/De syv små dværge from the left in the figure — Sleepy/Søvning, Sneezzy/Prosit, Bashful/Flovmand, Happy/Lystig, Doc/Brille, Dopey/Dumpe and Grumpy/Gnavpot, have all been drawn by Marianne Larsen and can be downloaded from: <http://www.papirclipzen.dk/>. © M. Larsen *not* Disney!
- [2] G. E. Moore, “Progress in digital integrated electronics,” In *International Electron Devices Meeting.*, Technical Digest pp. 11–13 (New York, 1975).
- [3] For more information visit the Intel museum: <http://www.intel.com/intel/intelis/museum/>.
- [4] M. Schulz, “The end of the road for silicon?,” *Nature* **399**, 729–730 (1999).
- [5] The International Technology Roadmap for Semiconductors (Can be downloaded from <http://public.itrs.net/Files/2001ITRS/Home.htm> in pdf format).
- [6] R. P. Feynman, “There’s Plenty of Room at the Bottom,” 1959, talk at the Annual Meeting of The American Physical Society at California Institute of Technology. Available on the web at <http://www.zyvex.com/nanotech/feynman.html>.
- [7] R. Dagani, “Taking baby steps to ‘moletronics’,” *Chemical and Engineering News* **January 3**, 22–26 (2000).
- [8] M. A. Reed and J. M. Tour, “Computing with Molecules,” *Sci. Am.* **June**, 68–75 (2000).
- [9] J. Park, A. N. Pasupathy, J. I. Goldsmith, C. Chang, Y. Yaish, J. R. Petta, M. Rinkoski, J. P. Sethna, H. D. Abruña, P. L. McEuen and D. C. Ralph, “Coulomb blockade and the Kondo effect in single-atom transistors,” *Nature* **417**, 722–725 (2002).
- [10] W. Liang, M. P. Shores, M. Bockrath, J. R. Long, and H. Park, “Kondo resonance in a single-molecule transistor,” *Nature* **417**, 725–729 (2002).
- [11] Breakthrough of the year: Nanocircuits, *Science* **294**, issue 5551, (2001). See R. F. Service, “Molecules Get Wired,” 2442–2443.

- 
- [12] Y. Kondo and K. Takayanagi, “Gold Nanobridge Stabilized by Surface Structure,” *Phys. Rev. Lett.* **79**, 3455–3458 (1997).
- [13] Y. Kondo and K. Takayanagi, “Synthesis and Characterization of Helical Multi-Shell Gold Nanowires,” *Science* **289**, 606–508 (2000).
- [14] Y. Oshima, H. Koizumi, K. Mouri, H. Hirayama, K. Takayanagi, and Y. Kondo, “Evidence of a single-wall platinum nanotube,” *Phys. Rev. B* **65**, 121401 (2002).
- [15] V. Rodrigues, T. Fuhrer, and D. Ugarte, “Signature of Atomic Structure in the Quantum Conductance of Gold Nanowires,” *Phys. Rev. Lett.* **85**, 4124–4127 (2000).
- [16] S. B. Legoas, D. S. Galvão, V. Rodrigues, and D. Ugarte, “Origin of Anomalously Long Interatomic Distances in Suspended Gold Chains,” *Phys. Rev. Lett.* **88**, 076105 (2002).
- [17] M. A. Topinka, J. LeRoy, S. E. J. Shaw, E. J. Heller, R. M. Westervelt, K. D. Maranowski, and A. C. Gossard, “Imaging Coherent Electron Flow from a Quantum Point Contact,” *Science* **289**, 2323–2326 (2000).
- [18] M. A. Topinka, B. J. LeRoy, R. M. Westervelt, S. E. J. Shaw, R. Fleischmann, E. J. Heller, K. D. Maranowskik, and A. C. Gossardk, “Coherent branched flow in a two-dimensional electron gas,” *Nature* **410**, 183–186 (2001).
- [19] G.-P. He, S.-L. Zhu, and Z. D. Wang, “Conductance of a quantum point contact in the presence of a scanning probe microscope tip,” *Phys. Rev. B* **65**, 205321 (2002).
- [20] N. N. Greenwood and A. Earnshaw, *Chemistry of the Elements* (Butterworth-Heinemann Ltd., Linacre House, Jordan Hill, Oxford, 1984), definition of the platinum and coinage metals can be found on page 1242 and 1364, respectively.
- [21] B. Hammer and J. K. Nørskov, “Why gold is the noblest of all the metals,” *Nature* **376**, 238–240 (1995).

## Chapter 2

# Theory of Conductance

Throughout all the experiments presented in this thesis, we are basically measuring the resistance  $R$  of atomic-sized metal contacts. We try, however, to do this in a sophisticated manner, using many different experimental conditions, to obtain useful information on the properties of these metal nanostructures. Rather than the resistance, the equivalent conductance  $G = 1/R$  will be used, since, as we shall see, conductance is the most natural quantity in the description of electron transport through metal contacts.

This chapter presents a brief introduction to the theory of conductance for atomic-sized contacts (ASCs). I begin with a discussion of the three fundamentally different regimes which guide the electron transport in a contact, when its dimension decreases the several orders of magnitude from macroscopic to atomic size (see Fig. 2.1). I will then compare the ASC with a *circular orifice* before introducing the Landauer-Büttiker formalism used to describe the electron transport in ASCs, where inclusion of quantum effects is essential. With the adiabatic approximation the phenomenon of *quantized conductance* (QC) can be explained, which is finally related to the fact, that the electrons are conducted through individual transmission channels — the so-called *eigenchannels*, which can actually be investigated experimentally, not only theoretical.

### 2.1 From macroscopic to atomic-sized contacts

Although the line width of interconnects on today's microchips is only 130 nm wide [1] this is still many orders of magnitude larger than an ASC, as illustrated in Fig. 2.1. With this ruler, I indicate the dimension range over which the three

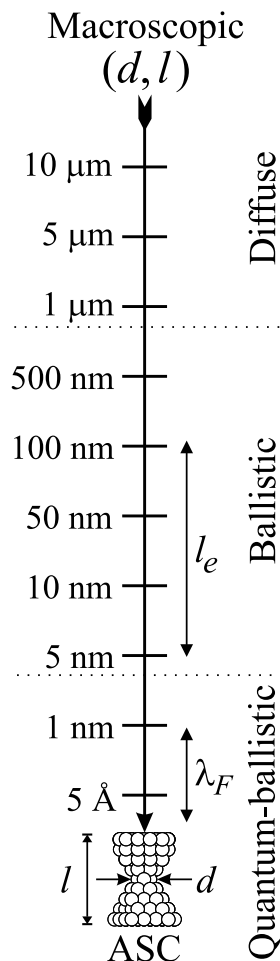


Figure 2.1: Dimension ruler, for contact diameter and length  $(d, l)$ , extending from macroscopic to ASCs. The typical length scales for the three different electron transport regimes are indicated.

different electron transport regimes determine the conductance. Also typical spans for the mean free path of the electron  $l_e$  and the Fermi wavelength  $\lambda_F$  are shown. The type of electron transport will depend on whether or not one of these length scales are comparable to the dimension of the contact, i.e. its diameter and length  $(d, l)$ .

Although the ruler stretches over many orders of magnitude, it will in general always be possible to describe any contact, even those from each end of the ruler, by three different section types: Contact, transition areas and electrodes. In Fig. 2.2 this is illustrated for a contact (diameter  $d$  and length  $l$ ) connected through the transition areas to the surrounding world, i.e. the two 3DEG electrodes.

As the macroscopic world is three-dimensional (3D), the electrodes will behave like a 3D electron gas (3DEG), in which the electron transport is diffuse. If also the contact size is macroscopic the electron transport will be diffuse over the entire constriction. In the diffuse electron transport regime electrons will mainly scatter in bulk, and the influence of scattering at the boundary of the constriction is limited. This will be valid as long as the dimension of the contact is much larger than the mean free path of the electrons:  $(d, l) \gg l_e$ . The mean free path of the electron will be in the 1–100 nm

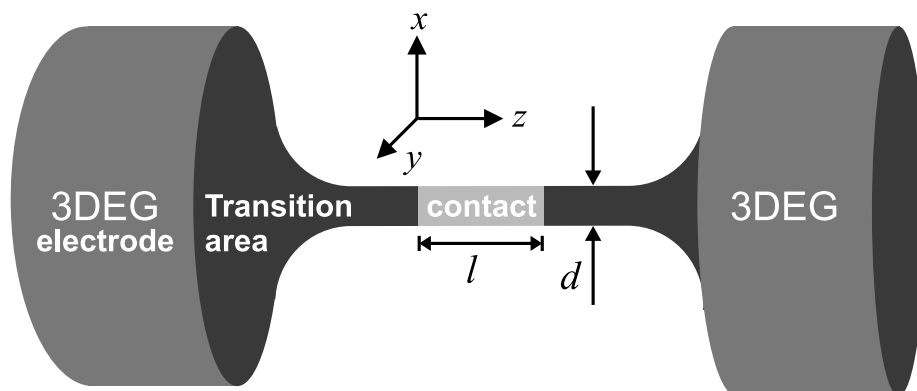


Figure 2.2: Model of a cylinder-symmetric *constriction* consisting of a *contact* with length  $l$  and diameter  $d$  connected with two macroscopic 3DEG *electrodes* through the *transition areas*. All contacts consist of these three sections. The current flows through the contact parallel to the  $z$ -direction. (Adapted from: [3]).

range<sup>1</sup> at room temperature (RT) [2], and the diffuse electron transport regime will cover all “macroscopic” constrictions with dimensions  $(d, l)$  down to but not much smaller than the micrometer-scale (see Fig. 2.1).

When discussing electron transport in relation to Fig. 2.2, I distinguish the conductance of the actual contact  $G_{\text{contact}}$ , from the total conductance of the entire constriction  $G$ . The *constriction* conductance will both depend on  $G_{\text{contact}}$  and on the connection of the electrodes with the contact through the transition areas, which becomes exceedingly important as the contact dimensions decreases into the realm of the microscopic world.

The transition areas are in general microscopic and will only make a small contribution to the total conductance  $G$  of a macroscopic constriction. In this case  $G_{\text{contact}}$  will for most experimental measurements be indistinguishable from  $G$  and can be calculated independently of the transitions areas from the contact geometry and the material-dependent conductivity  $\sigma$ .

A particularly simple relation is found when the contact is a macroscopic

<sup>1</sup>The mean free path for the metals investigated in this thesis — the noble and the platinum metals (cf. Fig. 1.1 on page 5) — are typically in the 10 nm range at RT [2].

wire with length  $L$  and area  $A$ :

$$G_{\text{wire}} = \frac{\sigma A}{L}. \quad (2.1)$$

From this relation the unit for  $\sigma$  is inferred to be conductance per length ( $\Omega^{-1}/\text{m}$ ). Relations similar to Eq. (2.1) can be used to find the diffuse conductance of any macroscopic contact geometry.

In general, the *total* conductance of a constriction like in Fig. 2.2 can be found experimentally by measuring the current  $I$  resulting from an applied voltage  $V$ . The conductance is then given by Ohm's law:

$$G = \frac{I}{V}. \quad (2.2)$$

If the transition areas can be disregarded (i.e. macroscopic contacts) the total conductance  $G$  obtained from Ohm's law<sup>2</sup> will be indistinguishable from  $G_{\text{contact}}$  obtained from equations like (2.1).

When the size of a contact decreases the transition areas become increasingly important for the total conductance  $G$  of the constriction (cf. Fig. 2.2). This relation arises since the electron behavior will be determined by three fundamentally different types of transport, which changes from the *diffuse* over the *ballistic* into the *quantum-ballistic* electron transport regime, as we slide down the ruler in Fig. 2.1 from macroscopic to atomic dimensions.

Whereas Ohm's law [Eq. (2.2)] is applicable in all three regimes, a relation like Eq. (2.1) breaks down when the contact dimensions become comparable to  $l_e$ , [ $(d, l) \sim l_e$ ]. Here, scattering with the boundaries of the constriction is too important to be neglected, and the electron transport in the contact is no longer diffusive but quasi-ballistic. In the limit where  $l_e \gg (d, l)$  the electron transport becomes truly ballistic, scattering in the interior of the contact can be neglected, and electrons move ballistically through the contact. In the ballistic electron transport regime the only scattering occurs elastically at the boundaries of the contact, and no energy is lost to inelastic scattering in the interior of the contact.<sup>3</sup>

When the contact size decreases down to atomic-scale (i.e. an ASC) its dimensions will be on the Ångström length scale. This is comparable to the Fermi

<sup>2</sup>For a contact with constant  $G$  (e.g. macroscopic resistors in electronic circuits), the current-voltage ( $I$ - $V$ ) characteristic will be linear. This is often referred to as Ohmic behavior, and the concept will be used later, as for example in the title of Sec. 7.2.

<sup>3</sup>For a contact with  $d$  and/or  $l \lesssim 10$  nm there is of course only a very small volume available for scattering, in accordance with the resulting ballistic electron transport.

wavelength  $\lambda_F$ , which, for most metals, lie in the 3–10 Å range [2]. Quantum effects will be important, and in the quantum-ballistic electron transport regime the electrons can form standing waves orthogonal to the current flow (see Fig. 2.5). This can result in a quantization of the conductance in units of

$$G_0 = \frac{2e^2}{h} \simeq \frac{1}{12.9 \text{ k}\Omega}, \quad (2.3)$$

where  $e$  is the elementary charge and  $h$  is Planck's constant.  $G_0$  is the fundamental unit of conductance, used extensively throughout this thesis. Electron transport in such a contact is to a good approximation one-dimensional (1D). The value of  $G_0$  will be derived for exactly such a geometry in Sec. 2.3.

## 2.2 The circular orifice

The circular orifice is a good approximation for the geometry of a small contact between two large electrodes, both for macroscopic contacts and especially for an ASC, as illustrated in Fig. 2.3. In the figure, both the contact atoms of the ASC (left) and the circular orifice (right) are white. In this way they can easily be distinguished from the connecting metal electrodes (grey).

Each electrode is modeled as occupying the entire half space on their respective side of the ASC/orifice, and in the case of the ASC, a “perfect” vacuum separates these from each other [Fig. 2.3 (left)]. In the model (right), a similar separation of the orifice electrodes corresponding to this vacuum, is realized by placing an infinitesimally thin, but perfectly insulating plane, indicated by the black slab, between the two semi-infinite electrodes. The only connection between the two electrodes will be through a small hole in the plane with diameter  $d$  and area  $A = \pi(d/2)^2$ : The *circular orifice*.

The model also applies when  $d$  is macroscopic and the electron transport is diffuse. In this case the orifice resembles a wire with zero length ( $L = l \equiv 0$ ). This geometry should in principle give rise to an infinite conductance [Eq. (2.1)] ( $R = 1/G \equiv 0$ ), but this is not what is observed. The orifice do in fact not qualify as a true macroscopic contact, since it is infinitesimally thin. In reality, it only consist of the two endpoints, and we can of course no longer neglect the transition areas (see Fig. 2.2). We now need to take into account the connection between the orifice and the electrodes through these areas, and what we actually find is the total conductance  $G$  of the entire constriction.

The conductance of an orifice with a macroscopic diameter was calculated

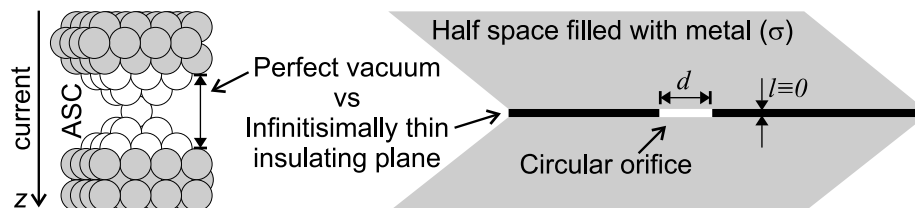


Figure 2.3: The figure displays the similarities between an ASC (the monatomic contact to the left) and the model used to describe a circular orifice with a diameter  $d$  and zero length  $l$  (right). The current flows parallel to the  $z$ -direction through the white contact atoms/orifice connected to the grey electrodes. The black slab ( $l \equiv 0$ ) corresponds to the vacuum at the ASC. It isolates the two semi-infinite half spaces filled with metal of conductivity  $\sigma$  completely from each other, and a current between them, can only flow through the small hole with diameter  $d$ : The *circular orifice*.

by Maxwell as early as in 1892 [4]. When the metal has a conductivity  $\sigma$ , the conductance of the Maxwellian orifice is:

$$G_M = \sigma d. \quad (2.4)$$

Since the only length scale describing the circular orifice is the diameter  $d$ , this is also the only combination with  $\sigma$  resulting in the correct unit of conductance.

It is interesting that the area  $A$  only relates to the conductance through  $d$  which was not the case in Eq. (2.1). However, these two equations should not be compared directly, since Eq. (2.1) gives  $G_{\text{wire}}$  for a macroscopic wire, with a length much longer than the diameter  $l \gg d$ , whereas Eq. (2.4) gives  $G_M$  for an infinitely short wire, the orifice, with  $l \equiv 0 \ll d$ .

Since Maxwell's calculation assumes that the electron transport is diffuse, it will no longer hold when the contact size decreases so that  $d$  becomes comparable to  $l_e$ . In the limit where  $d \ll l_e$ , ballistic electron transport determines the conductance. In general it is always possible to calculate the conductance for the ballistic orifice [5], but the band structure  $E(\mathbf{k})$  must be taken into account.

In the case of a free-electron metal, a particularly simple formula was derived in 1965 by Sharvin [6]:

$$G_S = \frac{\pi A}{\lambda_F^2} G_0. \quad (2.5)$$

In the expression for the Sharvin conductance  $G_S$ , the fundamental unit of conductance  $G_0$  [Eq. (2.3)] appears for the first time. Here it is the area  $A$ , which relates the dependence of the constriction geometry. The conductance no longer depends on  $\sigma$ , but the material dependence still enters through  $\lambda_F$ . The simplicity of the formula comes from the spherical Fermi surface of a free-electron metal resulting in a simple band structure. The alkali metals, with a single  $s$  electron in the outer shell, represent the best approximation to this [2]. The noble metals are also almost free-electron-like [2], since their outer electron structure is similar to that of the alkali metals. The noble metals (cf. Fig. 1.1 on page 5) will be investigated extensively in later chapters.

As for the Maxwellian orifice, the conductance is not infinite in the Sharvin formula, due to the connection of the orifice with the surrounding world through the transition areas. Since the electrons move ballistically, no energy will, however, be lost to inelastic scattering in the contact. The energy will instead, be dissipated<sup>4</sup> at the interface between the ballistic electron transport region and the electron reservoirs (electrodes). The ballistic region has an extension of the order of  $l_e$ , and the interface can in principle be located far away relative to the contacts dimensions.

The conductance of the orifice itself may actually be infinite, which can be found if the four-terminal conductance<sup>5</sup> is measured [8]. In general we always measure the two-terminal conductance in our experiments and it will not be possible to disregard the connection between contact and electrodes through the transition areas.

The Sharvin result is valid down to a conductance around 3–4  $G_0$  (for most metals this will correspond to ASCs with only a few atoms at the apex), but it will break down at a conductance below this limit [9–12]. Even with different corrections applied [9, 10], not all quantum effects can be included. In order to understand the behavior of the constriction conductance in the quantum-ballistic electron transport regime, we must now consult the Landauer-Büttiker formalism.

---

<sup>4</sup>Since  $G_S$  is finite, energy *will* be dissipated when a current runs through the constriction [7], but this will not happen in the actual contact.

<sup>5</sup>In the four-terminal geometry a current is driven through the far ends of the constriction, and the conductance is extracted from the voltage drop measured between the inner two terminals placed at the contact. Since these do not interfere directly, but only probes the electric potential, they bypass any contributions from the transition areas, and gives the conductance of the actual contact  $G_{\text{contact}}$  [8]. The two outer terminals would measure the normal two-terminal conductance  $G$  as found in Eqs. (2.4) and (2.5).

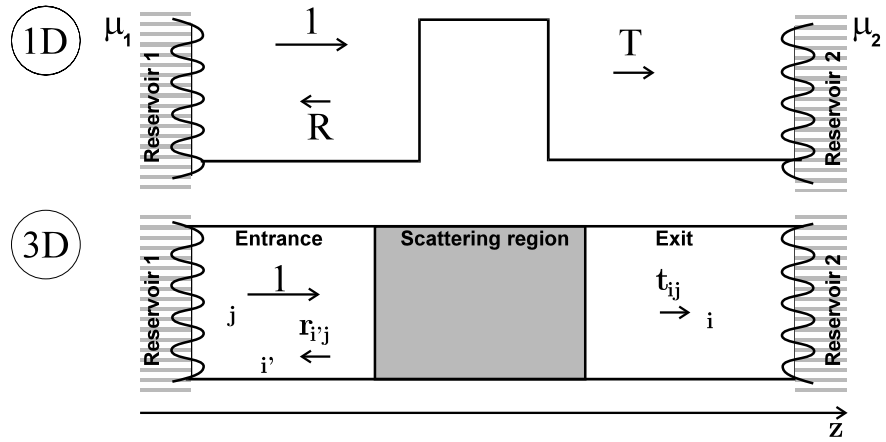


Figure 2.4: The Landauer model: The *electron reservoirs* are characterized by their chemical potential  $\mu_1$  and  $\mu_2$ . With  $\mu_1 \gtrsim \mu_2$  electrons move to the right ( $z$ -direction), and current flows to the left. For the 1D conductor the reservoirs connect to a simple potential barrier described by its transmission and reflection of an incoming channel ( $T, R, 1$ ). The 3D reservoirs are connected through the *entrance/exit* with the *scattering region* represented by transmission and reflection amplitudes for the complete set of incoming channels at the Fermi energy  $E_F$  ( $t_{ij}, r_{i'j}, \mathbf{1}$ ) (Adapted from: [18]).

## 2.3 The Landauer-Büttiker formalism

The Landauer-Büttiker formalism [13–17] describes the electronic transport through ASCs taking quantum effects into account. I will treat both the simple 1D model and the realistic 3D system depicted in Fig. 2.4.

### The one-dimensional case

The 1D conductor in Fig. 2.4 has a simple potential barrier characterized by the transmission probability  $T$ . Two macroscopic electrodes acting as electron reservoirs connects with the conductor. There is an infinitesimal difference in the chemical potential  $\mu$  between the two electrodes ( $\mu_1 \gtrsim \mu_2$ ) and the electrons will move to the right resulting in a current to the left.

In the 1D case, current  $I$  and current density  $j$  are equivalent quantities and

generally the transmitted current will hence be given as the product of charge  $e$ , mean velocity  $v_e$  and density  $n_e$  of the electrons multiplied with the transmission probability  $T$ . With a 1D density of states  $dn_e/dE$ , where  $E$  refers to the band structure  $E(k)$ , and a current carried by electrons in the energy window  $[\mu_1; \mu_2]$ <sup>6</sup> we find

$$I = e \frac{dn_e}{dE} (\mu_2 - \mu_1) v_e T. \quad (2.6)$$

We write the density of states  $dn_e/dE$  as  $(dn_e/dk)(dk/dE) = 1/\pi(dk/dE)$ . The density of  $k$ -states  $dn_e/dk = 1/\pi$ , since an extra factor of two, due to the spin degeneracy,<sup>7</sup> should be multiplied to  $1/2\pi$ , the density of  $k$ -points in 1D [2].

The 1D mean electron velocity is given by  $v_e = (2\pi/h)(dE/dk)$  [2], and we observe that all dependence on the band structure  $E(k)$  disappears from Eq. (2.6). Introducing the voltage drop  $V$  over the electrodes by substituting  $eV = (\mu_2 - \mu_1)$  the current is obtained as:

$$I = \frac{2e^2}{h} VT = G_0 VT. \quad (2.7)$$

Here the fundamental unit of conductance<sup>7</sup> [Eq. (2.3)] finally drops out of the calculations, and using Ohm's law [Eq. (2.2)], we find the two-terminal 1D conductance [15, 19–21]

$$G_{1D} = G_0 T. \quad (2.8)$$

Even for a perfect conductor ( $T = 1$ ), the conductance will be finite. This is no longer surprising since it is the cause of the coupling between the 1D conductor (contact) and the electron reservoirs (the electrodes) as was the case with the Sharvin result in Eq. (2.5). Note that in the expression for the conductance there is no longer any material-dependent parameters. In Sec. 2.6, I briefly mention how the choice of material will affect the conductance anyway.

<sup>6</sup>At zero temperature (0 K) we have  $[\mu_1; \mu_2] \equiv [(\mu_2 - E_F) - (\mu_1 - E_F)] = \mu_2 - \mu_1$ . At finite temperatures, the energy window will extend to energies further away from the Fermi energy  $E_F$  due to the thermal activation of electrons. This will, however, not cause a problem, since it is possible to find the current by integrating over the electrons Fermi-Dirac distribution [15, 16].

<sup>7</sup>If the spin degeneracy disappears, like for a ferromagnetic metal placed in a magnetic field, the fundamental unit of conductance will rather be  $G_0/2 = e^2/h$ . This unit is observed with the quantum Hall effect. See also the description of ferromagnetic metals in Sec. 4.4.

## The three-dimensional case

Using the same arguments leading to the 1D result in Eq. (2.8) it is straightforward to obtain a similar result in three dimensions. The 3D model in Fig. 2.4 can be directly related with the different section types composing the constriction in Fig. 2.2. We find the following correspondence:

### The **constriction** vs The **3D model**

3DEG electrodes  $\Leftrightarrow$  Electron reservoirs

Transition areas  $\Leftrightarrow$  Entrance/exit

Contact  $\Leftrightarrow$  Scattering region

As can be seen in Fig. 2.4 we now have to consider a complete set of eigenstates or channels at the Fermi energy  $E_F$  on both sides of the constriction. When a channel  $j$  is incident on the constriction from the left, it can either be transmitted to channel  $i$  on the right side of the scattering region or be reflected back to channel  $i'$  on the left side. We are interested in calculating the corresponding transmission amplitude  $t_{ij}$ . The two-terminal conductance will then be given on the same form as Eq. (2.8), and we obtain the Landauer-Büttiker formula [14, 15]

$$G_{3D} = G_0 \text{Tr} (\mathbf{t}^\dagger \mathbf{t}) , \quad (2.9)$$

where  $\text{Tr}$  denotes the trace and  $\mathbf{t}$  is a transmission matrix containing the elements  $t_{ij}$ .<sup>8</sup> In the Landauer-Büttiker formula it is clearly stated that “conductance is transmission” [22]. The total transmission

$$T_{\text{tot}} \equiv \text{Tr} (\mathbf{t}^\dagger \mathbf{t}) = \sum_{i,j} |t_{ij}|^2 \quad (2.10)$$

depends on the actual constriction geometry and will be affected if the geometry is changed, e.g by removing individual atoms from the contact region<sup>9</sup> as in our experiments were ASCs are formed, stretched and finally broken (see next chapter).

<sup>8</sup>The dagger symbol denotes the Hermitian conjugate.

<sup>9</sup>In the quantum-ballistic electron transport regime where the Landauer-Büttiker formalism will be used, the contact will always be atomic-sized (ASCs).

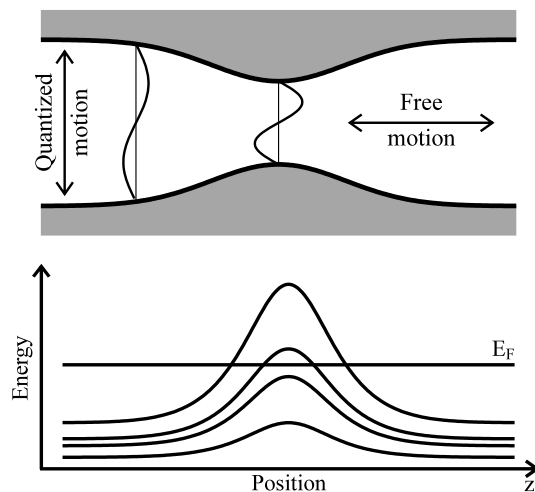


Figure 2.5: The adiabatic picture. The upper panel illustrates the two orthogonal types of electron motion occurring in a smooth atomic-sized contact configuration: Free motion along the  $z$ -direction (current flow), and quantized motion orthogonal to  $z$  (standing waves). The lower panel gives the variation of the transverse kinetic energy  $E_i^\perp(z)$  for four transmission channels as a function of the position  $z$  in the contact. The horizontal line indicates the level of the Fermi energy  $E_F$ . Channels entirely below  $E_F$  are open, but when  $E_i^\perp(z) > E_F$  for any  $z$ , the channel will behave like an energy barrier preventing direct transmission of the electrons. Tunneling may, however, occur [26]. (Adapted from: [25]).

## 2.4 The adiabatic approximation

The adiabatic approximation [23–25] can be applied when the constriction cross section varies slowly on the scale of  $\lambda_F$ . This will resemble the smooth contact configuration depicted in the upper panel of Fig. 2.5. In the approximation the transverse quantized motion is separated from the free motion. If the constriction is considered as having a hard wall, with zero potential inside and infinite potential outside, the transverse motion is reduced to that of a two-dimensional particle in a box. The individual transmission channel  $i$  will have the kinetic energy  $E_i^\perp(z)$  due to the transverse motion. The  $z$ -coordinate refers to the position in the constriction, which is also the direction of free motion and hence

current flow. In the lower panel of Fig. 2.5 the variation of  $E_i^\perp(z)$  is plotted for four different transmission channels as a function of the position in the smoothly varying constriction. Each of these resembles a potential barrier, one of which must be passed in order for an electron to be transmitted through the contact.

The channels never cross each other due to the decoupling of the transverse and free motion in the adiabatic approximation. From this we get that the off-diagonal elements in the transmission matrix  $\mathbf{t}$  from the Landauer-Büttiker formula [Eq. (2.9)] will be zero since there is no mixing between the channels. Then  $\text{Tr}(\mathbf{t}^\dagger\mathbf{t}) = \sum_i |t_{ii}|^2 = \sum_i T_i$ , where  $T_i = |t_{ii}|^2$  is the transmission probability for traversing the effective potential barrier in  $E_i^\perp(z)$ , and we can now write the adiabatic conductance as

$$G_{\text{ad}} = G_0 \sum_i T_i. \quad (2.11)$$

In this way the 3D Landauer-Büttiker formula is simplified to resemble the 1D formula in Eq. (2.8).

## 2.5 Quantized conductance

If the adiabatic approximation is taken to the limit, the potential barriers in  $E_i^\perp(z)$  caused by the transverse kinetic energy will be very wide on the scale of  $\lambda_F$ . For such a situation the transmission probability  $T_i$  of an adiabatic channel will be a step function, switching from one, when  $E_i^\perp(z)$  stays completely below  $E_F$ , to zero if  $E_i^\perp(z)$  reaches above  $E_F$  for any value of  $z$ . In the lower panel of Fig. 2.5 the behavior of  $E_i^\perp(z)$  is illustrated with four channels. Since the two upper channels are above  $E_F$  they are closed. Hence only two channels are open and the conductance of the constriction will be  $G = 2 G_0$ .

The energy  $E_i^\perp(z)$  will increase if the diameter of the constriction decreases. This will eventually force the next channel to cross  $E_F$  reducing the conductance with  $1 G_0$ . In general, when the diameter of an adiabatic constriction becomes smaller, the conductance will decrease in sharp steps between integer values of  $G_0$ . This effect is called *quantized conductance* (QC).

Experimentally, QC was first observed in a two-dimensional electron gas (2DEG) on GaAs-AlGaAs heterostructures [27, 28]. In these structures the mean free path of the electron is, however, much longer (1–10  $\mu\text{m}$ ) than in metals (cf. Fig. 2.1). Nevertheless, a behavior resembling QC has also been observed for ASCs formed from most of the free-electron-like metals, i.e. the noble [25, 29–34] and the alkali metals [3, 34, 35]. Most often this has been observed using the conductance histograms, as discussed in Chapter 4, where

also examples of noble metal histograms will be presented (Fig. 4.3 on page 49). For all free-electron-like metals a clear histogram peak at  $G \simeq 1 G_0$  is found. Peaks at higher conductances will, on the other hand, not always be situated exactly at an integer value of  $G_0$  (see Sec. 4.2).

## 2.6 Eigenchannels

In the general case (lower panel of Fig. 2.4) it is always possible to make a unitary transformation of the basis set of incoming and outgoing states thereby defining a special set of channels that do not mix under any circumstances [17, 36–38]. This is the *eigenchannels* for which all off-diagonal elements in the transformed transmission amplitude matrix  $\bar{\mathbf{t}}$  are zero. Since the trace of a matrix is invariant under unitary transformations, we now have

$$\mathrm{Tr}(\mathbf{t}^\dagger \mathbf{t}) = \mathrm{Tr}(\bar{\mathbf{t}}^\dagger \bar{\mathbf{t}}) = \sum_i |\bar{t}_{ii}|^2. \quad (2.12)$$

From this the two-terminal 3D Landauer-Büttiker formula [Eq. (2.9)] can be simplified to

$$G_{3D} = G_0 \sum_i T_i, \quad (2.13)$$

where  $T_i = |\bar{t}_{ii}|^2$  is the eigenchannel *transmission probability* of the  $i$ th eigenchannel. This transformation is advantageous since the behavior of the conductance is then, again, determined by the transmission probabilities of single, independent channels as was the case in the adiabatic approximation [Eq. (2.11)].

Eigenchannels are not only a mathematical abstraction. They can actually be measured experimentally by use of several different methods [34, 39–45] described briefly in the review of Sec. 4.2. A very important conclusion from these experiments is that the maximum number of conducting eigenchannels for a monatomic metal contact is equivalent to the number of valence electrons [40], i.e. one channel for Au, three for aluminum (Al), six for platinum (Pt) and so on. In this way the conductance will still depend on the choice of metal, even though there is no direct material-dependence in Eq. (2.13). These valence channels are, however, not always fully open; some may even be completely closed, as for Pt where only four partially open channels contribute to the conductance of a monatomic contact (see Sec. 7.2.3). Only the free-electron-like metals display QC, and even for these metals the quantization will disappear at a conductance above a few  $G_0$ .

## References

- [1] The International Technology Roadmap for Semiconductors (Can be downloaded from <http://public.itrs.net/Files/2001ITRS/Home.htm> in pdf format).
- [2] N. W. Ashcroft and N. D. Mermin, *Solid State Physics* (Holt, Rinehart and Winston, New York, 1976).
- [3] A. I. Yanson, “Atomic Chains and Electronic Shells: Quantum Mechanisms for the Formation of Nanowires,” PhD thesis, Rijksuniversiteit Leiden, 2001. (Can be downloaded from <http://lions1.leidenuniv.nl/wwwhome/ruitenbe/ThesisAlex.pdf>).
- [4] J. C. Maxwell, *A Treatise on Electricity and Magnetism* (Oxford University Press, London, 1892), Vol. 1, p. 426–434.
- [5] D. Sánchez-Portal, C. Untiedt, J. M. Soler, J. J. Sáenz, and N. Agraït, “Nanocontacts: Probing Electronic Structure under Extreme Uniaxial Strains,” *Phys. Rev. Lett.* **79**, 4198–4201 (1997).
- [6] Y. V. Sharvin, “A possible method for measuring Fermi surfaces,” *Zh. Eksp. Teor. Fiz.* **48**, 984–985 (1965), [*Sov. Phys. JETP* **21**, 655 (1965)].
- [7] T. N. Todorov, “Local heating in ballistic atomic-scale contacts,” *Philos. Mag. B* **77**, 965–973 (1998).
- [8] R. de Picciotto, H. L. Stormer, L. N. Pfeiffer, K. W. Baldwin, and K. W. West, “Four-terminal resistance of ballistic quantum wire,” *Nature* **411**, 51–54 (2001).
- [9] J. A. Torres, J. L. Pascual, and J. J. Sáenz, “Theory of conduction through narrow constrictions in a three-dimensional electron gas,” *Phys. Rev. B* **49**, 16581–16584 (1994).
- [10] A. García-Martín, J. A. Torres, and J. J. Sáenz, “Finite size corrections to the conductance of ballistic wires,” *Phys. Rev. B* **54**, 13448–13451 (1996).
- [11] A. M. Bratkovsky, A. P. Sutton, and T. N. Todorov, “Conditions for conductance quantization in realistic models of atomic-scale metallic contacts,” *Phys. Rev. B* **52**, 5036–5051 (1995).
- [12] E. N. Bogachek, A. G. Scherbakov, and U. Landman, “Shape effects on conductance quantization in three-dimensional nanowires: Hard versus soft potentials,” *Phys. Rev. B* **56**, 1065–1068 (1997).

- 
- [13] R. Landauer, "Spatial Variation of Currents and Fields Due to Localized Scatterers in Metallic Conduction," *IBM J. Res. Dev.* **1**, 223–231 (1957).
- [14] D. S. Fisher and P. A. Lee, "Relation between conductivity and transmission matrix," *Phys. Rev. B* **23**, 6851–6854 (1981).
- [15] Y. Imry, "Physics of mesoscopic systems," in *Directions in Condensed Matter Physics*, G. Grinstein and G. Mazenko, eds., (World Scientific, Singapore, 1986), pp. 101–163.
- [16] M. Büttiker, Y. Imry, R. Landauer, and S. Pinhas, "Generalized many-channel conductance formula with application to small rings," *Phys. Rev. B* **31**, 6207–6215 (1985).
- [17] M. Büttiker, "Coherent and sequential tunneling in series barriers," *IBM J. Res. Dev.* **32**, 63–75 (1988).
- [18] M. Brandbyge, "Conductance of Metal Nanocontacts," PhD thesis, Technical University of Denmark, 1997.
- [19] E. N. Economou and C. M. Soukoulis, "Static Conductance and Scaling Theory of Localization in One Dimension," *Phys. Rev. Lett.* **46**, 618–621 (1981).
- [20] R. Landauer, "Electrical Transport in Open and Closed Systems," *Z. Phys. B* **68**, 217–228 (1987).
- [21] R. Landauer, "Conductance determined by transmission: probes and quantised constriction resistance," *J. Phys. Cond. Matt.* **1**, 8099–8110 (1989).
- [22] Y. Imry and R. Landauer, "Conductance viewed as transmission," *Rev. Mod. Phys.* **71**, S306–S312 (1999).
- [23] L. I. Glazman, G. B. Lesovik, D. E. Khmel'nitskii, and R. I. Shekhter, "Reflectionless quantum transport and fundamental ballistic-resistance steps in microscopic constrictions," *Pis'ma Zh. Eksp. Teor. Fiz.* **48**, 218–220 (1988), [*JETP Lett.* **48**, 238 (1988)].
- [24] É. N. Bogachev, A. N. Zagoskin, and I. O. Kulik, "Conductance jumps and magnetic flux quantization in ballistic point contacts," *Fiz. Nizk. Temp.* **16**, 1404–1411 (1990), [*Sov. J. Low Temp. Phys.* **16**, 796 (1990)].

- 
- [25] M. Brandbyge, J. Schiøtz, M. R. Sørensen, P. Stoltze, K. W. Jacobsen, J. K. Nørskov, L. Olesen, E. Lægsgaard, I. Stensgaard, and F. Besenbacher, “Quantized conductance in atom-sized wires between two metals,” *Phys. Rev. B* **52**, 8499–8514 (1995).
- [26] A. García-Martín, T. López-Ciudad, J. A. Torres, A. J. Caamaño, J. I. Pascual, and J. J. Sáenz, “Differential conductance in atomic-scale metallic contacts,” *Ultramicroscopy* **73**, 199–203 (1998).
- [27] B. J. van Wees, H. van Houten, C. W. J. Beenakker, J. G. Williamson, L. P. Kouwenhoven, D. van der Marel, and C. T. Foxon, “Quantized Conductance of Point Contacts in a Two-Dimensional Electron Gas,” *Phys. Rev. Lett.* **60**, 848–850 (1988).
- [28] D. A. Wharam, T. J. Thornton, R. Newbury, M. Pepper, H. Ahmed, J. E. F. Frost, D. G. Hasko, D. C. Peacock, D. A. Ritchie, and G. A. C. Jones, “One-dimensional transport and the quantisation of the ballistic resistance,” *J. Phys. C* **21**, L209–L214 (1988).
- [29] N. Agraït, J. G. Rodrigo, and S. Vieira, “Conductance steps and quantization in atomic-size contacts,” *Phys. Rev. B* **47**, 12345–12348 (1993).
- [30] J. I. Pascual, J. Méndez, J. Gómez-Herrero, A. M. Baró, N. García, and V. T. Binh, “Quantum Contact in Gold Nanostructures by Scanning Tunneling Microscopy,” *Phys. Rev. Lett.* **71**, 1852–1855 (1993).
- [31] J. M. Krasn, C. J. Muller, I. K. Yanson, T. C. M. Govaert, R. Hesper, and J. M. van Ruitenbeek, “One-atom point contacts,” *Phys. Rev. B* **48**, 14721–14724 (1993).
- [32] L. Olesen, E. Lægsgaard, I. Stensgaard, F. Besenbacher, J. Schiøtz, P. Stoltze, K. W. Jacobsen, and J. K. Nørskov, “Quantized Conductance in an Atom-Sized Point Contact,” *Phys. Rev. Lett.* **72**, 2251–2254 (1994).
- [33] K. Hansen, E. Lægsgaard, I. Stensgaard, and F. Besenbacher, “Quantized Conductance in Relays,” *Phys. Rev. B* **56**, 2208–2220 (1997).
- [34] B. Ludoph and J. M. van Ruitenbeek, “Conductance fluctuations as a tool for investigating the quantum modes in atomic size metallic contacts,” *Phys. Rev. B* **61**, 2273–2285 (2000).

- 
- [35] J. M. Krans, J. M. van Ruitenbeek, V. V. Fisun, I. K. Yanson, and L. J. de Jongh, “The signature of conductance quantization in metallic point contacts,” *Nature* **375**, 767–769 (1995).
- [36] T. Martin and R. Landauer, “Wave-packet approach to noise in multichannel mesoscopic systems,” *Phys. Rev. B* **45**, 1742–1755 (1992).
- [37] M. Brandbyge and K. W. Jacobsen, “Quantum transmission channels in perturbed 3D nanowires,” In *Proceedings of the NATO Advanced Research Workshop on Nanowires, Madrid 1996*, P. A. Serena and N. García, eds., NATO ASI pp. 61–78 (Kluwer, Dordrecht, 1997).
- [38] M. Brandbyge, M. R. Sørensen, and K. W. Jacobsen, “Conductance eigenchannels in nanocontacts,” *Phys. Rev. B* **56**, 14956–14959 (1997).
- [39] E. Scheer, P. Joyez, D. Esteve, C. Urbina, and M. H. Devoret, “Conduction Channel Transmissions of Atomic-Size Aluminum Contacts,” *Phys. Rev. Lett.* **78**, 3535–3538 (1997).
- [40] E. Scheer, N. Agraït, J. C. Cuevas, A. L. Yeyati, B. Ludoph, A. Martín-Rodero, G. R. Bollinger, J. M. van Ruitenbeek, and C. Urbina, “The signature of chemical valence in the electrical conduction through a single-atom contact,” *Nature* **394**, 154–157 (1998).
- [41] H. E. van den Brom and J. M. van Ruitenbeek, “Quantum Suppression of Shot Noise in Atom-Size Metallic Contacts,” *Phys. Rev. Lett.* **82**, 1526–1529 (1999).
- [42] B. Ludoph, M. H. Devoret, D. Esteve, C. Urbina, and J. M. van Ruitenbeek, “Evidence for Saturation of Channel Transmission from Conductance Fluctuations in Atomic-Size Point Contacts,” *Phys. Rev. Lett.* **82**, 1530–1533 (1999).
- [43] B. Ludoph and J. M. van Ruitenbeek, “Thermopower of atomic-size metallic contacts,” *Phys. Rev. B* **59**, 12290–12293 (1999).
- [44] H. E. van den Brom, “Noise properties of atomic-size contacts,” PhD thesis, Rijksuniversiteit Leiden, 2000.
- [45] B. Ludoph, “Quantum Conductance Properties of Atomic-size Contacts,” PhD thesis, Rijksuniversiteit Leiden, 1999.



## Chapter 3

# Experimental Realization of Atomic-Sized Contacts

When two macroscopic metal objects are placed in contact with each other they will not touch over their entire contact surface. Macroscopic objects are rough on the atomic scale, and the actual contact between the two metal surfaces only occurs at points where small protrusions emerge from the surface. In principle, *atomic-sized contacts* (ASCs) will form at each of these points as shown in Fig. 3.1. When these two surfaces are moved apart all the connections will break one by one, eventually separating the metals completely.

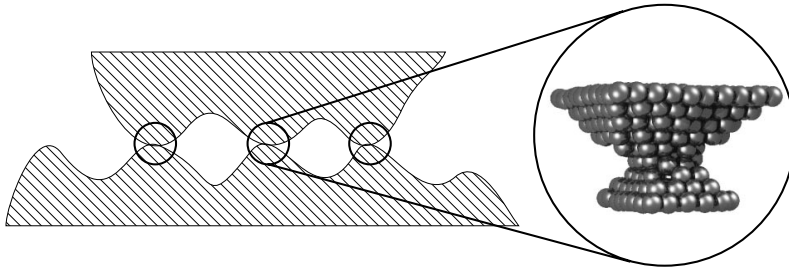


Figure 3.1: Illustrative sketch showing how the formation of atomic-sized contacts (ASCs) will occur between two metal surfaces when they are brought into close contact. (Adapted from: [1]).

Just before the separation is completed a single ASC may be the only connection left between the two macroscopic objects. While the distance between the surfaces continues to increase, atoms will be pulled out of this remaining contact, making it thinner until it consists, in the ultimate limit, of only one atom at the apex. This process is illustrated in Fig. 3.2 by four snapshots from a molecular dynamics simulation. It shows the atomic configuration during the indentation and subsequent retraction of a scanning tunneling microscope (STM) tip in contact with a flat surface [2].

Even though the monatomic contact represents the thinnest possible metal wire, its conductance will usually be much larger than that from tunneling between the two connecting metal surfaces. This implies that the current resulting from an applied voltage difference between the two metal surfaces will run entirely through the contact. By measuring this current we can obtain valuable information on the conductance and several other properties of ASCs.

To do so, experimental setups are, however, required with which the formation of ASCs can be controlled, keeping them stable long enough for the experiments to be performed. In this chapter different methods used to obtain ASCs will be discussed and a detailed description of the two methods used for the experiments presented in this thesis will be given.

### 3.1 Introduction

One of the first methods used to investigate ASCs was the STM, which when developed in 1982 [3] was a breakthrough in surface science, since it became possible to image the position of individual atoms on a conducting surface in real-space. The imaging process is a non-contact method, where the tunneling current between tip and sample is kept constant while the tip scans the surface. By indenting the tip into the sample surface a contact is formed and a slow retraction of the tip allows the formation of an ASC, as illustrated in Fig. 3.2.

The formation of ASCs using the STM was first investigated in 1987 [4]. It was, however, not until the early nineties that the STM was used to investigate the electrical properties of ASCs, resulting in the discovery of quantized conductance (QC) [5, 6] (see Sec. 2.5 and 4.2). Since then the STM has been widely used to investigate ASCs, both in air at room temperature (RT) (ambient conditions) [6–11], under ultra-high vacuum (UHV) [2, 12–14] and at liquid helium (He) temperature (4.2 K) [5, 15–18].

The first mechanically controllable break-junction (MCBJ) [19, 20] was an improved version of a break junction constructed in order to perform experiments with superconducting tunneling [21]. In contrast to the STM, the sole

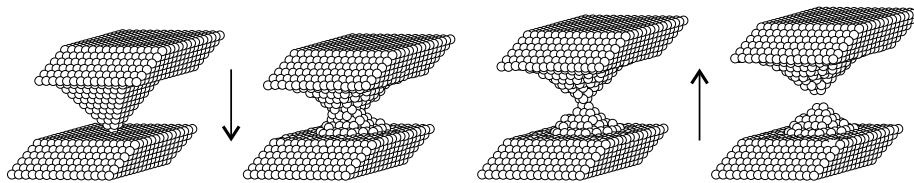


Figure 3.2: Four snapshots from a molecular dynamics simulation of the atomic configuration during the indentation and subsequent retraction of an STM tip. In the process an ASC is formed between the tip and sample surface, and right before the contact breaks there may only be a single atom at the apex. (Adapted from: [2]).

purpose of the MCBJ is to form ASCs. In the MCBJ a metal wire is broken under cryogenic vacuum at 4.2 K, and two freshly exposed surfaces are formed from bulk material. Since they have never been exposed to ambient conditions, they will be free from any external impurities. ASCs can now be formed by moving the two surfaces in and out of contact, resulting in a process similar to the one depicted for the STM in Fig. 3.2. Due to the cryogenic vacuum the system can remain free from contamination for days, allowing a detailed investigation of ASCs [17, 18, 22–31].

Apart from these two widely utilized methods, a few other techniques have been applied to form ASCs; of these mechanical relays are the most used [32–38]. The ASCs are formed when the relay contact is switched on and off. In some cases the relay is self-cleaning, as the electrodes slides against each other when the contact closes [32]. Apart from this no cleaning of the metal surface is possible. The relay contact has in a few experiments been under vacuum [32, 38] but UHV has not been used. Most experiments have been performed in air, although in some cases the relay has been encapsulated in an atmosphere of nitrogen ( $N_2$ ) with 5% hydrogen ( $H_2$ ) [36, 37], or submersed in liquid helium [34].

The final method to be mentioned here is also the most simple where the ASCs are formed between two macroscopic wires moving in and out of contact with each other [9, 39, 40]. The method is similar to the relay experiments, but here it is even more difficult to ensure clean contact surfaces.

The extreme importance of keeping the sample free of contamination when investigating the electronic properties of ASCs are discussed in Chapter 6. This is also one of the main reasons that we have used a UHV-STM (papers [I, II]) and a MCBJ (papers [III–VI]) for the work presented in this thesis. Below these two experimental methods will be described.

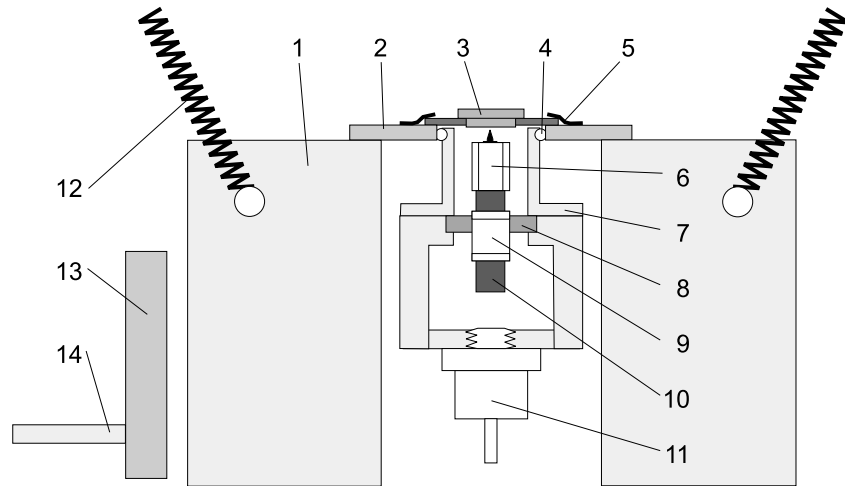


Figure 3.3: Cross-sectional sketch of the Aarhus STM. (1) Aluminum (Al) cradle, (2) top plate, (3) sample in sample holder, (4) quartz balls, (5) leaf springs, (6) scanner piezo tube and tip, (7) STM housing, (8) ceramic disc, (9) inchworm motor, (10) silicon carbide (SiC) axle, (11) zener diode, (12) suspending strings, (13) cold finger, (14) liquid nitrogen feed through. Minor differences are found in the design of the individual STMs, but the general features are always the same. (From: [43]).

## 3.2 Scanning tunneling microscope

The STM used in our experiments was developed at the University of Aarhus and it is known as the Aarhus STM [41, 42]. The STM is placed in a UHV chamber with a base pressure of  $10^{-10}$  mbar. The chamber is also equipped with sputtering and annealing facilities. A sketch of the STM is depicted in Fig. 3.3, and the numbers below refer to the legend of the figure. One of the advantages of the Aarhus STM is its compactness combined with the suspension of the aluminum (Al) cradle (1). Only very high mechanical resonance frequencies will affect the STM itself, and the suspension from the strings (12) effectively decouples the STM from any highfrequency noise in its surroundings. Due to this fact, amongst other, it is possible to obtain atomic resolution in the scanning mode on a daily basis (see Fig. 3.4a). In our experiments we focus on the ability to form ASCs, where this high stability is equally important.

One of the most complicated tasks is the coarse approach, i.e. moving the tip from macroscopic into atomic distances (1 mm to  $10 \text{ \AA}$ ). This is achieved by

moving the silicon carbide (SiC) axle (10) with the piezo inchworm motor (9) mounted on the ceramic disc (8). Fine approach is controlled by the scanner piezo tube (6). The tip (6) is usually made from tungsten (W) when the STM is used for scanning, whereas the same material is used for both tip and sample when ASCs are formed. The sample is mounted in the sample holder (3) and due to the loose mounting in the leaf springs (5) it can be changed with other samples placed inside the chamber. The top plate (2) connects the sample thermally to the Al cradle. The STM housing (7) is thermally isolated from the Al cradle via three quartz balls (4). Quartz is used because it is a very good thermic isolator. This isolation is needed in order to keep the STM at RT when cooling the sample. Cooling can be achieved by moving the cold finger (13) into contact with the Al cradle. By pumping liquid nitrogen ( $N_2$ ) at 77 K through the finger (14), a sample temperature down to around 130 K can be reached. Due to vibrations from the pumping of nitrogen, it is not possible to cool and measure at the same time. After cooling, the temperature rises slowly with 10–20 K/hour. The zener diode (11) is used to counter-heat the STM in order to avoid thermal drift. This implies that the tip is at RT even when the sample is cold; a fact to be considered when making lowtemperature experiments. The zener diode is UHV compatible, and a high voltage type is chosen due to the small current it requires to obtain a high power. This is important since only very thin electrical wires, which can carry a limited current, should be used inside the UHV chamber, to avoid vibrations and problems with too hot wires.

The STM experiments presented in this thesis have all been performed on gold (Au) ASCs. To ensure Au-Au contact both tip and sample are made of Au. Samples of Au(110) and Au(111) single crystals are used and the tip is cut from a 0.25 mm diameter, 99.99% pure Au wire. At the beginning of each day, the sample must be cleaned with several cycles (3–5) of sputtering with 1.5 keV argon (Ar) ions at 45° incidence followed by annealing to 550°C. The tip can be cleaned by applying voltage bursts between tip and sample or by repeated indentation of the tip into the sample ( $\sim 500$  Å). The sample surface is then examined in the STM scanning mode to see if it is atomically clean before forming the ASCs. STM images of the Au(111) surface displaying atomic resolution and the so-called “herringbone” reconstruction [44] are shown in Fig. 3.4. Both features indicate that the surface is clean on the atomic scale, and we take this as a proof that the sample surface is well-prepared. First then are the tip indented into the sample, and when retracting the tip again, ASCs on a scale down to monatomic contacts can be obtained. At RT, however, the ASCs will be very unstable and diffuse out of contact within milliseconds. In Chapter 5, the building of a fast setup to measure the current-voltage ( $I$ - $V$ ) behavior on these metastable contacts will be described.

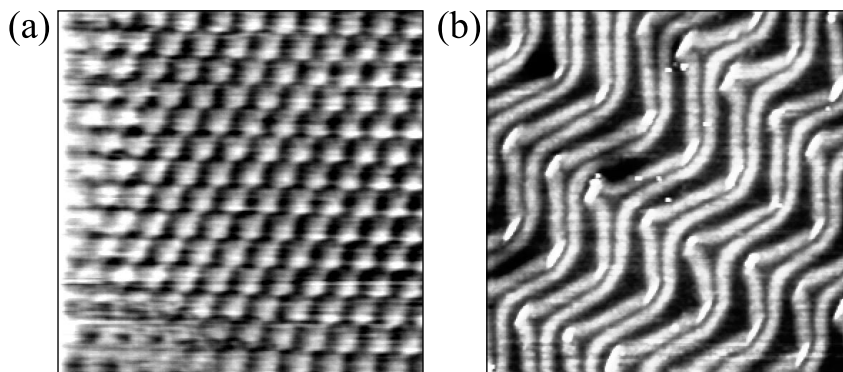


Figure 3.4: STM images of the clean Au(111) surface using a Au tip. (a) Atomically resolved surface ( $30 \times 30 \text{ \AA}^2$ ). (b) The “herringbone” reconstruction ( $500 \times 500 \text{ \AA}^2$ ) [44].

### 3.3 Mechanically controllable break-junction

The MCBJ was first constructed at Leiden University [19, 20], where all MCBJ experiments presented in this thesis have been performed. The MCBJ itself is only one part of the so-called insert used for the experiments. A sketch of the MCBJ is depicted in Fig. 3.5. The sample is made from a wire of high purity metal with a diameter of about 0.1 mm. A notch is cut into the center of the wire with a surgical knife creating a weak spot. Using two drops of epoxy stycast placed as close as possible (about 1 mm apart) on each side of the notch, the wire is glued to a bendable substrate. The substrate is a phosphor bronze plate about 1 mm thick, 4 mm wide and 20 mm long. On top of the plate a thin layer of kapton foil isolates the sample wire from the metal substrate. The wire is connected to the experimental setup through copper wires attached at each end with silver paint. The sample is mounted in a three-point bending device consisting of the stacked piezo crystal at the center of the sample (under the notch) and two counter supports. The MCBJ is placed in a vacuum pot positioned at the end of a one meter long metal tube, which makes it possible to lower the entire pot into liquid helium. All wiring, pumping and mechanical control of the axle holding the piezo go through the pipe to the top of the insert. After pre-pumping to below  $10^{-6}$  mbar, the insert is lowered into a helium vessel and the vacuum pot with the MCBJ is completely submerged under liquid helium. When the temperature reaches the 4.2 K of liquid helium, a cryogenic vacuum is obtained in which all gases, with the exception of helium,

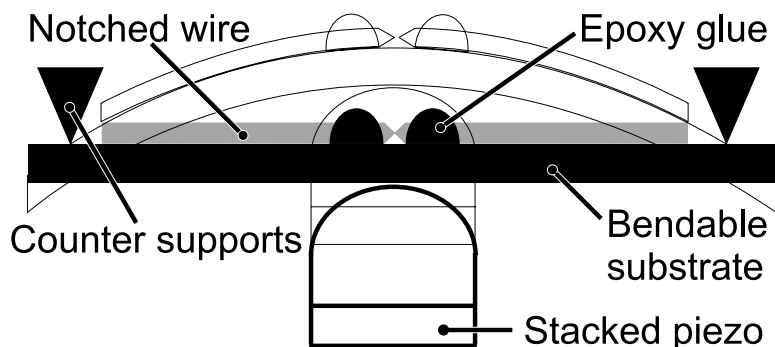


Figure 3.5: Sketch of the MCBJ (see text). Bending of the substrate, by use of the stacked piezo, results in the indicated break of the sample wire at the notch. The sketch is approximate to scale (1:5), but the bending of the sample is exaggerated.

have solidified on the inner surfaces of the vacuum pot. In a cryogenic vacuum all other gases than helium and hydrogen will have a partial pressure far below  $10^{-16}$  mbar [45].<sup>1</sup> For hydrogen, the vapor pressure is  $10^{-6}$  mbar at 4.2 K [45]. Since only small amounts of helium and hydrogen are found in the atmosphere, and due to the pre-pumping, we also expect the partial pressure of these two gases to be very low.<sup>2</sup> It is, however, not possible to measure the actual pressure at the contact inside the vacuum pot.

Under these extremely clean conditions the wire is broken mechanically at the notch by bending the substrate with the center axle as indicated in Fig. 3.5. The break exposes clean fracture surfaces of bulk material, which can stay clean for days due to the low pressure. By retracting the center axle the two new electrode surfaces move back into contact and ASCs can be formed and controlled down to monatomic contacts using the stacked piezo element situated at the end of the axle. The absence of thermal vibration at 4.2 K allows the ASCs to remain stable on a minute timescale and for some metals (e.g. Au) even monatomic contacts can be sustained for minutes.

<sup>1</sup>The third highest partial pressure belongs to the noble gas neon (Ne). At 4.8 K the partial pressure is close to  $10^{-16}$  mbar, but already at 4.2 K the pressure has dropped another two orders of magnitude [45]. All other gases have an even much lower partial pressure [45].

<sup>2</sup>In Sec. 6.7.2 and 6.7.3 the influence of helium on Au and of hydrogen on platinum (Pt) will be discussed, respectively. In both cases the changes in the behavior of the metals are understood. These effects are only observed when letting extra hydrogen or helium into the insert, and we conclude that under normal conditions the partial pressure of hydrogen and helium is so low that it will not affect the experimental results.

When it comes to the investigation of ASCs, the MCBJ has several advantages over the STM:

1. It is a much simpler instrument built with the purpose of forming ASCs.
2. Having only one moving part, the MCBJ is a more stable construction than the STM, which can move in all three dimensions. This increases the stability of the ASCs.
3. The low temperature further increases the stability of the ASCs allowing the measurement to be performed in a completely different time regime compared to RT experiments.
4. The low diffusion rate at a temperature of 4.2 K will help avoid impurities moving into the contact region. This is important as the reactivity increases for the under-coordinated atoms in an ASC (see Sec. 6.7.2).
5. Cryogenic vacuum is better than UHV, with lower partial pressure for all gases but the inert helium. The pressure of hydrogen might be higher than under UHV, but due to the low diffusion rate the risk of contamination will be even further limited at this low temperature.
6. Cryogenic vacuum can be obtained much faster after the vacuum has been broken compared to an UHV chamber. The chamber must be baked 24 hours at  $>120^{\circ}\text{C}$  to obtain UHV conditions again after exposure to air.
7. The MCBJ enables us to investigate many different materials. Samples are more easily obtained from a metal wire than from the perfect crystals needed in the STM. We can control the samples' crystal orientation in the STM, but this is a small advantage when forming ASCs, since we have no knowledge of the crystal orientation of the STM tip.

The UHV-STM has the advantage of being able to measure at high temperatures. With the MCBJ, the clean environment depends on the low temperature. It is possible to heat only the sample, but if the temperature becomes too high, some of the solidified gases on the sample wire will be able to diffuse around, ending up in the contact region.

The first experiments we performed (paper [II]) were only possible with the STM. The investigations were to be compared with other RT measurements, and the possibility of cleaning a contaminated sample was crucial for obtaining the results described in Chapter 6. In order to measure at RT we needed to develop an ultra-fast setup, which will be described in Chapter 5. In the next chapter I will, however, first describe a very simple type of experiments often used in the investigation of ASCs: *Conductance histograms*.

## References

- [1] M. Brandbyge, “Conductance of Metal Nanocontacts,” PhD thesis, Technical University of Denmark, 1997.
- [2] M. Brandbyge, J. Schiøtz, M. R. Sørensen, P. Stoltze, K. W. Jacobsen, J. K. Nørskov, L. Olesen, E. Lægsgaard, I. Stensgaard, and F. Besenbacher, “Quantized conductance in atom-sized wires between two metals,” *Phys. Rev. B* **52**, 8499–8514 (1995).
- [3] G. Binnig, H. Rohrer, C. Gerber, and E. Weibel, “Surface Studies by Scanning Tunneling Microscopy,” *Phys. Rev. Lett.* **49**, 57–61 (1982).
- [4] J. K. Gimzewski and R. Möller, “Transition from the tunneling regime to point contact studied using scanning tunneling microscopy,” *Phys. Rev. B* **36**, 1284–1287 (1987).
- [5] N. Agrait, J. G. Rodrigo, and S. Vieira, “Conductance steps and quantization in atomic-size contacts,” *Phys. Rev. B* **47**, 12345–12348 (1993).
- [6] J. I. Pascual, J. Méndez, J. Gómez-Herrero, A. M. Baró, N. García, and V. T. Binh, “Quantum Contact in Gold Nanostructures by Scanning Tunneling Microscopy,” *Phys. Rev. Lett.* **71**, 1852–1855 (1993).
- [7] J. Abellán, R. Chicón, and A. Arenas, “Properties of nanowires in air. Controlled values of the conductance,” *Surf. Sci.* **418**, 493–501 (1998).
- [8] J. L. Costa-Krämer, “Conductance quantization at room temperature in magnetic and nonmagnetic metallic nanowires,” *Phys. Rev. B* **55**, R4875–R4878 (1997).
- [9] J. L. Costa-Krämer, N. García, P. García-Mochales, P. A. Serena, M. I. Marqués, and A. Correia, “Conductance quantization in nanowires formed between micro and macroscopic metallic electrodes,” *Phys. Rev. B* **55**, 5416–5424 (1997).
- [10] J. I. Pascual, J. Méndez, J. Gómez-Herrero, A. M. Baró, N. García, U. Landman, W. D. Luedtke, E. N. Bogachek, and H.-P. Cheng, “Properties of Metallic Nanowires: From Conductance Quantization to Localization,” *Science* **267**, 1793–1795 (1995).
- [11] G. Rubio, N. Agrait, and S. Vieira, “Atomic-Sized Metallic Contacts: Mechanical Properties and Electronic Transport,” *Phys. Rev. Lett.* **76**, 2302–2305 (1996).

- 
- [12] H. Ohnishi, Y. Kondo, and K. Takayanagi, “Quantized conductance through individual rows of suspended gold atoms,” *Nature* **395**, 780–783 (1998).
- [13] L. Olesen, E. Lægsgaard, I. Stensgaard, F. Besenbacher, J. Schiøtz, P. Stoltze, K. W. Jacobsen, and J. K. Nørskov, “Quantized Conductance in an Atom-Sized Point Contact,” *Phys. Rev. Lett.* **72**, 2251–2254 (1994).
- [14] L. Olesen, E. Lægsgaard, I. Stensgaard, F. Besenbacher, J. Schiøtz, P. Stoltze, K. W. Jacobsen, and J. K. Nørskov, “Reply to ‘Comment on ‘Quantized conductance in an Atom-Sized Point Contact’,’” *Phys. Rev. Lett.* **74**, 2147 (1995).
- [15] J. L. Costa-Krämer, N. García, and H. Olin, “Conductance quantization histograms of gold nanowires at 4 K,” *Phys. Rev. B* **55**, 12910–12913 (1997).
- [16] G. Rubio-Bollinger, S. R. Bahn, N. Agraït, K. W. Jacobsen, and S. Vieira, “Mechanical Properties and Formation Mechanisms of a Wire of Single Gold Atoms,” *Phys. Rev. Lett.* **87**, 026101 (2001).
- [17] E. Scheer, N. Agraït, J. C. Cuevas, A. L. Yeyati, B. Ludoph, A. Martín-Rodero, G. R. Bollinger, J. M. van Ruitenbeek, and C. Urbina, “The signature of chemical valence in the electrical conduction through a single-atom contact,” *Nature* **394**, 154–157 (1998).
- [18] A. I. Yanson, G. R. Bollinger, H. E. van den Brom, N. Agraït, and J. M. van Ruitenbeek, “Formation and manipulation of a metallic wire of single gold atoms,” *Nature* **395**, 783–785 (1998).
- [19] C. J. Muller, J. M. van Ruitenbeek, and L. J. de Jongh, “Experimental observation of the transition from weak link to tunnel junction,” *Physica C* **191**, 485–504 (1992).
- [20] C. J. Muller, J. M. van Ruitenbeek, and L. J. de Jongh, “Conductance and Supercurrent Discontinuities in Atomic-Scale Metallic Constrictions of Variable Width,” *Phys. Rev. Lett.* **69**, 140–143 (1992).
- [21] J. Moreland and J. W. Ekin, “Electron tunneling experiments using Nb-Sn “break” junctions,” *J. Appl. Phys.* **58**, 3888–3895 (1985).
- [22] H. E. van den Brom and J. M. van Ruitenbeek, “Quantum Suppression of Shot Noise in Atom-Size Metallic Contacts,” *Phys. Rev. Lett.* **82**, 1526–1529 (1999).

- 
- [23] J. M. Krans, C. J. Muller, I. K. Yanson, T. C. M. Govaert, R. Hesper, and J. M. van Ruitenbeek, "One-atom point contacts," *Phys. Rev. B* **48**, 14721–14724 (1993).
- [24] J. M. Krans, C. J. Muller, N. van der Post, F. R. Postma, A. P. Sutton, T. N. Todorov, and J. M. van Ruitenbeek, "Comment on "Quantized Conductance in an Atom-Sized Point Contact"," *Phys. Rev. Lett.* **74**, 2146 (1995).
- [25] J. M. Krans, J. M. van Ruitenbeek, V. V. Fisun, I. K. Yanson, and L. J. de Jongh, "The signature of conductance quantization in metallic point contacts," *Nature* **375**, 767–769 (1995).
- [26] B. Ludoph, M. H. Devoret, D. Esteve, C. Urbina, and J. M. van Ruitenbeek, "Evidence for Saturation of Channel Transmission from Conductance Fluctuations in Atomic-Size Point Contacts," *Phys. Rev. Lett.* **82**, 1530–1533 (1999).
- [27] B. Ludoph and J. M. van Ruitenbeek, "Thermopower of atomic-size metallic contacts," *Phys. Rev. B* **59**, 12290–12293 (1999).
- [28] B. Ludoph and J. M. van Ruitenbeek, "Conductance fluctuations as a tool for investigating the quantum modes in atomic size metallic contacts," *Phys. Rev. B* **61**, 2273–2285 (2000).
- [29] E. Scheer, P. Joyez, D. Esteve, C. Urbina, and M. H. Devoret, "Conduction Channel Transmissions of Atomic-Size Aluminum Contacts," *Phys. Rev. Lett.* **78**, 3535–3538 (1997).
- [30] R. H. M. Smit, C. Untiedt, A. I. Yanson, and J. M. van Ruitenbeek, "Common Origin for Surface Reconstruction and the Formation of Chains of Metal Atoms," *Phys. Rev. Lett.* **87**, 266102 (2001).
- [31] A. I. Yanson and J. M. van Ruitenbeek, "Do Histograms Constitute a Proof for Conductance Quantization?," *Phys. Rev. Lett.* **79**, 2157 (1997).
- [32] K. Hansen, E. Lægsgaard, I. Stensgaard, and F. Besenbacher, "Quantized Conductance in Relays," *Phys. Rev. B* **56**, 2208–2220 (1997).
- [33] H. Yasuda and A. Sakai, "Conductance of atomic-scale gold contacts under high-bias voltages," *Phys. Rev. B* **56**, 1069–1072 (1997).
- [34] K. Yuki, A. Enomoto, and A. Sakai, "Bias-dependence of the conductance of Au nanocontacts at 4 K," *Appl. Surf. Sci.* **169–170**, 489–492 (2001).

- [35] K. Itakura, K. Yuki, S. Kurokawa, H. Yasuda, and A. Sakai, "Bias dependence of the conductance of Au nanocontacts," *Phys. Rev. B* **60**, 11163–11170 (1999).
- [36] K. Yuki, S. Kurokawa, and A. Sakai, "Quantized Conductance in Pt Nanocontacts," *Jpn. J. of Appl. Phys.* **39**, 4593–4595 (2000).
- [37] K. Yuki, S. Kurokawa, and A. Sakai, "Conductance in Breaking Nanocontacts of Some Transition Metals," *Jpn. J. of Appl. Phys.* **40**, 803–808 (2001).
- [38] A. Enomoto, S. Kurokawa, and A. Sakai, "Quantized conductance in Au-Pd and Au-Ag alloy nanocontacts," *Phys. Rev. B* **65**, 125410 (2002).
- [39] J. L. Costa-Krämer, N. García, P. García-Mochales, and P. A. Serena, "Nanowire formation in macroscopic metallic contacts: quantum mechanical conductance tapping a table top," *Surf. Sci.* **342**, L1144–L1149 (1995).
- [40] D. M. Gillingham, I. Linington, and J. A. C. Bland, " $e^2/h$  quantization of the conduction in Cu nanowires," *J. Phys. Cond. Matt.* **14**, L567–L570 (2002).
- [41] F. Besenbacher, E. Lægsgaard, K. Mortensen, U. Nielsen, and I. Stensgaard, "Compact, high-stability, "thimble-size" scanning tunneling microscope," *Rev. Sci. Instrum.* **59**, 1035–1038 (1988).
- [42] E. Lægsgaard, L. Österlund, P. Thostrup, P. B. Rasmussen, I. Stensgaard, and F. Besenbacher, "A high-pressure scanning tunneling microscope," *Rev. Sci. Instrum.* **72**, 3537–3542 (2001).
- [43] M. Schunack, "Scanning Tunneling Microscopy Studies of Organic Molecules on Metals Surfaces," PhD thesis, University of Aarhus, 2002.
- [44] J. V. Barth, H. Brune, G. Ertl, and R. J. Behm, "Scanning tunneling microscopy observations on the reconstructed Au(111) surface: Atomic structure, long-range superstructure, rotational domains, and surface defects," *Phys. Rev. B* **42**, 9307–9318 (1990).
- [45] Extrapolated from data of R. E. Honig and H. O. Hook. "Vapor pressure data for some common gases," *RCA Review*, **21**, 360, 1960.

## Chapter 4

# Conductance Histograms

When the interest in atomic-sized contacts (ASCs) exploded in the mid nineties [1], one experiment which was often repeated, was the measurement of *conductance histograms* on ASCs of gold (Au). In Fig. 4.1, we show such a conductance histogram (histogram from now on), in which the peaks reveal the preferred conductance values obtained by breaking ASCs of Au.

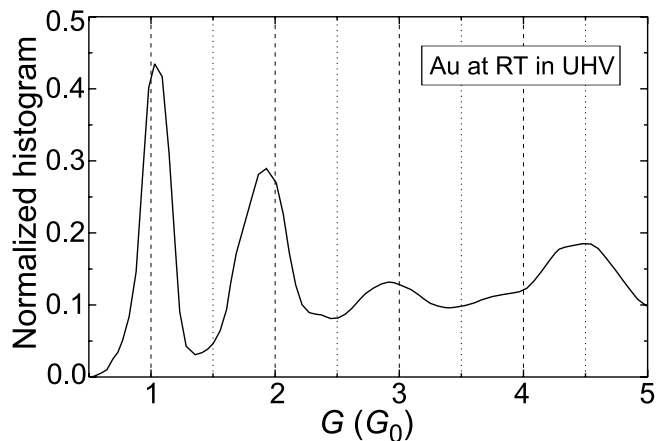


Figure 4.1: Conductance histogram for Au compiled from 485 conductance traces recorded at a bias of 200 mV on breaking ASCs. The contacts were created at room temperature (RT) with the scanning tunneling microscope (STM) between a Au tip and a Au(111) sample surface, cleaned under ultra-high vacuum (UHV) (see Sec. 3.2).

The main reason for this particular interest in Au histograms, was the observation of peaks near integer values of the fundamental unit of conductance  $G_0$ .<sup>1</sup>

This is clear from Fig. 4.1 which displays three peaks at  $nG_0$  with  $n = 1, 2$  and 3, before the quantization breaks with the fourth peak situated at  $4.5 G_0$ . The histogram was recorded with a scanning tunneling microscope (STM) at room temperature (RT) under ultra-high vacuum (UHV) conditions on a cleaned Au(111) sample surface. It has since been shown that similar results can be obtained using many different methods, e.g. at liquid helium (He) temperatures (4.2 K) under cryogenic vacuum in the mechanically controllable break-junction (MCBJ) [see Fig. 4.3a], or even under ambient conditions (in air at RT), e.g. with ASCs formed using mechanical relays<sup>2</sup> [2].

This robustness of the Au histograms was at first concluded to be an effect of quantized conductance (QC). In Sec. 2.5, QC was defined as a state where only fully open transmission channels (eigenchannels) contribute to the conductance of the ASC. Since each fully open channel result in a conductance of  $1 G_0$ , the total conductance will be given on the form  $nG_0$  with  $n$  an integer. It certainly seemed to be the case for Au when  $n \leq 3$  (Fig. 4.1). However, in this chapter, we will show that this conclusion is not entirely correct.

Below the concept of histograms are described, followed by a review of the development and understanding of these. Finally, examples of histograms will be presented for the six metals treated in this thesis (cf. Fig. 1.1 on page 5).

## 4.1 Concept

Histograms, like the one in Fig. 4.1, are created from several (100–10000) *conductance traces* measured while breaking or forming ASCs. In the left part of Fig. 4.2 five conductance traces measured on *breaking* Au ASCs formed at 4.2 K under cryogenic vacuum with the MCBJ, are given as an example.

All histograms presented in this chapter, are compiled from traces of *breaking* ASCs. Nevertheless, in Chapter 9, we show that the resulting histograms may depend on whether the traces are recorded while *breaking* or *forming* the contacts. Except for the experiments presented in Sec. 9.5 and for contacts formed using soft indentations (see Sec. 6.2), all other investigations in this thesis are performed with ASCs, created from a larger contact by retracting the electrodes. This type of ASCs will resemble those used when compiling histograms from traces recorded on *breaking* contacts. It should hence be possible to compare most results in later chapters directly with the histograms presented here.

<sup>1</sup> $G_0$  is defined in Eq. (2.3) on page 15.

<sup>2</sup>The use of the STM and the MCBJ to form ASCs is described in Sec. 3.2 and 3.3, respectively. Relay experiments are discussed briefly in Sec. 3.1.

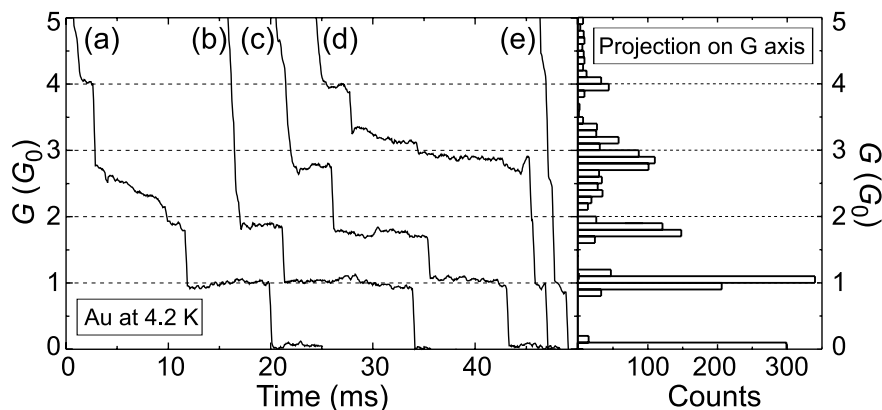


Figure 4.2: Left: Five conductance traces of breaking Au ASCs. Experiments are performed with the MCBJ under cryogenic vacuum at 4.2 K, and the traces are recorded while the electrodes move apart with constant speed. This means that the time is proportional to the distance covered by the electrodes. The actual separation length is, however, unknown. The traces are picked out from the 1000 traces used to compile the histogram for Au presented in Fig. 4.3a. Right: The five traces have been projected onto the conductance axis, and the number of data points in each bin ( $\Delta G = 0.1 G_0$ ) have been counted and is shown on the lower axis. The resulting “histogram” can be compared with the histograms in Fig. 4.1 and Fig. 4.3a (see text).

After the break of an ASC, the next is not formed until the two electrodes have been pushed back together, creating a large contact with high conductance ( $G > 50 G_0$ ). In this way we ensure that the next ASC, obtained when retracting the electrodes, will have a new underlying macroscopic contact configuration. This implies that no two contacts are exactly alike, and every conductance trace will be different, as it is the case in Fig. 4.2.

The conductance in traces (a)–(c) falls from  $G$  near  $2 G_0$  down to  $1 G_0$ , where it remains stable for about ten milliseconds before the contacts finally break and  $G$  falls all the way down to zero. In spite of this, these traces behave quite differently from each other at higher  $G$ . Trace (a) has a small plateau at  $4 G_0$  before dropping below  $3 G_0$ ; then it decreases continuously from there to  $2 G_0$ . Trace (b) reaches  $2 G_0$  directly from higher  $G$ , whereas trace (c) has a plateau below  $3 G_0$  before falling directly to  $2 G_0$ . The two remaining traces fall directly to zero from high conductance: (d) from  $3 G_0$  and (e) from a conductance above  $5 G_0$ . For both these traces a very short plateau ( $\sim 1$  ms) can be seen around  $1 G_0$ . This is the only plateau all five traces have in common.

From these few traces it might look like ASCs of Au always take on a conductance of  $1 G_0$  before finally breaking, but it is difficult to distinguish any general behavior at higher conductances. In any case it is risky to base a conclusion on such a limited amount of data chosen from the 1000 traces recorded during the entire experimental run. It is neither interesting nor possible to plot the amount of traces needed to obtain a good statistical representation. The solution comes with the *conductance histogram*, which provides a clear overview of the general trends of the large numbers of measured conductance traces.

The conductance histogram is created by projecting all the conductance traces onto the conductance axis, and then counting how many data points falls within conductance bins of width  $\Delta G$ . At the right in Fig. 4.2, this procedure has been applied to the five conductance traces, and a very large peak at  $1 G_0$  appears. This is in accordance with the above mentioned observation, but also two clear peaks are situated below  $2$  and  $3 G_0$ , and a small peak around  $4 G_0$  is visible. The peaks, in this limited histogram, reveal the most commonly obtained conductance values for the five traces. Even for this small data set, the histogram resembles to great extend the one in Fig. 4.1, but the peak at  $4 G_0$  is not seen here. This peak is also not found in Fig. 4.3a, where all the 1000 traces, from which the five in Fig. 4.2 have been selected, are used to compile a histogram. Several differences are found when comparing these two histograms.

The problem when using only a few traces is clear: A long plateau in just one trace, results in a peak at the conductance of this plateau. The  $4 G_0$  peak in Fig. 4.2, is entirely caused by traces (a) and (d). We could easily have chosen two other traces, similar to these, but without the small  $4 G_0$  plateau, and then this peak would be missing from the five-trace “histogram”. Since these traces were selected manually, in an effort to present the general trends for large amounts of data, it is likely that the resulting histogram, could be influenced by what we try to illustrate. The best way to obtain reliable histograms, is to compile them from all recorded traces without using any kind of selection criteria which might influence the outcome.<sup>3</sup>

Several different methods have been used for the construction of histograms, with the most common a simple counting as in Fig. 4.2. In this thesis we *calculate* the histograms from all the measured conductance traces [2, 3], but first after correcting them for differential non-linearity (DNL) [2] (see Sec. 5.5).

---

<sup>3</sup>Traces that break almost directly like trace (e) in Fig. 4.2 will not contribute much to the histogram in the interesting conductance range, and there is hence no reason to remove them. However, if traces actually contribute to the conductance in this interesting range, it will be difficult to find a valid reason for excluding them from the histogram!

We define the histogram values as

$$H(G_i) \equiv \frac{N_i}{N\Delta G}. \quad (4.1)$$

where  $G_i$  is the conductance of bin number  $i$  (width  $\Delta G$ ),  $N_i$  the number of counts in the bin accumulated from all the traces in a single experiment, and  $N$  is the total number of data points in all traces. Normalizing, by dividing with  $N$ , ensures that the integrated area under the histogram is close to one. The histogram in Fig. 4.1 is obtained in this way, and since the histogram values are arbitrary we simply write *normalized histogram* on the axis. For individual peaks it is hence, only the position and relative size that matters, and it will often be difficult to compare the intensity of histogram peaks measured under different experimental conditions. This is discussed further in Sec. 9.6.

## 4.2 Review

In 1992 the first conductance traces on metal ASCs were presented using a platinum (Pt) sample in a MCBJ at 4.2 K under cryogenic vacuum [4]. Although jumps in the conductance of the order of  $G_0$  were observed all the way down to  $G \simeq 2 G_0$ , no sign of QC was found.

However, already in 1993, was QC used to describe observations on both Au ASCs formed with the STM at 4.2 K under vacuum [5], as well as under ambient conditions [6], and also on ASCs of copper (Cu) formed with the MCBJ at 1.3 K under cryogenic vacuum conditions [7]. In all three cases plateaus at  $1 G_0$  were observed in the conductance traces of breaking ASCs, and conductance steps with magnitudes of  $nG_0$ , like trace (a)–(c) in Fig. 4.2, were reported. On the other hand traces for lead (Pb) [5] and Pt [7] did not have plateaus at  $1 G_0$ , and although plateaus close to  $nG_0$  were found for aluminum (Al) they were clearly shifted away from integer values [7].

Then in 1994 QC was reported for both Cu, Pt and nickel (Ni) in experiments carried out at RT under UHV with the STM [8]. From a simulation and the experimental results the authors concluded that the jumps in the conductance were a direct consequence of QC [8]. This conclusion was discussed in a comment to the paper [9], where the main point was that preferred atomic configurations *together* with QC would be the cause of the integer values of  $G_0$ . Conductance traces can be very different from contact to contact, and although traces can be found with plateaus exclusively at  $nG_0$ , most traces also have plateaus at

non-integer values of  $G_0$ . In an effort to back up the initial statements from [8], the *first* conductance histogram was created<sup>4</sup> and presented in a reply [10].

The concept of histograms were used again by two different groups already in 1995, and histograms with peaks at  $nG_0$  were reported [3, 13]. The first paper [13] presented histograms of sodium (Na) and Cu obtained at 4.2 K under cryogenic vacuum using the MCBJ. For both metals a clear peak at  $1 G_0$  was observed. Other peaks were positioned at 3, 5 and 6  $G_0$  for Na and below 2 and at 3  $G_0$  for Cu. The second paper [3] showed a histogram for Au very similar to the one in Fig. 4.1, and also recorded under similar experimental conditions.

Au and Cu belonging to the noble metals (cf. Fig. 1.1 on page 5) and Na from the alkali metals have one thing in common: They are all free-electron-like metals with an almost spherical Fermi surface [14] and a single  $s$  electron in their outer electron shell. It has since been shown that the last noble metal, silver (Ag) [2, 15], as well as two of the remaining alkali metals, lithium (Li) and potassium (K) [16], also have a clear histogram peak at  $1 G_0$ . In general the alkali metals display clear peaks at 1, 3, 5 and 6  $G_0$ , whereas for the noble metals only the first peak is situated exactly at  $1 G_0$ ; the next two peaks are clearly shifted below 2 and 3  $G_0$ , respectively. The histograms for the individual metals within each group do show some minor differences, and in the next section this will be discussed for the noble metals.

The understanding of the behavior of histograms was greatly improved, when, in 1997, the first experiment directly measuring the number of open conductance eigenchannels in ASCs was performed [17]. Superconducting Al ASCs, formed with the MCBJ under cryogenic vacuum at a temperature as low as 30 mK, were used. On these contacts, highly non-linear current-voltage ( $I$ - $V$ ) curves were measured, and it was found that at least two and often three partially open channels contributed to the conductance of the smallest (monatomic) Al contacts. As a reaction to this, a histogram for Al, measured at 4.2 K under cryogenic vacuum with the MCBJ, was soon published [18]. In the histogram four peaks were visible, but although they were positioned close to  $nG_0$ , they were clearly shifted away from integer values, in agreement with [7]. The first peak was situated at  $0.8 G_0$ , and according to the eigenchannel experiment, contacts with this conductance should have three partially open channels. It was hereby shown, that a histogram peak close to an integer value of  $G_0$ , could be

---

<sup>4</sup>This histogram on Pt was constructed from only 59 traces [10], chosen under several selection criteria [11]. It shows peaks at  $nG_0$  with  $n = 1, 2, 3$  and 4 supporting the conclusions from [8]. These peak positions were in disagreement with earlier observations [7] and could be caused by the presence of hydrogen ( $H_2$ ) [12] (see Sec. 6.7.3). Below we present a Pt histogram with the first peak centered around  $1.5 G_0$  (Fig. 4.4a) in agreement with both [7] and [12].

caused by several partially open eigenchannels and not only by QC.

The continued work on superconducting junctions found that the number of open channels for the smallest contacts were related to the number of valence electrons [19]. These experiments were performed on Pb, Al, niobium (Nb) and even Au. In the latter case a thin Au layer was evaporated onto Al electrodes. When Al went into the superconducting state the method also worked for Au. In this experiment it was then shown that only *one* channel contributes to the conductance of the smallest contact of Au. This channel was, however, not completely open, yielding a conductance significantly below  $1 G_0$ . This was attributed to disorder in the thin Au layer [19].

In general, a relation between the valence electrons and the number of open channels were found. The maximum of open channels equals the number of available orbitals, i.e. one channel for *s* metals like Au, three for *p* metals like Al and Pd, and five for transition metals with open *d* shells as Nb [19], maybe even six if the *s* shell is also open.<sup>5</sup>

In 1999 three different methods were applied to ASCs of Au, formed at 4.2 K under cryogenic vacuum in the MCBJ, finally proving that contacts with  $G = 1 G_0$  were almost entirely due to one completely open eigenchannel [20–22]. The methods included shot noise [20, 23], conductance fluctuations [15, 21, 24] and thermopower fluctuations [22, 24]. All three papers focus on parameters that will have a minimum when only completely open channels contribute to the conductance. A sharp minimum at a conductance of  $1 G_0$ , was observed in all cases and in the conductance fluctuations experiment similar minima, although not so sharp, were also clear both at 2, 3 and even  $4 G_0$  [21]. While the observed minima coincide with integer values of  $G_0$ , it was noted that the peaks in the Au histogram above  $1 G_0$  did not coincide with  $nG_0$ . In conclusion, the first peak of the Au histogram is due to an atomic configuration (monatomic) with only one fully open channel contributing to the conductance. This peak is thereby an effect of both QC and of a preferred atomic configuration. It is possible to have Au ASCs with a conductance at  $nG_0$  for  $n$  larger than one, but the peaks in the histogram do not coincide with quantized values of  $G_0$  and must, hence, mainly be caused by preferable atomic configurations with at least one channel only partially open [21].

Follow up investigations of the conductance fluctuations on other metals [15], showed that also the two noble metals Cu and Ag display a behavior similar to that of Au, although not so clear when  $G$  rises above  $1 G_0$ . The alkali metal Na also shows this type of behavior for the peaks at 1, 3 and  $6 G_0$ , but not for the

---

<sup>5</sup>For Pt we performed density functional theory (DFT) calculations showing that although there were six channels available only four of these were open, see Sec. 7.2.3.

$5 G_0$  peak [15].<sup>6</sup> On the other hand, for the metals Al, Nb and iron (Fe) no signs of completely open channels contributing to the conductance were found [15]. A very important conclusion from this paper was that the first peak in the histograms resemble the conductance of the monatomic contact [15].

In the discussion above we find that conductance histograms in general do not present conclusive evidence that peaks at  $nG_0$  are signs of QC. For the alkali metals it may seem as if more than one peak are caused by QC in the sense, that for these atomic configurations the conductance is only due to completely open channels. Alkali metals are near perfect free-electron-like metals [14]. For the almost free-electron-like noble metals [14], the first peak at  $1 G_0$  is an effect of QC, but although the other peaks are close to  $nG_0$  they are not exactly at integer values and can not be connected directly with QC. For other metals there is no connection between the position of the histogram peaks and QC, and the observed peaks are generally very broad and only coincidentally situated close to  $nG_0$  [25]. These peaks will entirely be caused by preferred atomic configurations.

There is, however, an important property revealed by the first peak in the histogram: The conductance of the monatomic contact [15]; a very vital information for many of the experiments presented in this thesis. When theoretical simulations are performed, it will often be on exactly this atomic configuration, as it is the most simple. These calculations should be compared with measurements on monatomic contacts, which can be recognized by the conductance associated with the first histogram peak. Furthermore, in the experiment on current-induced disruptions in Chapter 8 we only use monatomic contacts. This ensures that a reproducible atomic configuration is used, and simplifies an already complicated experiment.

### 4.3 The noble metals: Au, Ag and Cu

Conductance histograms for the noble metals (cf. Fig. 1.1 on page 5), recorded at 4.2 K and calculated using Eq. (4.1), are presented in Fig. 4.3. The histogram for Au (Fig. 4.3a) is in accordance with many previous observations measured under several different conditions [2, 3, 11, 15, 16, 24, 26–39]. It is also very similar to the histogram measured at RT in Fig. 4.1, with a sharp peak at  $1 G_0$  and smaller peaks below 2 and  $3 G_0$ . At 4.2 K the peak at  $1 G_0$  is, however, even bigger relative to the next two peaks, and these have clearly moved further down below the quantized values than in the RT histogram.

<sup>6</sup>The  $5 G_0$  peak is attributed to a preferred five atom configuration typical for the alkali metal ASCs [9]. It seems like more than five channels contributed to the conductance of this type of contact, and at least two of these are only partially open [15].

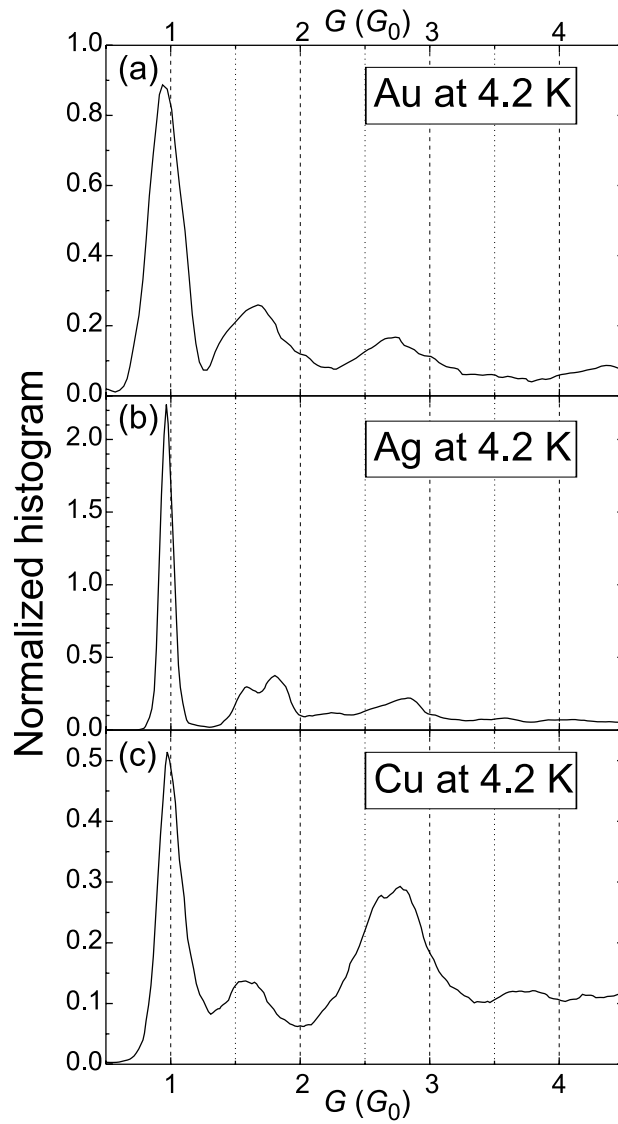


Figure 4.3: Conductance histograms for (a) Au, (b) Ag and (c) Cu, all recorded under cryogenic vacuum at 4.2 K using the MCBJ. Each histogram is compiled from 1000 traces of breaking ASCs measured at a bias of 400 mV for Au and 500 mV for the other two.

The increased intensity of the  $1 G_0$  peak, is most likely caused by the ability of Au to form monatomic chains [40–43]. The formation of chains gives rise to long conductance plateaus at  $1 G_0$  [like traces (a)–(c) in Fig. 4.2], increasing the size of the first peak. Since chains will be more stable at low temperature the intensity of the first peak increases when the temperature decreases. Cu and Ag do not form monatomic chains [42, 43].

Although not as much studied as Au, there are still several reports on histograms of Cu [2, 11, 13, 15, 16, 24, 26, 31, 38] and a few on Ag [2, 15, 16, 24, 37, 38], which all more or less agrees with those presented in Fig. 4.3b and c, respectively. These histograms are very similar to that of Au with a sharp peak centered at  $1 G_0$  and smaller peaks close to, but below  $2$  and  $3 G_0$ . There are, however, some minor differences.

For Ag (Fig. 4.3b) the peak below  $2 G_0$  splits into two separate peaks. This feature has been observed before [16], although the two peaks sometimes combine to resemble the typical  $2 G_0$  Au peak. On the other hand, we have observed a similar split of the  $2 G_0$  peak for Au in a few cases, and histograms with this feature have previously been published [30]. This split is another indication that the second peak has no relation with QC. The third peak in the Ag histogram is very small, but significant, since there is a clear drop in the histogram intensity after the peak.

In the case of Cu (Fig. 4.3c) the second peak is almost centered at  $1.5 G_0$  and it is much smaller than the peak below  $3 G_0$  [16]. It has turned out to be very difficult to stabilize ASCs of Cu with  $G \approx 2 G_0$ . The peak at  $3 G_0$  is, on the other hand, relatively much larger in relation to the  $1 G_0$  peak than in the histograms for Au and Ag. This indicates either a very stable three-atom configuration or a relatively less stable monatomic Cu contact. Still the  $3 G_0$  peak is clearly shifted below the integer conductance value. Cu histograms obtained at RT under UHV using the STM looks similar, only here the peak below  $2 G_0$  is completely missing [11]. The  $2 G_0$  contact configuration is probably too unstable at RT.

Tight-binding (TB) calculations of the conductance of ASCs of Cu gave the expected result ( $G = 1 G_0$ ) for the monatomic Cu contact [25]. The calculation for ASCs consisting of one to nine atoms at the apex, actually fits with our histogram (Fig. 4.3c), but not quite the way we would have expected. The two-atom contact gives  $G = 1.5 G_0$  agreeing with our histogram, but then the conductance almost stays constant below  $2 G_0$ , both for three and four-atom contacts. First at the five-atom contact do the conductance jump to  $3 G_0$ , where it remains until eight-atom contacts [25]. This could explain the large  $3 G_0$  peak, but then again, it does not explain why the second peak is so small.

From previous experiments we do, however, expect that the third peak in the histogram corresponds to a three atom configuration [15]. If this turns out to be wrong, it will not affect any of our later conclusions, since none of these are based on atomic configurations with more than two atoms at the apex. Mostly monatomic contacts will be used, amongst other for the majority of the theoretical calculations. For these small ASCs we completely agree with the results of the TB study [25].

Even though some differences can be found between the preferred atomic configurations of the noble metals, their monatomic contacts display similar behavior. For these the conductance is very close to  $1 G_0$  and it will almost entirely be due to one completely open eigenchannel [15].

In the caption of Fig. 4.3 it is mentioned that the Au histogram is measured at a lower bias than the other two. In general we have only found very little if any bias dependence at all on the peak size or position from low bias and up to 1 V. Similar results on Au have been reported previously [16, 34–36]. At even higher biases the peaks become smaller until even the peak at  $1 G_0$  disappears completely at a bias of 1.9–2.3 V depending on the temperature [34–36]. In spite of the decreasing intensity, did the  $1 G_0$  peak not shift its position at any bias.

## 4.4 The platinum metals: Pt, Pd and Ni

The behavior of the platinum metals (cf. Fig. 1.1 on page 5) are completely different from the noble metals yielding conductance histograms with almost no intensity around  $1 G_0$ . In Fig. 4.4 conductance histograms for these three metals, recorded at 4.2 K and calculated using Eq. (4.1), display how the first peak, although much broader than for the noble metals, have moved entirely above  $1 G_0$ , to be centered close to  $1.5 G_0$ .

The Pt histogram (Fig. 4.4a) also has a smaller peak around  $3 G_0$ . The minimum between these two peaks lies around  $2.5 G_0$ , and the shift between monatomic contacts and two atom contacts is expected to happen in the conductance region from  $2.3$  to  $2.6 G_0$  [43] (see Sec. 7.2.4).

Before the first histogram was obtained, conductance traces of Pt in accordance with a histogram peak between  $1.5$ – $2 G_0$  were measured [4, 7], and later histograms similar to the one in Fig. 4.4a were reported [12, 16, 33, 43]. This is in contrast to the first histogram ever published, which was indeed measured on Pt [10] (see footnote 4 on page 46). Here a clear peak at  $1 G_0$  was found. This peak [26, 27, 44, 45], and other peaks at  $nG_0$  [26, 27], were presented in

later publications. These experiments were all performed at RT and *not* in vacuum. In two cases the contacts were even encapsulated in an atmosphere of nitrogen ( $N_2$ ) with 5% hydrogen ( $H_2$ ) [44, 45]. Recent experiments show that the presence of hydrogen changes the Pt histogram, by shifting the first histogram peak from  $G = 1.5 G_0$  down to a conductance of  $1 G_0$  [12] (see Sec. 6.7.3). In conclusion, it is very important to keep the Pt electrodes free of contamination in order to measure on clean ASCs. Under ambient conditions, tunneling through contaminating molecules (see Sec. 6.5), e.g. hydrogen, may alter the histogram, giving rise to peaks around  $1 G_0$ .

For the palladium (Pd) histogram (Fig. 4.4b), the first peak is situated at  $1.7 G_0$ . At higher  $G$  the intensity of the histogram do not drop as low as in the Pt histogram and there is no clear structure. Only few reports on Pd histograms are found in the literature. One of these is the experiment where the contacts were encapsulated in a hydrogen-rich atmosphere at RT [45]. No structure was observed in the resulting histograms. In a recent paper from the same group, Pd histograms without structure have again been observed using ASCs formed at RT, but this time under vacuum [37]. The lacking structure could be caused by the higher temperature (RT) compared to the 4.2 K in our experiment. It is, on the other hand, possible that the presence of hydrogen or other impurities causes unstable contacts with no structure in the histogram as a result. In an experiment, performed with the same technique and conditions used in Fig. 4.4, the first peak position has been reported to be in the conductance window from  $0.5$ – $2.4 G_0$  [43], in accordance with our histogram.

The Ni histogram (Fig. 4.4c) is very different from the two histograms for Pt and Pd. The first peak centered around  $1.5 G_0$  is not sharp and almost splits into two peaks. Furthermore, the peak has a low intensity when compared to the rest of the histogram at conductances above  $2.5 G_0$ . The peak position agrees with most of the few Ni histograms published in the literature [11, 16, 33, 46]. A Ni histogram measured under ambient conditions showed no structure [27]. We do, however, not expect that it is possible to make reliable measurements on the reactive Ni surface when it has been exposed to ambient conditions [46] (see Sec. 6.7.1).

When we measure  $I$ - $V$  curves on Ni ASCs (Sec. 7.4), an instability is observed for contacts with  $G$  around  $1.5 G_0$ . This is in accordance with the small first peak in the Ni histogram (Fig. 4.4c). Ni is a very brittle material from which it is hard to form stable ASCs, and monatomic contacts are very difficult to obtain even at 4.2 K (see Sec. 7.1).

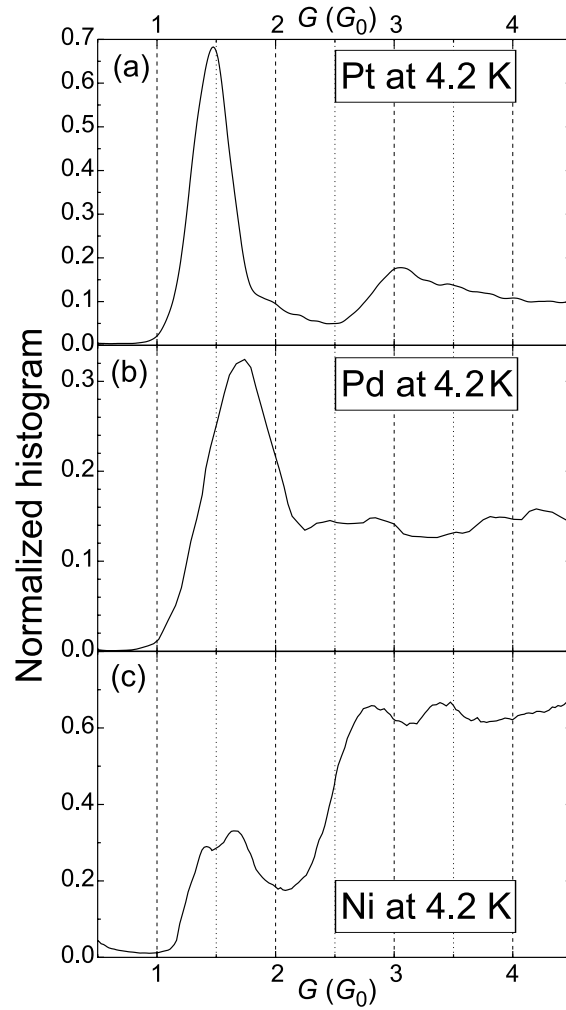


Figure 4.4: Conductance histograms for the platinum metals, all measured on breaking ASCs using the MCBJ under cryogenic vacuum at 4.2 K. (a) Pt histogram compiled from 3000 traces (bias 100 mV). (b) Pd histogram compiled from 1000 traces (bias 100 mV). (c) Ni histogram compiled from 2000 traces (bias 300 mV).

## Ferromagnetic metals

Ni is a ferromagnetic metal and there have been some investigations on the effect of an applied magnetic field [46–48]. A magnetic field splits up the spin states so the conductance is no longer  $G_0$  for each fully open eigenchannel, but only  $G_0/2 = e^2/h$  (see footnote 7 on page 19). Here  $e$  is the elementary charge and  $h$  is Planck’s constant. In the experiment where the zero-magnetic field results agree with our histograms, the magnetic field removes the first peak [46]. Another experiment actually observed peaks both at  $nG_0$  without the field, and at  $nG_0/2$  when the field was applied [47]. In this case, the zero field results disagree with the other papers as well as those presented here. The most recent of the papers [48] tries to explain the results from [47] theoretically. However, even though this experiment was performed in vacuum (not UHV), no cleaning procedures were mentioned. Again care is recommended when interpreting data from ASCs formed from a sample material which has been exposed to air, without subsequent cleaning under UHV.

Another theoretical simulation of the histogram for Ni has been performed, but this time without magnetic field [49]. Although no peak is observed at  $1.5 G_0$ , there is a significant increase in the histogram above  $2 G_0$  [49], which is comparable to the one after the small  $1.5 G_0$  peak in Fig. 4.4c. This is in accordance with the observed instability of the monatomic Ni contact ( $G = 1.5 G_0$ ) in the  $I$ - $V$  experiments. The above mentioned TB study [25] also calculated the conductance of Ni ASCs, and indeed found the conductance for the monatomic contact to be  $1.5 G_0$  in accordance with our histogram [25].

Finally we mention, that for Fe — another ferromagnetic metal, peaks at  $nG_0/2$  were observed even without applying a magnetic field [50, 51]. The experiments were performed with STM at 4.2 K under UHV. The amount of data were, however, very limited (100 conductance traces) and the result disagrees with MCBJ experiments performed at 4.2 K under cryogenic vacuum [15]. Here the only structure in an Fe histogram compiled from 700 traces is the first peak situated slightly above  $2 G_0$  [15]. So far it is still inconclusive if there is any  $nG_0/2$  peaks in histograms from ASCs of ferromagnetic metals.

A recent experiment on Cu [52] actually also found  $nG_0/2$  peaks! The experiments were performed without magnetic field, but Cu is not a ferromagnetic metal anyway. The ASCs were simply formed by vibrating macroscopic Cu wires in and out of contact under ambient conditions (see Sec. 3.1). There is hence, reason to believe that the wires were contaminated, since no cleaning procedure is mentioned and no other precautions were taken [52] (see Sec. 6.7.1). Also the traces, used to compile the histograms, were subjected to selection criteria and the number of traces used in the final histogram is not stated [52] (see footnotes 3 and 4 on page 44 and 46, respectively).

## Bias dependence

Contrary to the noble metals, the peak positions of the platinum metals histograms are somewhat dependent on the bias [16, 44, 45]. The histograms presented in Fig. 4.4 should, nevertheless, be adequate for representing the approximate conductance for the monatomic contacts for these metals. We are though aware, that the 300 mV bias used when obtaining the Ni histogram (Fig. 4.4c) seems relatively high when compared to the bias of 100 mV used for obtaining the Pt and Pd histograms. Especially with the discussion on the instability of exactly the monatomic Ni contact. We did, in spite of this, choose this particular histogram, since it displays the typical features for Ni even more clearly than any histogram we recorded at lower bias.

In histograms for Pt, the position of the first peak, shifts  $0.3 G_0$  towards higher conductance values when the bias increases past a certain value [16]. This effect is discussed in Chapter 9, and the explanation for the behavior seems to be, that Pt, as Au, forms monatomic chains [42, 43]. At higher bias the chains do not form and this results in the changing peak position.

Again, as for the noble metals, the lighter elements Pd and Ni do not form these chains [42, 43]. This could be part of the explanation why the first Pt histogram peak is relatively so much larger than for the other two platinum metals when compared to the intensity of the histograms at higher conductances.

After this presentation of conductance histograms, I move on to the most important subject of this thesis: Investigating the current-voltage ( $I$ - $V$ ) behavior of ASCs. However, in order to allow fast and accurate measurements, we needed to develop the electronic setup, described in the next chapter. First with this tool, could we turn our full attention to the investigation of  $I$ - $V$  curves presented in Chapters 6 and 7.

## References

- [1] For a review, see J. M. van Ruitenbeek, “Conductance Quantisation in Metallic Point Contacts,” in *Metal Clusters on Surfaces: Structure, Quantum Properties, Physical Chemistry, Cluster Physics*, K.-H. Meiwes-Broer, ed., (Springer-Verlag, Heidelberg, 2000), Chap. 6, pp. 175–210.
- [2] K. Hansen, E. Lægsgaard, I. Stensgaard, and F. Besenbacher, “Quantized Conductance in Relays,” *Phys. Rev. B* **56**, 2208–2220 (1997).
- [3] M. Brandbyge, J. Schiøtz, M. R. Sørensen, P. Stoltze, K. W. Jacobsen, J. K. Nørskov, L. Olesen, E. Lægsgaard, I. Stensgaard, and F. Besenbacher, “Quantized conductance in atom-sized wires between two metals,” *Phys. Rev. B* **52**, 8499–8514 (1995).
- [4] C. J. Muller, J. M. van Ruitenbeek, and L. J. de Jongh, “Conductance and Supercurrent Discontinuities in Atomic-Scale Metallic Constrictions of Variable Width,” *Phys. Rev. Lett.* **69**, 140–143 (1992).
- [5] N. Agraït, J. G. Rodrigo, and S. Vieira, “Conductance steps and quantization in atomic-size contacts,” *Phys. Rev. B* **47**, 12345–12348 (1993).
- [6] J. I. Pascual, J. Méndez, J. Gómez-Herrero, A. M. Baró, N. García, and V. T. Binh, “Quantum Contact in Gold Nanostructures by Scanning Tunneling Microscopy,” *Phys. Rev. Lett.* **71**, 1852–1855 (1993).
- [7] J. M. Krans, C. J. Muller, I. K. Yanson, T. C. M. Govaert, R. Hesper, and J. M. van Ruitenbeek, “One-atom point contacts,” *Phys. Rev. B* **48**, 14721–14724 (1993).
- [8] L. Olesen, E. Lægsgaard, I. Stensgaard, F. Besenbacher, J. Schiøtz, P. Stoltze, K. W. Jacobsen, and J. K. Nørskov, “Quantized Conductance in an Atom-Sized Point Contact,” *Phys. Rev. Lett.* **72**, 2251–2254 (1994).
- [9] J. M. Krans, C. J. Muller, N. van der Post, F. R. Postma, A. P. Sutton, T. N. Todorov, and J. M. van Ruitenbeek, “Comment on “Quantized Conductance in an Atom-Sized Point Contact”,” *Phys. Rev. Lett.* **74**, 2146 (1995).
- [10] L. Olesen, E. Lægsgaard, I. Stensgaard, F. Besenbacher, J. Schiøtz, P. Stoltze, K. W. Jacobsen, and J. K. Nørskov, “Reply to “Comment on ‘Quantized conductance in an Atom-Sized Point Contact’”,” *Phys. Rev. Lett.* **74**, 2147 (1995).

- 
- [11] L. Olesen, “Experimental Investigation of the Junction in a Scanning Tunneling Microscope,” PhD thesis, University of Aarhus, 1996.
- [12] R. H. M. Smit, Y. Noat, C. Untiedt, N. D. Lang, M. van Hemert, and J. M. van Ruitenbeek, “Measurement of the conductance of a hydrogen molecule,” accepted for publication in *Nature*, (2002), <http://xxx.lanl.gov/pdf/cond-mat/0208407>, (unpublished).
- [13] J. M. Krans, J. M. van Ruitenbeek, V. V. Fisun, I. K. Yanson, and L. J. de Jongh, “The signature of conductance quantization in metallic point contacts,” *Nature* **375**, 767–769 (1995).
- [14] N. W. Ashcroft and N. D. Mermin, *Solid State Physics* (Holt, Rinehart and Winston, New York, 1976).
- [15] B. Ludoph and J. M. van Ruitenbeek, “Conductance fluctuations as a tool for investigating the quantum modes in atomic size metallic contacts,” *Phys. Rev. B* **61**, 2273–2285 (2000).
- [16] A. I. Yanson, “Atomic Chains and Electronic Shells: Quantum Mechanisms for the Formation of Nanowires,” PhD thesis, Rijksuniversiteit Leiden, 2001. (Can be downloaded from <http://lions1.leidenuniv.nl/wwwhome/ruitenbe/ThesisAlex.pdf>).
- [17] E. Scheer, P. Joyez, D. Esteve, C. Urbina, and M. H. Devoret, “Conduction Channel Transmissions of Atomic-Size Aluminum Contacts,” *Phys. Rev. Lett.* **78**, 3535–3538 (1997).
- [18] A. I. Yanson and J. M. van Ruitenbeek, “Do Histograms Constitute a Proof for Conductance Quantization?,” *Phys. Rev. Lett.* **79**, 2157 (1997).
- [19] E. Scheer, N. Agraït, J. C. Cuevas, A. L. Yeyati, B. Ludoph, A. Martín-Rodero, G. R. Bollinger, J. M. van Ruitenbeek, and C. Urbina, “The signature of chemical valence in the electrical conduction through a single-atom contact,” *Nature* **394**, 154–157 (1998).
- [20] H. E. van den Brom and J. M. van Ruitenbeek, “Quantum Suppression of Shot Noise in Atom-Size Metallic Contacts,” *Phys. Rev. Lett.* **82**, 1526–1529 (1999).
- [21] B. Ludoph, M. H. Devoret, D. Esteve, C. Urbina, and J. M. van Ruitenbeek, “Evidence for Saturation of Channel Transmission from Conductance Fluctuations in Atomic-Size Point Contacts,” *Phys. Rev. Lett.* **82**, 1530–1533 (1999).

- 
- [22] B. Ludoph and J. M. van Ruitenbeek, “Thermopower of atomic-size metallic contacts,” *Phys. Rev. B* **59**, 12290–12293 (1999).
- [23] H. E. van den Brom, “Noise properties of atomic-size contacts,” PhD thesis, Rijksuniversiteit Leiden, 2000.
- [24] B. Ludoph, “Quantum Conductance Properties of Atomic-size Contacts,” PhD thesis, Rijksuniversiteit Leiden, 1999.
- [25] S. Krompiewski and M. Zwierzycki, “Conductance of atomic-scale metallic contacts with controllable interface hopping integrals,” *J. Magn. Magn. Mat.* **240**, 209–211 (2002).
- [26] J. L. Costa-Krämer, N. García, P. García-Mochales, and P. A. Serena, “Nanowire formation in macroscopic metallic contacts: quantum mechanical conductance tapping a table top,” *Surf. Sci.* **342**, L1144–L1149 (1995).
- [27] J. L. Costa-Krämer, “Conductance quantization at room temperature in magnetic and nonmagnetic metallic nanowires,” *Phys. Rev. B* **55**, R4875–R4878 (1997).
- [28] J. L. Costa-Krämer, N. García, and H. Olin, “Conductance quantization histograms of gold nanowires at 4 K,” *Phys. Rev. B* **55**, 12910–12913 (1997).
- [29] J. L. Costa-Krämer, N. García, P. García-Mochales, P. A. Serena, M. I. Marqués, and A. Correia, “Conductance quantization in nanowires formed between micro and macroscopic metallic electrodes,” *Phys. Rev. B* **55**, 5416–5424 (1997).
- [30] Z. Gai, Y. He, H. Yu, and W. S. Yang, “Observation of conductance quantization of ballistic metallic point contacts at room temperature,” *Phys. Rev. B* **53**, 1042–1045 (1996).
- [31] C. J. Muller, J. M. Krans, T. N. Todorov, and M. A. Reed, “Quantization effects in the conductance of metallic contacts at room temperature,” *Phys. Rev. B* **53**, 1022–1025 (1996).
- [32] C. Sirvent, J. G. Rodrigo, N. Agrait, and S. Vieira, “STM study of the atomic contact between metallic electrodes,” *Physica B* **218**, 238–241 (1996).

- 
- [33] C. Sirvent, J. G. Rodrigo, S. Vieira, L. Jurczyszyn, N. Mingo, and F. Flores, "Conductance step for single-atom contact in the scanning tunneling microscope: Noble and transition metals," *Phys. Rev. B* **53**, 16086–16090 (1996).
- [34] H. Yasuda and A. Sakai, "Conductance of atomic-scale gold contacts under high-bias voltages," *Phys. Rev. B* **56**, 1069–1072 (1997).
- [35] K. Itakura, K. Yuki, S. Kurokawa, H. Yasuda, and A. Sakai, "Bias dependence of the conductance of Au nanocontacts," *Phys. Rev. B* **60**, 11163–11170 (1999).
- [36] K. Yuki, A. Enomoto, and A. Sakai, "Bias-dependence of the conductance of Au nanocontacts at 4 K," *Appl. Surf. Sci.* **169–170**, 489–492 (2001).
- [37] A. Enomoto, S. Kurokawa, and A. Sakai, "Quantized conductance in Au-Pd and Au-Ag alloy nanocontacts," *Phys. Rev. B* **65**, 125410 (2002).
- [38] K. Hansen, "Electrical Properties of Atomic-Sized Metal Contacts," PhD thesis, University of Aarhus, 2000. (Can be downloaded from <http://www.ifa.au.dk/~kimh/pdf/thesis.pdf>).
- [39] M. Brandbyge, "Conductance of Metal Nanocontacts," PhD thesis, Technical University of Denmark, 1997.
- [40] H. Ohnishi, Y. Kondo, and K. Takayanagi, "Quantized conductance through individual rows of suspended gold atoms," *Nature* **395**, 780–783 (1998).
- [41] A. I. Yanson, G. R. Bollinger, H. E. van den Brom, N. Agrait, and J. M. van Ruitenbeek, "Formation and manipulation of a metallic wire of single gold atoms," *Nature* **395**, 783–785 (1998).
- [42] S. R. Bahn and K. W. Jacobsen, "Chain Formation of Metal Atoms," *Phys. Rev. Lett.* **87**, 266101 (2001).
- [43] R. H. M. Smit, C. Untiedt, A. I. Yanson, and J. M. van Ruitenbeek, "Common Origin for Surface Reconstruction and the Formation of Chains of Metal Atoms," *Phys. Rev. Lett.* **87**, 266102 (2001).
- [44] K. Yuki, S. Kurokawa, and A. Sakai, "Quantized Conductance in Pt Nanocontacts," *Jpn. J. of Appl. Phys.* **39**, 4593–4595 (2000).

- 
- [45] K. Yuki, S. Kurokawa, and A. Sakai, "Conductance in Breaking Nanocontacts of Some Transition Metals," *Jpn. J. of Appl. Phys.* **40**, 803–808 (2001).
- [46] H. Oshima and K. Miyano, "Spin-dependent conductance quantization in nickel point contacts," *Appl. Phys. Lett.* **73**, 2203–2205 (1998).
- [47] T. Ono, Y. Ooka, H. Miyajima, and Y. Otani, " $2e^2/h$  to  $e^2/h$  switching of quantum conductance associated with a change in nanoscale ferromagnetic domain structure," *Appl. Phys. Lett.* **75**, 1622–1624 (1999).
- [48] A. Smogunov, A. D. Corso, and E. Tosatti, "Selective d-state conduction blocking in nickel nanocontacts," *Surf. Sci.* **507–510**, 609–614 (2002).
- [49] H. Mehrez and S. Ciraci, "Conductance of ferromagnetic nanowires," *Phys. Rev. B* **58**, 9674–9676 (1998).
- [50] F. Komori and K. Nakatsuji, "Quantized Conductance through Atomic-sized Iron Contacts at 4.2 K," *J. Phys. Soc. Jap.* **68**, 3786–3789 (1999).
- [51] F. Komori and K. Nakatsuji, "Quantized conductance through iron point contacts," *Mater. Sci. Eng., B* **84**, 102–106 (2001).
- [52] D. M. Gillingham, I. Lington, and J. A. C. Bland, " $e^2/h$  quantization of the conduction in Cu nanowires," *J. Phys. Cond. Matt.* **14**, L567–L570 (2002).

## Chapter 5

# Fast and Accurate Electronic Setup

This chapter will give a description of the fast setup built for acquiring accurate current voltage ( $I$ - $V$ ) curves. See paper [I] for further details.

### 5.1 Introduction

After the intense investigation of the quantized conductance (QC) observed in gold (Au) conductance histograms (see previous chapter), a growing interest emerged for measuring  $I$ - $V$  curves of atomic sized contacts (ASCs) to obtain further information on their electrical properties [1–10]. At liquid helium (He) temperatures (4.2 K) or below, the ASCs can be very stable for a long period of time. Under such conditions, highly nonlinear  $I$ - $V$  curves on ASCs formed between superconducting electrodes at bias voltages extending up to the mV regime have been recorded and used to successfully determine the transmission of each mode contributing to the current [7, 8]. Measurements of fluctuations in the differential conductance  $dI/dV$  of noble-metal ASCs up to 100 mV at 4.2 K have shown that the conduction eigenchannels tend to close one by one during rupture of the contacts [9, 10] (see the review in Sec. 4.2).

At room temperature (RT), the ASCs tend to be much more unstable due to thermal fluctuations. In spite of this, there has been a number of reports on the formation of stable Au ASCs at RT [1–6, 11–15]. For these contacts, nonlinear  $I$ - $V$  curves extending up to 1 V have been recorded during a timescale of seconds [1–6].

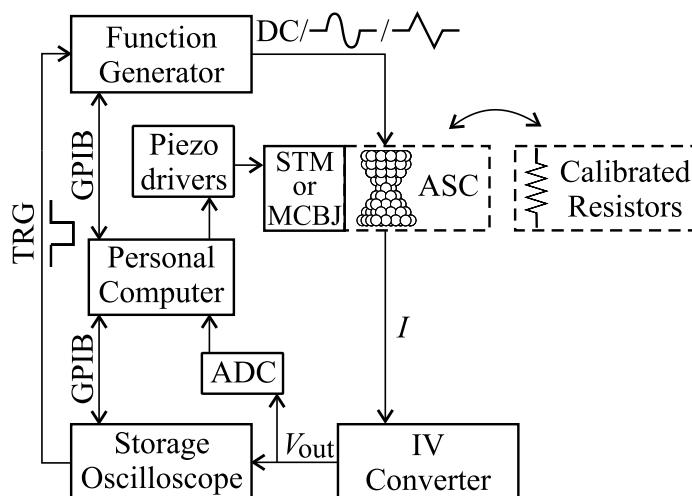


Figure 5.1: Block diagram of the experimental setup.

When working in a clean ultra-high vacuum (UHV) environment at RT, we find that Au ASCs tend to break spontaneously over a period of less than a millisecond. During the break, the conductance falls down in a series of metastable steps, each corresponding to a specific atomic configuration [16]. The duration of a single step is typically less than  $\approx 100 \mu\text{s}$ , whereas the size of a step is close to  $1 G_0$ .<sup>1</sup>

To capture the  $I$ - $V$  curves of these metastable states, we have therefore developed a novel setup which is capable of acquiring a full  $I$ - $V$  curve during a period of down to  $10 \mu\text{s}$  with an acquisition rate of  $100 \text{ Msamples/s}$ .

## 5.2 Block diagram of the setup

A block diagram of the experimental setup is shown in Fig. 5.1. A Hewlett Packard 33120A, 15 MHz arbitrary waveform/function generator (FG) supplies a bias voltage to an ASC. A home-built current-to-voltage ( $I$ - $V$ ) converter is used to convert the resulting current  $I$  into a voltage signal  $V_{\text{out}}$ , which in turn is measured with a 10 bit true resolution,  $100 \text{ Msamples/s}$ , four-channel Yokogawa DL 4100 digital storage oscilloscope (DSO). Individual voltage traces

<sup>1</sup>The fundamental unit of conductance  $G_0$  is defined in Eq. (2.3) on page 15.

each consisting of up to 100k data points are transferred from the DSO to a personal computer (PC), using a general purpose interface bus (GPIB). Each trace is stored for later analysis. All relevant settings on the DSO and FG are stored along with the trace.

The ASCs, formed either in the scanning tunneling microscope (STM) or the mechanically controllable break-junction (MCBJ) as described in Chapter 3, can be replaced with a resistor as indicated in Fig. 5.1. In this way the system can be calibrated as described below.

While the ASCs are formed the FG supplies a constant bias voltage  $V_{\text{bias}}$  used to monitor the conductance. When the FG is triggered by the DSO, a burst is added to the signal. The parameters of the burst are set on the FG directly from the PC through the GPIB. These parameters are waveform (sinusoidal or triangular), number of burst cycles, amplitude (0.1–5 V) and frequency ( $\leq 100$  kHz). Only triangular bursts were used in the experiments.

The home-build  $I$ - $V$  converter is constructed especially for this setup, and has to fulfill several demands to make the fast RT measurements possible.

### 5.3 The current-to-voltage converter

In experiments where the conductance of ASCs is measured, different setups have been used to convert the current into a voltage signal  $V_{\text{out}}$ . The two most widely used methods are transimpedance [11, 17, 18] and shunt converters [19–21], which will be discussed below. In these experiments constant bias is used. When working with fast changing current, it is important that the  $I$ - $V$  converter has a flat frequency response, in order for the signal to be transmitted without degradation. Since the burst only consists of a few cycles, we have to consider that it will lead to a broad distribution of Fourier frequency components with a maximum peak at the frequency set by the FG. This means that when the maximum frequency of 100 kHz is used, there will be some components at even higher frequencies. To measure precise  $I$ - $V$  curves, all these components must be transmitted equally.

In Fig. 5.2a the transimpedance setup is shown. A resistor  $R_F$  placed in the feedback of an operational amplifier (OA) converts the current to a voltage signal  $V_{\text{out}}$ . From the diagram the input impedance can be found as:

$$R_{\text{in}}^t = \frac{R_F}{1 + A(f)}. \quad (5.1)$$

Here  $A(f)$  is the frequency-dependent open loop gain of the OA. This is typically of the order of  $10^5$  under DC condition, but will fall when the frequency rises,

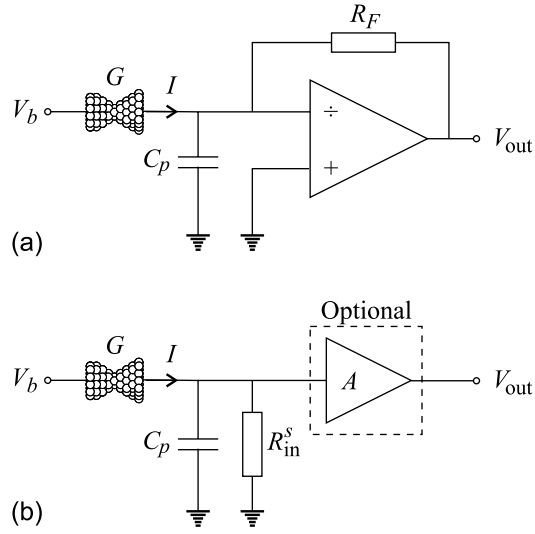


Figure 5.2: (a) Transimpedance and (b) shunt method for measuring the conductance in an ASC.

reaching unity gain in the MHz range. In typical setups ( $R_F = 10 \text{ k}\Omega - 1 \text{ M}\Omega$ )  $R_{in}^t$  can be neglected at low frequencies, but at high frequencies  $R_{in}^t$  can be compared to the resistance  $G^{-1}$  of the ASC (Usually  $G = 1-10 G_0$  corresponding to  $1.3-13 \text{ k}\Omega$ ). The voltage  $V_{out}(f)$  is given by:

$$V_{out}(f) = -\frac{A(f)}{1 + A(f)} R_F I(f). \quad (5.2)$$

It is seen that a time-dependent current signal  $I(t)$  composed of many frequency components, will not be transmitted evenly through the converter, because of the frequency-dependent transimpedance.

The shunt method is shown in Fig. 5.2b. It has the advantage over the transimpedance converter that the current is converted to a voltage signal in a resistor removing the frequency dependence from the setup. The resistance of  $R_{in}^s$  will typically be less than  $2 \text{ k}\Omega$ . Without the low output impedance from the optional OA, the use of short wires from the converter to the DSO is, however, necessary to keep the parasitic capacitance  $C_p$  down. For fast changing current the time constant of the  $RC$  circuit has to be considered. When the conductance of the ASC is in the interesting range ( $1-10 G_0$ ),  $C_p$

will mainly be discharged through the resistor leading to a time constant of  $\tau = R_{\text{in}}^s C_p$ . The cutoff frequency  $f_{\text{cut}} = (2\pi\tau)^{-1}$  must be high enough for the current signal to be fully transmitted. It is therefore important to keep  $C_p$  as low as possible. By placing a low gain, low noise, high input impedance, flat frequency response voltage amplifier immediately after  $R_{\text{in}}^s$ ,  $C_p$  will be kept at a minimum, the voltage signal will increase and long transmission lines between the output terminal and the DSO can be used.

When using the STM (see Sec. 3.2), the ASCs are formed in the UHV chamber and because the  $I$ - $V$  converter is outside some wiring cannot be avoided. From this we get  $C_p \approx 50$  pF. With a typical  $R_{\text{in}}^s$  of  $500 \Omega$ , this gives  $\tau = 25$  ns and a cutoff frequency of 6 MHz. For the MCBJ, the wiring has to go through the 1 m pipe of the insert (see Sec. 3.3), and it is not possible to place the  $I$ - $V$  converter close to the ASCs. This gives a much higher  $C_p$  and thereby a much lower cutoff frequency. Already at frequencies of a few kHz the measurements are affected. This is, however, not a serious problem because at 4.2 K the ASCs are stable on a second time scale, and there is no need to use kHz frequencies to measure  $I$ - $V$  curves. The fast setup is not actually necessary for measuring  $I$ - $V$  curves at 4.2 K, but high burst frequencies are still needed when measuring the current-induced disruptions presented in Chapter 8.<sup>2</sup>

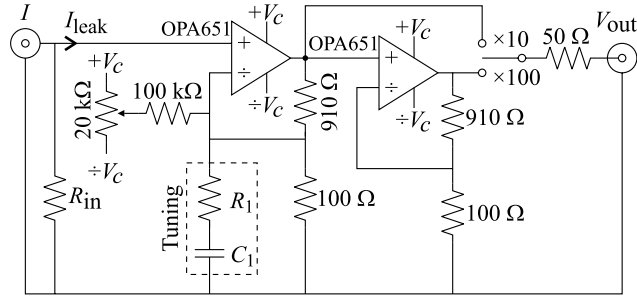
We have based our  $I$ - $V$  converter on the shunt setup designing an OA with the desired properties as mentioned above. The diagram is shown in Fig. 5.3.

It is based on two non-inverting amplifier stages each built up around an OPA651 (Burr-Brown) operational amplifier.<sup>3</sup> Both stages have a gain of  $A \approx 10$  as determined by the 100 and 910  $\Omega$  resistors, and with a switch one or two stages can be chosen. The tuning part components were inserted after the frequency response had been tested to make it even flatter. This will be discussed below.

The impedance seen by the two inputs on an OA are not necessarily the same. It depends on the value of the interchangeable metal-film shunt resistor  $R_{\text{in}}$  (0.2–2 k $\Omega$ ) mounted in a socket. Since the OA has a sizeable input bias current of approximately 4  $\mu\text{A}$ ,<sup>3</sup> this mismatch in impedance leads to an offset voltage of several mV on the output of the first stage. Consequently, a 20 k $\Omega$  multi-turn potentiometer connected to the supply voltages  $\pm V_c$  ( $V_c = 5$  V) is used together with a 100 k $\Omega$  resistor for adjusting the offset voltage each time  $R_{\text{in}}$  is changed. The amplification stage is series terminated with a 50  $\Omega$  resistor to match the impedance of the 4 m coaxial cable that leads to the DSO. The cable is also terminated at the DSO with 50  $\Omega$  to preserve the integrity

<sup>2</sup>In these experiments we would actually have preferred the ability to use higher frequencies!

<sup>3</sup>The OPA651 is stable in gains  $\geq 2\text{V/V}$ , has a gain bandwidth product of 340 MHz, a 12-bit settling time in 16 ns, an input bias current of 4  $\mu\text{A}$  and an input voltage noise of 4.6 nV/ $\sqrt{\text{Hz}}$  above 10 kHz.

Figure 5.3: Diagram of the home-built  $I$ - $V$  converter.

of the signal. This causes a 6 dB attenuation loss, meaning that the actual amplification is 5 (50) for one (two) stage(s).

We tuned the  $I$ - $V$  converter to flatten the frequency response further. With the FG and the DSO we measured the gain of the converter by collecting a harmonic signal supplied by the FG before and after it had passed the converter. These two signals were fitted to this equation:

$$V(t) = V_0 \sin(2\pi ft + \phi) + V_{\text{off}}, \quad (5.3)$$

where  $t$  is the time-dependent variable and the frequency  $f$  is kept fixed.  $V_0$  is the amplitude,  $V_{\text{off}}$  the offset voltage and  $\phi$  the phase. The gain was found as the ratio between the output and the input amplitudes. Both the gain and the phase shift as a function of frequency can be seen in Fig. 5.4. The frequency response was already very flat before the fine tuning (open circles), but the gain decreases 1.2% from low (1–10 kHz) to high (30 kHz–1 MHz) frequencies. This is not something that can be predicted, because it depends on minute details in the layout of the converter. That is why the tuning resistor  $R_1$  and capacitor  $C_1$  are inserted (see Fig. 5.3) to make the gain increase approximately 1.2% as the frequency increases past 20 kHz. This was achieved with  $R_1 = 6.5$  kΩ and  $C_1 = 1$  nF, and the improvement is seen in Fig. 5.4 (solid squares).

We only found it necessary to tune the first amplification stage. Due to an increase in the noise level when both stages are used, the second stage was only used in some initial experiments. All the experimental data presented in this thesis have been recorded using only the first stage of the converter.

What are the limitations of the setup? We can measure the voltage in 10 ns intervals with the DSO, and the response time of the system is  $\approx 25$  ns. The gain of the  $I$ - $V$  converter is constant within 0.5% for frequencies up to 800 kHz.

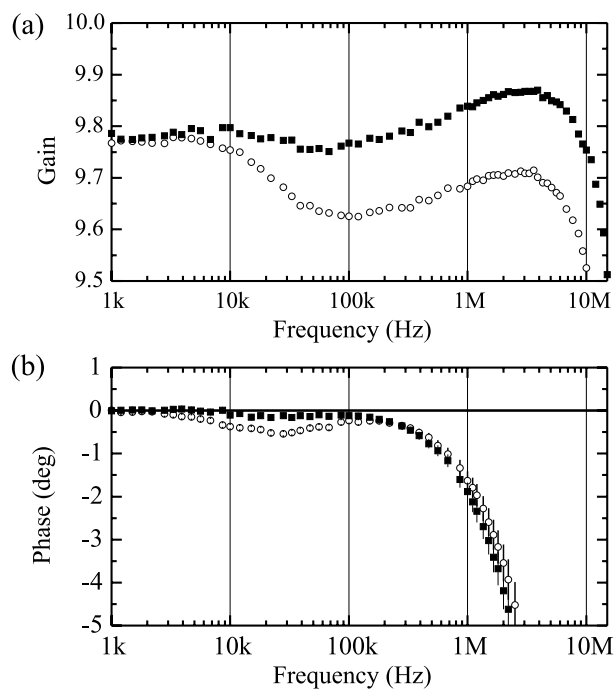


Figure 5.4: Frequency dependence for the  $I-V$  converter. (a) Gain and (b) phase as a function of frequency before (open circles) and after (solid squares) fine tuning. Note the small gain scale.

Since we only use burst frequencies below 100 kHz the setup seems to meet our demands. The higher Fourier frequency components of a short burst need, however, to be investigated.<sup>4</sup> In order to find out if this poses a problem, the power spectral density (PSD) of a single period burst was calculated, both for a sinusoidal and a triangular wave, and the results are plotted in Fig. 5.5.

The PSD is the norm square of the Fourier transform, and one period is chosen because this is the extrema leading to the highest frequency components. The figure clearly shows that the PSD is negligible for frequencies above three times the burst frequency both for sinusoidal and triangular bursts. This means that 100 kHz pulses only cause frequency components up to 300 kHz, which is in the region where the  $I-V$  converter's frequency response is very flat.

<sup>4</sup>This is only necessary with the STM, not for the low frequency MCBJ experiments.

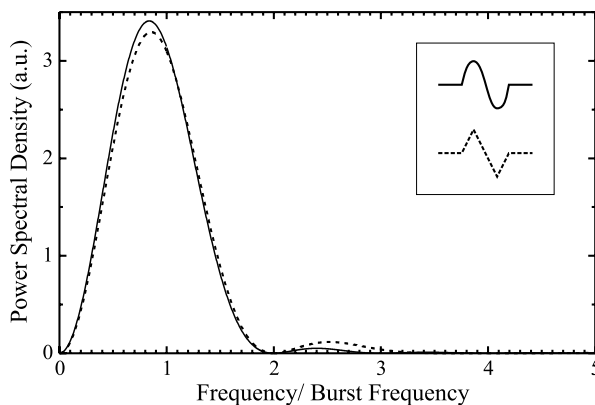


Figure 5.5: Power spectral density of a single period sinusoidal (solid) or triangular (dashed) burst.

## 5.4 Model of the circuit

As indicated in Fig. 5.1, we calibrate the setup by interchanging the ASCs with a set of calibrated resistors and measuring  $V_{\text{out}}$  as a function of bias voltage for each resistor. Hereby a set of parameters, such as  $R_{\text{in}}^s$  and  $A$  in Fig. 5.2b, which accurately describe the behavior of the circuit, can be found.

However, for our setup, more than two parameters are needed for an accurate calibration. A realistic model based on five parameters is shown in Fig. 5.6. This is a DC model, where all parasitic inductances and capacitances are disregarded. This is justified since we always operate in the flat frequency response regime. The finite output impedance of the FG ( $\approx 50 \Omega$ ) is represented by  $R_{\text{FG}}$ . We write the conductance of a calibrated resistor/the ASC as  $G = gG_0$  implying that  $g$  is the conductance measured in quantum units. The current  $I$  that flows through the ASC is divided between the input impedance  $R_{\text{in}}$  and the OA input bias current, which is represented by the current sink  $I_{\text{leak}}$ . The voltage amplifier is represented by a frequency-independent gain  $A$  and an offset voltage  $V_{\text{off}}$ , such that

$$V_{\text{out}} = AV_{\text{in}} + V_{\text{off}}. \quad (5.4)$$

where  $V_{\text{in}}$  is the input voltage on the  $I$ - $V$  converter. The 6 dB attenuation loss due to the impedance matched transmission line between the converter and

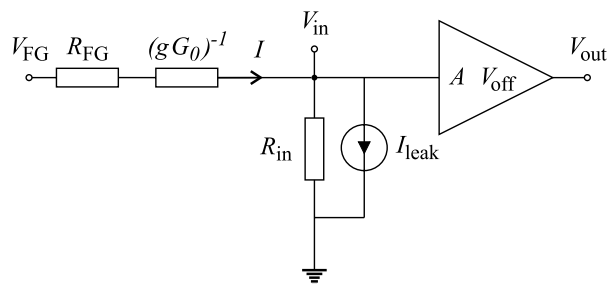


Figure 5.6: The model used for calculating the transfer characteristics of the setup.

the DSO as well as the voltage scaling error on the DSO are absorbed in  $A$ . Similarly, the voltage axis offset error on the DSO is absorbed in  $V_{\text{off}}$ .

From the model in Fig. 5.6, we get

$$V_{\text{in}} = \frac{R_{\text{in}}}{R_{\text{FG}} + (gG_0)^{-1} + R_{\text{in}}} V_{\text{FG}} - \left\{ R_{\text{in}}^{-1} + \left[ R_{\text{FG}} + (gG_0)^{-1} \right]^{-1} \right\}^{-1} I_{\text{leak}}. \quad (5.5)$$

When Eq. (5.5) is inserted in Eq. (5.4),  $V_{\text{out}}$  may be written as

$$V_{\text{out}} = f_1(g)V_{\text{FG}} + f_2(g), \quad (5.6)$$

where

$$f_i(g) = \frac{\alpha_i g}{g + \beta_i} + \gamma_i, \quad i = 1, 2 \quad (5.7)$$

are nonlinear functions of  $g$ . The parameters  $\alpha_i$ ,  $\beta_i$  and  $\gamma_i$  are given by

$$\alpha_1 = \frac{A}{1 + R_{\text{FG}}/R_{\text{in}}}, \quad (5.8a)$$

$$\alpha_2 = \frac{AI_{\text{leak}}R_{\text{in}}}{1 + R_{\text{FG}}/R_{\text{in}}}, \quad (5.8b)$$

$$\beta_1 = \beta_2 = \frac{1}{G_0(R_{\text{FG}} + R_{\text{in}})}, \quad (5.8c)$$

$$\gamma_1 = 0, \quad (5.8d)$$

$$\gamma_2 = -AI_{\text{leak}}R_{\text{in}} + V_{\text{off}}. \quad (5.8e)$$

## 5.5 Calibration

To avoid thermal drift, it is important to warm up the equipment at least one hour before the calibration. A calibration is only reliable when the V/div setting on the DSO is kept constant throughout the calibration and experiment. Due to thermal drift a new calibration must be made daily.

The setup is calibrated using a set of 12 calibrated resistors with conductances  $g_j$ ,  $j = 1 \dots 12$  around 0, 0.5, 1, 2, 3.5, 6, 9, 12, 25, 50, 100, and 400 (in units of  $G_0$ ). For each of these resistors 10 constant voltage traces are recorded with the DSO. To ensure that systematic errors are averaged out, the function generator voltage  $V_{FG}$  is chosen randomly between the maximum and minimum values, where the output voltage can be measured by the DSO including both limits. The traces are transferred to the PC and corrected for differential non-linearity (DNL) [22]. DNL is caused by the analog-to-digital converters (ADC) on the input line of the DSO, because the width of the voltage bins changes from bin to bin. From the corrected traces the output voltage is calculated as the mean value [22].

For each conductance  $g_j$ , the corresponding function values  $f_1(g_j)$  and  $f_2(g_j)$  can now be found by making a linear fit to Eq. (5.6). The parameters in Eq. (5.7) are subsequently found by fitting the twelve known values of  $f_1(g_j)$  and  $f_2(g_j)$  (and their uncertainties) to Eq. (5.7) using the Levenberg-Marquandt method for minimizing  $\chi^2$  [23]. Initial guesses of the parameters are obtained from Eq. (5.8) and the approximate circuit parameters in Fig. 5.6. Although  $\beta_1 = \beta_2$  according to Eq. (5.8c), we relax this restriction in the fitting procedure. Thus, we determine five free parameters, which is also the number of free parameters in our original model, cf. Fig. 5.6 ( $\gamma_1 = 0$  is fixed during fitting).

Care should be taken when fitting to a functional form like Eq. (5.7). Usually  $\beta_i$  in Eq. (5.8c) has a value of 6–50. When  $g \ll \beta_i$ , the parameters  $\alpha_i$  and  $\beta_i$  will be fully dependent<sup>5</sup> since  $f_i$  will only depend on the fraction  $\alpha_i/\beta_i$ . Similarly, when  $g \gg \beta_i$ , there will be full dependency between  $\alpha_i$  and  $\gamma_i$ . Therefore, to keep the dependencies between all parameters at a reasonable level, it is important to calibrate with several resistors that span a wide range of conductances. With our set of calibrated resistors, the dependency between any two parameters is always smaller than 90% and typically around 50%.<sup>5</sup> This is sufficient for our purpose.

<sup>5</sup>The covariance matrix  $C_{ij}$  for the fitted parameters can be estimated from the fitting procedure. [23] The uncertainty of a parameter  $i$  is given by  $\sqrt{C_{ii}}$ . The dependency between two parameters  $i$  and  $j$  is given by  $C_{ij}/\sqrt{C_{ii}C_{jj}}$ .

## 5.6 Calculating $G$ , $I$ , and $V$

The calibration procedure allows us to calculate  $V_{\text{out}}(g, V_{\text{FG}})$  using Eqs. (5.6) and (5.7). However, in experiments, we are interested in finding  $g(V_{\text{FG}}, V_{\text{out}})$ . This is done as follows: If we insert Eq. (5.7) in Eq. (5.6) and solve for  $g$ , we obtain a quadratic equation with the usual solution

$$g = \frac{-b \pm \sqrt{b^2 - 4ac}}{2a}. \quad (5.9)$$

With  $\gamma_1 = 0$  and independent values for  $\beta_1$  and  $\beta_2$ , the coefficients in Eq. (5.9) are given by

$$a = \alpha_2 + \gamma_2 + \alpha_1 V_{\text{FG}} - V_{\text{out}}, \quad (5.10a)$$

$$b = (\beta_1 + \beta_2)(\gamma_2 - V_{\text{out}}) + \alpha_2 \beta_1 + \alpha_1 \beta_2 V_{\text{FG}}, \quad (5.10b)$$

$$c = \beta_1 \beta_2 (\gamma_2 - V_{\text{out}}). \quad (5.10c)$$

The sign in Eq. (5.9) depends in a rather complicated way on the sizes and signs of the voltages and parameters in Eq. (5.10). The correct sign can be found by checking which solution solves Eq. (5.6).

When  $g$  is known, the current  $I$  can be found from the model in Fig. 5.6 as

$$I = \frac{V_{\text{FG}} + R_{\text{in}} I_{\text{leak}}}{R_{\text{FG}} + (gG_0)^{-1} + R_{\text{in}}}.$$

This expression can be written in terms of the known voltages and calibration parameters in Eq. (5.7) by using Eqs. (5.8a–c)

$$I = \frac{V_{\text{FG}} + \alpha_2/\alpha_1}{\beta_1^{-1} + g^{-1}} G_0. \quad (5.11)$$

According to Eq. (5.8c) we are free to use either  $\beta_1$  or  $\beta_2$  in Eq. (5.11). We use  $\beta_1$  because it has the smallest uncertainty. We have checked the validity of Eq. (5.11) by inserting an ammeter and measuring the current through calibrated resistors under DC conditions (its inner resistance is absorbed in  $R_{\text{FG}}$  during calibration).

Finally, using Ohms law, the voltage drop across the ASC can be calculated from Eqs. (5.9) and (5.11)

$$V = \frac{I}{gG_0}. \quad (5.12)$$

## 5.7 Timing the burst

In our experiments, we only measure  $V_{\text{out}}$ . In order to calculate the conductance of and current through an ASC, we also need to know  $V_{\text{FG}}$  according to Eqs. (5.9), (5.10) and (5.11). This is no problem during the calibration procedure, since here  $V_{\text{FG}}$  has a constant, known value (the offset voltage). When we work with voltage bursts, this is no longer the case. It is impossible to measure  $V_{\text{FG}}$  directly with another input channel on the DSO, since  $V_{\text{FG}}$  is the voltage to which the FG is set to internally (cf. Fig. 5.6). The voltage that can be measured at the output terminal is different due to the voltage drop in  $R_{\text{FG}}$ . Furthermore,  $R_{\text{FG}}$  cannot be found from the calibration parameters in Eq. (5.8) (four equations with five unknowns).

Instead, we *assume* that the FG sends out an ideal signal with the requested properties (frequency, amplitude, etc.) and calculate  $V_{\text{FG}}$ . This has turned out to be a good assumption for our FG provided the burst frequency is not larger than 100 kHz. However, the proper synchronization of the calculated FG signal  $V_{\text{FG}}$  with  $V_{\text{out}}$  still remains. This is best illustrated with an example.

In Fig. 5.7 is shown a measured voltage trace of  $V_{\text{out}}$  vs time when a triangular voltage burst is applied to a calibrated resistor. This particular voltage trace will be used as an example in this and the following section. At a given time the operator gives the DSO a trigger signal corresponding to  $t = 0$  on the time axis. In response to this, the DSO sends out a trigger signal to the FG (Fig. 5.1). This happens within 150 ns. Upon receipt of the trigger signal, the FG spends another  $1300 \pm 25$  ns before the burst is sent out (the burst latency). With the STM setup we have to add approximately 50 ns due to the propagation time through the cables, and the burst signal will be delayed by up to  $1.5 \mu\text{s}$  as compared to the DSO trigger time. This can be seen in Fig. 5.7, where there is a  $1\text{--}2 \mu\text{s}$  delay between the DSO trigger time and the onset of the burst.

When using the MCBJ (see Sec. 3.3), adjustment of the delay is not important, even though the delay in the transmission cables will be longer than for the STM. The reason for this is the much lower frequencies used for the measurement resulting in bursts that last 1–50 ms. For these experiments a delay of a few  $\mu\text{s}$  will be unimportant, meaning that the burst and the output signal are already synchronized within the relevant timescale, even when the delay is set to zero.

Finding the correct delay has turned out to be of great importance in the STM experiments, as can be seen from Fig. 5.8 where a change in the delay of 30 ns (0.2%) causes a significant change in the calculated conductance. The noisy part of the conductance trace before and after the burst in Fig. 5.8 stems from the small bias signal  $V_{\text{bias}} = 0.03$  V. When the output voltage is small

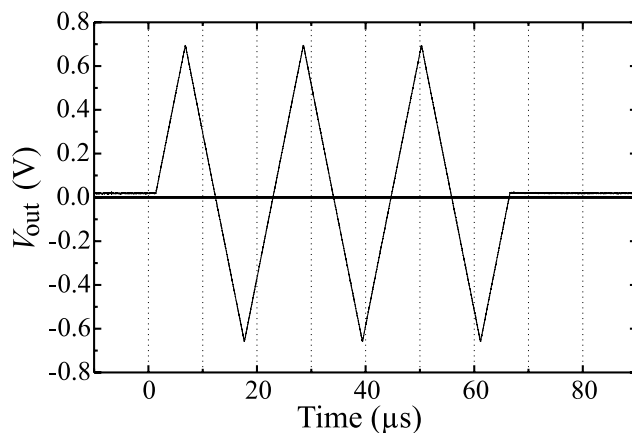


Figure 5.7: An example of the measured  $V_{\text{out}}$  vs time, when a 3 cycle triangular burst with frequency  $f = 46$  kHz, amplitude  $A = 1.15$  V, and bias  $V_{\text{bias}} = 0.03$  V is applied to a resistor with a conductance of  $g = 3.5373$ . There are 10k data points (100 Msamples/s). The DSO is triggered at  $t = 0$ . A delay in the beginning of the burst is clearly seen.

the uncertainty is large. The noise decreases as the burst begins and the signal increases, but every time  $V_{\text{out}}$  crosses zero the signal is lost and the noise will grow towards infinity (compare with Fig. 5.7). Notice, that no matter what the noise level is, the mean value of the conductance trace is constant on the value of the resistor.

Because of the jitter in the delay from the DSO and the FG, the delay changes from trace to trace. A semi-automatic program has been written to adjust these delays. It is based on a figure-of-merit function  $F_{\text{asym}}(t_{bd})$ , which is at a minimum when  $t_{bd}$  is close to the optimal delay. As can be seen from Fig. 5.8 there is an asymmetry around the crossings when the chosen delay has a wrong timing. This is used to construct  $F_{\text{asym}}$ . If  $g_c$  is the conductance at the crossing (calculated from the slope of the  $I$ - $V$  curve around the crossing), and  $t_c$  is the crossing time [ $V_{\text{FG}}(t_c) = 0$ ], we can describe the asymmetry by this function:

$$\sum_i (g_i - g_c) (t_i - t_c) , \quad (5.13)$$

where the summation is over all data points  $(g_i, t_i)$  within a given range from the

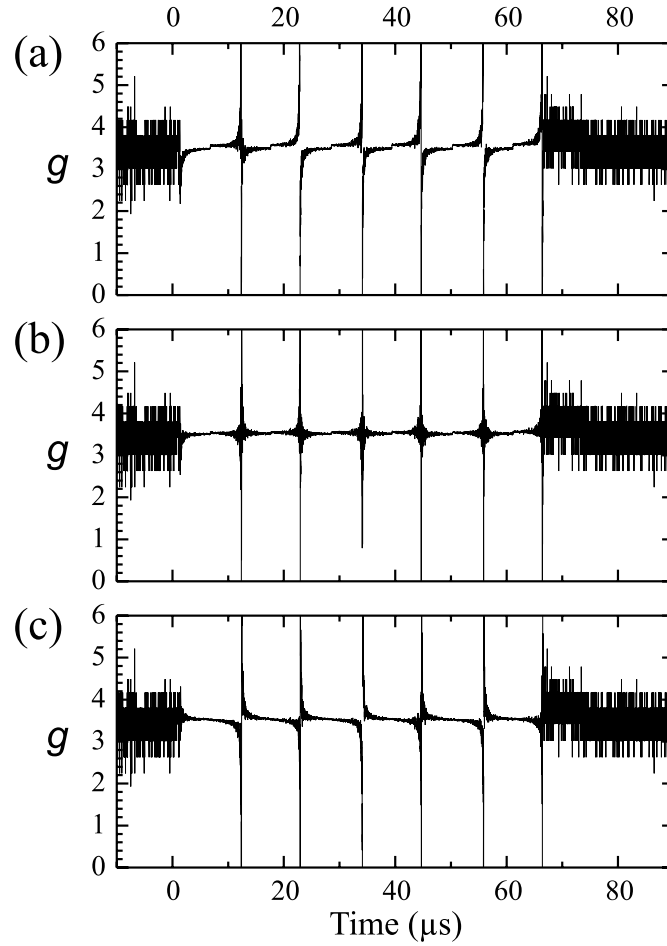


Figure 5.8: The calculated conductance  $g(t)$  from the trace in Fig. 5.7. In (b) the optimized delay  $t_{bd} = 1349$  ns has been used, while the delay in (a) is 30 ns shorter and in (c) 30 ns longer. The mean value of the conductance trace is constant on the value of the resistor  $g = 3.5373$ .

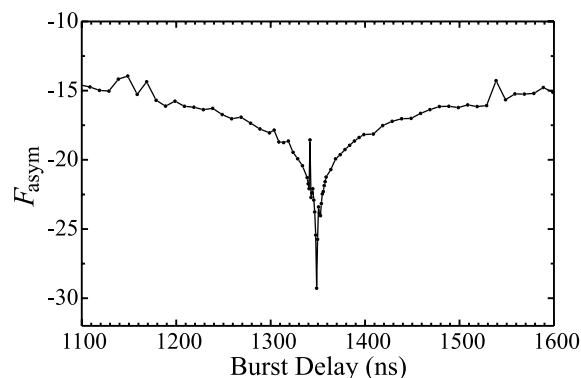


Figure 5.9: Plot of  $F_{\text{asym}}$  as a function of the burst delay for the trace from Fig. 5.7. The optimal delay is 1349 ns.

crossing. From Fig. 5.8 it can be seen that the sum will be negative (positive) when the delay is shorter (longer) than the correct delay, and finding where the sum is closest to zero as a function of  $t_{bd}$  will optimize the delay.

To further improve the expression, all crossings are included and the result is squared. The final function is defined as:

$$F_{\text{asym}}(t_{bd}) \equiv \ln \left( \left\{ \sum_{c,i} [g_i(t_{bd}) - g_c][t_i - t_c(t_{bd})] \right\}^2 \right), \quad (5.14)$$

where the logarithm is introduced because the sum can extend over several orders of magnitude, and now  $t_{bd}$  is found by minimizing  $F_{\text{asym}}$ . When evaluating  $F_{\text{asym}}$  we usually include 100 data points around each crossing.

The graph of  $F_{\text{asym}}$  corresponding to Fig. 5.8b is shown in Fig. 5.9. The procedure works almost as well with actual measurements on ASCs as the example here on a calibrated resistor. In most cases (80%), the program can find the delay, but for the rest a large glitch in  $F_{\text{asym}}$  causes the procedure to find the wrong delay. For these cases the delay has to be corrected manually. An example of a small glitch can be seen in Fig. 5.9 at 1340 ns.

## 5.8 Performance on resistors

The performance of the setup after calibration and optimization of the burst delay can conveniently be tested using calibrated resistors. In Fig. 5.10a we show the final, calculated  $I$ - $V$  curve for a  $g = 3.5373$  resistor based on the voltage trace in Fig. 5.7. Note, that although the voltage burst consists of three cycles, all the curves collapse onto one straight line. The acquisition time is  $65 \mu\text{s}$  (cf. Fig. 5.7).

To check for nonlinearities in the  $I$ - $V$  curve, we fit the calculated curve to the following third order polynomial in  $V$

$$I(V) = I_0 + g^{(0)} G_0 V + \frac{1}{2} g^{(1)} G_0 V^2 + \frac{1}{6} g^{(2)} G_0 V^3, \quad (5.15)$$

where  $I_0$  is a constant offset current. The other terms are related to the voltage-dependent *differential* conductance measured in quantum units  $g_d(V)$ , which is given by

$$\begin{aligned} g_d(V) &\equiv \frac{1}{G_0} \frac{\partial I}{\partial V} \\ &= g^{(0)} + g^{(1)} V + \frac{1}{2} g^{(2)} V^2. \end{aligned} \quad (5.16)$$

From this equation, it is clear that  $g^{(0)}$  is the differential (and total) conductance at zero bias measured in quantum units, whereas  $g^{(1)}$  and  $g^{(2)}$  are the first and second partial derivatives of  $g_d$  with respect to  $V$ . The fitting parameters for the  $I$ - $V$  curve in Fig. 5.10a are given in Table 5.1. The dominant linear term  $g^{(0)}$  is 0.3–0.4% below the calibrated value.

The residual current signal after subtracting the linear term from Fig. 5.10a is shown in Fig. 5.10b. It is dominated by noise. On close inspection, the residual current tends to split into two signals at large magnitudes of the voltage. This originates from the different voltage sweeps, which do not overlap completely. In this case a rising (falling) voltage flank gives a curve with a small negative (positive)  $g^{(1)}$ . This is probably due to a not 100% correct burst delay. However, if data from an integer number of full burst cycles are included in the fit (as is the case here), the curvature tends to average to zero, as can be seen in Table 5.1, where  $g^{(1)}$  is very small and zero within the uncertainty of the fit.

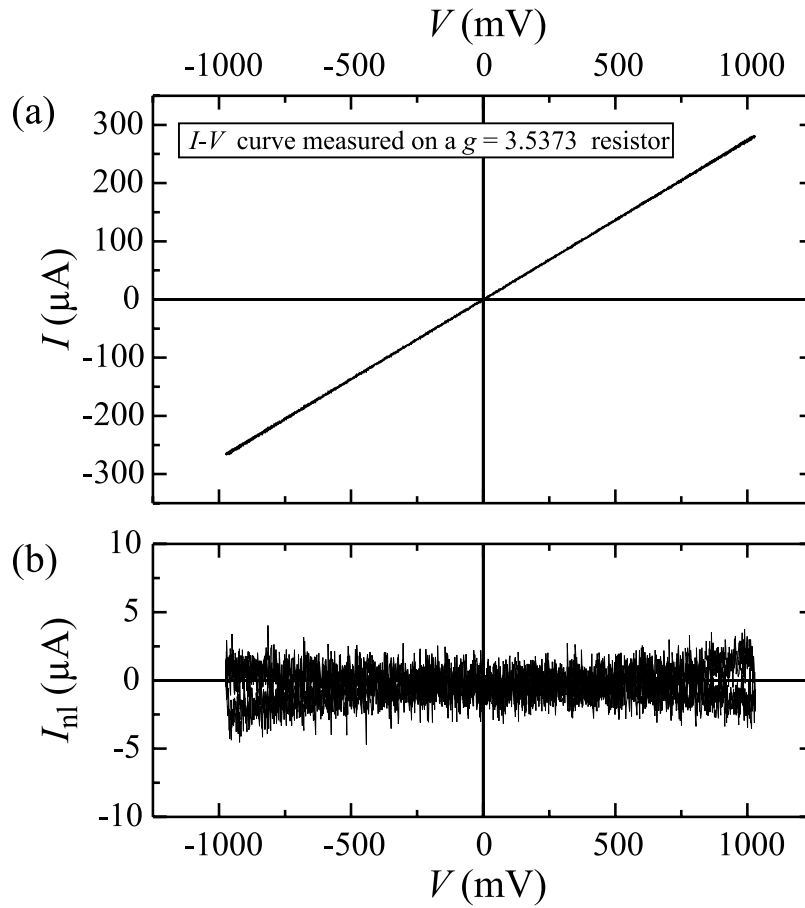


Figure 5.10: (a)  $I$ - $V$  curve of a calibrated resistor with conductance  $g = 3.5373$  calculated from Eqs. (5.11) and (5.12) using the burst part of the measured voltage trace in Fig. 5.7, the calibration parameters, and the optimized burst delay  $t_{bd}^0$  found in Fig. 5.9. When the  $I$ - $V$  curve is fitted to the third order polynomial in Eq. (5.15), we get  $g^{(0)} = 3.5252 \pm 0.0008$ . (b) The residual part of the calculated  $I$ - $V$  curve after subtracting the fitted linear term.

$I_0$ (nA)	$-330\pm30$
$g^{(0)}$	$3.5252\pm0.0008$
$g^{(1)}$ ( $V^{-1}$ )	$-0.0002\pm0.0002$
$g^{(2)}$ ( $V^{-2}$ )	$0.030\pm0.008$

Table 5.1: Parameters for third-order polynomial fit [Eq. (5.15)] to  $I$ - $V$  curves on a  $g = 3.5373$  resistor (Fig. 5.10). The uncertainties include only random measurement errors. The dependency between  $g^{(0)}$  and  $g^{(2)}$  is 92% and  $-72\%$  between  $I_0$  and  $g^{(1)}$  (see footnote 5 on page 70).

The voltage trace in Fig. 5.7 was acquired several hours after the setup was calibrated, after more than 200  $I$ - $V$  curves on Au ASCs had been acquired. Thus, a small current offset error due to thermal drift is to be expected. This is confirmed in Table 5.1, where a small statistically significant  $I_0$  of about  $-300$  nA is found from the fits. Finally, the third order term  $g^{(2)}$  has a small, but statistically significant, positive value of about  $0.03$   $V^{-2}$ . This is not surprising since we have assumed that (1) the gain of the setup is frequency-independent; (2) the calculated FG signal is an ideal signal; and (3) the burst delay is correct. These assumptions are not strictly valid and will inevitably lead to small, systematic nonlinearities in the  $I$ - $V$  curves.

For the  $I$ - $V$  curve in Fig. 5.10a, the maximum nonlinear contribution to the  $I$ - $V$  curve occurs around  $-1.0$  V [since  $g^{(1)}$  is negative]. Here, the second and third order terms contribute less than 0.2% to the total current. If we decrease the burst amplitude, the nonlinear constants  $g^{(1)}$  and  $g^{(2)}$  tend to have larger magnitudes (see Appendix C). However, the maximum nonlinear contribution to the current is kept at the same low level since these terms depend on higher orders in  $V$ .

Tests on other calibrated resistors with conductances between 0.5 and 400  $G_0$  have also been performed using both sinusoidal and triangular bursts with frequencies in the range 1–100 kHz. In all cases, we have found that (1) the linear term  $g^{(0)}$  can be determined with an accuracy better than 1% (normally  $\approx 0.5\%$ ); and (2) the nonlinear contributions from  $g^{(1)}$  and  $g^{(2)}$  to the  $I$ - $V$  curves are smaller than 1% (normally  $\approx 0.3\%$ ). We have also checked how the fitting parameters depend on the burst delay. As long as  $t_{bd}$  is changed by only a few percent [like in Fig. 5.8a, where it is clear that the delay is inadequate] the change in the parameters is negligible.

## 5.9 Performance on a breaking gold ASC

We finally demonstrate how the setup can be successfully applied to measuring  $I$ - $V$  curves on Au ASCs formed between an STM Au tip and a Au(111) surface in UHV at RT. The Au(111) surface is cleaned by sputtering and annealing as described in Sec. 3.2. The Au tip is made by cutting a 0.25 mm diameter, 99.99% pure Au wire. The tip is “cleaned” prior to the experiments by indenting it repeatedly into the surface to a depth of 500 Å.

The topography of the Au surface is imaged in constant current mode using a conventional set of STM electronics. Images displaying atomic resolution and the so-called “herringbone” reconstruction [24] are obtained to ensure that the surface is clean on the atomic scale (cf. Fig. 3.4 on page 34). After the initial STM inspection, the tip is retracted a few  $\mu\text{m}$ , and the fast electronics for acquiring  $I$ - $V$  curves (Fig. 5.1) is connected to the STM.

By means of the inchworm motor, the tip is approached to the surface until the conductance increases above  $1 G_0$ . The computer-controlled feedback loop is then enabled wherein  $V_{\text{out}}$  is acquired repeatedly from the ADC (cf. Fig. 5.1), and the corresponding conductance is calculated using Eq. (5.9). In this manner it is quite easy to stabilize the Au contact at a conductance larger than  $10 G_0$ . However, smaller contacts tend to be quite unstable, and we cannot stabilize them using the computer controlled feedback since it has a rather long response time of  $\approx 10$  ms.

We often observe that ASCs with a conductance smaller than  $10 G_0$  tend to break spontaneously. This is probably due to a spontaneous ‘diffusion out of contact’. External vibrations do not seem to cause the breaks since we have been able to acquire images with atomic resolution (see Fig. 3.4a on page 34).

The DSO is triggered by events in which the conductance goes below  $\approx 3 G_0$  such that a voltage burst is initiated immediately before the contact is broken. Hereby it is possible to study the  $I$ - $V$  curves of several metastable configurations in the contact during the final stages of the breaking process. An example of this is given in Fig. 5.11, where a three-cycle, 10 kHz triangular burst with an amplitude of 1.1 V, superimposed on a 40 mV offset voltage, is applied to a Au ASC with an initial value of the conductance around  $3 G_0$  [see inset in Fig. 5.11a, only the first two cycles are shown].

The calculated time evolution of the total conductance is shown in Fig. 5.11a. The conductance trace is composed of four very well defined plateaus close to  $3, 2, 1,$  and  $0 G_0$ . The noise in the signal is large before the onset of the burst and diverges at the crossings of  $V_{\text{FG}}$  as discussed in relation to Fig. 5.8. The conductance on a plateau is almost independent of the bias voltage, and the

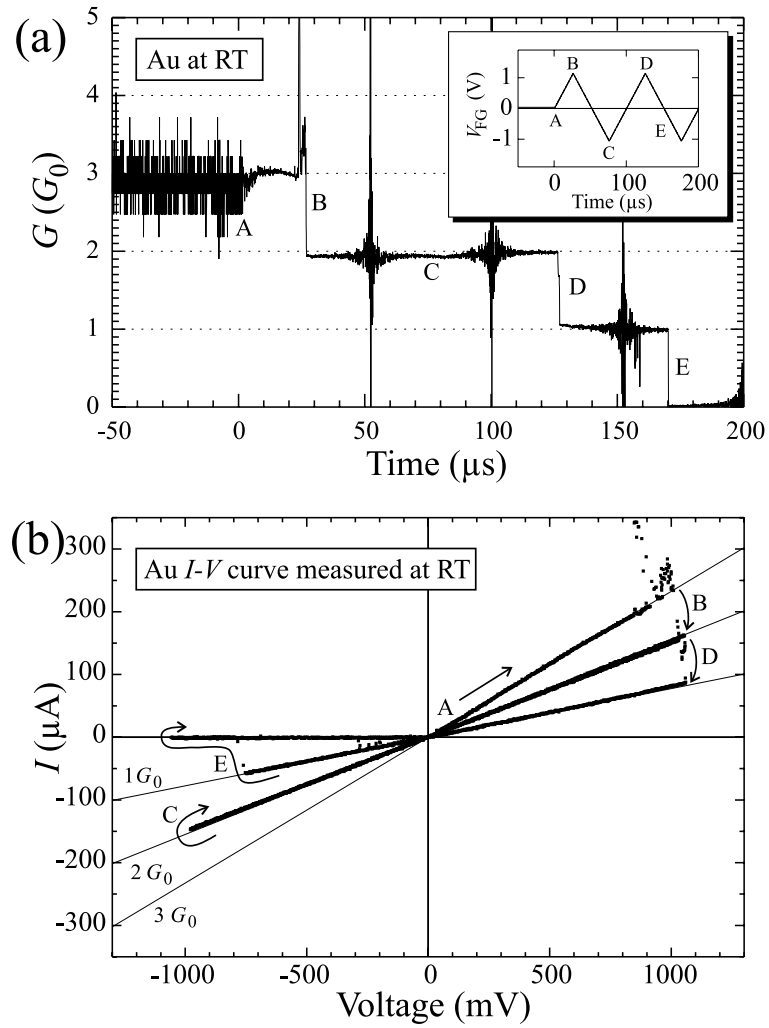


Figure 5.11: (a) Calculated total conductance on a breaking Au ASC under an applied voltage burst (inset). (b) The corresponding calculated  $I$ - $V$  curve. Lines corresponding to integer values of the conductance quantum have been inserted to guide the eye. There are 5000 data points in the plot (50 ns/point).

transition between plateaus occurs very quickly. Glitches in the conductance occur immediately before B and 10–15  $\mu\text{s}$  before E. An intermediate plateau around  $1.7 G_0$  is observed for a very short period of time (0.6  $\mu\text{s}$ ) at D. The overall behavior of the trace in Fig. 5.11a is quite similar to what is usually observed in Au ASCs under constant bias voltage conditions at RT [1, 3, 16, 22, 25–31].

In Fig. 5.11b, we show the calculated  $I$ - $V$  curve for the conductance trace in Fig. 5.11a. It consists of segments of almost straight lines through the origin. The segments closely follow lines corresponding to quantized and voltage-independent values of the conductance. This is at variance with all previous  $I$ - $V$  curves recorded on *stable* Au contacts at RT [1–6]. The origin of these apparent discrepancies will be discussed in the next chapter.

## 5.10 Summary

We have constructed a setup which is capable of acquiring accurate  $I$ - $V$  curves on metal ASCs during a period which may be as short as 10  $\mu\text{s}$ . Tests on resistors show that nonlinear contributions to the  $I$ - $V$  curves are typically smaller than 0.3% (always better than 1%). From the slope of the  $I$ - $V$  curve, the conductance can be found with an accuracy of typically 0.5% (always better than 1%). The time resolution of the setup is typically 25–100 ns. Initial tests on metastable Au ASCs at RT reveal almost Ohmic  $I$ - $V$  curves with nonlinearities much smaller than reported for stable contacts [1–6]

## References

- [1] J. I. Pascual, J. Méndez, J. Gómez-Herrero, A. M. Baró, N. García, U. Landman, W. D. Luedtke, E. N. Bogachek, and H.-P. Cheng, “Properties of Metallic Nanowires: From Conductance Quantization to Localization,” *Science* **267**, 1793–1795 (1995).
- [2] B. Rodell, V. Korenivski, J. Costa, and K. V. Rao, “Quantized conductivity in STM drawn 100Å nanowires of Au and Ni,” *Nanostruct. Mater.* **7**, 229–235 (1996).
- [3] J. L. Costa-Krämer, N. García, P. García-Mochales, P. A. Serena, M. I. Marqués, and A. Correia, “Conductance quantization in nanowires formed between micro and macroscopic metallic electrodes,” *Phys. Rev. B* **55**, 5416–5424 (1997).
- [4] J. Abellán, R. Chicón, and A. Arenas, “Properties of nanowires in air. Controlled values of the conductance,” *Surf. Sci.* **418**, 493–501 (1998).
- [5] A. Correia, J.-L. Costa-Krämer, Y. W. Zhao, and N. García, “Non-linear contribution to intensity-voltage characteristics of gold nanowires,” *Nanostruct. Mater.* **12**, 1015–1020 (1999).
- [6] H. Mehrez, A. Wlasenko, B. Larade, J. Taylor, P. Grütter, and H. Guo, “ $I$ - $V$  characteristics and differential conductance fluctuations of Au nanowires,” *Phys. Rev. B* **65**, 195419 (2002).
- [7] E. Scheer, P. Joyez, D. Esteve, C. Urbina, and M. H. Devoret, “Conduction Channel Transmissions of Atomic-Size Aluminum Contacts,” *Phys. Rev. Lett.* **78**, 3535–3538 (1997).
- [8] E. Scheer, N. Agrait, J. C. Cuevas, A. L. Yeyati, B. Ludoph, A. Martín-Rodero, G. R. Bollinger, J. M. van Ruitenbeek, and C. Urbina, “The signature of chemical valence in the electrical conduction through a single-atom contact,” *Nature* **394**, 154–157 (1998).
- [9] B. Ludoph, M. H. Devoret, D. Esteve, C. Urbina, and J. M. van Ruitenbeek, “Evidence for Saturation of Channel Transmission from Conductance Fluctuations in Atomic-Size Point Contacts,” *Phys. Rev. Lett.* **82**, 1530–1533 (1999).

- 
- [10] B. Ludoph and J. M. van Ruitenbeek, "Conductance fluctuations as a tool for investigating the quantum modes in atomic size metallic contacts," *Phys. Rev. B* **61**, 2273–2285 (2000).
- [11] H. Ohnishi, Y. Kondo, and K. Takayanagi, "Quantized conductance through individual rows of suspended gold atoms," *Nature* **395**, 780–783 (1998).
- [12] Y. Kondo and K. Takayanagi, "Synthesis and Characterization of Helical Multi-Shell Gold Nanowires," *Science* **289**, 606–508 (2000).
- [13] V. Rodrigues, T. Fuhrer, and D. Ugarte, "Signature of Atomic Structure in the Quantum Conductance of Gold Nanowires," *Phys. Rev. Lett.* **85**, 4124–4127 (2000).
- [14] Y. Takai, T. Kawasaki, Y. Kimura, T. Ikuta, and R. Shimizu, "Dynamic Observation of an Atom-Sized Gold Wire by Phase Electron Microscopy," *Phys. Rev. Lett.* **87**, 106105 (2001).
- [15] T. Kizuka, S. Umehara, and S. Fujisawa, "Metal-Insulator Transition in Stable One-Dimensional Arrangements," *Jpn. J. of Appl. Phys.* **40**, L71–L74 (2001).
- [16] G. Rubio, N. Agraït, and S. Vieira, "Atomic-Sized Metallic Contacts: Mechanical Properties and Electronic Transport," *Phys. Rev. Lett.* **76**, 2302–2305 (1996).
- [17] D. P. E. Smith, "Quantum Point Contact Switches," *Science* **269**, 371–373 (1995).
- [18] E. L. Foley, D. Candela, K. M. Martini, and M. T. Tuominen, "An undergraduate laboratory experiment on quantized conductance in nanocontacts," *Am. J. Phys.* **67**, 389–393 (1999).
- [19] U. Landman, W. D. Luedtke, B. E. Salisbury, and R. L. Whetten, "Reversible Manipulations of Room Temperature Mechanical and Quantum Transport Properties in Nanowire Junctions," *Phys. Rev. Lett.* **77**, 1362–1365 (1996).
- [20] H. Yasuda and A. Sakai, "Conductance of atomic-scale gold contacts under high-bias voltages," *Phys. Rev. B* **56**, 1069–1072 (1997).

- 
- [21] W. A. de Heer, S. Frank, and D. Ugarte, “Fractional quantum conductance in Gold nanowires,” *Z. Phys. B* **104**, 469–473 (1997).
- [22] K. Hansen, E. Lægsgaard, I. Stensgaard, and F. Besenbacher, “Quantized Conductance in Relays,” *Phys. Rev. B* **56**, 2208–2220 (1997).
- [23] W. H. Press, B. P. Flannery, S. A. Teukolsky, and W. T. Vetterling, *Numerical Recipes in Pascal* (Cambridge University Press, Cambridge, 1989).
- [24] J. V. Barth, H. Brune, G. Ertl, and R. J. Behm, “Scanning tunneling microscopy observations on the reconstructed Au(111) surface: Atomic structure, long-range superstructure, rotational domains, and surface defects,” *Phys. Rev. B* **42**, 9307–9318 (1990).
- [25] J. I. Pascual, J. Méndez, J. Gómez-Herrero, A. M. Baró, N. García, and V. T. Binh, “Quantum Contact in Gold Nanostructures by Scanning Tunneling Microscopy,” *Phys. Rev. Lett.* **71**, 1852–1855 (1993).
- [26] M. Brandbyge, J. Schiøtz, M. R. Sørensen, P. Stoltze, K. W. Jacobsen, J. K. Nørskov, L. Olesen, E. Lægsgaard, I. Stensgaard, and F. Besenbacher, “Quantized conductance in atom-sized wires between two metals,” *Phys. Rev. B* **52**, 8499–8514 (1995).
- [27] J. L. Costa-Krämer, N. García, P. García-Mochales, and P. A. Serena, “Nanowire formation in macroscopic metallic contacts: quantum mechanical conductance tapping a table top,” *Surf. Sci.* **342**, L1144–L1149 (1995).
- [28] C. J. Muller, J. M. Krans, T. N. Todorov, and M. A. Reed, “Quantization effects in the conductance of metallic contacts at room temperature,” *Phys. Rev. B* **53**, 1022–1025 (1996).
- [29] Z. Gai, Y. He, H. Yu, and W. S. Yang, “Observation of conductance quantization of ballistic metallic point contacts at room temperature,” *Phys. Rev. B* **53**, 1042–1045 (1996).
- [30] N. García and J. L. Costa-Krämer, “Quantum-Level Phenomena in Nanowires,” *Europhys. News* **27**, 89–91 (1996).
- [31] W. B. Jian, C. S. Chang, W. Y. Li, and T. T. Tsong, “Geometrical dependence of conductance quantization in metal point contacts,” *Phys. Rev. B* **59**, 3168–3172 (1999).

## Chapter 6

# Effect of Impurities on Current-Voltage Curves of Gold

With the development of the fast setup, described in the prechapter, we had an adequate setup for investigating the current-voltage ( $I$ - $V$ ) characteristics of atomic-sized contacts (ASCs). In this chapter, based on paper [II], we present the results obtained by using the fast setup together with the scanning tunneling microscope (STM) to measure on gold (Au) ASCs.

When forming Au ASCs under ultra-clean conditions, we find that the measured  $I$ - $V$  curves are linear, in contrast to previous reports [1–6]. We have also observed non-linear  $I$ - $V$  curves, but only when a sample that has not been cleaned properly after exposure to air is used. These results are compared with self-consistent *spd* tight-binding (TB) calculations on one and two-atom contacts (performed by Mads Brandbyge) and excellent agreement with the experiments are found. We suggest that the non-linear curves observed in our experiments are due to tunneling through a thin contaminant layer of organic molecules in the tip-sample interface. This is confirmed by fitting the  $I$ - $V$  curve to a simple parabolic barrier model, put forward by Mads Brandbyge and Kim Hansen.

The effect of contamination is very important to consider when dealing with ASCs, but the cleanliness of the contacts has not always been taken into account in a proper way. In Sec. 6.7, a general review will give several examples

where impurities may have influenced the properties of ASCs. This is especially experiments performed under ambient conditions [i.e. in air at room temperature (RT)]. These results are directly related to those presented in this chapter. I also discuss the extremely long bond lengths observed in free suspended monatomic chains, and finally an experiment where the influence of hydrogen ( $H_2$ ) on platinum (Pt) is investigated, will be used to show how also other experiments could have been influenced by the presence of gases.

## 6.1 Introduction

With the ongoing quest of miniaturizing electronic components, there is an increasing interest in fabricating and controlling atomic-scale quantum devices such as ASCs [7–9]. In this realm of reduced size and dimensionality, new and exciting phenomena can be observed [8–15]. For Au ASCs these include conductance quantization [10, 11], and the formation of stable, monatomic chains [8, 9].

The first experiments on ASCs mainly focused on the behavior of the conductance in the low bias voltage regime ( $V < 100$  mV). At higher bias important questions concerning nonlinear conductance [1–6, 16–21], electromigration [20–26] and heating [27, 28] arise. At the present stage, however, the available experimental results [1–6, 22–24] on finite bias conduction in Au ASCs are contradictory, and the theoretical interpretation of the results is unclear [16–19].

Sakai and co-workers [22–24] have studied conductance histograms acquired from breaking Au contacts in a relay and found that the  $1 G_0$ <sup>1</sup> peak did not change its position as the bias voltage was gradually increased to 2 V. This observation suggests that the conductance of monatomic Au contacts (which have a conductance close to  $1 G_0$  [13–15]) is almost independent of voltage. This is in contrast to several reports [1–6] of  $I$ - $V$  characteristics measured on stable Au contacts at RT, which display clear nonlinearities for voltages larger than 0.1–0.5 V.

## 6.2 Experimental details

Previous measurements of  $I$ - $V$  curves on Au contacts [1–6] were done over a time scale of  $\approx 0.1$  s, thus restricting the measurements to contacts which were

---

<sup>1</sup>The fundamental unit of conductance  $G_0$  is defined in Eq. (2.3) on page 15.

stable over relatively long time-scales. Instead, we decided to use the fast setup already described in Chapter 5 whereby an  $I$ - $V$  curve can be acquired within only 20  $\mu$ s, and transient contact geometries can be studied.

### Contact formation techniques

The ASCs are formed at RT<sup>2</sup> between a polycrystalline Au tip mounted in an STM and a Au(110)<sup>2</sup> single crystal surface under ultra-high vacuum (UHV) conditions (see Sec. 3.2). Two fundamentally different methods are used to obtain the contacts:

1. *Hard* indentations. The tip is first indented 40–100 Å into the surface and retracted at a speed of  $\approx 100$  Å/s. The  $I$ - $V$  curve is acquired automatically during the break when the conductance drops below a user defined preset.
2. *Soft* indentations. The indentation is stopped the first time the conductance surpasses a preset value chosen between 1–5  $G_0$ . In a feedback loop, the vertical position of the tip is then continuously adjusted to keep the conductance as stable as possible. When stabilized, an  $I$ - $V$  curve is acquired upon request from the user.

When using soft indentations, only contacts with stable atomic configurations will be investigated, since the time-scale relies on human response. This is not the case for the hard indentations where the voltage burst is applied automatically. When the conductance reaches the preset value, the burst will only be delayed about 1.5  $\mu$ s as we found in Sec. 5.7. Even though the burst is applied almost instantly to the ASC, this will not guaranty that the atomic configuration remains stable during the entire burst. Fitting an  $I$ - $V$  curve to a polynomial like we did in Sec. 5.8 is only interesting, if the contact remains stable during a full burst cycle, so the curve is smooth. If the conductance jumps to another value during the burst, due to atomic rearrangement in the contact region, a fit has no meaning (see Fig. 5.11 on page 80). Only traces that remain stable during a full burst cycle are accepted and presented here (see Appendix B).

---

<sup>2</sup>We also performed experiments on the Au(111) surface, and at temperatures down to 140 K, using the STM. The results did not differ much from those presented here, and they will only be mentioned briefly. See [29] for further details.

## Cleaning procedures

We have also investigated how the cleanliness of the Au(110) sample influences the measured  $I$ - $V$  curves by using two different sample preparation techniques:

1. A clean surface (verified by STM imaging with atomic-scale resolution, see Fig. 3.4 on page 34) is produced by sputtering and annealing under UHV conditions as explained in Sec. 3.2.
2. The sample is rinsed in water and ethanol under ambient conditions before being placed in a UHV chamber.

## 6.3 Current-voltage curves

Examples of measured  $I$ - $V$  curves are shown in Fig. 6.1. They are almost linear if the sample is properly cleaned or the contacts are formed by hard indentations [curves (a) and (b)].<sup>3</sup> In contrast, non-linear  $I$ - $V$  curves are almost exclusively found when the sample is rinsed in air *and* the indentations are soft [curve (c)].

We find that ASCs exhibiting nonlinear  $I$ - $V$  curves are more robust than their linear counterparts: Reproducible  $I$ - $V$  curves can be obtained at voltages up to  $\pm 2$  V, and the contacts can be stable for hours. In contrast, contacts corresponding to linear  $I$ - $V$  curves tend to destabilize at voltages larger than  $\approx 0.75$  V (at RT) and contacts with a conductance smaller than  $5 G_0$  typically break spontaneously within milliseconds.

Independent of the contact formation technique and the cleaning procedure, we find that the  $I$ - $V$  curves can be fitted with good accuracy (see dashed lines in Fig. 6.1) to a third-order polynomial in the applied voltage [4-6]

$$I(V) = GV + G'V^2 + G''V^3. \quad (6.1)$$

Here  $G$  is the low bias conductance, and  $G'$  is a constant describing the polarity-dependence of the current due to asymmetries in the contact region. For most curves  $|G'| < 0.1 G/\text{Volt}$ . The fitting parameters to the curves in Fig. 6.1 can be found in Table 6.1. In the following we will focus on the nonlinear parameter  $G''$  and its dependence on  $G$  (see Appendix A).

Fitted values for  $G$  and  $G''$  based on  $I$ - $V$  curves obtained from 148 different ASCs are shown in Fig. 6.2. For  $I$ - $V$  curves formed in hard indentations or on a properly cleaned sample, the majority of points collapse onto two well-defined regions which have a small third order term ( $|G''| < 0.2 G_0/\text{Volt}^2$ ) and a low

<sup>3</sup>We can only stabilize contacts formed in soft indentations on a properly cleaned surface with a conductance smaller than  $4 G_0$  by cooling the sample to approximately 170 K (see Sec. 3.2).  $I$ - $V$  curves from such contacts resemble curves (a) and (b) in Fig. 6.1 [29].

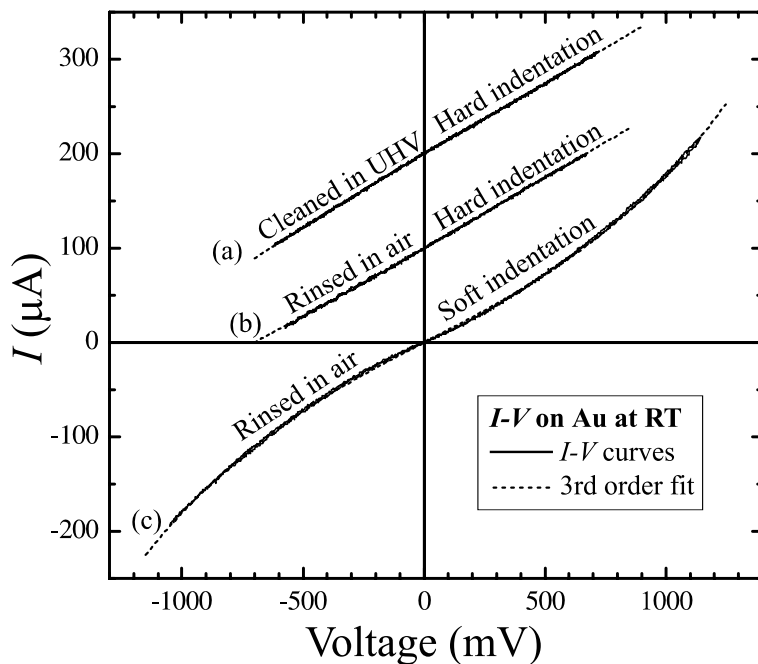


Figure 6.1: Examples of measured  $I$ - $V$  curves of Au ASCs formed with the STM at RT under UHV using different sample preparation/contact formation techniques. Each curve is acquired during  $20 \mu\text{s}$ , a single period of the 50 kHz triangular voltage burst used. Best fits to Eq. (6.1) are shown as the dashed lines and the fitting parameters can be found in Table 6.1.  $I$ - $V$  curves with  $G \simeq 2 G_0$  have been selected to allow a more direct comparison between the individual curves which are shifted by  $100 \mu\text{A}$  for clarity.

Curve	$G$ ( $G_0$ )	$G'$ ( $G_0/\text{Volt}$ )	$G''$ ( $G_0/\text{Volt}^2$ )
(a)	1.95	-0.08	0.07
(b)	1.91	0.07	-0.05
(c)	1.72	-0.02	0.59

Table 6.1: Parameters of fit to Eq. (6.1) for the three  $I$ - $V$  curves in Fig. 6.1.

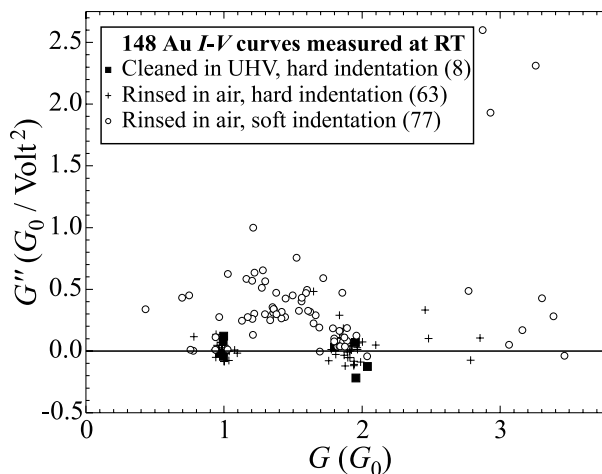


Figure 6.2: Nonlinear term  $G''$  vs low bias conductance  $G$  obtained by fitting measured  $I$ - $V$  curves to Eq. (6.1) for different sample preparation/contact formation techniques. Only fits to nearly polarity independent  $I$ - $V$  curves ( $|G'| < 0.05 G_0/\text{Volt}$ ) with small uncertainties of the cubic term ( $\sigma_{G''} < 0.01 G_0/\text{Volt}^2$ ) are shown (see Appendix B). Numbers in parenthesis indicate the number of  $I$ - $V$  curves.

bias conductance close to  $1 G_0$  or slightly below  $2 G_0$ . About 80% of the  $I$ - $V$  curves obtained from soft indentations on a rinsed sample have non-linear terms, which exceed  $0.2 G_0/\text{Volt}^2$  and arbitrary values of  $G$ . The remaining 20% are found in the above-mentioned regions. At higher conductance ( $4$ – $12 G_0$ ) the non-linear term becomes positive for most curves, although the value is still much higher for the data from contacts formed by soft indentations on a rinsed sample [29]. Even for data from the clean sample no clustering of  $G$  around integer values of  $G_0$  is found in this conductance range [29].

## 6.4 Tight-binding calculations

To further elucidate our experimental findings, we have performed transport calculations for two simple contact geometries on the (110) surface shown in Fig. 6.3 (inset). The contacts have either (a) one or (b) two atoms in their smallest cross section. We use a TB model (with  $s$ ,  $p$  and  $d$  orbitals) to calculate the electronic structure and current self-consistently at finite bias [19]. It is mainly the  $6s$  valence electrons which conduct. In agreement with earlier

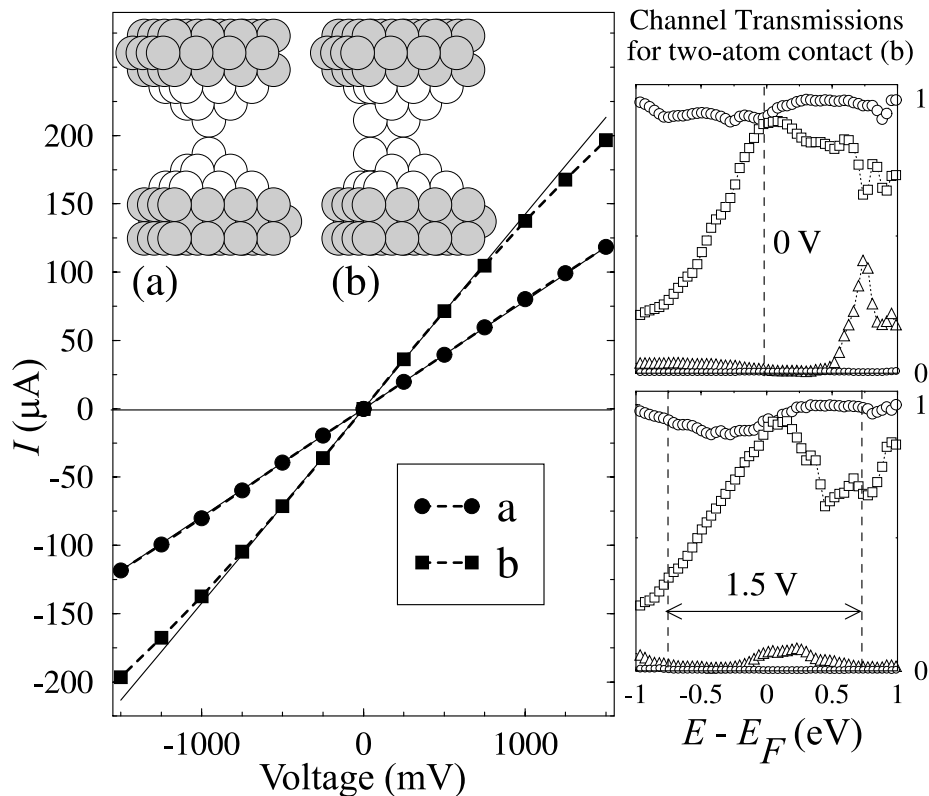


Figure 6.3: Left:  $I$ - $V$  characteristics calculated using a self-consistent TB model for (a) the one, and (b) the two-atom contacts shown in the inset. All interatomic distances are taken to be equal to the bulk value. Solid lines are zero-bias extrapolations corresponding to (a)  $G = 1.02 G_0$ , (b)  $G = 1.88 G_0$ . The  $I$ - $V$  curve for (b) has  $G'' = -0.07 G_0/\text{Volt}^2$ , whereas for (a)  $G'' \simeq 0$ . Since these contacts are symmetric  $G' \equiv 0$ . Right: The channel transmissions for (b) (sorted by size and labeled by  $\{\circ, \square, \triangle, \circ\}$ ) are shown for 0 V and 1.5 V. The vertical dashed lines define the “voltage window” spanning  $\pm eV/2$  on each side of  $E_F$ , used when calculating the current. (Calculations performed by Mads Brandbyge).

calculations [19], we find a conductance of the one-atom contact close to  $1 G_0$ . At zero bias the individual channel transmissions<sup>4</sup> ( $> 0.005$ ) are  $\{1.00, 0.02\}$ . (For comparison, the total transmission through a three atom chain is reduced by 0.04 to  $\{0.98\}$ , due to loss of tunneling contributions through neighboring atoms [16, 17]). The transmissions vs energy for the two-atom contact are shown in the panels to the right in Fig. 6.3 for 0 V and 1.5 V. For 0 V we find a conductance slightly below  $2 G_0$ , which is dominated by two channels with high transmissions  $\{0.95, 0.91, 0.01, 0.01\}$ . We find that the  $I$ - $V$  curve is very linear for the one-atom contact, and has a slight down bend for the two-atom contact which comes mainly from the decrease of one of the main channel transmissions below the Fermi energy ( $E_F$ ): Although there are substantial variations in the transmissions, only modest variations are seen in the  $I$ - $V$  curve, since the total transmission is found by averaging the sum of individual channel transmissions over the “voltage window”  $[E_F - eV/2; E_F + eV/2]$ .

## 6.5 Tunneling through a thin insulating film

Although Au is the noblest of metals [30], a thin layer of contaminant organic molecules forms spontaneously on the clean surface when exposed to ambient conditions [31, 32] (see Fig. 6.4a and the discussion in Sec. 6.7.1).

By using a sample which has only been rinsed in air, there is a risk that this layer hinders the formation of a clean metal-metal contact. This is especially likely to occur if the contacts are formed using the soft indentation method. With this method, the tip may not break through the contaminant layer, as indicated by the sketch in Fig. 6.4b. For the hard indentation, however, the tip will usually break through the layer and metal-metal contacts are formed (Fig. 6.4c). Contacts formed on a contaminated sample are generally observed to be more stable than when formed on a clean sample, probably due to capillary forces between the molecules in the contaminant surface layer and the tip.

When a contact is formed as in Fig. 6.4b the current will be due to tunneling through an insulating layer instead of conduction through an ASC. It is well known [33] that this leads to  $I$ - $V$  curves with a sizeable positive value of  $G''$  in agreement with curve (c) in Fig. 6.1 and the open circles in Fig. 6.2.

Since transmission coefficients in tunneling are orders of magnitudes smaller than those typically encountered in metallic conduction, the contact area needed to reach a conductance of a few  $G_0$  will be much larger than atomic dimensions. This readily explains the high stability of these contacts, the continuous distribution of  $G$  in Fig. 6.2, and the fact that they can sustain larger voltages than metallic contacts [cf. curve (c) in Fig. 6.1].

<sup>4</sup>The concept of transmission eigenchannels is discussed in Sec. 2.6 .

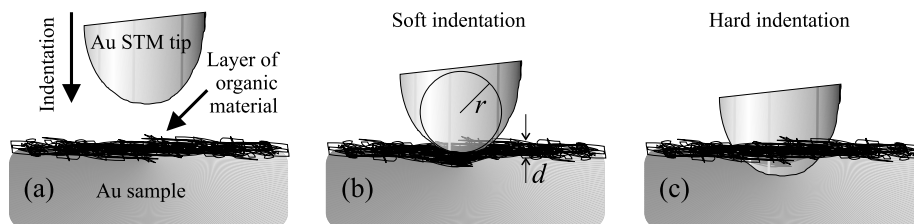


Figure 6.4: Sketch of what may happen when a Au tip is indented into a Au sample which has not been cleaned by sputtering *and* annealing after exposure to *air*. This will result in the formation of a thin contaminant layer of molecules on the sample surface. In (a) the tip is moved towards the sample and examples of the likely outcome of (b) a soft indentation and (c) a hard indentation are indicated. These two types of indentation were defined in Sec. 6.2. In (b) the parameters used in the parabolic barrier model are indicated:  $r$  tip radius and  $d$  barrier thickness (see Fig. 6.5).

In Fig. 6.5 we have fitted nonlinear  $I$ - $V$  curves to a parabolic barrier tunneling model, which has been described in detail elsewhere [29]. With the barrier thickness  $d$  and contact radius  $r$  as free parameters (see Fig. 6.4b), good agreement is found with reasonable values ( $d \sim 10$  Å,  $r = 6$ –25 nm, see figure caption).

In hard indentations, the thin contaminant layer is likely to be destroyed (see Fig. 6.4c), as evidenced by the preference for quantized values of the low bias conductance in Fig. 6.2. For the sputtered and annealed sample all  $I$ - $V$  curves are almost linear in perfect agreement with the TB calculations in Fig. 6.3 and the conductance histograms by Sakai and co-workers [22–24]. In contrast, none of the previous measurements of highly nonlinear  $I$ - $V$  curves on stable Au contacts at RT were performed on sputtered *and* annealed samples in UHV [1–6].

In a recent study, Mehrez *et al.* measured  $I$ - $V$  curves of Au under ambient conditions using the mechanically controllable break-junction (MCBJ) [34]. As expected the curves were clearly non-linear with a positive non-linear term  $G''$ . In the paper,  $I$ - $V$  curves were calculated for a monatomic Au chain, consisting of four atoms and they were found to be linear up to 0.5 V [34]. This is in agreement with our  $I$ - $V$  curves on a sample cleaned in UHV. At higher bias the calculated curves were not linear. This disagrees with our TB calculations in Fig. 6.3 and also with our MCBJ experiments performed at 4.2 K under cryogenic vacuum, even though we measured  $I$ - $V$  curves up to several volt (see Fig. 7.1a on page 117)

Mehrez *et al.* extended the calculations by using a structure where one of the Au atoms in the interface layer was replaced by a sulfur (S) atom [34]. In this case the calculated  $I$ - $V$  curves were similar to the experimental curves.

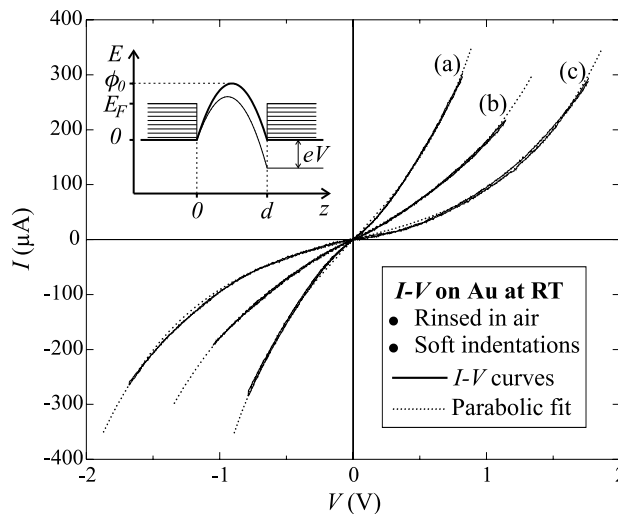


Figure 6.5: Examples of experimental  $I$ - $V$  curves obtained from soft indentations on a rinsed sample at RT under UHV with the STM. Dotted lines represents fits to the parabolic barrier model sketched in the inset [29], assuming a barrier height  $\phi_0 - E_F = 1.5$  eV and a temperature of 300 K. The fitted parameters; barrier thickness and contact radius ( $d, r$ ) (cf. Fig. 6.4b) are given here in units of ( $\text{\AA}, \text{nm}$ ): (a) (12.7, 24), (b) (9.7, 7.7), and (c) (10.7, 6.8). (The model [29], was put forward by Mads Brandbyge and Kim Hansen).

Although not the type of contamination we expect to be present in our setup, their result is in accordance with our observations: Non-linear Au  $I$ - $V$  curves are caused by contamination of the clean Au contact.

## 6.6 Conclusion

It has been suggested, that the previously observed highly non-linear  $I$ - $V$  curves on Au contacts could be a signature of Luttinger-liquid effects [1, 18]. However, our results suggest an alternative and more trivial explanation, namely that non-linearities are related to a contamination of the Au-Au interface. For clean Au ASCs, our measurements and TB calculations show, that the  $I$ - $V$  curves are almost linear. This will be confirmed in the next chapter with experiments performed at liquid helium (He) temperatures (4.2 K) under cryogenic vacuum with the MCBJ as well as with density functional theory (DFT) calculations. Below other possible effects of contamination will be discussed.

## 6.7 Other effects of contamination on ASCs

Above we showed that  $I$ - $V$  curves of Au ASCs are linear when the contacts are formed under ultra clean conditions, otherwise non-linear curves are found. Several experiments have emerged in which the observed behavior of ASCs may have been influenced by the presence of impurities. Some of these will be discussed in the following review.

### 6.7.1 Exposing ASCs of Au to ambient conditions

Since Au is the noblest of metals [30] it has often been deemed unnecessary to keep the working environment clean when forming Au ASCs. Recently several experiments have actually investigated the very effect of adsorbates on ASCs of Au [35–37] and in this way recognized the risk of contamination.

Many experiments on ASCs have been performed under ambient condition (at RT in air). When measuring conductance histograms (see Chapter 4) hard indentations will often help creating metallic contacts even through a contamination layer existing on the interface (e.g. self cleaning electrodes in a mechanical relay [38], see discussion in Sec. 3.1), but this is an insecure approach. It seems to work with Au in some cases, resulting in conductance histograms with peaks at 1, 2 and 3  $G_0$  [22–24, 38, 39] similar to those presented in Chapter 4. In other cases several extra peaks have been observed at even higher integer values of  $G_0$  [40, 41]. With more reactive metals this method is even more unreliable.

In the case of nickel (Ni) it has been mentioned that the mechanical contact between the electrodes could not break the impurity layer formed under ambient conditions [42]. In this experiment metallic contact could only be obtained after flashing the Ni wire momentarily to above 900 K in UHV. Several other metals have been investigated under these conditions. This is discussed in Chapter 4.

In the experiments presenting non-linear  $I$ - $V$  curves on Au many different conditions were used when preparing the samples. Often the curves were measured under ambient conditions [1, 2, 5, 34], other experiments were carried out under clean UHV conditions [4], and here the sample was in some cases even cleaned by annealing. However, all these experiments have one thing in common, the sample is never both sputtered *and* annealed after exposure to air.

Since the ASCs are stabilized at a given conductance, this will most likely resemble the soft indentation (cf. Fig. 6.4b). Based on our own experience we do not expect annealing alone to remove the layer of contamination. Only several cycles of sputtering and annealing can ensure this.

Even under UHV at RT the sample will only remain atomically clean for some hours after cleaning. It is thus of utmost importance either to be able to clean the sample *in situ* under UHV, or to prepare the sample directly in UHV or cryogenic vacuum (e.g. the MCBJ, see Sec. 3.3), to obtain reliable results.

### 6.7.2 Monatomic chains with extremely long bond lengths

In 1998 two simultaneous papers reported on the formation of monatomic Au chains [8, 9]. Especially a transmission electron microscopy (TEM) image of a linear chain of four Au atoms [8] (see Fig. 6.6) received considerable attention.

The observed bond length between atoms in this particular chain was, however, very long (3.5–4 Å) compared to the bulk bond length for Au (2.9 Å). This observation was, nevertheless, in accordance with the other paper [9] where the length of the last conductance plateau ( $G \simeq 1 G_0$ ) of breaking ASCs of Au was measured. Here ASCs were formed at 4.2 K under cryogenic vacuum using a MCBJ. From the measurements, a *plateau-length histogram*<sup>5</sup> was constructed showing peaks positioned at multiples of  $3.6 \pm 1.0$  Å [9].

The observations of long bond lengths were very surprising, because shorter than bulk bond length was to be expected [43], due to the extremely low coordination of atoms (2) in the chain. This can be compared to the coordination in the surface (9) or the bulk (12), and the electron density will be very low in a chain. In order to obtain a stronger bonding, the chain atoms must move closer together than in the bulk metal [43], contrary to what is observed [8, 9].

Since 1998 several other reports showing TEM images of chains with bond lengths longer than the bulk bond length have emerged [44–50]. In most TEM experiments chains are fabricated from samples of thin free standing metal films [8, 44–54] (see Fig. 6.6). The chains are prepared at RT under UHV by burning holes in the film with high intensity of the TEM electron beam. This is expected to clean the surface by burning away impurities, e.g. carbon (C) [45].

Monatomic chains were not obtained in all these TEM experiments, where amongst other, a new interesting phenomenon of helical multi-shell nano-wires were discovered [51, 53]. Of all these thin film TEM experiments did only one group observe monatomic Au chains with bond lengths in a range (2.5–2.9 Å) not longer than the bulk bond length [54]. Here it was actually observed that the chains behavior shifted between two stages. One stage with bond lengths like in the bulk (2.9 Å) and a second stage with shorter bond lengths (2.5 Å) [54].

Even with all the above evidence of the existence of chains with these very long bond lengths, an explanation was lacking. Simulations [55] showed that a monatomic Au chain will break or dimerize if the bond length increases above 3.1 Å, and they are not expected to be stable at RT [55]. Similar calcu-

<sup>5</sup>The first peak in a plateau-length histogram corresponds to the typical length at which an ASC breaks. If there are more than one peak this indicates chain formation, and the distance between the peaks gives the chain bond length. It is important not to confuse plateau-length histograms with the conductance histograms described in Chapter 4. Plateau-length histograms will be presented and discussed in Sec. 9.4.

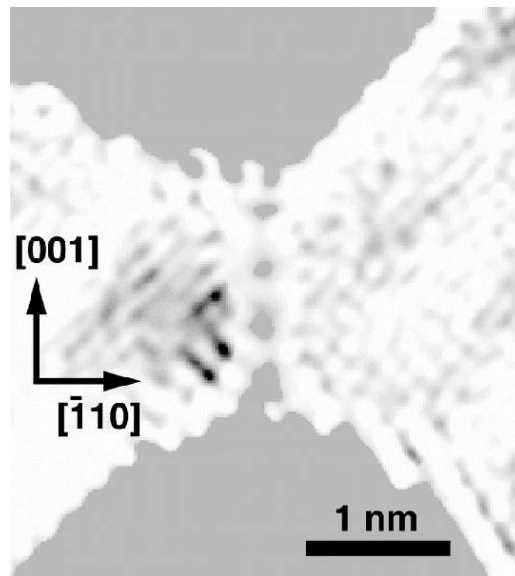


Figure 6.6: The famous RT-UHV-TEM image of a “linear strand of gold atoms forming a bridge between two Au films” [8], i.e. the four grey dots between the grey areas at the top and bottom. The chain is 1.8 nm long, and with five bonds, individual bond lengths exceed 3.5 Å on average. (Reprinted by permission from Nature [8] copyright (1998) Macmillan Publishers Ltd., and with the authors’ consent).

lations have shown that the incorporation of either carbon [47], oxygen (O) [55] or carbon monoxide (CO) [55] into the Au chain can explain long bond lengths.

The carbon calculations appeared in a report with TEM images of Au chains with bond length up to 5 Å formed from free standing films. Here it was calculated that the incorporation of carbon atoms could explain the long distances [47]. A single carbon atom resulted in distances up to 3.5 Å and two carbon atoms could explain even longer distances up to 5 Å.

Oxygen is especially interesting since it will not only stabilize the contact, making it more likely to remain stable even at RT, it will also leave the conductance unchanged at  $1 G_0$  [55]. It should here be noted that the conductance of the chains imaged with TEM usually cannot be measured. If a chain is part of a Au film, as explained above, it will be impossible to attach the electrodes at each end of the chain as will be required for such a measurement.

Only in one, of the above mentioned TEM experiments was the conductance measured for a Au chain while simultaneously imaged with TEM [8]. The chain was in this case formed between tip and sample of an STM placed inside the UHV-TEM. This chain had a conductance of  $1 G_0$ , proving that it was indeed monatomic. This could not be seen from the TEM images which did not display atomic resolution [8]. Hence, the bond lengths could not be determined, and they may actually have been shorter than in the bulk.

Similar experiments have used STM and Atomic Force Microscope (AFM) like methods together with TEM, to form and image nano-wires with varying quality of the resolution [56–61].

One of these methods forms the chains between two Au needles and hence the conductance could be measured [56]. In this case atomic resolution was obtained simultaneously and a Au chain with bond lengths no longer than in the bulk (2.5–2.9 Å) was observed [56].<sup>6</sup> This is in agreement with [54], which, as mentioned above, was the only Au film TEM experiment observing short bond lengths. However, in [56] the conductance of these monatomic chains drops to zero before the final rupture. This could be explained by the presence of CO which, apart from its ability to increase the bond length, also creates a band gap turning the chain into a large gap semiconductor [55]. The chain will, on the other hand, not be stabilized like with oxygen.

For all three type of impurities the atoms (O and C) are so light that they are not imaged by TEM, and only the heavy Au atoms will be visible showing the long bond length observed. Even though the sample is prepared and cleaned under UHV, this is not enough to ensure a contamination free chain, since trace amounts of the impurities may still be left. At RT small molecules will diffuse very fast on the Au surface and soon end up at the low coordinated sites of the chain. Due to the increased reactivity of the under coordinated Au atoms, impurities ending up in the chain region will easily be trapped and incorporated into the chain [55]. The electron beam intensity has to be turned down in the imaging mode and it will no longer help burn impurities away. This allows them to remain and help stabilizing the chain.

The above can, nonetheless, only explain the long chains from the TEM experiments. In the MCBJ experiment where a plateau-length histogram was obtained [9], the cryogenic vacuum ensures that none of the mentioned impurities are present. Still a bond length of  $3.6 \text{ \AA} \pm 1.0 \text{ \AA}$  was observed.

In [9], helium was used as an exchange gas, and was hence present in large amounts [62]. In a similar experiment where helium was not present [62], Smit *et al.* find that the monatomic chain bond length for Au is 2.5 Å, shorter than

---

<sup>6</sup>This paper [56] presents an amazing monatomic Au chains consisting of ten (10) atoms!

in the bulk as expected and agreeing with two of the above mentioned TEM experiments [54, 56]. The new value is just outside the uncertainty interval of the old result [9] and it turned out that it was the presence of helium which affected the work function of the Au surface.

The length of the last plateau was obtained from a calibration of the length-scale based on tunneling through the vacuum gap. The presence of helium changes the work function, and the calibration will be offset, resulting in an apparently longer bond length [63].

Recently also Pt chains has been imaged using the TEM method [48–51]. As for Au, it is found that the bond lengths in monatomic chains are extremely long (3.2–3.6 Å) [48–50] compared with the bulk value (2.8 Å). This is again contrary to the expected for the low coordinated atoms in the chain, where the bond length should be shorter than in bulk. In the Letter by Smit *et al.* where the short bond length for Au was found, also Pt and iridium (Ir) chains were observed [62]. For both these metals the bond length is found to be shorter than the bulk distance: 2.3 Å for Pt and 2.2 Å for Ir compared with their bulk bond length of 2.8 Å and 2.7 Å, respectively. The most likely explanation for the long Pt chain bond length observed in the TEM experiments, is, as for Au, the incorporation of impurities into the chain. But no calculations have been performed on this system yet.

Only Smit *et al.* reports on Au chains with a conductance of  $1 G_0$  and bond lengths shorter than bulk as expected [62]. Their experiments was also the only one performed under cryogenic vacuum and without the presence of helium exchange gas. The temperature of 4.2 K is furthermore so low that clean Au chains are expected to be stable [55].

With their experimental investigation [62], Smit *et al.* proved that the monatomic chain formation is related with a metals ability to form reconstructions of the low-index surfaces. We have already shown the “herringbone” reconstruction of the Au(111) surface (Fig. 3.4b on page 34). Other metals displaying this property include only Ir and Pt. These three heavy metals, neighbors at the bottom of the periodic table (cf. Fig. 1.1 on page 5), are the only metals for which these reconstructions are observed. This means that even their neighbors above them in the periodic table: Silver (Ag), Palladium (Pd), and Rhodium (Rh) which have a similar outer electron structure will *not* form these monatomic chains. This theory was also tested with the experiments presented in [62].

In a simultaneous Letter, Bahn *et al.* confirmed these observations for Au, Ag, Pt and Pd with molecular dynamics simulations [43]. Parallel to Smit *et al.* the investigations were extended to other metals, but upwards in the periodic system (see Fig. 1.1 on page 5). In this way their calculations confirmed, as

expected from the proposed theory, that neither copper (Cu) nor nickel (Ni), the two remaining metals investigated in this thesis, can form monatomic chains [43].

Nevertheless, a very recent TEM investigation of chains formed from free standing Ag films finds that even Ag on rare occasions can form monatomic chains [64]. This is contrary to the two Letters discussed above. Also for the Ag chains are the bond length longer than bulk (3.3–3.6 Å). Since this according to the above discussion should indicate a contamination of the chain, this may explain how monatomic Ag chains can remain stable long enough to be observed.

All previous reports on Au, Pt and Ag chains with long bond lengths are most likely influenced by impurities, and for these RT experiments this is probably the only explanation for why monatomic chains can remain stable. In conclusion it has been proven that Au chains exist at low temperature [43, 62]. Under clean conditions at RT it is, however, unlikely that chains are stable, and we do not expect chain formation to have any impact on the RT experiments presented previously in this chapter.

All the experiments in the remaining chapters of this thesis have been performed at 4.2 K under cryogenic vacuum using the MCBJ. With these conditions chain formation is likely for both Au and Pt. The implications of this will be discussed when appropriate.

### 6.7.3 Influence of hydrogen on platinum

Although Pt is much more reactive than Au, several examples can be found where conductance histograms (histograms from now on) on ASCs of Pt have been measured either under ambient conditions [39, 40] or in relays, where the contacts are encapsulated in an atmosphere of nitrogen ( $N_2$ ) with 5% hydrogen ( $H_2$ ) [20, 21] (see Sec. 4.2 and 4.4). In all these experiments, as well as one performed under UHV [65] (see footnote 4 on page 46), a peak at  $1 G_0$  is observed. This is not in accordance with the broad peak centered around  $1.5 G_0$  observed both in another UHV experiment [66], and in cryogenic vacuum experiments [62, 67, 68] similar to our own, where they, as we, observe the  $1.5 G_0$  peak (see Fig. 4.4a on page 53).

Pt is not, as Au, a free-electron-like metal, and the open  $d$  shell is not expected to result in a single open eigenchannel with  $G \simeq 1 G_0$  (see Sec. 7.2.3). If, on the other hand, a hydrogen molecule or a hydrogen atom (H) with a single  $s$  electron forms a bridge between two Pt atoms, it could give rise to a single completely open conductance eigenchannel of  $s$  character.

In one of the above mentioned experiments where the relay forming the ASCs were encapsulated in a hydrogen rich atmosphere, the peak at  $1 G_0$  is observed to disappear and a new peak at  $1.7 G_0$  appears when the bias increases

above 600 mV [20]. This is in accordance with the theory: At high bias the bonds between Pt and hydrogen becomes unstable and breaks enabling clean Pt-Pt contacts with a conductance around  $1.7 G_0$ .<sup>7</sup> This possibility was not discussed in the paper.

Recently the theory has been confirmed by Smit *et al.* in an experiment where ASCs of Pt are exposed to hydrogen under cryogenic vacuum (4.2 K) [68]. In this Letter two conductance histograms, measured using the MCBJ, are presented. The first is compiled from ASCs formed from Pt in an *unbroken* vacuum, giving rise to a clear histogram peak centered around  $1.5 G_0$ .<sup>7</sup> The second histogram has been recorded after hydrogen was introduced into the vacuum, and a histogram peak at  $1 G_0$  results [68]. These histograms are shown in Fig. 6.7. Also displayed, in the inset, are two conductance traces, one from each of the two histograms, and they clearly show the influence of hydrogen, on the behavior of Pt ASCs [68].

When the bias increases, the hydrogen is observed to *disappear* from the contact region so a histogram like the one for clean Pt reappears already at a bias of 200 mV [68]. This is much lower than the 600 mV observed in the experiments with relays in a hydrogen rich atmosphere [20]. The latter experiment was performed at RT at atmospheric pressure (5% H<sub>2</sub>) compared to the 4.2 K and a hydrogen pressure of  $10^{-6}$  mbar in [68]. This could be the reason for the higher voltage needed before the clean Pt histograms were observed again in [20].

Smit *et al.* furthermore show, by the use of conductance fluctuations, that a hydrogen molecule between the two Pt electrodes give rise to one almost fully open eigenchannel, with a conductance close to  $1 G_0$  [68]. Measuring the differential conductance proves that the hydrogen bridge in the experiments indeed consists of a hydrogen molecule rather than a single hydrogen atom [68]. It can, however, not be ruled out that single hydrogen atoms also contribute to the  $1 G_0$  histogram peak [68]. Whereas the results from this investigation do not prove that all earlier reports of Pt histograms with a peak near  $1 G_0$  are caused by hydrogen, it will nevertheless be likely that either hydrogen or other impurities have been involved.

We performed similar experiments with 5% H<sub>2</sub> in an argon (Ar) atmosphere forming ASCs in the MCBJ at 4.2 K — exactly the same conditions as in Fig. 6.7. The results will not be presented in this thesis, since it was very difficult to measure reliable *I-V* curves on the very unstable hydrogen contacts (see Appendix C). Those we did obtain were, however, very non-linear, similar to those for the Au sample not cleaned under UHV in Fig. 6.2, but clearly

<sup>7</sup>In Chapter 9 we find that the first peak in the Pt histogram shifts from  $1.5 G_0$  to  $1.8 G_0$  when the bias increases above 300 mV. This is in accordance with the  $1.7$  vs  $1.5 G_0$  peaks observed at high bias in [20] and at low bias in [68], respectively.

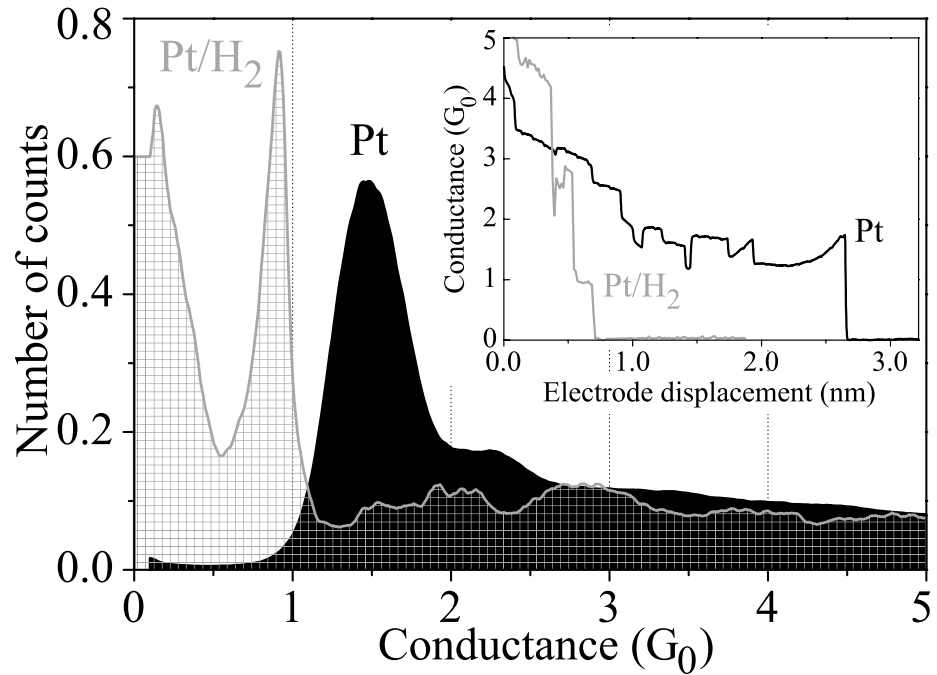


Figure 6.7: This figure presents the clear proof that the presence of hydrogen alters the conductance of the contact between two Pt electrodes. The *clean* Pt conductance histogram resembles the one presented in Fig. 9.1 on page 183. They are both recorded with 10 mV bias, under cryogenic vacuum (4.2 K) using the MCBJ to form the ASCs. The Pt/H<sub>2</sub> conductance histogram is recorded at 140 mV bias after hydrogen is introduced to the vacuum. The shape is completely different from the clean Pt histogram. The peak has moved to 1  $G_0$  and there is no sign of the original peak at 1.5  $G_0$ , even though this was the only clear feature observed for clean Pt. The inset shows the difference between conductance traces of ASCs of Pt, measured with and without hydrogen. The long plateau in the *clean* Pt trace, may indicate the formation of a monatomic chain, as mentioned above (see Fig. 9.4 on page 189). The conductance of the plateau fluctuates around 1.5  $G_0$  which is where the corresponding histogram peak is situated. The conductance in the Pt/H<sub>2</sub> trace drops very fast to zero when compared to the Pt trace. However, a short plateau near 1  $G_0$  is visible, and plateaus like this are responsible for the histogram peak. Both histograms are compiled from 10 000 traces. (Reprinted from [68] with permission from the authors').

quantized around  $G = 1 G_0$ . For Pt we saw the clear  $1 G_0$  histogram peak as in Fig. 6.7 and test experiments in a 100% Ar atmosphere showed conclusively that the changes to the Pt histogram was caused by the presence of hydrogen. We did not see any effect of the presence of hydrogen on Au ASCs.

#### 6.7.4 Conclusion

We have above presented several examples where the cleanliness of the investigated systems can be questioned. Many of the obtained results, can straightforwardly be explained by the presence of contaminant molecules, whereas it often turns out to be impossible to understand the observation based in a theory for the behavior of clean metallic ASCs.

The excitement caused by the conductance quantization of Au (see Sec. 4.2), observed even under ambient conditions, caused many to expect that Au in general would not be affected by the impurities present in air, and many results on this system were presented. This does, however, not explain why also other less noble metals have been investigated under these uncontrolled conditions.

It is unfortunate that it is so difficult to keep these systems ultra-clean, since it will be very difficult to use atomic-sized devices under ambient conditions. We may on the other hand find the solution in the incorporation of stabilizing molecules as oxygen into the Au chain [55]. It will be unimportant for the electrical system whether the wire is made from a Au-Au or from a Au-O-Au chains, as long as they are stable and the conductance remain the same. Another possibility to bypass the problems with contamination, could be the use of self-assembled monolayers (SAMs) [69] as discussed in the Outlook.

In conclusion it is of the utmost importance to keep the sample, and therefore also its environment, ultra-clean when ASCs of metals are under investigation. Even if the influence of a gas is investigated, an initially clean environment is crucial to ensure that any observed effects are actually caused by the presence of that particular gas. These extreme conditions can be achieved under UHV, but only if the sample is either sputtered *and* annealed for several cycles after exposure to air or if the sample is prepared directly *in situ*. Even then the sample will only remain free of contaminations for a few hours.

A much easier way to prepare clean samples and maintain them contamination free is the MCBJ technique (see Sec. 3.3). Under cryogenic vacuum the samples are prepared from bulk metal by breaking the sample wire and due to the extremely low pressure the samples can remain clean for days. Care should be taken, with the possible presence of helium and hydrogen, which might influence the results (This is, however, unlikely, see footnote 2 on page 35).

In the next three chapters we present results obtained using the MCBJ method to ensure a clean environment and reliable results.

## References

- [1] J. I. Pascual, J. Méndez, J. Gómez-Herrero, A. M. Baró, N. García, U. Landman, W. D. Luedtke, E. N. Bogachek, and H.-P. Cheng, “Properties of Metallic Nanowires: From Conductance Quantization to Localization,” *Science* **267**, 1793–1795 (1995).
- [2] V. V. Dremov and S. Y. Shapoval, “Quantization of the conductance of metal nanocontacts at room temperature,” *Pis'ma Zh. Eksp. Teor. Fiz.* **61**, 321–324 (1995), [*JEPT Lett.* **61**, 336 (1995)].
- [3] B. Rodell, V. Korenivski, J. Costa, and K. V. Rao, “Quantized conductivity in STM drawn 100Å nanowires of Au and Ni,” *Nanostruct. Mater.* **7**, 229–235 (1996).
- [4] J. L. Costa-Krämer, N. García, P. García-Mochales, P. A. Serena, M. I. Marqués, and A. Correia, “Conductance quantization in nanowires formed between micro and macroscopic metallic electrodes,” *Phys. Rev. B* **55**, 5416–5424 (1997).
- [5] J. Abellán, R. Chicón, and A. Arenas, “Properties of nanowires in air. Controlled values of the conductance,” *Surf. Sci.* **418**, 493–501 (1998).
- [6] A. Correia, J.-L. Costa-Krämer, Y. W. Zhao, and N. García, “Non-linear contribution to intensity-voltage characteristics of gold nanowires,” *Nanostruct. Mater.* **12**, 1015–1020 (1999).
- [7] T. Junno, S.-B. Carlsson, H. Xi, L. Montelius, and L. Samuelson, “Fabrication of quantum devices by Ångström-level manipulation of nanoparticles with an atomic force microscope,” *Appl. Phys. Lett.* **72**, 548–550 (1998).
- [8] H. Ohnishi, Y. Kondo, and K. Takayanagi, “Quantized conductance through individual rows of suspended gold atoms,” *Nature* **395**, 780–783 (1998).
- [9] A. I. Yanson, G. R. Bollinger, H. E. van den Brom, N. Agraït, and J. M. van Ruitenbeek, “Formation and manipulation of a metallic wire of single gold atoms,” *Nature* **395**, 783–785 (1998).
- [10] N. Agraït, J. G. Rodrigo, and S. Vieira, “Conductance steps and quantization in atomic-size contacts,” *Phys. Rev. B* **47**, 12345–12348 (1993).

- 
- [11] J. I. Pascual, J. Méndez, J. Gómez-Herrero, A. M. Baró, N. García, and V. T. Binh, “Quantum Contact in Gold Nanostructures by Scanning Tunneling Microscopy,” *Phys. Rev. Lett.* **71**, 1852–1855 (1993).
- [12] E. Scheer, N. Agraït, J. C. Cuevas, A. L. Yeyati, B. Ludoph, A. Martín-Rodero, G. R. Bollinger, J. M. van Ruitenbeek, and C. Urbina, “The signature of chemical valence in the electrical conduction through a single-atom contact,” *Nature* **394**, 154–157 (1998).
- [13] H. E. van den Brom and J. M. van Ruitenbeek, “Quantum Suppression of Shot Noise in Atom-Size Metallic Contacts,” *Phys. Rev. Lett.* **82**, 1526–1529 (1999).
- [14] B. Ludoph, M. H. Devoret, D. Esteve, C. Urbina, and J. M. van Ruitenbeek, “Evidence for Saturation of Channel Transmission from Conductance Fluctuations in Atomic-Size Point Contacts,” *Phys. Rev. Lett.* **82**, 1530–1533 (1999).
- [15] B. Ludoph and J. M. van Ruitenbeek, “Thermopower of atomic-size metallic contacts,” *Phys. Rev. B* **59**, 12290–12293 (1999).
- [16] J. I. Pascual, J. A. Torres, and J. J. Sáenz, “Nonlinear ballistic conductance in atomic-scale metallic contacts,” *Phys. Rev. B* **55**, R16029–R16032 (1997).
- [17] A. García-Martín, T. López-Ciudad, J. A. Torres, A. J. Caamaño, J. I. Pascual, and J. J. Sáenz, “Differential conductance in atomic-scale metallic contacts,” *Ultramicroscopy* **73**, 199–203 (1998).
- [18] M. Jonson, P. Sandström, R. I. Shekhter, and I. V. Krive, “Nonlinear conductance of nanowires: a signature of Luttinger liquid effects?,” *Superlattices and Microstructures* **23**, 957–967 (1998).
- [19] M. Brandbyge, N. Kobayashi, and M. Tsukada, “Conduction channels at finite bias in a single-atom gold contact,” *Phys. Rev. B* **60**, 17064–17070 (1999).
- [20] K. Yuki, S. Kurokawa, and A. Sakai, “Quantized Conductance in Pt Nanocontacts,” *Jpn. J. of Appl. Phys.* **39**, 4593–4595 (2000).
- [21] K. Yuki, S. Kurokawa, and A. Sakai, “Conductance in Breaking Nanocontacts of Some Transition Metals,” *Jpn. J. of Appl. Phys.* **40**, 803–808 (2001).

- 
- [22] H. Yasuda and A. Sakai, "Conductance of atomic-scale gold contacts under high-bias voltages," *Phys. Rev. B* **56**, 1069–1072 (1997).
- [23] K. Itakura, K. Yuki, S. Kurokawa, H. Yasuda, and A. Sakai, "Bias dependence of the conductance of Au nanocontacts," *Phys. Rev. B* **60**, 11163–11170 (1999).
- [24] K. Yuki, A. Enomoto, and A. Sakai, "Bias-dependence of the conductance of Au nanocontacts at 4 K," *Appl. Surf. Sci.* **169–170**, 489–492 (2001).
- [25] P. S. Ho and T. Kwok, "Electromigration in metals," *Rep. Prog. Phys.* **52**, 301–348 (1989).
- [26] R. S. Sorbello, "Theory of Electromigration," *Solid State Physics* **51**, 159–231 (1998).
- [27] T. N. Todorov, "Local heating in ballistic atomic-scale contacts," *Philos. Mag. B* **77**, 965–973 (1998).
- [28] N. Agraït, C. Untiedt, G. Rubio-Bollinger, and S. Vieira, "Onset of Energy Dissipation in Ballistic Atomic Wires," *Phys. Rev. Lett.* **88**, 216803 (2002).
- [29] K. Hansen, "Electrical Properties of Atomic-Sized Metal Contacts," PhD thesis, University of Aarhus, 2000. (Can be downloaded from <http://www.ifa.au.dk/~kimh/pdf/thesis.pdf>).
- [30] B. Hammer and J. K. Nørskov, "Why gold is the noblest of all the metals," *Nature* **376**, 238–240 (1995).
- [31] G. S. Ferguson, M. K. Chaundhury, G. B. Sigal, and G. M. Whitesides, "Contact Adhesion of Thin Gold Films on Elastomeric Supports: Cold Welding Under Ambient Conditions," *Science* **253**, 776–778 (1991).
- [32] G. W. Whitesides, (private communication).
- [33] R. Stratton, "Volt-current characteristics for tunneling through insulating films," *J. Phys. Chem. Solids* **23**, 1177–1190 (1962).
- [34] H. Mehrez, A. Wlasenko, B. Larade, J. Taylor, P. Grütter, and H. Guo, "*I-V* characteristics and differential conductance fluctuations of Au nanowires," *Phys. Rev. B* **65**, 195419 (2002).
- [35] C. Z. Li, H. Sha, and N. J. Tao, "Adsorbate effect on conductance quantization in metallic nanowires," *Phys. Rev. B* **58**, 6775–6778 (1998).

- 
- [36] H. Häkkinen, R. N. Barnett, and U. Landman, “Gold Nanowires and their Chemical Modifications,” *J. Phys. Chem. B* **103**, 8814–8816 (1999).
- [37] H. He and N. Tao, “Interactions of Molecules with Metallic Quantum Wires,” *Adv. Mater.* **14**, 161–164 (2002).
- [38] K. Hansen, E. Lægsgaard, I. Stensgaard, and F. Besenbacher, “Quantized Conductance in Relays,” *Phys. Rev. B* **56**, 2208–2220 (1997).
- [39] J. L. Costa-Krämer, “Conductance quantization at room temperature in magnetic and nonmagnetic metallic nanowires,” *Phys. Rev. B* **55**, R4875–R4878 (1997).
- [40] J. L. Costa-Krämer, N. García, P. García-Mochales, and P. A. Serena, “Nanowire formation in macroscopic metallic contacts: quantum mechanical conductance tapping a table top,” *Surf. Sci.* **342**, L1144–L1149 (1995).
- [41] J. L. Costa-Krämer, N. García, and H. Olin, “Conductance quantization histograms of gold nanowires at 4 K,” *Phys. Rev. B* **55**, 12910–12913 (1997).
- [42] H. Oshima and K. Miyano, “Spin-dependent conductance quantization in nickel point contacts,” *Appl. Phys. Lett.* **73**, 2203–2205 (1998).
- [43] S. R. Bahn and K. W. Jacobsen, “Chain Formation of Metal Atoms,” *Phys. Rev. Lett.* **87**, 266101 (2001).
- [44] V. Rodrigues, T. Fuhrer, and D. Ugarte, “Signature of Atomic Structure in the Quantum Conductance of Gold Nanowires,” *Phys. Rev. Lett.* **85**, 4124–4127 (2000).
- [45] V. Rodrigues and D. Ugarte, “Real-time imaging of atomistic process in one-atom-thick metal junctions,” *Phys. Rev. B* **63**, 073405 (2001).
- [46] V. Rodrigues and D. Ugarte, “Structural and electronic properties of gold nanowires,” *Eur. Phys. J. D* **16**, 395–398 (2001).
- [47] S. B. Legoas, D. S. Galvão, V. Rodrigues, and D. Ugarte, “Origin of Anomalously Long Interatomic Distances in Suspended Gold Chains,” *Phys. Rev. Lett.* **88**, 076105 (2002).
- [48] V. Rodrigues and D. Ugarte, “Atomic Arrangement and Conductance of Metal Nanowires,” *Phys. Stat. Sol. (b)* **230**, 481–489 (2002).

- 
- [49] V. Rodrigues and D. Ugarte, “Metal nanowires: atomic arrangement and electrical transport properties,” *Nanotech.* **13**, 404–408 (2002).
- [50] V. Rodrigues and D. Ugarte, submitted, “Atomic Structure and Defects Generation in Pt Nanowires Produced by Mechanical Deformation,” (2001) (unpublished).
- [51] Y. Oshima, H. Koizumi, K. Mouri, H. Hirayama, K. Takayanagi, and Y. Kondo, “Evidence of a single-wall platinum nanotube,” *Phys. Rev. B* **65**, 121401 (2002).
- [52] Y. Kondo and K. Takayanagi, “Gold Nanobridge Stabilized by Surface Structure,” *Phys. Rev. Lett.* **79**, 3455–3458 (1997).
- [53] Y. Kondo and K. Takayanagi, “Synthesis and Characterization of Helical Multi-Shell Gold Nanowires,” *Science* **289**, 606–508 (2000).
- [54] Y. Takai, T. Kawasaki, Y. Kimura, T. Ikuta, and R. Shimizu, “Dynamic Observation of an Atom-Sized Gold Wire by Phase Electron Microscopy,” *Phys. Rev. Lett.* **87**, 106105 (2001).
- [55] S. R. Bahn, “Computer Simulations of Nanochains,” PhD thesis, Technical University of Denmark, 2001.
- [56] T. Kizuka, S. Umehara, and S. Fujisawa, “Metal-Insulator Transition in Stable One-Dimensional Arrangements,” *Jpn. J. of Appl. Phys.* **40**, L71–L74 (2001).
- [57] T. Kizuka, K. Yamada, S. Deguchi, M. Naruse, and N. Tanaka, “Cross-sectional time-resolved high-resolution transmission electron microscopy of atomic-scale contact and noncontact-type scannings on gold surfaces,” *Phys. Rev. B* **55**, R7398–R7401 (1997).
- [58] T. Kizuka, “Atomic Process of Point Contact in Gold Studied by Time-Resolved High-Resolution Transmission Electron Microscopy,” *Phys. Rev. Lett.* **81**, 4448–4451 (1998).
- [59] T. Kizuka, “Atomistic visualization of deformation in gold,” *Phys. Rev. B* **57**, 11158–1163 (1998).
- [60] D. Ertz, H. Olin, L. Ryen, E. Ollson, and A. Thölén, “Maxwell and Sharvin conductance in gold point contacts investigated using TEM-STM,” *Phys. Rev. B* **61**, 12725–12727 (2000).

- 
- [61] D. Erts, A. Löhmus, R. Löhmus, and H. Olin, “Instrumentation of STM and AFM combined with transmission electron microscope,” *Appl. Phys. A* **72**, S71–S74 (2001).
- [62] R. H. M. Smit, C. Untiedt, A. I. Yanson, and J. M. van Ruitenbeek, “Common Origin for Surface Reconstruction and the Formation of Chains of Metal Atoms,” *Phys. Rev. Lett.* **87**, 266102 (2001).
- [63] C. Untiedt, A. Yanson, R. Grande, G. Rubio-Bollinger, N. Agrait, S. Vieira, and J. van Ruitenbeek, “Calibration of the length of a chain of single gold atoms,” submitted, (2002), <http://xxx.lanl.gov/pdf/cond-mat/0202349>, (unpublished).
- [64] V. Rodrigues, J. Bettini, A. R. Rocha, L. G. C. Rego, and D. Ugarte, “Quantum Conductance in Silver Nanowires: correlation between atomic structure and transport properties,” (2002), <http://xxx.lanl.gov/pdf/cond-mat/0201156> (unpublished).
- [65] L. Olesen, E. Lægsgaard, I. Stensgaard, F. Besenbacher, J. Schiøtz, P. Stoltze, K. W. Jacobsen, and J. K. Nørskov, “Reply to ‘Comment on ‘Quantized conductance in an Atom-Sized Point Contact’’,” *Phys. Rev. Lett.* **74**, 2147 (1995).
- [66] C. Sirvent, J. G. Rodrigo, S. Vieira, L. Jurczyszyn, N. Mingo, and F. Flores, “Conductance step for single-atom contact in the scanning tunneling microscope: Noble and transition metals,” *Phys. Rev. B* **53**, 16086–16090 (1996).
- [67] A. I. Yanson, “Atomic Chains and Electronic Shells: Quantum Mechanisms for the Formation of Nanowires,” PhD thesis, Rijksuniversiteit Leiden, 2001. (Can be downloaded from <http://lions1.leidenuniv.nl/wwwhome/ruitenbe/ThesisAlex.pdf>).
- [68] R. H. M. Smit, Y. Noat, C. Untiedt, N. D. Lang, M. van Hemert, and J. M. van Ruitenbeek, “Measurement of the conductance of a hydrogen molecule,” accepted for publication in *Nature*, (2002), <http://xxx.lanl.gov/pdf/cond-mat/0208407>, (unpublished).
- [69] For a recent review see F. Schreiber, “Structure and growth of self- assembling monolayers,” *Prog. Surf. Sci.* **50**, 151–256 (2000).



## Chapter 7

# Current-Voltage Curves of Atomic-Sized Transition Metal Contacts

In the previous chapter we showed that current-voltage ( $I$ - $V$ ) curves measured on atomic-sized contacts (ASCs) of gold (Au) are very linear. Au is a free-electron-like metal with a single  $s$  valence electron in the outer shell. This simple electronic structure can explain why the  $I$ - $V$  curves are linear. An obvious next step will hence be an investigation of other metals with a more complicated outer electronic structure. It is, however, important to remember that we encountered problems even for Au, the noblest of metals [1], when the sample had been exposed to air without subsequent cleaning under ultra-high vacuum (UHV) conditions. For other more reactive metals, it will be even more important to ensure a clean environment in order to obtain clean metal-metal contact (see Sec. 6.7.1). With this in mind we decided to switch from the scanning tunneling microscope (STM) experiments at room temperature (RT) under UHV to the mechanically controllable break-junction (MCBJ). By breaking the sample under cryogenic vacuum we obtain ultra-clean ASCs as described in Sec. 3.3. Furthermore the low temperature of 4.2 K makes it possible to keep ASCs stable on a much longer timescale than at RT, and even monatomic contacts can be kept stable for minutes.

Using this new method to form ASCs we return to investigate Au, both to confirm the RT results at 4.2 K but also to compare directly with the results obtained on the other metals. Our choice for the next metal was platinum (Pt)

neighbor to Au in the periodic table but with a fundamentally different electronic structure. This turned out to be a very interesting choice, since the  $I$ - $V$  behaviors of these two metals are very different from each other.

In this chapter based on papers [III] and [IV] we have investigated the  $I$ - $V$  curves of both the noble metals: Au, silver (Ag) and copper (Cu), and the platinum metals: Pt, palladium (Pd) and nickel (Ni) (cf. Fig. 1.1 on page 5). For Au we confirm that  $I$ - $V$  curves also are very linear at 4.2 K, and we find that this is the general trend for all noble metals. On the other hand, we observe clear non-linear effects for all the platinum metals. We compare the experimental results of Au and Pt with first principles density functional theory (DFT) calculations (performed by Mads Brandbyge) and good agreement is found. The difference in conducting properties for Pt vs Au can be explained by the underlying electron valence structure: Pt has an open  $d$ -shell while Au has not.

## 7.1 Experimental details

All experiments presented in this chapter have been performed at 4.2 K under cryogenic vacuum using the MCBJ to form the ASCs, as described in Sec. 3.3. The samples are made from Au, Ag, Cu, Pt, Pd or Ni wires with a purity of 99.999% and a diameter of 0.1 mm. The data presented here are measured on three different samples of Au, two different Pt samples and one sample for each of the four remaining metals. On each sample several different types of experiments (amongst others also those giving the results presented in the next two chapters) were performed over three to five days. Even after several days, the samples are still clean due to the low pressure of the cryogenic vacuum and the low diffusivity at 4.2 K. This is confirmed by the unchanging properties of the ASCs over time.

### Contact formation

When the wire has been broken under cryogenic vacuum, the two electrodes are moved back into contact to form ASCs. With the STM setup we used two different indentation methods: Hard and soft, as described in Sec. 6.2. For the hard indentations the voltage burst was applied automatically, whereas for the soft indentations the user decided when to apply the burst. Using the MCBJ we experimented with both methods and found that they gave similar results. With the MCBJ at 4.2 K the ASCs can be kept stable for a long time (minutes)

and there is no need for applying the burst instantly when the conductance falls below a preset value. Instead we developed an automatic procedure that in a way combines the two methods. The procedure begins by pressing the electrodes together until a “large” contact with a conductance above  $50 G_0$ <sup>1</sup> is formed ensuring that no two  $I$ - $V$  curves are measured on contacts with the exact same atomic configuration (this resembles the *hard* indentations). Then four steps follows in order to obtain the  $I$ - $V$  curves in a controlled and fully automatic manner:

1. The large contact is elongated by increasing the piezo voltage until the conductance falls below a preset value ( $1-5 G_0$ ).
2. A computer-controlled feedback loop adjusts the piezo voltage until the ASC is stabilized with a conductance within a few percent (10–25%) of the preset value (this resembles the *soft* indentations).
3. When the correct conductance is obtained the piezo voltage is kept constant to test if the ASC is stable.
  - (a) If the conductance changes, the feedback loop is activated again and we are back to step 2.
  - (b) If the conductance remains stable for a given time ( $\sim 1$  s), the computer triggers the system, a voltage burst is automatically applied, and an  $I$ - $V$  curve is measured by the oscilloscope.
4. The conductance is measured before the burst and again after the burst has been applied.
  - (a) If the conductance (i.e. the ASC) was left unchanged by the burst, the trace is acquired.
  - (b) Otherwise the trace is discarded.

Independently of the outcome of the procedure, a new automatic cycle will begin by again forming a large contact. The  $I$ - $V$  curve is only accepted if the conductance remained the same before and after the burst within a given range ( $0.1-1.0 G_0$ ), which depends both on the metal, on the size of the contacts (the conductance), and on the general experimental settings. With this procedure we ensure that only stable atomic configurations are examined. Since the method is automatic it was possible to obtain large amounts of data, which is an important factor for these experiments, since every ASCs will be different, and a large statistical material is needed before any conclusions can be reached.

<sup>1</sup>The fundamental unit of conductance  $G_0$  is defined in Eq. (2.3) on page 15.

Material	Au	Ag	Cu	Pt	Pd	Ni
$A$ (V)	1.0–2.0	0.4–1.0	0.6–1.0	0.5–0.9	0.25–0.5	0.25–0.4
Bias (mV)	100–200	50–200	50–100	50–100	20–30	20–50

Table 7.1: The range of burst amplitudes  $A$  and biases used for the different metals when measuring  $I$ - $V$  curves.

Only for Ni did we encounter problems with the formation of ASCs. Ni is a very brittle material and this is probably the cause of the problem. The exposed fractured surfaces are likely to be very rough and long whisker may extend from them. If they make the first contact, as the electrodes move together again, the forming ASCs could be very unstable. We solved the problem, “burning” the protrusions away, by moving the electrodes slowly into contact while applying a high bias [2]. This produced ASCs of Ni, stable enough for our purpose. Generally ASCs of Ni are the least stable of the six metals (see Sec. 8.6).

### Measuring $I$ - $V$ curves

To measure the  $I$ - $V$  curves we used the fast setup described in Chapter 5. When an ASC is formed using the above-described procedure, the function generator applies a voltage burst to the contact and an  $I$ - $V$  curve is acquired by the oscilloscope. The burst consists of a triangular waveform with a frequency<sup>2</sup> between 100–1500 Hz and an amplitude between 0.25–2.0 V superimposed on an offset bias of 20–200 mV. An  $I$ - $V$  curve, i.e. a full burst cycle, is typically measured during 1–10 ms. The large span on the applied voltages is due to the large stability differences for ASCs from metal to metal (see Appendix C). Whereas Au is very stable towards high voltages of up to a few volt, Ni contacts typically break before the voltage reaches 0.5 V. The range of amplitudes and biases used in the experiments for each metals are given in Table 7.1.

To include the most stable few-atom configurations in the experimental data set, we accept conductance values ranging from 0.9 to 5.0  $G_0$  for the noble metals and from 1.5 to 5.0  $G_0$  for the platinum metals. We avoid the exotic monatomic chain configurations known to exist for Au [3–6] and Pt [5, 6] by stopping the elongation promptly if the conductance reaches a value associated with that of the monatomic contacts. This is 0.9–1.1  $G_0$  for Au and 1.5–2.3  $G_0$  for Pt as inferred from the conductance histograms in Chapter 4.

<sup>2</sup>The lower limit of the maximum frequency compared to that of the RT STM experiments in Chapter 6 is due to the higher parasitic capacitance in the MCBJ setup as explained in Sec. 5.3. When working at 4.2 K, where the ASCs are much more stable than at RT, high frequencies are luckily no longer needed.

## 7.2 Why gold is Ohmic and platinum is not

In this section, which is based on paper [III], we present a detailed and thorough investigation of  $I$ - $V$  curves measured on ASCs of Au and Pt, neighbors in the periodic table (cf. Fig. 1.1 on page 5). We find that  $I$ - $V$  curves measured on ASCs of Au are highly linear on a 100 mV scale, whereas for Pt distinct non-linear effects exist as the conductance decreases with increasing voltage. First principles DFT calculations confirm the different  $I$ - $V$  behavior for Au and Pt, and we conclude that the difference is associated with the valence electron structure of the two metals: Au has a closed  $d$  shell ( $5d^{10}6s^1$ ) and the transport is dominated by a single, broad resonance mainly of  $s$  character while for Pt ( $5d^96s^1$ ) also the  $d$  electrons participate. The general implications for other metals will be discussed, and can be compared with the results presented in Sec. 7.3 and 7.4, for the four remaining noble and platinum metals.

Although neighbors in the periodic table, the single extra valence electron Au has compared to Pt, results in profound differences between the electronic properties of the two metals. In Sec. 6.1 a review was given of previously reported results on  $I$ - $V$  curves and several related experiments concerning Au. Contrary to this there has only been a few studies of Pt ASCs and previously no investigations of the  $I$ - $V$  dependence for ASCs of Pt have been published.

Values of the conductance of monatomic Pt contacts have been reported to vary between 1.0 and 2.5  $G_0$  [6–11]. Conductance values close to 1  $G_0$  are, however, most likely caused by impurities, e.g. hydrogen [10, 11] (see Sec. 6.7.3). In Sec. 4.4 we discussed these observations and presented a conductance histogram for Pt (Fig. 4.4a) with the first peak situated at a conductance of 1.5  $G_0$ .

### 7.2.1 Examples of current-voltage curves

In Fig. 7.1 typical  $I$ - $V$  curves measured on ASCs of (a) Au and (b) Pt are shown. The  $I$ - $V$  curves of Au are Ohmic, i.e. linear, whereas the  $I$ - $V$  curves of Pt are clearly non-linear. Monatomic Au contacts ( $G \simeq 1 G_0$ ) are very stable towards high voltages and often withstand burst amplitudes above 2 V without breaking. The stability towards voltage will decrease at higher  $G$ .

The inset in Fig. 7.1 shows an example of an  $I$ - $V$  curve on a monatomic Au contact that withstands two cycles of a 320 Hz burst with an amplitude of 2.5 V superimposed on a bias of 100 mV. Both cycles are plotted and although the voltage reaches a maximum<sup>3</sup> of 2.45 V they completely overlap. This implies that the contact remains stable even under these extreme circumstances where

<sup>3</sup>Although the maximum voltage of the function generator (FG) burst is 2.6 V, the actual voltage at the ASCs are smaller. This is due to the voltage drop over  $R_{FG}$  and  $R_{in}$  (see Fig. 5.6 on page 69) which amounts to about 5% for a contact with  $G = 1 G_0$ .

Material/label	$G$ ( $G_0$ )	$G'$ ( $G_0/\text{Volt}$ )	$G''$ ( $G_0/\text{Volt}^2$ )
Au	1.0 $G_0$	0.9905(8)	0.0039(6)
	2.0 $G_0$	1.9784(10)	-0.0017(9)
	3.1 $G_0$	3.0767(11)	0.0112(16)
	4.2 $G_0$	4.2155(12)	0.0344(18)
	Inset	0.9682(5)	-0.0095(2)
Pt	1.7 $G_0$	1.742(2)	-0.006(7)
	2.3 $G_0$	2.287(2)	-0.036(7)
	3.0 $G_0$	3.026(2)	0.091(8)
	4.1 $G_0$	4.090(3)	0.011(8)

Table 7.2: Parameters of fit to Eq. (7.1) for all  $I$ - $V$  curves from Fig. 7.1, with the uncertainty on the last digit given in brackets. As in the figure, the  $I$ - $V$  curves are labeled by their low bias conductance  $G$ , except for the inset.

the current reaches up to 160  $\mu\text{A}$ . Since this current runs through a single Au atom it gives rise to an amazing local current density of more than 2 GA/mm<sup>2</sup>!

Monatomic Pt contacts can generally not withstand such high voltages; half of them will break before the voltage reaches 0.7 V (see Fig. 8.8a on page 165). Due to the higher conductance, the current still reaches above 50  $\mu\text{A}$ . The stability of monatomic contacts towards high current will be the subject of Chapter 8 in which all six metals will be investigated as well. Au is found to be the most stable of these metals, sustaining by far the highest currents.

### 7.2.2 Fitting to a polynomial

As in Eq. (6.1) on page 88 we quantify the deviations from linearity by fitting the  $I$ - $V$  curves with a third order polynomial [12–14] (see Appendix A):

$$I(V) = GV + G'V^2 + G''V^3. \quad (7.1)$$

Again the term  $G''$  is used to indicate the degree of non-linearity,  $G$  represents the low bias conductance and  $G'$  describes the polarity-dependence of the current due to asymmetries in the contact region.

In Fig. 7.1, the polynomial fit to the experimentally recorded  $I$ - $V$  curves are shown. For Pt we have furthermore added straight, dashed lines representing the low bias conductance  $G$  as guides to the eye (Fig. 7.1b). The fitting parameters for the  $I$ - $V$  curves in the figure are displayed in Table 7.2. From the table it is obvious that  $G''$  is much larger for Pt than for Au. The larger uncertainty

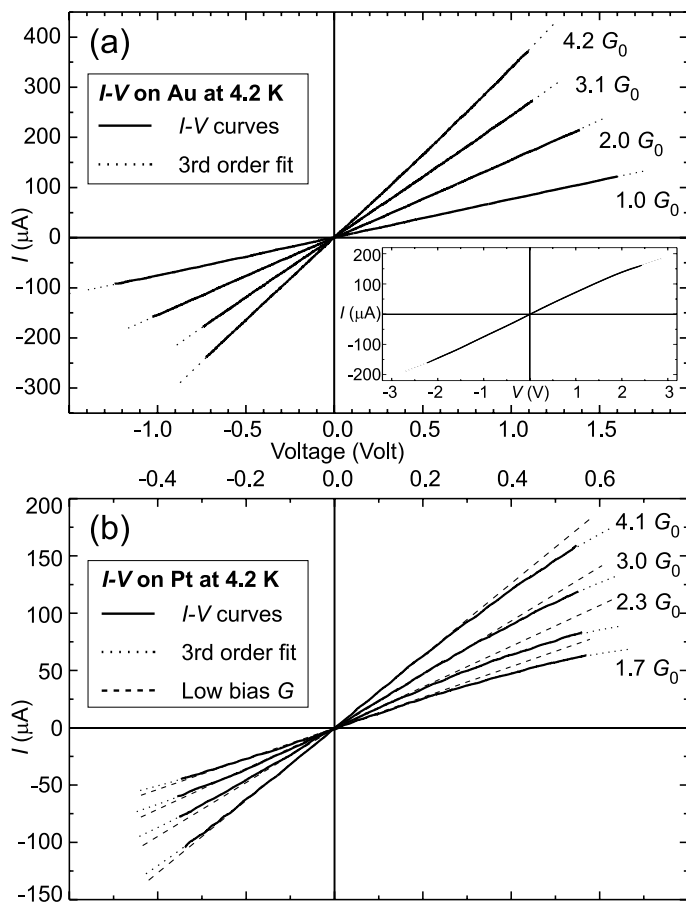


Figure 7.1: Representative  $I$ - $V$  curves of (a) Au and (b) Pt ASCs formed with the MCBJ under cryogenic vacuum at 4.2 K. The  $I$ - $V$  curves are fitted to the third-order polynomial from Eq. (7.1) and fits are plotted as dotted lines. Curves have been labeled by their low bias conductance  $G$  obtained from the fit and all fitting parameters can be found in Table 7.2. For Pt, the low bias conductance  $G$  for each curve is represented by straight, dashed lines. Note, that the voltage scale for Pt is a factor 2.5 smaller than for Au. The  $I$ - $V$  curves of Au [Pt], were acquired during 2.2 ms [1.5 ms], corresponding to a single period of the 460 Hz [680 Hz] triangular voltage burst used. The burst amplitude for Pt was 0.5 V superimposed on a bias of 100 mV. For Au, 200 mV bias was applied together with amplitudes of 1.5, 1.3, 1.0 and 1.0 V, respectively, for increasing  $G$ . The inset shows an  $I$ - $V$  curve on a monatomic Au contact ( $G = 0.97 G_0$ ) where the maximum voltage reaches 2.45 V (see text).

for Pt than for Au is due to the lower burst amplitude used with the less stable Pt contacts (see Appendix C).

It is interesting to examine the Au  $I$ - $V$  curve from the inset in Fig. 7.1. From the graph it is clear that the  $I$ - $V$  curve is slightly non-linear bending downwards at high positive voltage. In Table 7.2 it is revealed that the non-linear term for the curve in the inset has the same order of magnitude as the  $1.0 G_0$  curve in the main figure. The non-linearity will, however, not be visible at lower voltage (1.5 V) but first, as in the inset, for voltages above 2 V, due to the dependence of  $G''$  on the voltage squared.

Before accepting the fit from the  $I$ - $V$  curves we apply two selection criteria which are described in detail in Appendix B. Here we shortly mention that we firstly use the goodness of fit (GOF) to remove traces on ASCs where the conductance changes during the burst. Secondly we use  $|G'/G|$  as a selection criterion in order to remove clearly asymmetric  $I$ - $V$  curves. In this way we set an upper limit for the percentage of asymmetry. Curves with  $|G'/G| > 0.025/\text{Volt}$  for Au and  $|G'/G| > 0.05/\text{Volt}$  for Pt are excluded. The lower value for Au is due to the higher stability for ASCs of Au compared to Pt (see Appendix B). The theoretical calculations are for a symmetric contact configuration with  $G' \equiv 0$ , so this selection allows a more direct comparison between theory and experiment.

When we measure  $I$ - $V$  curves we use two or three burst cycles as in the inset of Fig. 5.11 on page 80, where two out of the three cycles are shown. We always fit to a full *extrema* burst cycle were the voltage changes from an extrema and back (i.e. from the maximum voltage  $A$  and back or *visa versa* with the minimum voltage  $-A$ ). In this way we avoid instabilities when the burst begins and ends (cf. Fig. 5.11). As can be seen in the inset of Fig. 5.11, there are two extrema cycles to chose from when the burst has two cycles, but with three cycles we can actually choose between four different extrema cycles. The choice is performed by an automatic procedure<sup>4</sup> which makes a fit to both/all four  $I$ - $V$  curves, and then chooses the one with the best GOF (see Appendix B).

This automatic procedure allows us to analyze large amounts of data very rapidly.<sup>5</sup> This is needed since all ASCs will be different, and it is very important to obtain a good statistical material in order to make sound conclusions. Hence,  $I$ - $V$  curves, fulfilling the selection criteria, from more than 1200 Au ASCs have been acquired and a  $(G, G'')$  scatter plot for fits to Eq. (7.1) is shown in Fig. 7.2.

For the monatomic Au contacts ( $G \simeq 1 G_0$ ),  $G$  is clearly quantized consistent with reported conductance histograms [9, 15–18] as the one presented in Fig. 4.3a on page 49. Only 5% of the 700 points with  $G < 1.5 G_0$

<sup>4</sup>Like most of our data analyzing programs, it has been written by Kim Hansen in *Delphi*.

<sup>5</sup>It was sadly not possible to make such an automatic procedure for the data analysis of the current-induced disruptions presented in the next chapter (see at the end of Sec. 8.3)

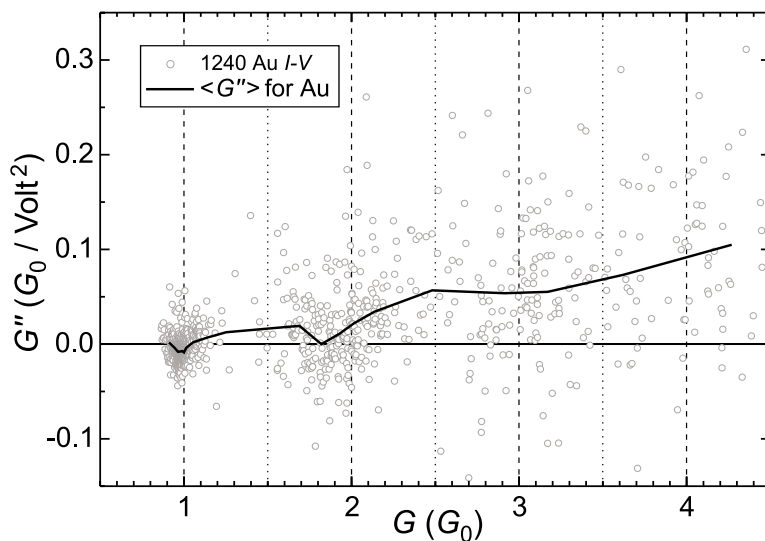


Figure 7.2: Non-linear term  $G''$  vs low bias conductance  $G$  for Au. Each point represents a fit to Eq. (7.1) of one  $I$ - $V$  curve on one ASC. There are points from 1240  $I$ - $V$  curves. The solid curve represents the mean value  $\langle G'' \rangle$  drawn through points found by averaging over at least 50 successive data points.<sup>6</sup>

lie outside the conductance window from  $0.9$  to  $1.1 G_0$ . The average for all points in this range gives  $G = 0.990(1) G_0$  and a nearly zero non-linear term  $G'' = -0.0051(5) G_0/\text{Volt}^2$ . These results are in accordance with our experiments at room temperature discussed in Chapter 6. The density of points around  $2$  and  $3 G_0$  is also higher than average but, as expected, the quantization in  $G$  gradually disappears with increasing conductance.

Since the density of the data points is very high in some areas, especially around  $1 G_0$ , it is difficult to see the preferred value of  $G''$  from the graph. In order to make this more clear we have calculated the mean value  $\langle G''(G) \rangle$  as a function of  $G$  by taking the average of at least 50 or more successive data points.<sup>6</sup> This mean value has been plotted as a solid line through the Au data in Fig. 7.2 as a guide. Although the interpretation based on this kind of representation should be handled with care, it gives valuable information on the

<sup>6</sup>Usually  $\langle G'' \rangle$  is calculated from all data points within a certain conductance window. The lower limit of 50 points is only used in conductance regions where there are few data points. In this way we avoid very rapid fluctuations of the mean value.

general behavior of  $G''$ .

In Fig. 7.2,  $\langle G'' \rangle$  clearly shows that Au  $I$ - $V$  curves measured on monatomic contacts are very linear. Around  $1 G_0$ , the mean value is very close to zero (slightly negative), and this shows that  $G''$  for a given  $I$ - $V$  curve has an equal chance of being positive or negative. Even the outliers on the graph almost never exceed  $\pm 0.05 G_0/\text{Volt}^2$  around  $1 G_0$ , making the 4.2 K data even more linear than the RT UHV data from the STM experiment presented in Fig. 6.2 on page 90. There are so few data between  $1.2$  and  $1.6 G_0$  that the positive  $\langle G'' \rangle$  should not be paid much attention. A minimum at  $1.8 G_0$  is, however, clear after which  $\langle G'' \rangle$  increases to around  $0.05 G_0/\text{Volt}^2$  where it remains stable before it increases slightly after  $3.5 G_0$ .

In Fig. 7.3a we present a  $(G, G'')$  scatter plot for Pt, with more than 800 data points. Along with the Pt data also the Au data from Fig. 7.2 are plotted for comparison to make the difference in the  $G''$  scale clear. Several interesting differences between the Au and Pt results are observed. In contrast to Au,  $G$  for the monatomic Pt contact is never close to  $1 G_0$  and there is no sign of quantization at  $2 G_0$ . Although half of the points are situated between  $1.5$  and  $2.5 G_0$ , only 30% of these lie in the interval from  $1.9$  to  $2.1 G_0$ . This is in good agreement with the Pt conductance histogram presented in Fig. 4.4a on page 53, without peaks close to  $1$  or  $2 G_0$ . The points spread over a large region both in  $G$  and  $G''$ , indicating a strong coupling of both the conductance and the  $I$ - $V$  behavior with the atomic configuration.

As with Au in Fig. 7.2 the mean value  $\langle G'' \rangle$  for Pt is represented by the solid curve drawn through the data. A zoom-in on this is displayed in Fig. 7.3b together with  $\langle G'' \rangle$  for Au.

The mean value for Pt, is always negative and the magnitude of  $\langle G''(G) \rangle$  is at least five times larger than for Au at any given  $G$ . It decreases to a minimum<sup>7</sup> of  $-0.68 G_0/\text{Volt}^2$  around  $G = 2.3 G_0$ , followed by a local maximum at  $2.6 G_0$  after which it decreases again with increasing  $G$ . This variation in  $G''$  for Pt, will be discussed in detail below.

### 7.2.3 Density functional theory calculations

To obtain further insight into these experimental findings, Mads Brandbyge has calculated  $I$ - $V$  curves using the TRANSIESTA program [19, 20]. The method is based on DFT and takes the voltage bias and current explicitly into account in the self-consistent calculation of electronic density and potential. We have considered the symmetric atomic configuration<sup>8</sup> depicted in Fig. 7.4a and varied

<sup>7</sup>Since  $\langle G'' \rangle$  is always negative, the minima in fact occur when the magnitude of  $G''$  is at a maximum, i.e. when the curves are the most non-linear.

<sup>8</sup>As mentioned  $G' \equiv 0$  for a symmetric contact.

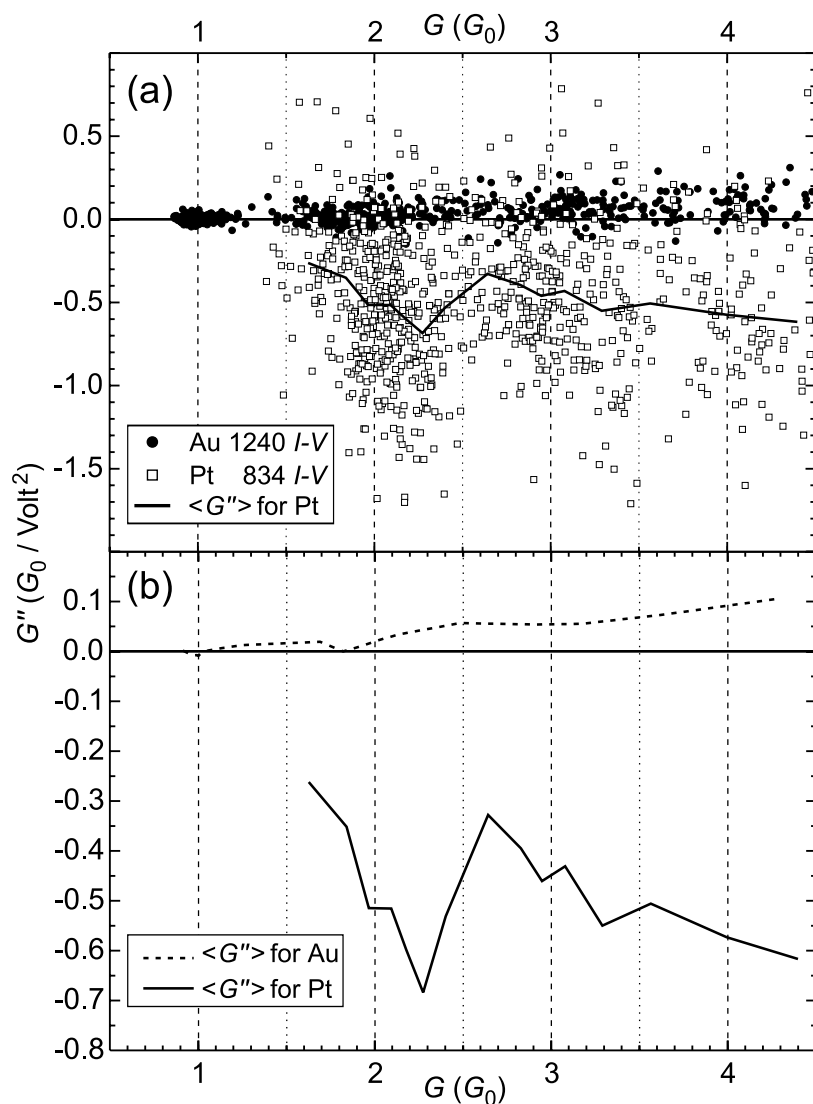


Figure 7.3: (a) Non-linear term  $G''$  vs low bias conductance  $G$  for Au and Pt ASCs. Each point represents a fit to Eq. (7.1) of one  $I-V$  curve on one ASC. There are points from 1240 Au and 834 Pt  $I-V$  curves. The solid curve represents the mean value  $\langle G'' \rangle$  for Pt. It is drawn through points found by averaging over at least 50 successive Pt points (see footnote 6 on page 119) (b) Zooming in on  $\langle G'' \rangle$  for Pt and comparing with the mean value for Au. (This is the same Au data as in Fig. 7.2).

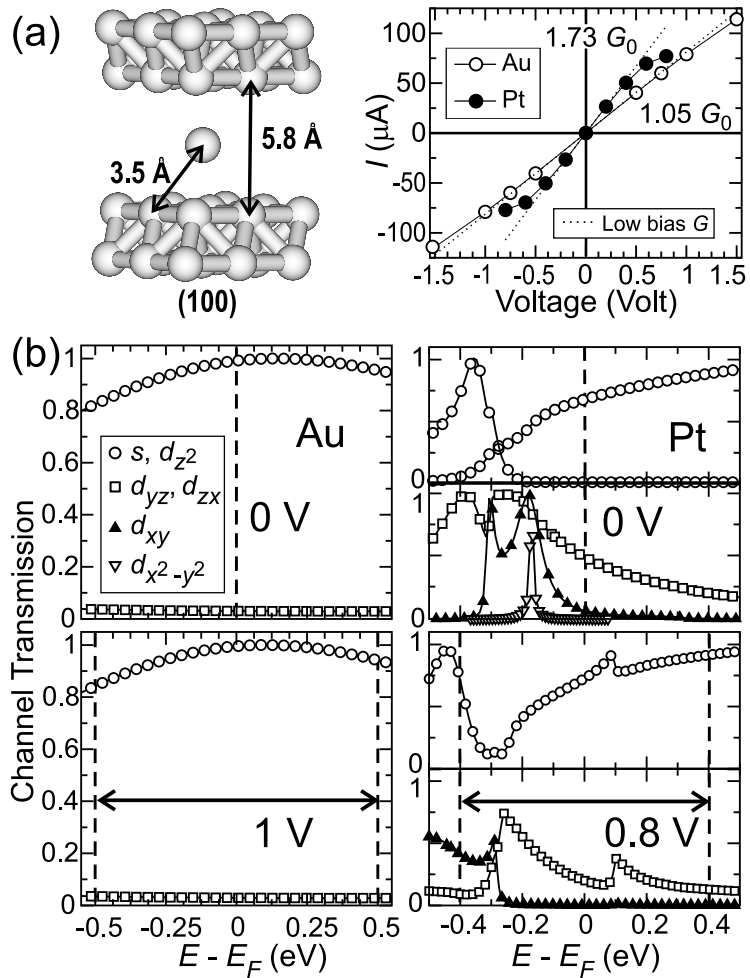


Figure 7.4: (a) The atomic structure of a symmetric monatomic contact of Au and Pt between (100) electrodes (left) and corresponding calculated  $I$ - $V$  curves (right). (b) Eigenchannel decomposition of the total transmission through the atoms for Au for 0 V and 1 V (left panels) and Pt for 0 V and 0.8 V (right panels). Due to the complicated structure for Pt, the graphs are split with the  $s, d_{z^2}$  channels in the upper window and the remaining channels in the lower window. The channels are labeled by their main orbital components ( $z$  is the direction perpendicular to the electrode surfaces, i.e. the direction of current flow).  $E_F$  is the Fermi energy at equilibrium and dashed lines indicate the “voltage window” spanning  $\pm eV/2$  on each side of  $E_F$ . (Calculations performed by Mads Brandbyge).

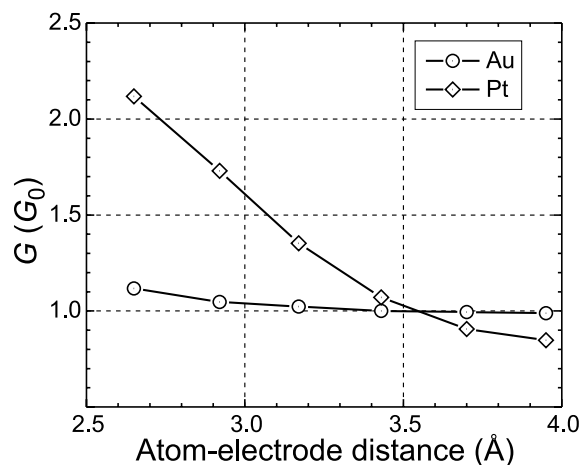


Figure 7.5: Calculated conductance  $G$  vs atom-electrode distance at zero voltage for a monatomic Au or Pt contact configuration like the one depicted in Fig. 7.4a. (Calculations performed by Mads Brandbyge).

the electrode-electrode distance. In this way we have calculated the conductance (at zero voltage) for Au and Pt vs electrode-atom distance as shown in Fig. 7.5.

For Au the conductance is almost constant with  $G$  only changing from 1.1 to 1.0  $G_0$  while the distance increases from 2.65 to 3.45 Å.<sup>9</sup> In contrast Pt displays a strong variation in the conductance with a decrease from 2.1 to 1.1  $G_0$  over the same distance interval. This variation is in accordance with the often reported narrow conductance histogram peak at 1  $G_0$  for Au [9, 15–18] and the broad peak centered around 1.5–2  $G_0$  observed for Pt [6, 9, 11]. (See also the conductance histograms for Au and Pt in Fig. 4.3a and 4.4a on page 49 and 53, respectively).

In Fig. 7.4a we show the calculated  $I$ - $V$  curves (right), corresponding to the atomic structure shown to the left with an atom-electrode distance of 2.9 Å. By fitting the calculated points to Eq. (7.1) we find that the Au  $I$ - $V$  curve is indeed almost linear<sup>10</sup> with  $(G, G'') = (1.05 G_0, -0.03 G_0/\text{Volt}^2)$  whereas the Pt  $I$ - $V$  curve is clearly non-linear with  $(G, G'') = (1.73 G_0, -0.82 G_0/\text{Volt}^2)$ , in good agreement with the experimental findings (cf. Fig. 7.3).

<sup>9</sup>We expect the monatomic contact to dimerize or break at 3.1 Å [21] long before reaching 3.45 Å (see Sec. 6.7.2). It is though very interesting that  $G$  remains so close to 1  $G_0$ .

<sup>10</sup>The electronic structure (projected band gap) of the (111) electrode itself yields a non-linear  $I$ - $V$  curve of Au [22]. The (100) and (110) electrodes (see Sec. 6.4 and [22]) yield linear  $I$ - $V$  curves of Au, and more realistic, somewhat disordered electrodes, as in the experiment, will most likely also belong to this same category.

According to the Landauer-Büttiker formalism (see Sec. 2.3) the conductance can be calculated from the total transmission as  $G = G_0 T_{\text{Tot}}$  [Eq. (2.13) on page 23]. The total transmission can be decomposed into non-mixing eigenchannels ( $T_i$ ) as [23]:

$$T_{\text{Tot}}(E) = \sum_i T_i(E). \quad (7.2)$$

In Fig. 7.4b the calculated eigenchannel decomposition for Au and Pt is shown both at zero and finite bias. For finite bias the conductance (in units of  $G_0$ ) is the average total transmission over the “voltage window” (dashed lines in Fig. 7.4b). For zero voltage this amounts to the transmission at the Fermi energy ( $E_F$ ). In the case of Au the transmission at 0 V is dominated by a single, broad channel of mainly  $s$  character resulting from a strong coupling between contact and electrode  $s$  orbitals. The slow variation of the channel transmissions with energy for Au, both at zero and finite bias (see left panel in Fig. 7.4b) results in a very linear  $I$ - $V$  curve (Fig. 7.4a).

The situation is, however, quite different for Pt, since we find four channels with significant contributions and a much stronger variation with energy for zero voltage (see right panel in Fig. 7.4b). Note that the  $d_{yz}, d_{zx}$  channels are degenerate while the  $d_{xy}$  and  $d_{x^2-y^2}$  channels are split due to the symmetry of the (100) electrodes. Additionally, the  $s$  and  $d_{z^2}$  orbitals combine at certain energies into two contributing channels. At finite bias a significant change in the channel structure is furthermore found as the  $\{d_{yz}, d_{zx}, d_{xy}\}$  derived channels become less transmitting and down-shifted in energy, and the  $d_{x^2-y^2}$  channel completely disappears. In contrast the broader  $s$ -derived channel is not prone to the shift in potential, although it no longer splits into two channels. The result is a clearly non-linear  $I$ - $V$  curve of Pt as seen in Fig. 7.4a.

## 7.2.4 Discussion

Before we try to compare two metals with so fundamentally different outer electron structure, as Au and Pt, we should first consider how easy the different types of electrons will scatter on an applied potential. Whereas only the highly delocalized  $s$  electrons contribute to the conductance for Au, also the much more localized  $d$  electrons are important for Pt.

Using the simplest tight-binding (TB) approach on a one dimensional (1D) chain of atoms, each with one orbital, we can find the band structure as [24]:

$$E(k) = E_0 - \beta \cos(k), \quad (7.3)$$

where  $E_0$  is the arbitrary on-site energy expressing the potential for the isolated atom, and  $\beta$  is the hopping matrix element which determines the actual energy scale [24].

By applying an electric field over the chain the potential is changed by  $\Delta E_0$ , which is of the same order as the applied voltage. The actual  $E_0$  is unimportant, as it acts like a zero-point, and has no influence on the way the scattering occurs. The only interesting parameters are  $\Delta E_0$  and  $\beta$ , because the likeliness for an electron to scatter depends on the ratio between the two:  $R = \Delta E_0/\beta$ . A large ratio, i.e. small  $\beta$ , implies that the electrons are easily scattered [24]. Since  $\beta$  increases the more delocalized the orbitals are, we find that the delocalized  $s$  electrons are less likely to scatter due to a shift in the potential than the localized  $d$  electrons.

For Pt, we can now attribute the decrease in conductance with voltage to the significant participation of the  $d$  electrons in the transport: The  $d$  electrons in Pt are more easily scattered by the voltage-induced potential than the  $s$  electrons in Au. In this case the potential is of the same order of magnitude as the strength of the coupling to the electrodes. The same argument goes for the variation with atom-electrode distance (see Fig. 7.5). Here it is essentially the  $d$  contributions which decrease when the distance increases. The  $s$  contribution remains constant and this explains the Au result.

These observations offer a possible explanation for the behavior of the Pt data in Fig. 7.3b. The mean value, represented by the solid curve, becomes more negative (increasing the non-linearity) as  $G$  increases. However, in the regime from 2.3–2.6  $G_0$  a rapid rise in  $\langle G'' \rangle$  occurs — this is the conductance region in which monatomic contacts are replaced by two-atom contacts, explaining the lack of data. Below 2.3  $G_0$  the conductance decreases when the contact is stretched. As this happens the  $d$  electrons contribution to the conductance decrease, which explains why the non-linearity is less pronounced at lower conductances. The pattern is repeated, although not as clearly, when  $G$  increases above 2.6  $G_0$ . This corresponds to compressing a two-atom contact increasing the contribution from the  $d$  electrons.

Along similar lines the dip in  $\langle G'' \rangle$  for Au at 1.8  $G_0$  in Fig. 7.2 could be explained by a relaxed atomic structure. The dip coincides with the peak in the Au conductance histogram (see Fig. 4.3a on page 49) which accordingly should resemble the preferred atomic configuration for a two-atom contact.

The mean value for Au is close to zero when compared to Pt (see Fig. 7.3b), but the Au data has a clear bias towards positive  $G''$  at higher  $G$ . Although not fully understood, it is most likely to be an effect of increasing electron tunneling when the contact size increases [25]. It should be noted that we have not included the direct tunneling between the electrodes in our DFT calculations.

In a recent experiment another possibility may have been presented [26]. The measurements are performed with the MCBJ under similar conditions as in our experiments, and using this method, was the thermal expansion of the electrodes investigated [26]. It is found that even for a very small tunneling current the expansion will cause the electrodes to move closer together, and in some cases jump to contact occurs [26]. Although only a limited amount of energy is dissipated in the contact itself, the temperature will increase in the region around the contact [27] (see discussion on page 17 of Sec. 2.2). If the resulting thermal expansion causes the electrodes to move together it will correspond to the compression discussed for the Pt contact above. In Fig. 7.5, we found a very small dependence on the interatomic distance for Au, but this was only calculated for a monatomic contact. If we have three or four atoms, it is likely that a compression may result in a more pronounced increase in the conductance. This could cause a slightly up-bending  $I$ - $V$  curve, with a positive  $G''$ .

Let us, as an example, consider a four atom Au contact with  $G \simeq 4 G_0$  at low bias. When a voltage burst is applied a rising temperature and the resulting thermal expansion could result in a compression of the contact. This gives a better overlap of the orbitals and hence a higher conductance.

For one and maybe also two-atom Au contacts, the dependence of  $G$  with distance may be too small for such an effect to be observed (cf. Fig. 7.5). With monatomic Au contacts we often observe a slightly negative  $G''$ , as also found from the DFT calculation. This effect can be explained by the eigenchannel decomposition in the left panels of Fig. 7.4b, from the decreasing transmission of the  $s$  channel at energies away from  $E_F$ . For Pt the effect of thermal compression is much smaller than the down-shift in the transmission channels (see right panels in Fig. 7.4b), and  $G'' < 0$  for all  $G$  (see Fig. 7.3b).

### 7.2.5 Conclusion

We have shown that the  $I$ - $V$  behavior of atomic-size contacts is highly dependent on the valence electron structure of the appropriate electronic materials. Linear  $I$ - $V$  curves can only be expected when exclusively  $s$ ,  $p_z$  and  $d_{z^2}$  electrons are involved in the transmission of the current. This is the case for the noble and the alkali metals, but for most other metals, open  $p$  or  $d$  shells will contribute to a complex electron structure. The consequence is an equally complex eigenchannel decomposition, which generally leads to non-linear  $I$ - $V$  curves, as observed for Pt.

The variety and richness in the behavior observed for the simplest atomic-scale conductors make it clear that the electronic structure of the electrode material itself will play an important role for the design of nano-scale devices in the future.

### 7.3 Current-voltage curves of noble metals

In order to test the conclusion from above we performed similar experiments using Ag, Cu, Pd and Ni. The Pd and Ni results can be found in the next section, where they are compared with the Pt results. In this section we compare experimental data from all the noble metals (cf. Fig. 1.1 on page 5).

All noble metals have a very similar outer electronic structure with one single  $s$  valence electron: Au ( $5d^{10}6s^1$ ); Ag ( $4d^{10}5s^1$ ); Cu ( $3d^{10}4s^1$ ). Both for Ag and Cu the transport is expected to be dominated by a single, broad resonance of  $s$  character, as we found for Au. In spite of this, some differences are found between these three metals.

In Fig. 4.3 on page 49 their conductance histograms are shown to be similar but with important differences. For Ag, the main difference from Au, is the split into two of the second peak, but more interesting is the second Cu peak which is very small and almost shifted down to  $1.5 G_0$ . The second peak for Au is closer to  $2 G_0$  and larger than the peak at  $3 G_0$ . For Cu the third peak below  $3 G_0$  is much larger than the second peak and relatively also much larger than the corresponding peak for both Ag and Au, when compared with the size of their first histogram peak. This indicates that ASCs of Cu prefer somewhat different atomic configurations than ASCs of the other two noble metals.

For all noble metals the first peak centered close to  $1 G_0$  is by far the most prominent feature in their conductance histograms. Based on this observations alone we may expect that monatomic contacts of noble metals behave similarly.

There is, however, one fundamental difference between Au and the other two noble metals. When ASCs of Au are stretched, monatomic chain formation is a possibility [3–6], whereas Ag and Cu cannot form chains [5, 6]. As mentioned above we avoided chain formation in the experiments with Au. Nevertheless the property that allows Au to form chains is likely to change the general behavior of the ASCs when compared to Cu and Ag. As we shall see in Chapter 8, monatomic contacts of Au are much more stable towards applied voltage than are the monatomic Ag and Cu contacts. This could be related to the property that makes the chain formation possible. As for Au, the monatomic contacts for Ag and Cu has a conductance from  $0.9$ – $1.1 G_0$ .

So far no results have been published on the  $I$ - $V$  dependence of neither Cu nor Ag. Other reports on ASCs of these metals are reviewed in Sec. 4.3. Below we compare  $I$ - $V$  curves of ASCs formed from all the noble metals.

#### Experimental results

In Fig. 7.6 typical  $I$ - $V$  curves measured on ASCs of (a) Ag and (b) Cu are shown. As for Au they only deviate little from linearity, which can be seen by

Material/label	$G$ ( $G_0$ )	$G'$ ( $G_0/\text{Volt}$ )	$G''$ ( $G_0/\text{Volt}^2$ )
Ag	1.0 $G_0$	0.9947(11)	-0.0271(13)
	2.4 $G_0$	2.3556(13)	0.0176(14)
	3.2 $G_0$	3.1534(14)	-0.0189(16)
Cu	1.1 $G_0$	1.0541(12)	0.0016(16)
	2.3 $G_0$	2.3347(15)	-0.049(2)
	3.0 $G_0$	2.9729(15)	-0.063(2)

Table 7.3: Parameters of fit to Eq. (7.1) for all  $I$ - $V$  curves from Fig. 7.6, with the uncertainty on the last digit given in brackets. As in the figure the  $I$ - $V$  curves are labeled by their low bias conductance  $G$ .

comparing the plot of the polynomial fit to Eq. (7.1) with the straight, dashed lines representing the low bias conductance  $G$ . The fitting parameters for the  $I$ - $V$  curves are displayed in Table 7.3.

For  $G$  above 1  $G_0$  the curves bend upwards for positive voltages with a slightly positive non-linear term  $G''$ . The Cu curve on the monatomic contact with  $G = 1.1 G_0$  is very linear with  $G''$  close to zero. For the monatomic Ag contact ( $G = 1.0 G_0$ ) the non-linear term is somewhat negative, much more than the similar curve of Au in Fig. 7.1a.

The burst amplitude used for the measurements are somewhat lower than for the monatomic contact of Au, indicating the mentioned difference in stability towards current.

As with Au and Pt large amounts of  $I$ - $V$  curves have been acquired and subjected to similar selection criteria. Since ASCs of Ag and Cu are less stable than those of Au, the limiting value for the asymmetry is set to  $|G'/G| > 0.05/\text{Volt}$  as for Pt (see Appendix B). All data points from polynomial fit of the remaining curves, 1600 for Ag and more than 1200 for Cu, are plotted in a  $(G, G'')$  scatter plot in Fig. 7.7. The Au data from Fig. 7.2 are also shown on the same scale for comparison.

The first feature to notice, is the spread in the data points, which grows larger and larger from Au over Ag to Cu. It is, however, also clear that even the Cu data spreads over a smaller region than the Pt data shown in Fig. 7.3a, and hence all the noble metals are less non-linear at all  $G$  than Pt.

For all three metals there is a clear bunching of points around 1  $G_0$  with almost no points below 0.9  $G_0$ ; the intensity of points decrease sharply after 1.1  $G_0$ , even for Ag, although it is difficult to see from the figure.

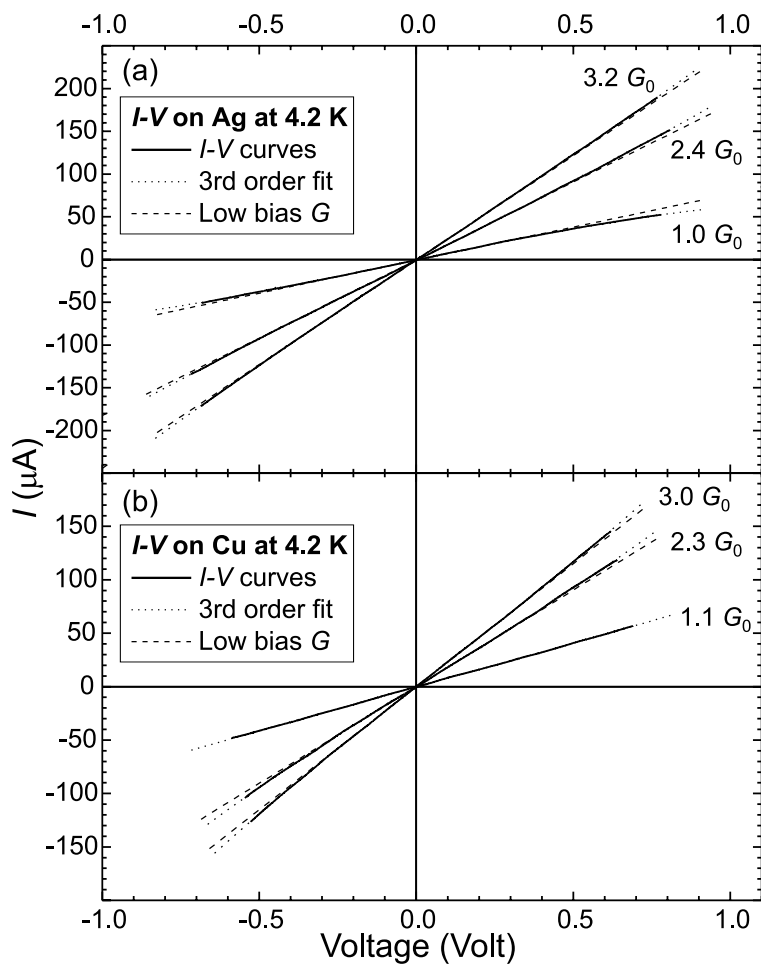


Figure 7.6: Representative  $I$ - $V$  curves of (a) Ag and (b) Cu ASCs formed with the MCBJ under cryogenic vacuum at 4.2 K. The  $I$ - $V$  curves are fitted to the third-order polynomial from Eq. (7.1) and fits are plotted as dotted lines. All fitting parameters can be found in Table 7.3 and curves have been labeled by their low bias conductance  $G$  obtained from the fit. Straight, dashed lines represents  $G$  for the curves, with the exception of the  $1.1 G_0$  Cu curve. This particular curve is almost linear ( $G'' \simeq 0$ ), and a straight line would completely overlap with the fit. All curves are measured in 1.5 ms which is the period of the 680 Hz triangular voltage burst used for the measurements. For Ag [Cu], the burst amplitude of 0.9 V [0.7 V] is superimposed on a bias of 50 mV.

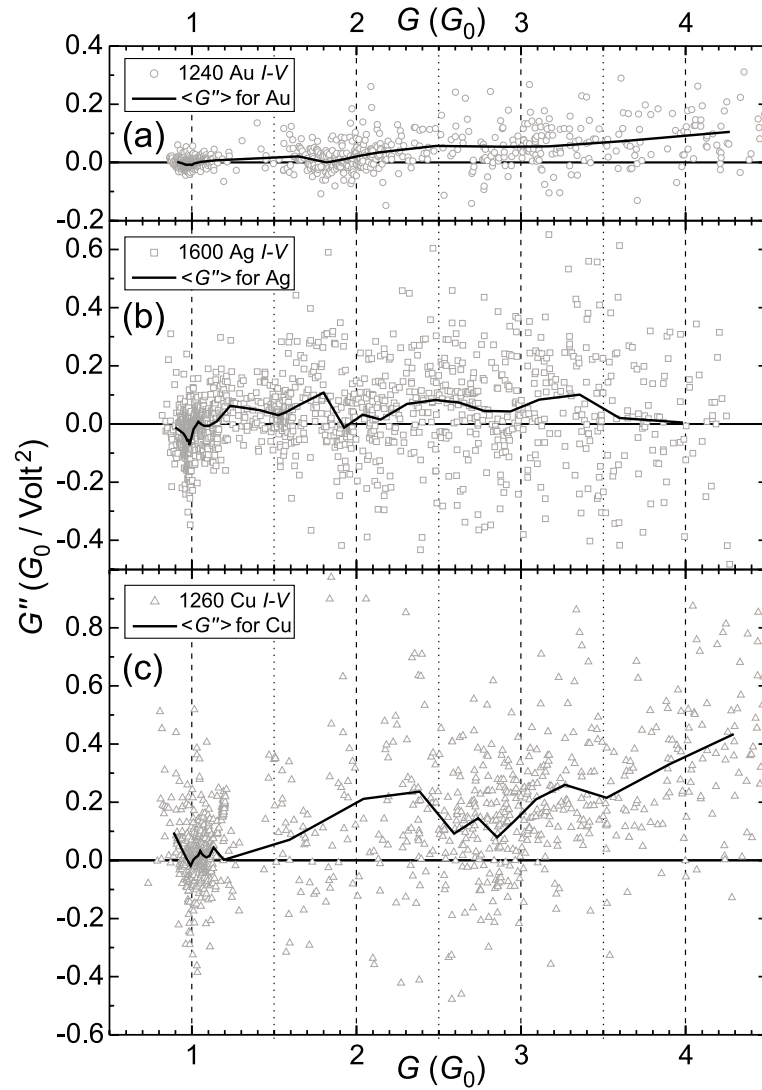


Figure 7.7: Comparing the non-linear term  $G''$  vs low bias conductance  $G$  for the noble metals. Each point represents a fit to Eq. (7.1) of one  $I$ - $V$  curve on one ASC. Points from (a) 1240 Au, (b) 1600 Ag and (c) 1260 Cu  $I$ - $V$  curves are shown. All three graphs are plotted on the same scale. Solid curves representing the mean value  $\langle G'' \rangle$  are drawn through points found by averaging over at least 50 successive data points (see footnote 6 on page 119). (The Au data was already presented in Fig. 7.2).

For Ag in Fig. 7.7b many points are found at a relatively large negative value of  $G''$  exactly at  $G = 1 G_0$ . Also the density of Ag points around  $1.5 G_0$  is higher when compared with that for the other two noble metals. This together with a slight increase in density around  $2 G_0$  is in accordance with the split second peak in the conductance histogram for Ag (see Fig. 4.3b on page 49). At higher  $G$  the data is more evenly distributed with a slight tendency to spread towards positive values of  $G''$ .

For Cu in Fig. 7.7c the graph clearly displays the lack of data between 1 and  $3 G_0$ , expected from the small second peak at  $1.5 G_0$  in the Cu conductance histogram (see Fig. 4.3c on page 49). Also, the large peak at  $3 G_0$  in the conductance histogram in accordance with the distribution of data.

As for Au and Pt in Fig. 7.3b, we also calculated the mean value  $\langle G'' \rangle$  for Ag and Cu. These are plotted through the data points in Fig. 7.7 as guides to the eye. Again this is done, to obtain a better idea of where the density of points is highest. Especially for Ag a clear dip at  $1 G_0$  shows the abundance of data points with large negative values of the non-linear term ( $\langle G'' \rangle \approx -0.1 G_0/\text{Volt}^2$ ). It may seem that the monatomic Ag contacts have a characteristic property not shared with the other two noble metals. There are only few points for Ag from  $1.1$  to  $1.4 G_0$ , but then around  $1.5 G_0$  the data density is again so high that we can rely on the calculated mean value, which has now risen to around  $0.05 G_0/\text{Volt}^2$ . After a clear dip of  $\langle G'' \rangle$  to zero at  $1.9 G_0$ , it almost increases to  $0.1 G_0/\text{Volt}^2$  where it remains fairly constant up to  $3.5 G_0$ . The decrease of  $\langle G'' \rangle$  after  $3.5 G_0$  should be considered with care, because of the few data points recorded in this region.

The Cu data generally spread over a larger region than both Au and Ag, but although Cu has several data points with a large negative value around  $G = 1 G_0$ , we find that here  $\langle G'' \rangle$  is still close to zero. This implies that it is equally likely for the monatomic Cu contact to have a small positive or negative value of  $G''$ . After this  $\langle G'' \rangle$  rises rapidly to above  $0.2 G_0/\text{Volt}^2$  through the data depleted region from  $1.2$  to  $2.5 G_0$ . Again the lack of data should be taken into account, and a dip in  $\langle G'' \rangle$  is also seen from  $2.6$  to  $2.8 G_0$  when the number of data points again increases. After this a final rise brings  $\langle G'' \rangle$  to a maximum of  $0.45 G_0/\text{Volt}^2$ . In the discussion we return to the mean values when comparing the noble metals with the platinum metals (Fig. 7.10).

## 7.4 Current-voltage curves of platinum metals

Finally we turn to the remaining platinum metals Pd and Ni. The platinum metals (cf. Fig. 1.1 on page 5) do not, like the noble metals, have an identical outer electronic structure. As discussed above, Pt ( $5d^96s^1$ ) has both open  $s$

and  $d$  shells contributing to the overall conductance of the ASCs. For Pd ( $4d^{10}5s^0$ ) the  $d$  shell is closed, whereas Ni ( $3d^84s^2$ ) on the other hand, has a closed  $s$  shell and instead the  $d$  shell lacks two electrons. Even when either one or the other shell is closed, will both  $s$  and  $d$  electrons still influence the conducting channel, since for these metals the  $s$  and the  $d$  bands overlap. This means that we cannot simply describe any observed differences between the platinum metals by their atomic electronic structure; theoretical calculations will be needed. When comparing with the noble metals, it will, however, still be possible to explain differences directly from the outer electron structure, as we already did for Pt and Au in Sec. 7.2.4.

The monatomic contacts for all three metals have a conductance in the range from 1.2 to 2.3  $G_0$  as seen from their conductance histograms presented in Fig. 4.4 on page 53.

So far no results exist on the  $I$ - $V$  dependence of Pd and in the single report on  $I$ - $V$  curves of Ni [28], there is no mention of any cleaning of the sample. The presented curves show the characteristic up-bending at positive voltages also seen for our Au  $I$ - $V$  curves when measured on samples not cleaned after exposure to air. We expect the non-linearity to be due to the impurity layer which will form on any metal surface when exposed to air [29, 30]. Below we will show that the non-linearity observed for Ni is mainly in the opposite direction of the results presented in [28]. Other investigations of platinum metal ASCs are reviewed in Sec. 4.4.

For the platinum metals it is only Pt, neighbor to Au in the periodic table, which can form monatomic chains [5, 6]. The two lighter elements Pd and Ni do, as Ag and Cu, not form chains [5, 6]. We avoided these exotic configurations for Pt in the experiments, but there are, like for Au vs Ag and Cu, a fundamental difference between the heavy Pt and the two lighter platinum metals which should be considered.

## Experimental results

In Fig. 7.8 typical  $I$ - $V$  curves measured on ASCs of Pd (a) and Ni (b) are shown. As for Pt, the  $I$ - $V$  curves of both Pd and Ni are clearly non-linear. The curves have been fitted to Eq. (7.1) and fits, plotted as dotted lines, can be compared with the straight, dashed lines, representing the low bias conductance  $G$ . The fitting parameters for the  $I$ - $V$  curves from the figure are displayed in Table 7.4.

When comparing the non-linear term  $G''$  with the Pt data from Table 7.2 it is obvious that Pd is even more non-linear than Pt. Pd has a negative value double that of the Pt curves at low conductance increasing to five times that of Pt for the high conductance curves.

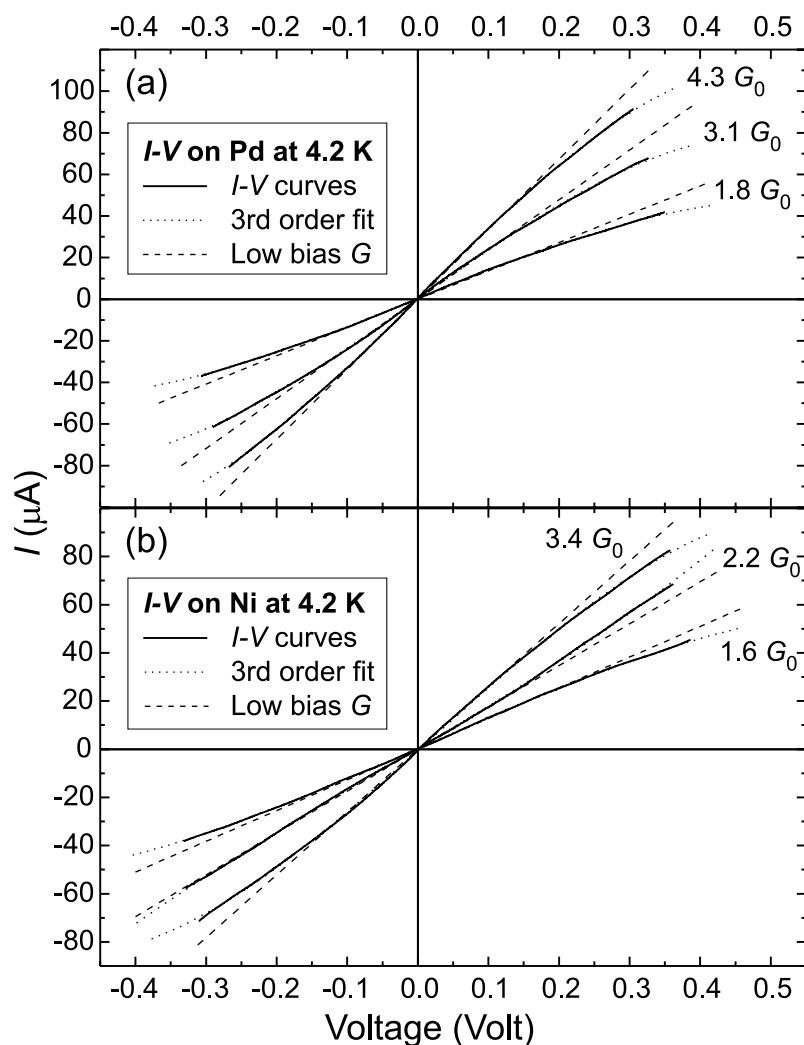


Figure 7.8: Representative  $I$ - $V$  curves of (a) Pd and (b) Ni ASCs formed with the MCBJ under cryogenic vacuum at 4.2 K. The  $I$ - $V$  curves are fitted to the third-order polynomial from Eq. (7.1) and fits are plotted as dotted lines. All fitting parameters can be found in Table 7.4, and curves have been labeled by their low bias conductance  $G$  obtained from the fit. This is also represented by the straight, dashed lines. All curves are measured in 1.5 ms using a 680 Hz triangular voltage burst with an amplitude of 0.4 V superimposed on a bias of 20 mV.

Material/label	$G$ ( $G_0$ )	$G'$ ( $G_0/\text{Volt}$ )	$G''$ ( $G_0/\text{Volt}^2$ )
Pd	1.8 $G_0$	1.7603(14)	0.009(4)
	3.1 $G_0$	3.087(2)	0.065(6)
	4.3 $G_0$	4.342(2)	0.155(6)
Ni	1.6 $G_0$	1.6450(14)	0.062(3)
	2.2 $G_0$	2.233(2)	0.207(5)
	3.4 $G_0$	3.373(2)	0.281(6)

Table 7.4: Parameters of fit to Eq. (7.1) for all  $I$ - $V$  curves from Fig. 7.8, with the uncertainty on the last digit given in brackets. As in the figure the  $I$ - $V$  curves are labeled by their low bias conductance  $G$ .

For Ni the low conductance  $G''$  is only slightly more negative than for Pt. But then something different is observed for the Ni curve with  $G = 2.2 G_0$ : The non-linear term is positive. This is also clear from the  $I$ - $V$  curve in Fig. 7.8b, which bends slightly up at positive voltages. Not only is  $G''$  positive, but the absolute magnitude is of the same order as the negative value for Pt in the same conductance region. This could be caused by a very unstable contact geometry, since this is the conductance range in which the conductance histogram for Ni has a minimum (see Fig. 4.4c on page 53). For the last curve at higher conductance  $G''$  is again negative with a value in between that of Pt and Pd.

The burst amplitude used for the measurements on Pd and Ni is even lower than for Pt and these two metals also have the least stable ASCs amongst the six metals. The large amount of  $I$ - $V$  curves acquired are subjected to similar selection criteria as for Pt. Ni turns out to be the least stable metal, and the limiting value for the asymmetry is set as high as  $|G'/G| > 0.1/\text{Volt}$  — twice the limit for Pd and Pt (see Appendix B). For the Ni curve with  $G = 2.2 G_0$  the asymmetric term  $G'$  is almost at the maximum value (see Table 7.4), and it is clear from Fig. 7.8b that this curve is somewhat asymmetric.

All data points from polynomial fits of the remaining curves (3450 for Pd and 1800 for Ni) are plotted in a  $(G, G'')$  scatter plot in Fig. 7.9. The Pt data from Fig. 7.3a are plotted together with the Pd data in Fig. 7.9a. The Ni data in Fig. 7.9b are plotted on the same scale to enable a direct comparison of data from all the platinum metals. Most noteworthy is the behavior of the Pd data. First of all they span over a very large range of  $G''$  values, but although there are a few positive outliers, almost all data are more negative than for Pt

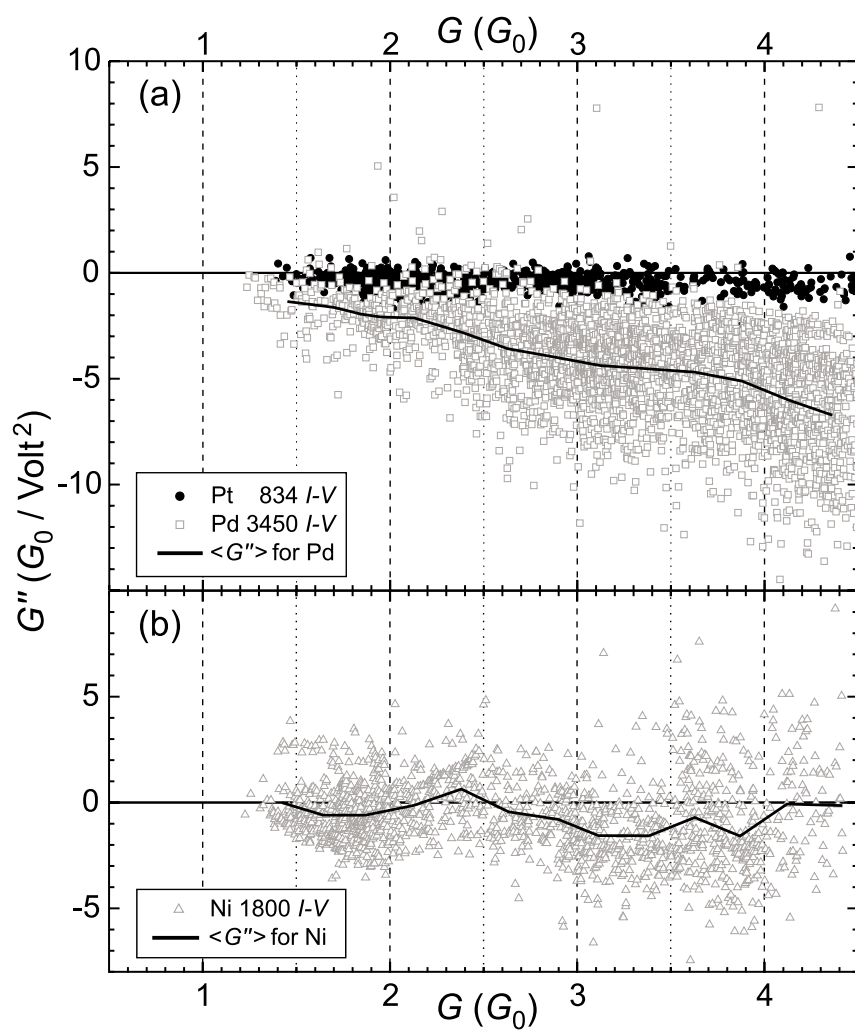


Figure 7.9: Non-linear term  $G''$  vs low bias conductance  $G$  for the platinum metals. (a) Points from 3450 Pd  $I$ - $V$  curves are compared with the 834 Pt data points previously shown in Fig. 7.3a. (b) Points from 1800 Ni  $I$ - $V$  curves. Both graphs are plotted on the same scale for comparison. Solid curves represent the mean value  $\langle G'' \rangle$  for Pd and Ni. They are drawn through points found by averaging at least 50 successive data points. (see footnote 6 on page 119).

at all conductances. At higher  $G$  the span becomes larger, but only towards more negative values. For the highest conductances all the Pd data points lies completely below the Pt points. Another important observation is that there is no obvious features in the spread of the points. Below  $1.7 G_0$  there are very few points, but from then on there are large amounts of points for all conductance values, unlike the depleted regions observed for all other metals. Even for Ni this depletion is observed around  $2.5 G_0$ , although it is difficult to see from the figure. This behavior of the Pd data is in accordance with the Pd conductance histogram which only has one clear peak, and from then on has a constant intensity (see Fig. 4.4b on page 53).

The Ni data in Fig. 7.9b behaves differently. Although the  $G''$  values spread over a larger region than for Pt, the region is much smaller than for Pd. On the other hand the intensity of points at positive  $G''$  cannot be neglected, especially not in the region  $2.0$ – $2.5 G_0$ . Here there is a dip in the intensity of the data as mentioned above, but there are still many data points compared with “empty” regions for e.g. Au between  $1.2$ – $1.7 G_0$  (cf. Fig. 7.2). We noted above that this conductance region coincides with the minima in the conductance histogram for Ni. At higher conductances there is a region where most data has negative  $G''$  but above  $3.5 G_0$  there is again a tendency to obtain positive values, although most data points here are still found below zero.

Also for Pd and Ni we have calculated the mean value  $\langle G'' \rangle$  and plotted it as solid lines through the data points in Fig. 7.9. Especially for Pd the curve follows the center of the data points. This indicates that just as for the conductance there is no preferred value of  $G''$ . It is thus equally likely for a Pd ASC to take on a value above or below the mean value. Since the distribution of data is so smooth we made a linear fit to all the Pd data. This line turns out to follow the calculated mean value very closely. The formula for the fit is:  $G'' = (1.3 G_0 - 1.76 G)/\text{Volt}^2$ . (It is plotted together with  $\langle G'' \rangle$  in Fig. 7.10b).

For Ni, a clearly positive  $\langle G'' \rangle$  between  $2.0$  and  $2.5 G_0$  shows that here most curves have positive  $G''$ . At low conductances,  $\langle G'' \rangle$  has a slightly negative value decreasing slowly with  $G$  until just below  $2 G_0$ , but then it rises to positive values, with a maximum of  $0.5 G_0/\text{Volt}^2$  at  $2.4 G_0$ . After this  $\langle G'' \rangle$  again becomes negative at  $2.5 G_0$ , and continues decreasing until the density of points with positive  $G''$  increases above  $3.5 G_0$ . The mean value becomes almost zero above  $4 G_0$ , but there are very few points in this region, and it might by a coincidence that there are an equal amount of data on both side of zero.

Especially for Ni care should be taken with the interpretation of the mean value, since the points spread over a large area on both sides of zero. From  $\langle G'' \rangle$  it can hence look like Ni is sometimes very linear, when in fact the ASCs merely shifts from having non-linear curves bending one way to the other, as for the Ni  $I$ - $V$  curve at  $2.2 G_0$ , compared with the other two curves in Fig. 7.8b.

## 7.5 Discussion

For all three noble metals, the single  $s$  valence electron ensures a broad  $s$ -derived channel. These electrons are not easily scattered by a shift in the potential, and this explains the linear  $I$ - $V$  curves observed. This is not the case for the platinum metals, where the active  $d$  electrons are responsible for the non-linear effects. From the results presented above we found that all the platinum metals indeed display clearly non-linear  $I$ - $V$  behavior, Pd more than both Ni and Pt. This indicates that the distribution of outer valence electrons have a great impact on the conducting properties of ASCs.

In the two previous sections, the data for each metal group were compared in Fig. 7.7 and 7.9, respectively. Especially, we calculated the mean value  $\langle G'' \rangle$ , to reveal features in the data, which could be hidden by a high density of data point. For a more direct comparison of the mean value for the six metals, we gather all these data and present them together in Fig. 7.10. In (a) we compare only the three noble metals with good reason; the platinum metals, especially Pd at the highest  $G$ , has very large magnitude of the mean value when compared to the noble metals. When we in Fig. 7.10b display  $\langle G'' \rangle$  for all six metals in the same graph, it is impossible to distinguish any finer details for the three noble metals. This way of representing the data really makes it clear, how much more non-linear  $I$ - $V$  curves, measured on ASCs of platinum metals, are when compared to curves obtained on ASCs of noble metals.

In Fig. 7.10a the mentioned dip in  $\langle G'' \rangle$  for Ag around  $1 G_0$  is much more clear; small dips are also visible at  $1.5$  and  $1.9 G_0$ . For Cu, the  $I$ - $V$  curves seems at first to be less linear at higher  $G$  than for the other two metals. However, we must remember that in the region from  $1.2$  to  $2.5 G_0$  only few data could be obtained. The same counts when  $G$  is above  $3.5 G_0$ . In between these regions ( $2.5$ – $3.5 G_0$ )  $\langle G'' \rangle$  for Cu is still slightly higher than for Ag and Au.

Although the graph for Ag always has a magnitude of  $\langle G'' \rangle$  close to that of Au, we observe that Au again stands out — this time by having the smoothest  $\langle G'' \rangle$  curve. Both Cu and Ag fluctuate much more on this scale than Au.

Although several differences exist between the three noble metals, they behave very similar when compared to the platinum metals, i.e. the three thin lines right above zero  $G''$  in Fig. 7.10b. All of them are very linear at  $1 G_0$ , and at higher conductances the mean value only rises slightly to positive  $G''$ . Even for the most non-linear Cu, the magnitude of  $\langle G'' \rangle$  is always below that of the platinum metals.<sup>11</sup> In general the platinum metal data points spread over a much wider range than the noble metals.

<sup>11</sup>This comparison is complicated by Ni, for which the mean value shift from negative to positive and back again. In spite of this, the statement still holds; when Ni fluctuates to positive  $G''$  values, it takes on even higher values than any of the noble metals.

Whereas the Au  $\langle G'' \rangle$  seems smooth on the scale of Fig. 7.10a it is now the Pt  $\langle G'' \rangle$  curve which in Fig. 7.10b behaves smoothly when compared to the other two platinum metals. In this way Au and Pt actually behave similarly in relation to their own group members. Although the magnitude of the Ni mean value is not much larger than for Pt at any  $G$ , it fluctuates much more, even to positive values. Compared to Ni even the Pd mean value looks smooth.

We again state what is obvious from Fig. 7.10b: The Pd  $I$ - $V$  curves are much more non-linear than curves of both Pt and Ni. It is very interesting that the Pd mean value decreases almost linear with  $G$ . To illustrate this point we have plotted the above mentioned linear fit to all the Pd data points in Fig. 7.8a. It is, hence, not a fit to the Pd  $\langle G'' \rangle$  curve, but it follows it very closely anyway.

This lack of structure is also observed in the Pd conductance histogram (Fig. 4.4b on page 53) and it may indicate that the ASCs of Pd can take on a multitude of different configurations. This means that for a given configuration with conductance  $G$ , it will always be possible to obtain another configuration with  $G \pm \delta$ , for any  $\delta$ . This can be obtained either from a small compression/stretching of the contact or by forming another yet very similar structure. In this way we can explain why there is only one peak in the histogram: Only the monatomic Pd contact, has so few configurations to “choose” from, that a peak appears above the background.

For these many contact configurations, the non-linearity will on average increase (more negative  $G''$ ) when the conductance increases, but it occurs in a smooth manner resulting in the almost linear decrease of the  $\langle G'' \rangle$  curve.<sup>12</sup>

When we are on the subject of comparing the  $\langle G'' \rangle$  curves with conductance histograms, we can turn to one of the most interesting features in Fig. 7.10b: The positive values of  $G''$  for ASCs of Ni, which peaks at  $G = 2.4 G_0$ . We have observed that ASCs of Ni in general are less stable than any of the other six metals, and the minimum in the conductance histogram after the first peak is situated between  $1.8$ – $2.5 G_0$  (see Fig. 4.4c on page 53). In this conductance region ASCs are expected to be very unstable. This may give rise to some strange atomic configurations, which could explain the many  $I$ - $V$  curves with positive  $G''$ . Both for Pd and Ni theoretical calculations will certainly be needed if we are to obtain a better understanding of the precise nature of the features observed. It is, however, very difficult to make simulations on these complicated electronic systems. The DFT simulation for Pt presented in Fig. 7.4 required many computer hours before the calculations were finished, explaining why we still lack DFT results for Pd and Ni.

<sup>12</sup>It feels a little weird with a *linear* curve for the *non-linear* mean value, or is it only me?

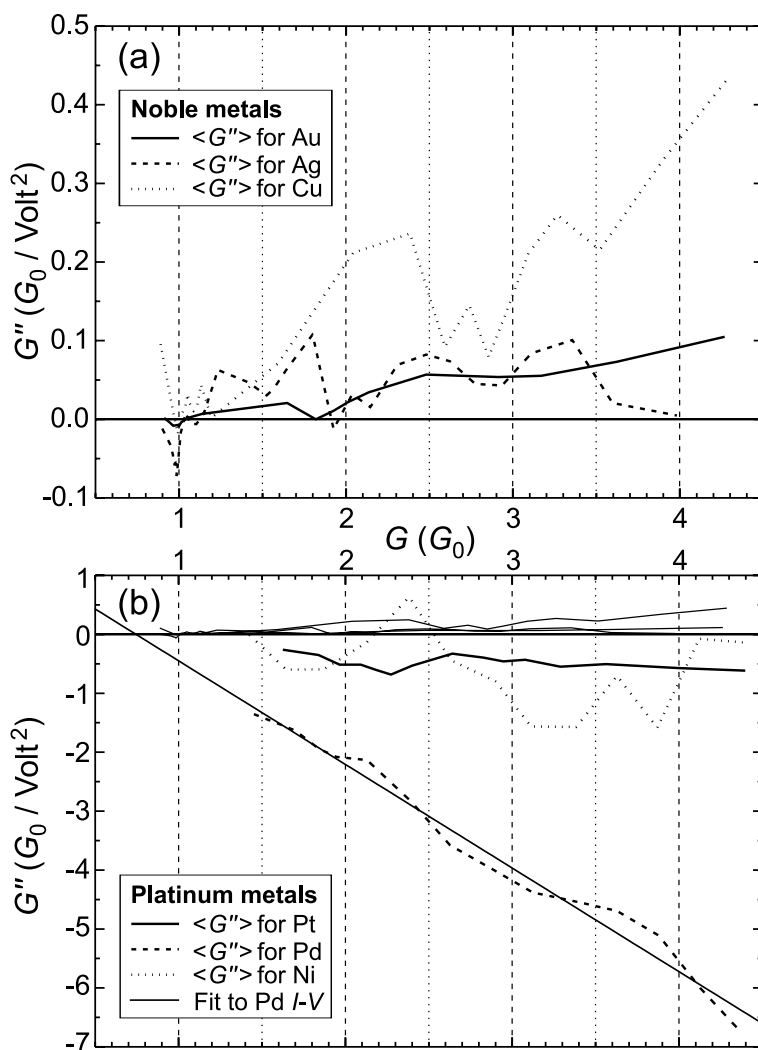


Figure 7.10: Comparing the mean value  $\langle G'' \rangle$  for (a) the noble and (b) the platinum metals. In (b) the thin solid line represents a linear fit to all the Pd data points shown in Fig. 7.8a;  $G'' = (1.3 G_0 - 1.76 G) / \text{Volt}^2$ . Also the three noble metals curves from (a) are represented here as the very thin solid lines situated at the top of the figure, in order to make the difference in  $G''$  scale clear. The curves are found by averaging at least 50 successive data points. (see footnote 6 on page 119).

We can relate the structure in the mean value of Pt to the corresponding histogram as well. The minimum at  $2.3 G_0$  almost coincides with the minimum between the first and the second peak in the Pt conductance histogram (see Fig. 4.4a on page 53). At a conductance higher than the  $1.5 G_0$  of the first histogram peak, the mean value decreases for all three platinum metals. This means that the most preferred monatomic contact configurations, i.e. those responsible for the peaks, are also those with the most linear  $I$ - $V$  curves (i.e.  $G''$  close to zero).

Similar relations holds for the noble metals, which all have a very small (in some cases slightly negative)  $G''$  for the monatomic contact ( $G \simeq 1 G_0$ ). We can find even more relations with the noble metals conductance histogram in Fig. 4.3 on page 49. For Au, there is a clear dip in  $\langle G'' \rangle$  at  $1.8 G_0$ ; the position of the second Au histogram peak.

For Ag, there are clear dips both at  $1.5$ ,  $1.9$  and below  $3 G_0$  coinciding with both peaks in the split second peak as well as the small third peak. Finally, for Cu, there is *no* dip coinciding with the small peak at  $1.5 G_0$ , but an even more clear dip are observed below  $3 G_0$  where the large third peak is situated.

## 7.6 Conclusion

We have seen that the general  $I$ - $V$  behavior changes drastically from metal to metal, especially from one group in the periodic table to another. Similar metals, e.g. the noble metals, have several features in common but even between these differences are observed. The platinum metals display an even more profound change in behavior from metal to metal.

Our first conclusion based on the Au and Pt results still stands: When only  $s$  electrons are involved in the transmission of the current almost linear  $I$ - $V$  curves can be obtained. We give three examples in the noble metals: Au, Ag and Cu. Although Cu is less linear at higher conductance than the other two, their  $I$ - $V$  curves are very linear when measured on the monatomic contacts ( $G \simeq 1 G_0$ ). For the platinum metals the conductance will always be influenced by the outer  $d$  electrons with non-linear  $I$ - $V$  curves as the results.

In the above discussion we find that minima in the mean value of the non-linear term  $G''$  often seems to coincide with features (peaks or valleys) in the corresponding conductance histograms. This is in some way related to several of the methods used to determine the number of open eigenchannels for ASCs, i.e. shot noise [31], conductance fluctuations [32] and thermopower fluctuations [33]. These experiments focus on parameters that will have a minimum when only

completely open channels contribute to the conductance (see the discussion on page 47 in Sec. 4.2). The minima will occur at integer values of  $G_0$ , and in conductance fluctuation experiment [32], it is in particular noted that these minima do not coincide with the conductance histogram peaks.

We have here presented a parameter  $\langle G'' \rangle$ , which seems to have minima coinciding with the peaks. Peaks are caused by contacts which have the most stable (preferred) atomic configurations. This indicates that ASCs having the same conductance as a histogram peak will be different from the less stable contacts with other conductances. It is reasonable to suggest that stable contacts must behave differently from unstable ASCs, and hence the minima in the mean value coinciding with histogram peaks can be explained from this. In a stable atomic configuration the applied voltage potential will have less influence on the structure, and the conductance will only change due to the scattering of the electrons, as described in Sec. 7.2.4.

So far we have only presented an investigation of  $I$ - $V$  curves measured on  $s$  metals (the noble metals) and  $d$  metals (the platinum metals). It would now be interesting to see how  $p$  metals behave. According to our theory, they should be non-linear if  $p_x$  and/or  $p_y$  electrons contribute to the conductance. Our preliminary experiments on the  $p$  metal aluminum (Al), indicate that  $I$ - $V$  curves of this type of metal are also non-linear, but in this case  $G''$  was mainly positive. Further investigations and theoretical calculations are, however, needed to improve the understanding of all these interesting observations.

## References

- [1] B. Hammer and J. K. Nørskov, “Why gold is the noblest of all the metals,” *Nature* **376**, 238–240 (1995).
- [2] R. H. M. Smit, (private communication).
- [3] H. Ohnishi, Y. Kondo, and K. Takayanagi, “Quantized conductance through individual rows of suspended gold atoms,” *Nature* **395**, 780–783 (1998).
- [4] A. I. Yanson, G. R. Bollinger, H. E. van den Brom, N. Agraït, and J. M. van Ruitenbeek, “Formation and manipulation of a metallic wire of single gold atoms,” *Nature* **395**, 783–785 (1998).
- [5] S. R. Bahn and K. W. Jacobsen, “Chain Formation of Metal Atoms,” *Phys. Rev. Lett.* **87**, 266101 (2001).
- [6] R. H. M. Smit, C. Untiedt, A. I. Yanson, and J. M. van Ruitenbeek, “Common Origin for Surface Reconstruction and the Formation of Chains of Metal Atoms,” *Phys. Rev. Lett.* **87**, 266102 (2001).
- [7] J. M. Krans, C. J. Muller, I. K. Yanson, T. C. M. Govaert, R. Hesper, and J. M. van Ruitenbeek, “One-atom point contacts,” *Phys. Rev. B* **48**, 14721–14724 (1993).
- [8] L. Olesen, E. Lægsgaard, I. Stensgaard, F. Besenbacher, J. Schiøtz, P. Stoltze, K. W. Jacobsen, and J. K. Nørskov, “Reply to ‘Comment on ‘Quantized conductance in an Atom-Sized Point Contact’’,” *Phys. Rev. Lett.* **74**, 2147 (1995).
- [9] C. Sirvent, J. G. Rodrigo, S. Vieira, L. Jurczyszyn, N. Mingo, and F. Flores, “Conductance step for single-atom contact in the scanning tunneling microscope: Noble and transition metals,” *Phys. Rev. B* **53**, 16086–16090 (1996).
- [10] K. Yuki, S. Kurokawa, and A. Sakai, “Quantized Conductance in Pt Nanocontacts,” *Jpn. J. of Appl. Phys.* **39**, 4593–4595 (2000).
- [11] R. H. M. Smit, Y. Noat, C. Untiedt, N. D. Lang, M. van Hemert, and J. M. van Ruitenbeek, “Measurement of the conductance of a hydrogen molecule,” accepted for publication in *Nature*, (2002), <http://xxx.lanl.gov/pdf/cond-mat/0208407>, (unpublished).

- 
- [12] J. L. Costa-Krämer, N. García, P. García-Mochales, P. A. Serena, M. I. Marqués, and A. Correia, “Conductance quantization in nanowires formed between micro and macroscopic metallic electrodes,” *Phys. Rev. B* **55**, 5416–5424 (1997).
- [13] J. Abellán, R. Chicón, and A. Arenas, “Properties of nanowires in air. Controlled values of the conductance,” *Surf. Sci.* **418**, 493–501 (1998).
- [14] A. Correia, J.-L. Costa-Krämer, Y. W. Zhao, and N. García, “Non-linear contribution to intensity-voltage characteristics of gold nanowires,” *Nanostruct. Mater.* **12**, 1015–1020 (1999).
- [15] M. Brandbyge, J. Schiøtz, M. R. Sørensen, P. Stoltze, K. W. Jacobsen, J. K. Nørskov, L. Olesen, E. Lægsgaard, I. Stensgaard, and F. Besenbacher, “Quantized conductance in atom-sized wires between two metals,” *Phys. Rev. B* **52**, 8499–8514 (1995).
- [16] B. Ludoph and J. M. van Ruitenbeek, “Conductance fluctuations as a tool for investigating the quantum modes in atomic size metallic contacts,” *Phys. Rev. B* **61**, 2273–2285 (2000).
- [17] K. Hansen, E. Lægsgaard, I. Stensgaard, and F. Besenbacher, “Quantized Conductance in Relays,” *Phys. Rev. B* **56**, 2208–2220 (1997).
- [18] H. Yasuda and A. Sakai, “Conductance of atomic-scale gold contacts under high-bias voltages,” *Phys. Rev. B* **56**, 1069–1072 (1997).
- [19] M. Brandbyge, J.-L. Mozos, P. Ordejón, J. Taylor, Kurt Stokbro, “Density functional method for nonequilibrium electron transport,” *Phys. Rev. B* **65**, 165401 (2002). Here, we use the same parameters except the orientation of the electrodes is (100) instead of (111).
- [20] J. M. Soler, E. Artacho, J. D. Gale, A. García, J. Junquera, P. Ordejón, and D. Sánchez-Portal, “The SIESTA method for ab initio order-N materials simulation,” *J. Phys. Cond. Matt.* **14**, 2745–2779 (2002).
- [21] S. R. Bahn, “Computer Simulations of Nanochains,” PhD thesis, Technical University of Denmark, 2001.
- [22] M. Brandbyge, N. Kobayashi, and M. Tsukada, “Conduction channels at finite bias in a single-atom gold contact,” *Phys. Rev. B* **60**, 17064–17070 (1999).

- 
- [23] M. Brandbyge, M. R. Sørensen, and K. W. Jacobsen, “Conductance eigenchannels in nanocontacts,” *Phys. Rev. B* **56**, 14956–14959 (1997).
- [24] A. P. Sutton, *Electronic Structure of Materials* (Oxford University Press, Walton Street, Oxford OX2 6DP, 1993), chapters 2 and 3.
- [25] A. García-Martin, J. A. Torres, J. J. Sáenz, and N. Nieto-Vesperinas, “Intensity Distribution of Modes in Surface Corrugated Waveguides,” *Phys. Rev. Lett.* **80**, 4165–4168 (1998).
- [26] O. Y. Kolesnychenko, A. J. Toonen, O. I. Shklyarevskii, and H. van Kempen, “Millisecond dynamics of thermal expansion of mechanically controllable break junction electrodes studied in the tunneling regime,” *Appl. Phys. Lett.* **79**, 2707–2709 (2001).
- [27] T. N. Todorov, “Local heating in ballistic atomic-scale contacts,” *Philos. Mag. B* **77**, 965–973 (1998).
- [28] B. Rodell, V. Korenivski, J. Costa, and K. V. Rao, “Quantized conductivity in STM drawn 100Å nanowires of Au and Ni,” *Nanostruct. Mater.* **7**, 229–235 (1996).
- [29] G. S. Ferguson, M. K. Chaundhury, G. B. Sigal, and G. M. Whitesides, “Contact Adhesion of Thin Gold Films on Elastomeric Supports: Cold Welding Under Ambient Conditions,” *Science* **253**, 776–778 (1991).
- [30] G. W. Whitesides, (private communication).
- [31] H. E. van den Brom and J. M. van Ruitenbeek, “Quantum Suppression of Shot Noise in Atom-Size Metallic Contacts,” *Phys. Rev. Lett.* **82**, 1526–1529 (1999).
- [32] B. Ludoph, M. H. Devoret, D. Esteve, C. Urbina, and J. M. van Ruitenbeek, “Evidence for Saturation of Channel Transmission from Conductance Fluctuations in Atomic-Size Point Contacts,” *Phys. Rev. Lett.* **82**, 1530–1533 (1999).
- [33] B. Ludoph and J. M. van Ruitenbeek, “Thermopower of atomic-size metallic contacts,” *Phys. Rev. B* **59**, 12290–12293 (1999).

## Chapter 8

# Current-Induced Disruptions

At room temperature (RT), atomic-sized contacts (ASCs) are unstable and disrupts on a millisecond time scale. At liquid helium temperature (4.2 K) they can, however, remain stable for minutes. It would be very interesting to understand the processes that induces the disruption of an ASC.

In this chapter, based on paper [V], our investigation of the *current-induced disruption* of monatomic metal contacts will be described.

### 8.1 Motivation

During our measurements of current-voltage ( $I$ - $V$ ) curves, we found that the ASCs became unstable, eventually breaking, when the amplitude of the applied voltage bursts were too high. This was illustrated in Fig. 5.11b on page 80, by the  $I$ - $V$  curves measured on an ASC while it was breaking. From these curves it is clear that the contact mainly experiences changes in the atomic configuration, resulting in jumps to lower conductances, when the burst voltage is at a maximum; an indication that it is the burst that induces the rearrangement.

In order to acquire  $I$ - $V$  curves we needed the contacts to remain stable during a full burst cycle. This was accomplished by only using burst amplitudes below a certain limit depending on the metal as described in Sec. 7.1. In the scanning tunneling microscope (STM) at RT we could only use amplitudes below 1 V for clean gold (Au) contacts (see Sec. 6.3). This increased to 2 V when

measuring  $I$ - $V$  curves on monatomic Au contacts at 4.2 K using the mechanically controllable break junction (MCBJ) (see Sec. 7.1). In some cases a contact could even sustain higher voltages for several burst cycles, like the  $I$ - $V$  curve in the inset of Fig. 7.1a on page 117. This particular monatomic contact remained stable even at the maximum voltage of 2.45 V, where the local current density exceeded 2 GA/mm<sup>2</sup>.

The stability towards high voltages and extreme current densities caught our attention and we decided to investigate current-induced disruptions for the noble metals: Au,<sup>1</sup> silver (Ag) and copper (Cu), and the platinum metals: Platinum (Pt), palladium (Pd) and nickel (Ni) (see Fig. 1.1 on page 5). We observed significant differences in the breaking current between the metals, with Au sustaining by far the highest currents before breaking. The increased stability of Au is probably related to the single open transmission channel, since also the other noble metals are more stable than their platinum metals neighbor in the periodic table. The property that allows the formation of monatomic chains for Au and Pt may, however, also be very important. This is supported by the fact that Pt is much more stable than the two other platinum metals Pd and Ni.

## 8.2 Introduction

It has previously been noted that monatomic chains of Au can withstand extreme current densities without breaking [1]. That there is a limit to this stability was shown in experiments investigating the bias dependence of Au [2–4] and also Pt [5] conductance histograms. Here it was found that the peaks of the histograms disappear when recorded at a bias above a maximum value which depends on material and temperature (1.9–2.3 V for Au and 1.4 V for Pt). The lacking peaks indicated that ASCs are no longer stable above this maximum bias. The reason for the instability of the contact was interpreted as being due to electromigration caused by the high current density [2]. This is confirmed by theoretical calculations, showing that atomic bonds in a metallic chain are weakened by a high current density due to electron wind forces [6–8].

Finally, an increased temperature due to Joule heating has been investigated [9–11]. Even though the electron transport through ASCs is ballistic (see Sec. 2.2), it is shown theoretically that the contact will experience a local

---

<sup>1</sup>In Sec. 8.5.3 we describe our preliminary STM experiments on Au. After these experiments we moved on to the MCBJ, which is more suited for testing the stability of ASCs.

heating [10], which will destabilize the atomic structure. The dissipation will not occur in the contact itself [12], and recent experiments show that the energy dissipation only sets in at a finite bias [11]. It is found that in monatomic Au chains, there is a threshold current below which no phonon excitation occurs [11]. First above a current of  $1 \mu\text{A}$  will the contact area begin to heat up due to excitations. This is though, a very small current compared to the breaking current, which is found to be above  $100 \mu\text{A}$  in the same experiment [11].

In this paper it is furthermore found that the behavior of the contact is very sensitive to strain [11]. This is in accordance with both experimental [13, 14] and theoretical [15, 16] studies showing that jumps in the conductance of ASCs are related to the applied strain. The strain can also be influenced by increasing temperatures, due to thermal expansion [17].

### 8.3 Experimental details

The experiments are all performed at 4.2 K under cryogenic vacuum using the MCBJ as described in Sec. 3.3. The samples used for the experiments are the same as those prepared for measuring  $I$ - $V$  curves in Chapter 7. The six metals Au, Ag, Cu, Pt, Pd and Ni are used. For details regarding the sample preparation and contact formation technique refer to Sec. 7.1.

One exception to the rule is presented in Sec. 8.5.3 where our preliminary STM experiments [18] are presented in relation to a description of the Kolmogorov-Smirnov (KS) test [19]. These investigations were performed under ultra-high vacuum (UHV) at much higher temperatures (140–240 K) than in the MCBJ. Contact formation and sample preparation methods for this STM study are the same as those described in Sec. 6.2, but here the sample is a Au(111) crystal. We only used hard indentations on a cleaned sample. The STM and the cooling procedure are described in Sec. 3.2.

When ASCs consisting of several atoms at the apex become unstable due to an applied bias, they will typically not break completely. Rather they will change their atomic configuration by removing atoms from the contact region. This will lower the conductance, and hence the current, in steps as displayed in Fig. 5.11b on page 80. First when a contact only consists of a single atom (monatomic), will further instabilities ensure the complete break, where the conductance drops entirely to zero ( $G = 0 G_0$ ).<sup>2</sup>

<sup>2</sup>The fundamental unit of conductance  $G_0$  is defined in Eq. (2.3) on page 15.

With monatomic contacts it will therefore be easy to determine when the break actually occurs, whereas this can be complicated for the general few atom contact.<sup>3</sup> Since monatomic contacts also represent the simplest atomic configuration, important when performing the already complicated theoretical calculations to which we hope to compare these experimental results, we decided to focus entirely on the induced disruptions of this type of ASCs.

In Sec. 7.1 we describe how to obtain monatomic contacts making sure to avoid chain formation in the case of Au and Pt [20, 21]. The range of conductance accepted in these experiments is 0.7–1.2  $G_0$  for the noble metals, and 1.3–2.0  $G_0$  for the platinum metals. This is in accordance with the conductance of the first peak in the conductance histograms presented in Chapter 4.

When a new monatomic contact is formed from a “large” contact with  $G > 50 G_0$  to ensure a new atomic configuration, a voltage ramp is applied with an amplitude large enough to disrupt the contact. In Fig. 8.1a we show a typical example of a measurement on a monatomic Au contact. The thick solid line represents the voltage signal supplied by the function generator (FG).

From the measured output voltage we calculate  $G$ ,  $I$  and  $V$  as described in Sec. 5.6, and in Fig. 8.1a we also show the evolution of the conductance of the monatomic Au contact during the burst. As described in Sec. 5.7, the noise in the calculated conductance is high when the bias is low as seen during the first 0.1 ms, before the burst. When the burst begins the noise decreases.

In spite of the noise, the average conductance is close to 1  $G_0$  at all times, as expected for a monatomic Au contact. When the contact finally breaks after 0.55 ms, long before  $V_{FG}$  reaches the maximum voltage, the conductance drops to zero almost instantly on this timescale.<sup>4</sup> Before the break occurs, the conductance decreases slightly below 1  $G_0$  to a conductance around 0.96  $G_0$  (the break-conductance  $G_{\text{break}}$ ). This is in accordance with the slightly negative non-linear term  $G''$  observed for the monatomic Au contacts (see Fig. 7.2 on page 119).

For the conductance trace in Fig. 8.1a we obtain the calculated  $I$ - $V$  curve shown in Fig. 8.1b. From such graphs we obtain both the break-current  $I_{\text{break}}$  and the break-voltage  $V_{\text{break}}$ , which are 162  $\mu\text{A}$  and 2.15 V, respectively for

<sup>3</sup>When we investigate two-atom contacts ( $G \simeq 2 G_0$ ) we have to consider if we will accept it as a “break” if the conductance only drops from 2  $G_0$  down to 1  $G_0$  instead of all the way down to zero. This happens when one of the two atoms moves out of the contact leaving a monatomic contact behind. It is our experience that this is the typical behavior for Au and a break from 2  $G_0$  directly to 0  $G_0$  only rarely occurs. The other metals behaves similarly.

<sup>4</sup>There are 10 000 points in the conductance trace which is measured in 1 ms. With only 100 ns between each data point, the break can be seen to occur almost instantly as only three data points are measured while the conductance drops to zero. These few points are due to the finite relaxation time of the setup. The relaxation time is clearly visible in Fig. 8.1b due to the vertical line indicating the break-voltage.

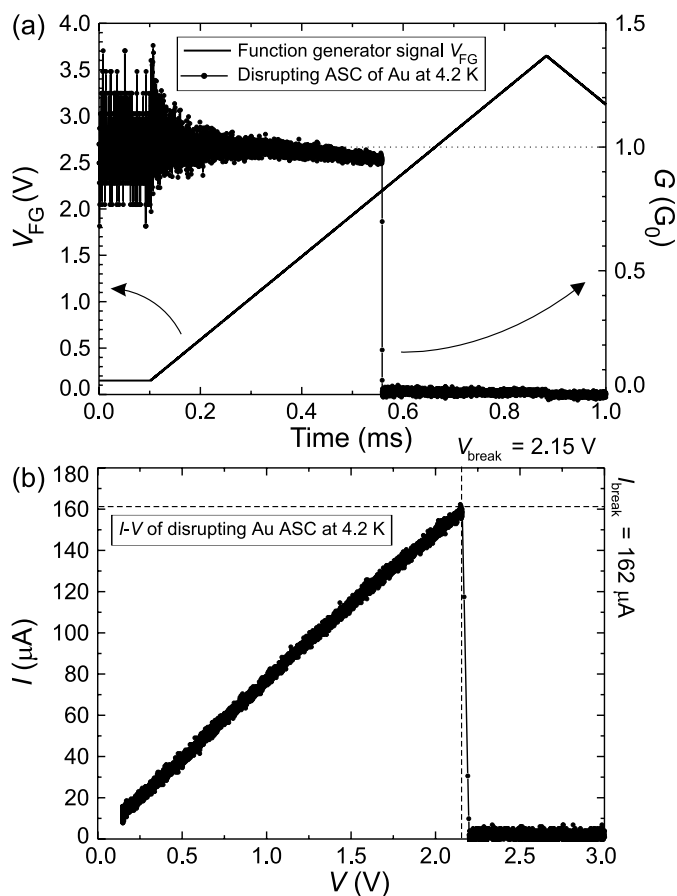


Figure 8.1: Inducing a disruption of a monatomic Au contact formed with the MCBJ at 4.2 K under cryogenic vacuum. (a) The thick solid line, belonging to the left axis, shows the applied function generator (FG) voltage  $V_{FG}$  as a function of time. It is a 320 Hz burst with an amplitude of 3.5 V superimposed on 150 mV bias. The burst begins after 0.1 ms, and reaches the maximum voltage in less than one millisecond since  $dV_{FG}/dt = 4Af = 4.5$  kV/s. From the measured output signal, the corresponding conductance of the contact is calculated. This is shown as the thin solid line through the full circles belonging to the right axis. The average conductance is close to 1  $G_0$  (dotted line) until the monatomic Au contact breaks. (b) The calculated  $I$ - $V$  curve corresponding to the conductance trace in (a). The break-current  $I_{break} = 162$   $\mu$ A and break-voltage  $V_{break} = 2.15$  V are found from the graph ( $P_{break} = 348$   $\mu$ W).

Material	Au	Ag	Cu	Pt	Pd	Ni
$A$ (V)	3.5	3.0	2.5	1.5	1.0	1.0
Bias (mV)	150	100	100	150	50	50

Table 8.1: The burst amplitude  $A$  and bias used for the different metals to ensure that all contacts break before the maximum voltage is reached. Note that  $A$  is the actual burst amplitude, not the peak to peak voltage. After the FG voltage burst in Fig. 8.1a reaches the maximum, it decrease to  $V_{\text{FG}} = -A$ .

this particular trace. We can also calculate the power ( $P = IV$ ), and we find a break-power  $P_{\text{break}} = I_{\text{break}} \times V_{\text{break}} = 348 \mu\text{W}$ . These break parameters are those we will investigate in this chapter. An extremely high current density will be the result of this, for a single Au atom, very large current. The trace is, nevertheless, typical for our Au data, with values of the break parameters close to the median break values as we shall see in Sec. 8.6.

It turns out that the value of these break parameters will be very different from contact to contact. For a metal subjected to given experimental conditions there will be an underlying distribution of break parameters. What we actually measure is a break probability distribution drawn from this underlying true distribution of break parameters. This implies that we have to investigate statistical behaviors by obtaining a large amount of material and compare the distribution of entire data sets rather than breaks of individual contacts. We also have to consider which experimental conditions we control and which we do not control, and how they each will affect the underlying distribution.

It will never be possible to measure the true distribution, but we approach it the more breaks we measure for a given experimental setup. Since we attempt to obtain the best possible representation of the true distribution it will be very important to use a burst amplitude which is high enough to ensure that all contacts break. If some contacts do not break our measurements will not cover the full distribution and this renders the entire data set useless

From our observations we have found that there are huge differences in the stability from metal to metal, and different amplitude and bias are required for each metal. The chosen values can be found in Table 8.1. We could, in principle, have used the burst amplitude for Au in all experiments, as the monatomic contacts of all metals would then be sure to break. Like with the  $I$ - $V$  curve experiments, we choose precise measurements over the advantage of using the same burst parameters (see Appendix C).

The experimental parameters that we control are:

1. Temperature  $T$
2. Bias voltage  $V_{\text{bias}}$
3. Burst frequency  $f$
4. Burst amplitude  $A$

We do not control the crystal orientation of the ASCs, and in particular we have no knowledge of the atomic configuration of the electrodes connecting with the contact. The contact itself should, however, consist of a single atom. Nevertheless, this will be a very important parameter, which may influence the experiments. The configuration will be different for each contact due to the way we form them, and we have to take this fact into account when analyzing data.

It would be interesting to increase the temperature above 4.2 K, but as discussed in Sec. 3.3 this could cause the contact region to be contaminated. This will happen when solidified gases begin to diffuse into the contact region due to the increasing temperature.

The bias is less interesting. It will be important to keep it low, so it will not interfere with the range of voltages where the monatomic contacts actually break. This varies considerably from metal to metal (see Table 8.1). The noise will be large for low bias and we avoided biases below 50 mV in these experiments.

This only leaves us in control of amplitude and frequency. It is these two parameters which determine the speed with which the function generator voltage increases (cf. Fig. 8.1a). This actually also turns out to be a very interesting parameter to investigate. The voltage ramp rate (voltage rate or  $dV/dt$  from now on) is given as  $dV/dt = 4V_{\text{max}}f$ , where  $V_{\text{max}}$  is the maximum voltage over the contact and  $f$  is the burst frequency as set on the FG. For the FG signal in Fig. 8.1a  $dV_{\text{FG}}/dt = 4Af = 4480$  V/s, but due to the voltage drop over  $R_{\text{FG}}$  and  $R_{\text{in}}$  (see Fig. 5.6 on page 69) the actual maximum voltage  $V_{\text{max}}$  over the contact is about 5% smaller for a contact with  $G = 1 G_0$ . Hence we find that  $dV/dt \simeq 4256$  V/s for the  $I$ - $V$  curve in Fig. 8.1b. The conductance changes from contact to contact, and even more from metal to metal. This means that  $dV/dt$  cannot be stated precisely even when the FG settings are the same for an entire experiment. In general we will only give  $dV/dt$  with two significant digits (e.g. 4.3 kV/s rather than 4256 V/s).

When keeping the amplitude constant for the individual metals, in order to ensure that all contacts break, the voltage rate will be determined solely by the frequency. This has been varied in the range from 1 Hz to 1 kHz for all metals, and the resulting range of  $dV/dt$  (4 V/s–13 kV/s) covers more than three orders of magnitude. Since  $dV/dt$  still depends on the amplitude, which is different for each metal, the highest  $dV/dt$  will only be reached for experiments on the most stable metal Au, whereas the lowest rates will belong to Pd and Ni, the least stable of the six metals, with correspondingly smaller burst amplitudes (see Table 8.1).

### Selection criteria

Some selection criteria are applied to the traces before a disruption is accepted and included in the data set. By using the contact formation technique of Sec. 7.1, we are already sure that the monatomic contacts have been stable on a time scale of seconds before the burst is applied. It is thus very likely that all breaks will be induced by the burst, as this only lasts a fraction of a second.

We do, in spite of this, sometimes observe traces where the conductance becomes unstable during the burst, some time before the actual break occurs. The result can be jumps to higher conductances before the contact finally breaks. In other cases the conductance will not fall directly to zero when the break occurs, but rather stay for a short period at an intermediate conductance value between zero and the conductance of the monatomic contact. This could be due to tunneling between the electrodes, which may remain very close to each other, even after the break, because of the low temperature. The high voltage will increase the tunneling to a significant conductance level (0.1–0.3  $G_0$ ) as we saw in Sec. 6.5. Another possibility is, however, that some impurity was present in the contact region and this could have influenced the break parameters.

Traces of the above described type are not accepted. If, on the other hand, the conductance remains stable within a few percent, and the only changes are related to the typical  $I$ - $V$  curve behavior of the given metal, as the slight down-bending in Fig. 8.1a, the trace is accepted.

I have performed the selection manually while obtaining the break values from each individual trace. This was a huge assignment (25 000 traces), which we found necessary, since our selection criteria, although straightforward, would have been very difficult to emulate in an automatic computer procedure (see footnote 5 on page 118).

## 8.4 Cumulated break probability

During an experiment, we usually acquire traces of thousands of breaking monatomic contacts while using different voltage rates. The question is how to compare the resulting break probability distributions. Comparing the average values for individual data sets only reveals a very limited information. A histogram will reveal much more information, but also here we may lose information. The histogram shape will depend on the bin width used to create it; small bins result in more noise and cruder histograms are obtained with larger bins.

We have chosen to plot the *cumulated break probability distribution* for our data. With three break parameters there are as many different distribution types. We will at first focus on the cumulated break-current (CBC) probability distribution, but later we also encounter the cumulated break-voltage (CBV) and the cumulated break-power (CBP) probability distributions.

The CBC probability distribution  $P_{\text{cumu}}$  represents the underlying true distribution, of the probability that a given contact will break before reaching a certain current [19]. From now on we will simply use the acronym CBC(s) instead of writing CBC probability distribution(s) out in full (and similar when we use CBV and CBP).

The CBC for a given data set will be zero ( $P_{\text{cumu}} = 0$ ) until the current reaches the value where the least stable contact breaks. From then it rises stepwise each time the current passes values where contacts break. As the current rises towards infinity (or reaches the maximum break-current for the distribution) the probability will approach 100%, i.e.  $P_{\text{cumu}} = 1$ .

In Fig. 8.2 we illustrate this for a CBC compiled from 85 breaks of monatomic Au contacts.<sup>5</sup> The unit of the probability distribution axis is given as  $P_{\text{cumu}}(I_{\text{break}} < I)$ , indicating the probability that the break-current is smaller than the current  $I$  on the lower axis (similar relations will be used for CBV and CBP).

For this particular CBC the first contact did not break until the current reached above  $75 \mu\text{A}$ . There is in general a clear gap between the bias current<sup>6</sup> and the current where the first contact breaks, but the span up to the current of the last break is even larger. Here a current of  $240 \mu\text{A}$  was needed to disrupt the most stable contact out of the 85.

<sup>5</sup>Since we simply sort the data in ascending order of the break-current, and then calculate the corresponding  $P_{\text{cumu}}$ , we have not operated with any type of uncertainty. The distribution will be more precise when more data are included, but it will not be possible to obtain a perfect match with the true distribution anyway.

<sup>6</sup>The bias of 150 mV corresponds to a current of  $\sim 10 \mu\text{A}$  for a monatomic Au contact.

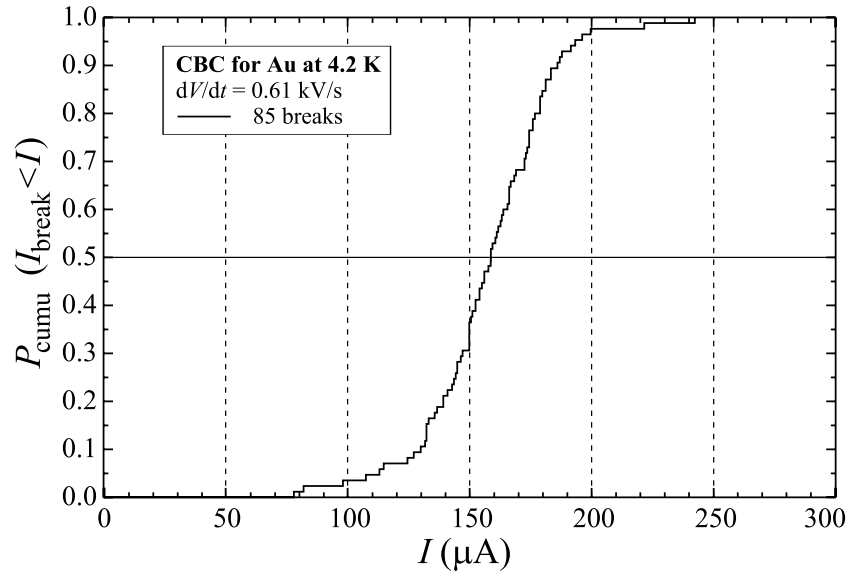


Figure 8.2: Cumulated break-current probability distribution for breaks of 85 monatomic Au contacts formed with the MCBJ at 4.2 K under cryogenic vacuum. The vertical line at  $P_{\text{cumu}} = 0.5$  crosses the CBC at the median break-current  $I_m = 158 \mu\text{A}$ . This value is close to the average break-current for all 85 breaks:  $156 \mu\text{A}$ .

Whereas the minimum and especially the maximum value can be exiting (see the record in Fig. 8.9), it is, however, more interesting to note the steep rise of the CBC between  $130$  and  $185 \mu\text{A}$ . Although the entire range of break-currents span almost  $165 \mu\text{A}$ ,  $80\%$  of the contacts ( $0.1 < P_{\text{cumu}} < 0.9$ ) break in this  $55 \mu\text{A}$  interval. Most contacts break around  $150 \mu\text{A}$ , and the average of all 85 breaks ( $156 \mu\text{A}$ ) is also close to this value.

The horizontal line in Fig. 8.2 indicates the value where half of the contacts have broken ( $P_{\text{cumu}} = 0.5$ ). Here we find that the median current  $I_m = 158 \mu\text{A}$  is close to the value of the average. We will use  $I_m$  rather than the average since it is easy to read directly from a plot of the CBC, and the value is also in general very close to the average.

In Chapter 7 we noted that a current of more than  $150 \mu\text{A}$  through a single Au atom results in an extremely high current density of the order  $2 \text{ GA}/\text{mm}^2$ . Nevertheless, for the CBC in Fig. 8.2 more than half of the 85 monatomic Au contacts have not broken yet at this current.

There seems to be a narrow range of currents where most contacts break, but it is also seen from Fig. 8.2 that the entire break distribution spans over a much broader interval. We need a large amount of data to obtain good statistics, as was also the case with the  $I$ - $V$  curve data in Chapter 7. The measured cumulated break-current probability distribution is taken from the true underlying distribution and it is very likely that 85 breaks is not enough to obtain a good representation.

The CBC in Fig. 8.2 was recorded with a voltage rate  $dV/dt = 0.61$  kV/s. This is the parameter we control and in the next section we investigate the dependence of the voltage rate on the measured cumulated break-current probability distribution.

## 8.5 Dependence on voltage rate

When the voltage increases the contact will be influenced by several different effects. As mentioned in the introduction the atomic bonds will be weakened by the electric field. The increasing current will give rise to electron wind forces and although the electron transport is ballistic, energy will be dissipated, if not in the contact, then in the electrode banks. This can lead to increasing local temperature, depending on how fast the excess energy can be transported away. The total effect of this will be an increased probability that a contact breaks when the voltage increases, and at a certain voltage the break will occur.

By investigating the voltage rate dependence of the cumulated break-current probability distribution we may obtain information that can help us distinguish between the possible effects which can cause the disruptions. Especially integrated effects, like the dissipation of energy, should be clearly visible when different  $dV/dt$  spanning several orders of magnitude are used.

### 8.5.1 Cumulated break-current for gold

It is thus expected that higher voltage rates result in higher break-currents, but this is not at all obvious from the three cumulated break-current probability distributions shown in Fig. 8.3. These have been measured on monatomic Au contacts using three different voltage rates ranging over two orders of magnitude, but no clear dependence is visible. The CBC measured with the fastest rate is at the highest currents most of the time, but the CBC measured with the slowest rate has a different shape than the other two. It switches back and forth between being at highest or lowest break-currents at different  $P_{\text{cumu}}$ . This is surprising since we would expect the lowest voltage rate to result in the lowest break-currents. In all three CBCs less than 100 breaks are included.

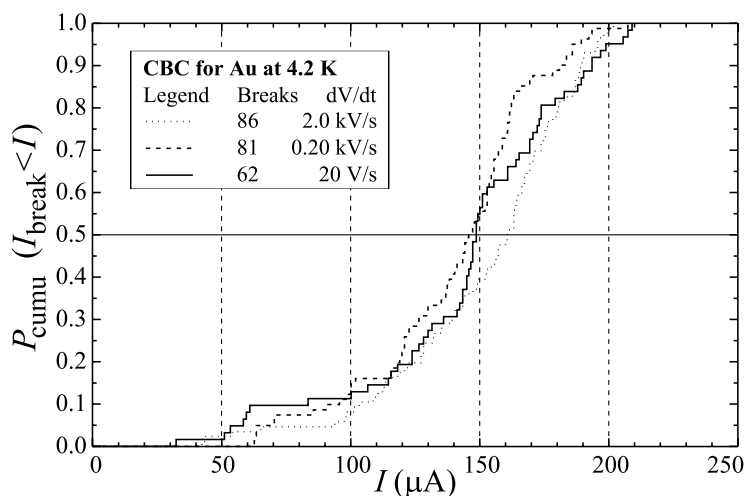


Figure 8.3: Dependence of voltage rate  $dV/dt$  on the cumulated break-current probability distribution for monatomic contacts of Au. The three distributions are recorded in succession on the same sample by breaking monatomic contacts formed at 4.2 K with the MCBJ under cryogenic vacuum.

### 8.5.2 Cumulated break-current for copper

We increased the statistic material in our experiments on Cu to see if this would make the dependence on  $dV/dt$  clearer. In Fig. 8.4a, four cumulated break-current probability distributions, each compiled from breaks of more than 200 monatomic Cu contacts, are shown. Now it seems like there, as expected, is a slight dependence on the voltage rate, which ranges from 14 V/s to 6.5 kV/s. The two probability distributions measured with the fastest rates have higher break-currents than the others for most values of  $P_{\text{cumu}}$ . Within these two groupings, the order is reversed (see for example at  $P_{\text{cumu}} = 0.5$ ), but here the difference in voltage rate is very small (a factor 5), compared to the factor 100 between the groups. It should, however, be noted that the 14 V/s CBC is at the same level of current as the 6.5 kV/s CBC at low  $P_{\text{cumu}}$  (i.e. at low currents).

The Cu data were acquired by measuring 100 breaks at a given  $dV/dt$ , and then changing  $dV/dt$  through the four settings. After 400 breaks a full cycle of data was obtained with 100 breaks for each  $dV/dt$ . About half of these fulfilled the selection criteria and in five cycles we obtained about 250 valid breaks for

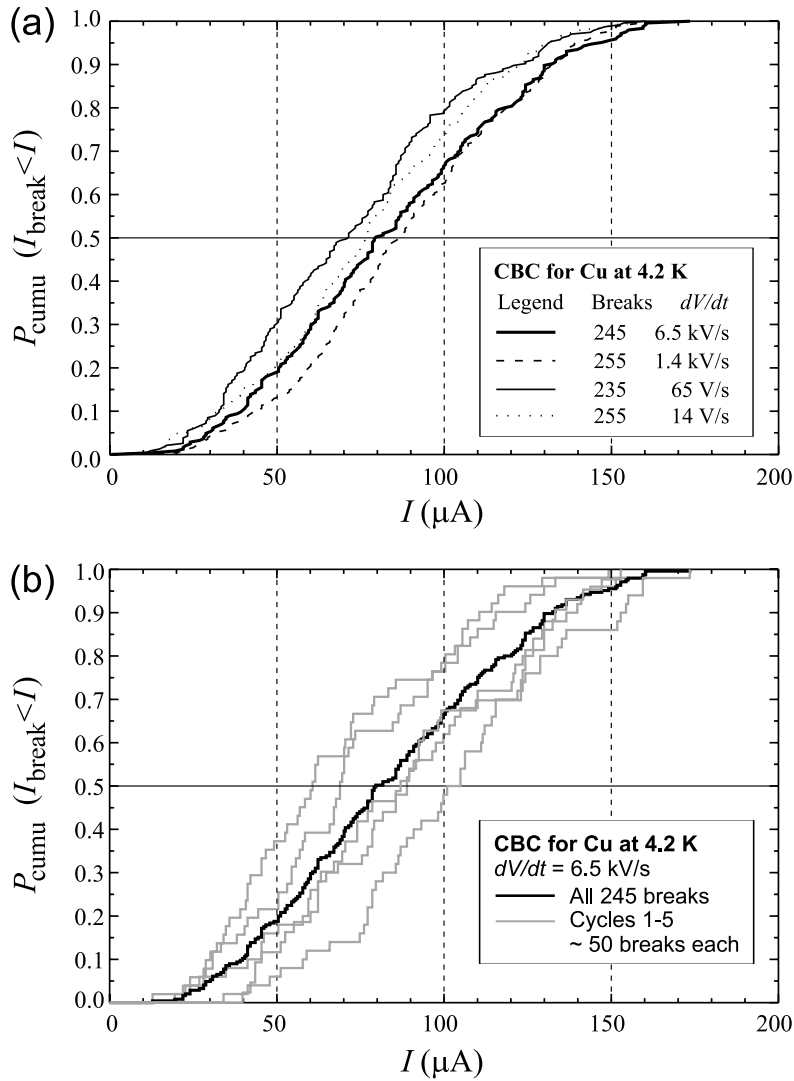


Figure 8.4: (a) Voltage rate dependence of the cumulated break-current probability distribution for Cu. (b) The five individual CBC cycles (grey) recorded at  $dV/dt = 6.5$  kV/s from about 50 breaks each. These are compiled into the thick black solid line, i.e. the 6.5 kV/s CBC from (a) (see text). All data are measured on monatomic contacts formed at 4.2 K under cryogenic vacuum with the MCBJ.

each setting. By using this method we ensured that any changes in the overall behavior of the contacts during the experiment, would affect all four CBCs. This procedure revealed that there are large fluctuations in the CBC over the few hours of the experiment even when identical parameters are used.

To illustrate this, we show in Fig. 8.4b the five probability distributions (grey) obtained from data for each of the individual cycles measured with  $dV/dt = 6.5$  kV/s. The black line represents the combination of these five cycles and this is the 6.5 kV/s CBC already shown in Fig. 8.4a. The five individual cycles do not appear in any general order with regards to the break-current values. We can make this clear by noting that the first cycle as well as the last cycle to be measured are among the three CBCs to the left of the black curve, that is at higher break-currents than the mean value for all five cycles. This indicates that there is no general trend in the changes, and we believe they are caused by random fluctuations in the atomic configuration during the experimental run.

Comparing the two panels in Fig. 8.4, we see that the individual cycles in (b) spread over a broader range than all the four CBCs in (a) although these are measured with very different  $dV/dt$ . Plots of the five individual cycles for the other CBCs display similar behavior. Since there can be so much difference between individual cycles measured at the same  $dV/dt$ , it is clear that there must be another important parameter not affected by  $dV/dt$  which has a large impact on the break-current. This is, however, a parameter that we cannot control directly with our setup: The *atomic configuration*.

The conclusion we draw from the Au and Cu CBCs is that the break-current is affected more by changes in the underlying atomic configuration for the contact than by shifting the voltage rate over the three orders of magnitude spanned by the  $dV/dt$  range used. A new atomic configuration should be obtained each time a new contact is formed by the MCBJ, but there seems to be periods during the experiment where the contacts behave a certain way for some time, and then this can change to a somewhat different behavior later. This is likely to be due to some sort of recurring contact configuration which is not changed when new contact is formed or “burned” away by the high currents.

For the remaining noble metal Ag and for Pt the behavior is very similar to that of Cu. For all these metals there is a slight voltage rate dependence where the CBCs measured with fast  $dV/dt$  are situated at the highest break-currents. In spite of this, we sometimes observe that one of the CBCs measured with a slow voltage rate is situated entirely at higher currents than all the other cumulated break probability distributions measured during that experimental run.

### 8.5.3 Kolmogorov-Smirnov test and STM experiments

We did at one point try to test if two distributions were different [18], by using the Kolmogorov-Smirnov (KS) test [19], which answers the following question:

*Assuming that two distributions are drawn from the same underlying distribution, what is the probability of observing an even worse agreement between the two distributions if the measurements are repeated?*

If the distributions are drawn from the same underlying distribution, this probability should be distributed uniformly between zero and one. The lower the probability is, the worse is the agreement between the two distributions. If it is smaller than 1% it is usually said that the two distributions are different [19].

It is here important to realize, that even though it is possible to say that two distributions are different, it is not possible to go the other way. This is because an infinitely small difference between two distributions can only be discovered with an infinite number of data points [19].

The three cumulated break-voltage probability distributions we used together with this test are shown in Fig. 8.5. It is preliminary experiments measured under UHV with the STM at a temperature of 140–240 K. This temperature is somewhat lower than RT, and was necessary to keep the monatomic contacts stable long enough for the experiments. It is on the other hand a much higher temperature than the 4.2 K of the MCBJ experiments.

Even at this temperature the life time of the ASCs are only microseconds, and much faster frequencies needed to be used (10–100 kHz). This was possible with the STM, since here we do not have the long wires between the current-to-voltage converter and the ASCs, as we do in the MCBJ (see Sec. 5.3). With a burst amplitude of 3 V the voltage rate is of the order MV/s, or V/ $\mu$ s.

Under these different conditions a mean break-voltage  $V_m$  of 1.5 V for the two CBVs recorded with the slow rates and 1.8 V for the CBV recorded with the fastest rate are found from Fig. 8.5. This corresponds to  $I_m = 120$  and  $140 \mu$ A, respectively.

Using the KS test we found that the 1.1 MV/s CBV was different<sup>7</sup> from the other two measured with slower rates [18] (see Fig. 8.5). These two are very similar (78%), but due to the nature of statistics, we can neither say that they

<sup>7</sup>The very small probabilities that the 1.1 MV/s CBV should be the same as the 0.11 MV/s and the 0.25 MV/s CBVs are  $7.5 \cdot 10^{-6}$  and  $3.1 \cdot 10^{-5}$ , respectively.

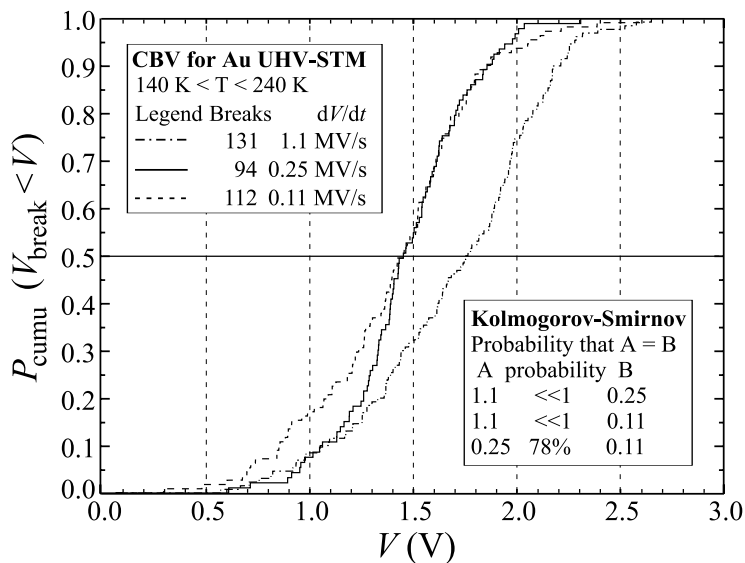


Figure 8.5: Dependence of voltage rate  $dV/dt$  on the cumulated break-voltage probability distribution for monatomic contacts of Au. The three distributions are measured on contacts formed in a UHV-STM in the temperature range 140–240 K. Regarding the KS test see text.

are different nor that they are drawn from the same underlying distribution. At low voltage the 0.25 MV/s CBV is actually closer to the 1.1 MV/s CBV than to the 0.11 MV/s CBV.

With only three cumulated break probability distributions it seemed like a good idea to use the KS test. However, after having measured more than fifty of these and with the above observations in mind it no longer seems like a useful approach. The spread in the CBCs presented above for Au and Cu are so large that we can instantly see that most of them will be deemed different using the KS test. With the huge shift from cycle to cycle observed in Fig. 8.4b, the test is rendered useless for the MCBJ experiments.

This do not necessarily imply that it was useless to use the KS test with CBV obtained in the STM experiment. Here we were in a completely different time regime, and also the elevated temperature could influence the behavior. We will, nevertheless, refrain from using the KS test on the probability distributions obtained from the MCBJ experiments.

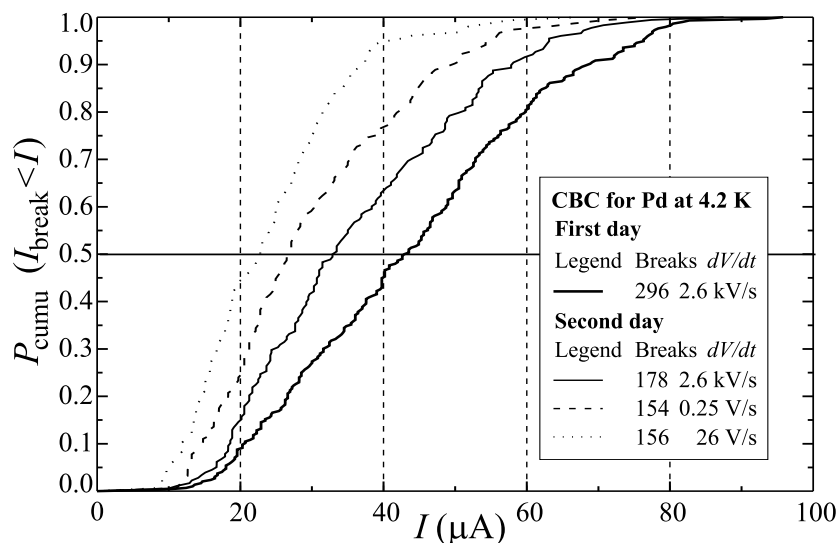


Figure 8.6: Cumulated break-current probability distribution for Pd. The three thin lines display the voltage rate dependence. These data are measured simultaneously like for Cu, with 100 breaks measured for each setting and then changing through the voltage rates completing three cycles in all. Monatomic contacts formed with the MCBJ at 4.2 K under cryogenic vacuum are used. The thick solid line represents a probability distribution obtained using the same  $dV/dt$  as for the thin solid line, but measured the day before.

#### 8.5.4 Cumulated break-current for palladium

Contrary to the noble metals and Pt it seems that the CBCs for the two remaining platinum metals, Pd and Ni, depend more clearly on  $dV/dt$ . They behave very similarly and in Fig. 8.6 we show the cumulated break-current probability distribution for Pd. Focusing at first on the three thin lines, we see a clear dependence on  $dV/dt$ , with the fastest rate giving the CBC at the highest current and *visa versa*, as expected.

This clear interpretation of the data is somewhat distorted when we compare with the thick solid line representing a CBC measured the day before the other three with  $dV/dt = 2.6$  kV/s. This is the same voltage rate as for the thin solid line, but the thick curve is shifted to considerably higher break-currents.

With so much difference from day to day on the same sample, it is difficult to compare the influence of changing other parameters as  $dV/dt$ . A change might be caused by impurities collecting on the sample between the two experiments, but this is unlikely under the low pressure of the cryogenic vacuum. Again it seems that it is the overall atomic configuration that changes.

It is more likely that there has been a shift in the macroscopic electrode configuration, because we also observed the  $dV/dt$  dependence on the first day, only here the CBCs were generally shifted to higher currents. The explanation for this clear voltage rate dependence compared to the noble metals and Pt, can lie in the shorter inelastic scattering length for Pd and Ni compared with the other metals. This means that the ballistic interface region around the contact will be smaller, and this is the region where the energy will be dissipated (see discussion on page 17 in Sec. 2.2). Heating of a small area is also the most likely process to occur on these microsecond to millisecond time scales, compared to the usual picosecond relaxation (phonon) time scale. If we could use higher voltage rates, the effect might become more clear for some of the other metals. It was, however, not possible to use higher voltage rates for the MCBJ experiments as explained in Sec. 5.3.

Although we so far have only presented cumulated break-current probability distributions (for the MCBJ experiments, CBVs in the STM experiment), we have also investigated the cumulated break-voltage and the cumulated break-power  $P_{\text{break}} = I_{\text{break}} \times V_{\text{break}}$ . As for the CBC no clear dependence are observed of the voltage rate on neither the cumulated break-voltage probability distribution nor the cumulated break-power probability distribution (CBV and CBP from now on). For the noble metals, the CBCs and CBVs have very similar shapes because the conductance of the monatomic contacts will always be close to  $1 G_0$ , e.g.  $I \simeq 1 G_0 \times V$ . For the platinum metals the monatomic contact has a higher conductance spanning a wider range of values. The current is, as opposed to the voltage, determined by the conductance, thus in the sections above we decided to use break-current instead of break-voltage to present the experimental results obtained with the MCBJ.

Since the power gives the rate of energy dissipation, we were surprised not to see a more clear effect regarding the voltage rate dependence on the CBP, when  $dV/dt$  was varied over several orders of magnitude. We will return to the implications of this in the discussion, but for now we note that the differences between the individual metals become even more obvious for the break-power than when using the other two parameters. This will be clear in the next section where we compare the three types of cumulated break probability distributions for all six metals.

## 8.6 Comparing the six metals

In the last section we did not mention the clear difference between the ranges of break-currents observed for the different metals. For Au (Fig. 8.2 and 8.3),  $I_m$  is close to  $150 \mu\text{A}$ ,<sup>8</sup> much larger than any of the CBCs measured for Cu, where  $I_m$  ranges from  $60\text{--}100 \mu\text{A}$  (Fig. 8.4). This is again clearly higher than for the Pd CBCs for which  $I_m$  always stays below  $50 \mu\text{A}$  (Fig. 8.6).

Since the voltage rate seems to have a much smaller effect on the cumulated break probability distributions than changes in the atomic configuration, we have included all data from the individual metals disregarding the voltage rate. In this way we obtain a very large statistical material offering a better comparison, less influenced by rare atomic configurations. As the experiments for all metals were performed using a similar range of  $dV/dt$ , we expect that any actual effect of changing the voltage rate will average out.

The cumulated break-current probability distributions for all six metals, obtained from thousands of breaking monatomic contacts, are compared in Fig. 8.7. The extreme stability of Au compared to all the other metals leaps immediately to the eye. For Au,  $I_m = 158 \mu\text{A}$  more than 60% higher than for both Pt and the two noble metals Ag and Cu. These three lie very close having  $I_m$  of 95, 89 and  $82 \mu\text{A}$  with Pt between the two noble metals. This order should be treated with caution, due to the large spread in the break values from one experiment to the next, observed in the previous section. At even lower currents we find the remaining platinum metals Pd and Ni, with almost identical CBCs and  $I_m \simeq 34 \mu\text{A}$  (see Table 8.2).

Although we did not find it necessary to show CBVs and CBPs and instead used CBCs in the last section, it is still interesting to see how the break-voltage and break-power behave among the six metals. In Fig. 8.8 we have plotted (a) the cumulated break-voltage probability distributions (CBVs) and (b) the cumulated break-power probability distributions (CBPs) for all six metals. For the CBVs in (a), the overall behavior is almost the same as for the CBCs in Fig. 8.7. The only obvious difference is for Pt, which is now clearly below all the noble metals due to the higher conductance of monatomic Pt contacts when compared to the conductance of monatomic noble metal contacts. The median break-voltage  $V_m$  for Au is as high as  $2.2 \text{ V}$ ,<sup>8</sup> much higher than for any of the other metals (see Table 8.2).

For the CBPs in Fig. 8.8b, the order of the metals is the same as for the CBVs. Due to the high current and voltage for Au, the difference is, however,

<sup>8</sup>For the RT-UHV-STM experiments, presented in Fig. 8.5, we found that  $I_m$  was  $120\text{--}140 \mu\text{A}$ , clearly lower than at  $4.2 \text{ K}$ , but still higher than for Cu at  $4.2 \text{ K}$ .

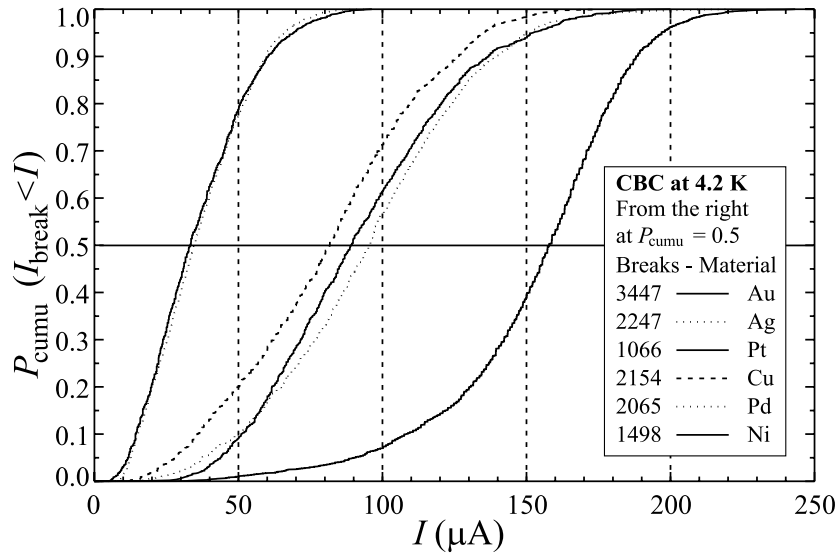


Figure 8.7: Cumulated break-current probability distributions for all six metals. The number of broken monatomic contacts are quoted next to the legend representing the different materials. Note that the same legends have been used more than once, but the metals are cited from the right in the order of highest  $I_m$  indicated by the line at  $P_{\text{cumu}} = 0.5$ . The data for each metal has been measured over several days (for Au and Pt on more than one sample) using the entire  $dV/dt$  range. All data are measured on monatomic contacts formed at 4.2 K under cryogenic vacuum with the MCBJ.

extremely large between Au and the other metals. To enable a more direct comparison of the median values for all the metals we state them in Table 8.2 together with the average break-conductance ( $\langle G_{\text{break}} \rangle$ ) and the total number of breaking contacts. The typical Au contact sustains more than  $350 \mu\text{W}$  without breaking, three times as much as the two other noble metals. The implications of such a high power dissipated in a monatomic contact is discussed in the caption of Fig. 8.9, where the record Au trace is on display. The platinum metals are even further down, again with Pd and Ni at the very bottom with only  $9\text{--}10 \mu\text{W}$ .

In Fig. 8.7 and 8.8 we note a very interesting relation when comparing Au and Pt with the two lighter metals within their own group in the periodic table (cf. Fig. 1.1 on page 5). Although Au is much more stable than any of the other

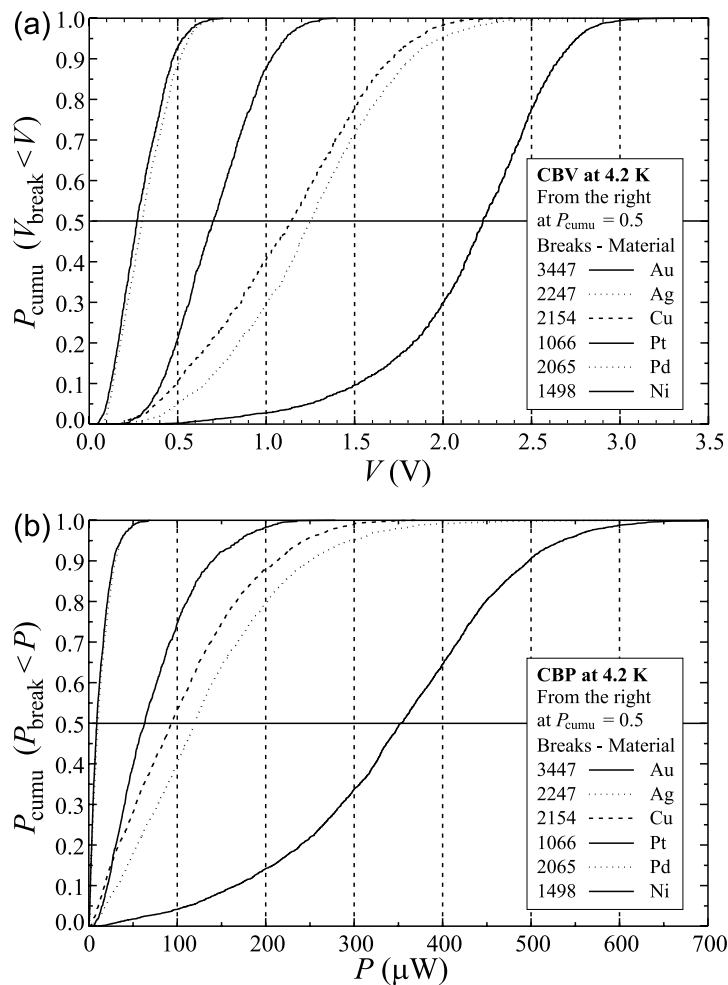


Figure 8.8: (a) Cumulated break-voltage and (b) cumulated break-power probability distributions for all six metals. The number of broken contacts are quoted next to the legend representing the different materials. Note that the same legends have been used more than once, but the metals are cited from the right in the order of highest median break value ( $V_m$  and  $P_m$ ) as indicated by the lines at  $P_{\text{cummu}} = 0.5$ . The data for each metal has been measured over several days (for Au and Pt on more than one sample) using the entire  $dV/dt$  range. All data are measured on monatomic contacts formed at 4.2 K under cryogenic vacuum with the MCBJ.

Metal	$I_m$ ( $\mu\text{A}$ )		$V_m$ (V)		$P_m$ ( $\mu\text{W}$ )		$\langle G_{\text{break}} \rangle$	Breaks
<b>Noble metals</b>								
Au	158	(243)	2.22	(3.47)	353	(809)	0.92 $G_0$	3447
Ag	95	(221)	1.25	(2.93)	119	(648)	0.98 $G_0$	2247
Cu	82	(175)	1.11	(2.39)	103	(372)	0.94 $G_0$	2154
<b>Platinum metals</b>								
Pt	89	(200)	0.70	(1.39)	63	(279)	1.67 $G_0$	1066
Pd	35	(96)	0.30	(0.78)	10	(71)	1.50 $G_0$	2065
Ni	33	(96)	0.27	(0.76)	9	(69)	1.59 $G_0$	1498

Table 8.2: The median value of the break-current, break-voltage and break-power for the six metals. The highest value measured for each metal is given in brackets. The three records for a given metal will not necessarily belong to the same contact, as the conductance changes from contact to contact (see Fig. 8.9). The average break-conductance and number of contact breaks recorded for each metal are also given.

metals, the relation between Au and the remaining noble metals, is similar to that between Pt and the other two platinum metals. Focusing on the break-current we find from Table 8.2 that  $I_m$  for Au is 1.7 (1.9) times higher than for Ag (Cu). In the same way we find that for Pt  $I_m$  is 2.6 times higher than the value for both Pd and Ni. The ratio is bigger for the platinum metals than between the noble metals, but there is a trend. Although Pt breaks at a much lower current than Au, they are both much more stable than their lighter counterparts. We will return to the interpretation of this in the discussion.

In Table 8.2 we also state the average break-conductance  $\langle G_{\text{break}} \rangle$ , which for the noble metals lies slightly below 1  $G_0$ , and for the platinum metals ranges from 1.5–1.7  $G_0$ . It is this higher conductance that causes  $I_m$  for Pt to be similar to  $I_m$  for the two noble metals Ag and Cu, even though  $V_{\text{break}}$  is clearly smallest for Pt.

Several interesting features can be derived. First we note that because of the negative non-linear terms  $G''$  for all the platinum metals monatomic contacts (see Fig. 7.9 on page 135), we would expect a somewhat smaller  $\langle G_{\text{break}} \rangle$  than the corresponding low bias conductance  $G$  of the first histogram peak (see Fig. 4.4 on page 53). This effect should especially be clear for Pt which

actually sustains voltages above 1 V without breaking (maximum 1.39 V). Here the non-linear effects begins to matter due to the proportionality to the voltage squared [cf. Eq. (9.2) on page 186]. Still we find  $G_{\text{break}} = 1.67 G_0$  for Pt, clearly higher than the  $1.5 G_0$  of the first peak for the Pt conductance histogram in Fig. 4.4a on page 53. This is, on the other hand, in accordance with the results presented in the next section, where a shift of the first histogram peak from  $1.5$  to  $1.8 G_0$  is observed when the bias increases past 300 mV (Fig. 9.2 on page 184). The contacts that result in a peak at  $1.8 G_0$  are those that are most stable (i.e. monatomic contacts as opposed to the probably less stable monatomic chains formed by both Au and Pt [20, 21]). It will be these contacts that remain stable up to high voltages where the non-linearity can explain a  $G_{\text{break}}$  of  $1.67 G_0$ , lower than the  $1.8 G_0$  of the histogram peak. Since we avoid chains for both Au and Pt, this explains why there are not enough Pt contacts with a conductance around  $1.5 G_0$  which could have lowered the average conductance further.

For Pd, which has the most non-linear  $I$ - $V$  curves, is the break-conductance lower than the  $1.7 G_0$  of the first, and only, histogram peak (Fig. 4.4b on page 53). The peak for Ni [(c) in the same figure], is too broad for making similar suggestions.

We can instead turn to the noble metals. The monatomic contact should in all cases have a conductance close to  $1 G_0$ , but in general we observed a small down-bending of the  $I$ - $V$  curves ( $G'' < 0$ ) for all the monatomic noble metal contacts. Ag is the most non-linear in this respect, but with the much higher voltages applied to Au contacts before they break, this may explain why Au has the lowest  $\langle G_{\text{break}} \rangle$ . This do, however, not explain why  $\langle G_{\text{break}} \rangle$  is higher for Ag than for Cu. In any case all metals within each group, have the same average break-conductance within the uncertainty (around  $\pm 0.1 G_0$  for the noble metals, and just below  $\pm 0.2 G_0$  for the platinum metals.)

In Fig. 8.9 we show the  $I$ - $V$  curve for the *record* contact, and as expected, Au holds all three records by having the absolute highest break-current, break-voltage and break-power measured on any monatomic contact. There are no challengers among the other five metals as seen from Table 8.2 where all maximum values for the six metals are given in brackets.

In the caption of Fig. 8.9, I ponder on the amazingly huge currents and powers sustained by this monatomic contact. This wonderment is general, since the median values for Au are more than half of the record values. This is by the way one more feature which Au does not share with the other metals and we return to this (i.e. the shape of the CBP), in the discussion (Fig. 8.11).

With a current of  $234 \mu\text{A}$  running through the single Au atom before the contact breaks, the current density reaches  $3.3 \text{ GA}/\text{mm}^2$ , which to our best

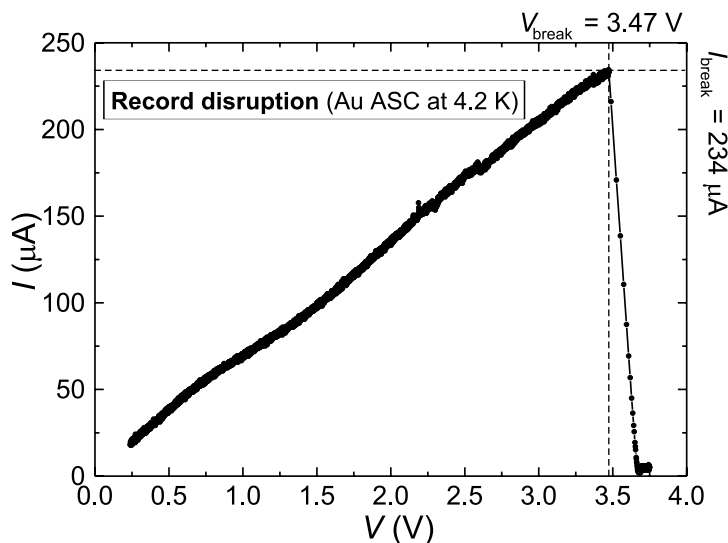


Figure 8.9: **The record!** The  $I$ - $V$  curve on *the* monatomic Au contact that sustained the highest power ( $810 \mu\text{W}$ ) and withstood the highest voltage ( $3.47 \text{ V}$ ) before disrupting. The  $I$ - $V$  curve is measured with  $dV/dt = 9 \text{ kV/s}$  using the MCBJ to form the contact at  $4.2 \text{ K}$  under cryogenic vacuum. Before the break, at a relatively low conductance of  $0.87 G_0$ , the single Au atom carried a current of  $234 \mu\text{A}$  sustaining the highest current density ever measured:  $3.3 \text{ GA/mm}^2$ ! This was, however, not the highest break-current measured, see text. With such a high current we find that almost three electrons must pass through the single open eigenchannel of the atom every other femtosecond. From the power we find that it amounts to  $5 \text{ eV/fs}$ . This is only right before the break occurs, but the  $I$ - $V$  curve is almost linear, so the average power will be half of the maximum i.e.  $400 \mu\text{W}$ . Since the burst last  $\sim 400 \mu\text{s}$ , we find the total energy dissipated during the burst:  $\Delta E \simeq 160 \text{ nJ} = 1 \text{ TeV}$ ! According to the discussion on ballistic electron transport on page 17 in Sec. 2.2, this energy will be dissipated “far away” from the contact atom, in a half sphere with a radius of the mean free path of the electron ( $l_e \simeq 10 \text{ nm}$  for Au). Maybe a longer distance should be used in a calculation of the dissipated energy per atom, so lets say there is one million Au atoms to take part in the local energy dissipation (about three times that in the half sphere volume). Then each atom takes away  $1 \text{ MeV}$ , but does so during  $400 \mu\text{s}$ . If we expect a phonon frequency  $\nu = 10^{12} \text{ s}^{-1}$  (a relaxation time  $\tau = 10^{-12} \text{ s}$ ), the individual atoms will only receive  $2.5 \text{ meV}/\tau$ . It thus seems like it is not the actual heating of individual atoms that causes the final instability. The energy dissipation will, nevertheless, result in a higher local temperature, and together with the high electric field and electron wind forces this will weaken the bond, and a break occurs.

knowledge is the highest current density ever measured.<sup>9</sup> The power of this contact reached an amazing  $810 \mu\text{W}$ , much higher than the second highest with  $727 \mu\text{W}$ . Only four Au contacts reached a power over  $700 \mu\text{W}$  explaining why the scale in Fig. 8.8b stops already here.

The contact in Fig. 8.9 was the only one that came really close to surviving the maximum burst voltage. The reason it survived so long is probably due to a low conductance during the last stages of the break. As can be seen from the curve there is a clear non-linearity around 1 V, where the conductance decreases from about  $1 G_0$  down to around  $0.87 G_0$ .<sup>10</sup> There were a few other contacts with a break-current in the same range but these had a higher conductance and a correspondingly lower break-voltage and break-power. The highest break-current measured was actually  $243 \mu\text{A}$  (cf. Table 8.2). This was, however, on a contact with a conductance slightly above  $1 G_0$ , revealing that at least one other conducting channel was partially open, and we cannot be sure that this current actually runs through a single atom. For the contact in Fig. 8.9 we expect that only one atom with one partially open channel sustains the gigantic current density.

Ag is the only other metal to come even close to  $V_{\text{break}} = 3.0 \text{ V}$ , with  $2.93 \text{ V}$ , and this particular contact also has a high  $I_{\text{break}} = 221 \mu\text{A}$ . Whereas the Au record trace, only holds two of the records, this Ag trace takes all three Ag records. The  $I$ - $V$  curve was almost linear, with a conductance staying close to  $0.96 G_0$  until the break. The break-power of  $648 \mu\text{W}$  stands out for Ag, since the second highest only had a power of  $558 \mu\text{W}$ , and only five traces made it above  $500 \mu\text{W}$ . Both Au and Ag records show how one in 2000–3000 contacts can suddenly be much more stable, and indicates how difficult it will be to obtain a good description of the entire underlying distribution

## 8.7 Simple model

In order to obtain a better understanding of the cumulated break probability distribution we have developed a simple model for voltage-induced disruptions.<sup>11</sup> As we shall see below, voltage is chosen over current because it is a parameter we can control directly.

---

<sup>9</sup>Previously,  $80 \mu\text{A}$  was measured through monatomic Au chains at 4.2 K [1] and recently  $155 \mu\text{A}$  were observed for ASCs, also formed at 4.2 K [11]. (In the similar experiments we performed, using the STM at a temperature of 140–240 K the maximum current observed was  $190 \mu\text{A}$  [18].

<sup>10</sup>Since this transition occurs smoothly, the trace qualifies through our selection criteria.

<sup>11</sup>The model was put forward in collaboration with Mads Brandbyge and Kim Hansen.

### 8.7.1 Basic assumptions

The model is not fully developed yet, but the basic assumptions are as follows:

#### Arrhenius rate in the harmonic approximation

Since the contact breaks occur on an experimental time scale of microseconds or millisecond and the atomic vibrations occur on a time scale of picoseconds, we are in a rare event regime, where the contact breaking process can be considered an activated process, parameterized by the barrier height  $U$  and attempt frequency  $\nu$ . The contact break rate  $R$  is then given by the Arrhenius form

$$R = \nu \exp(-U/kT), \quad (8.1)$$

where  $T$  is the contact temperature and  $k$  is Boltzmann's constant. The attempt frequency  $\nu$  is determined by the curvature of the local minimum of the equipotential surface of the contact geometry. In the harmonic approximation,  $\nu$  will be independent of temperature. For simplicity, we assume this is the case. We expect that  $\nu$  will be of the order of the phonon frequency  $\sim 10^{12} \text{ s}^{-1}$ .

#### Activation energy independent of contact geometry

A new contact is formed prior to each voltage-induced disruption experiment. Thus, the cumulated break-voltage probability distribution (CBV) which is found for a given contact material at a given  $dV/dt$  originates from a large ensemble of different contact geometries, corresponding to an ensemble of different activation energy barriers.

We have no knowledge of the distribution of activation energies, and will neglect this spread in the model. This simplification is probably the most severe restriction of the model, since our results indicate a large effect of different geometries. It is nevertheless included in order to keep the number of free parameters in the model at a minimum.

#### Activation energy is voltage dependent

The activation energy changes at finite bias due to electrostatic forces, electron wind forces and changes in the electronic structure. Most likely, these physical effects cause the activation energy to lower with increased bias. Most breaks occur around the median break-voltage, so we will use this voltage as the reference point. For convenience, we change the nomenclature from  $V_m$  to  $V_0$  and

let this be the median break-voltage for a given contact material. For voltages  $V$  close to  $V_0$ ,  $U(V)$  can therefore be written as

$$U(V) = U_0 - \gamma e (V - V_0) , \quad (8.2)$$

where  $U_0 \equiv U(V_0)$ ,  $e$  is the electron charge and  $\gamma$  is a (probably  $> 0$ ) coefficient, which describes how fast the activation energy lowers with voltage near  $V_0$ .

### Quasi-thermal equilibrium

The contact temperature  $T$  depends on the power dissipated in the contact region and thus on the voltage. If the voltage changes on a time scale, which is comparable to the relaxation time for obtaining thermal equilibrium,  $T(V)$  will depend not only on the voltage at time  $t$ , but also on the voltage at all previous times  $t' < t$ , i.e.,  $T(V) = T[V(t - t')]$ . Here we will assume that  $dV/dt$  is so small that the contact is in quasi-thermal equilibrium. That is,  $T(V) = T[V(t)]$ . This approximation is in agreement with the lacking dependence of the CBP on the voltage rate (at least for Au). If the temperature was increasing slower than  $dV/dt$  the break-power would be highly dependent on the rate.

The temperature increases with increasing voltage and for voltages close to  $V_0$ , we have to first order in  $V - V_0$

$$kT(V) = kT_0 + \alpha e (V - V_0) . \quad (8.3)$$

Here  $T_0 \equiv T(V_0)$ , and  $\alpha > 0$  is a coefficient, which describes how fast the temperature increases with voltage around the median break-voltage.  $T_0$  increases with increasing ambient temperature  $T_{\text{amb}}$ .

### Time-dependence of applied voltage

Let  $P(t)$  be the accumulated break-voltage probability at time  $t$ , and no contacts have broken at time  $t = 0$

$$P(0) = 0 . \quad (8.4)$$

Hereafter, a linear voltage ramp is applied to the contact

$$V(t) = (dV/dt) t . \quad (8.5)$$

In the experiments we actually have  $V(t) = V_{\text{bias}} + (dV/dt) t$ , but since we observe for most materials, especially Au, that there is a voltage gap between

$V_{\text{bias}}$  and the voltage at which the first contact breaks,  $V_{\text{bias}}$  can be ignored. For Au the first break occurs at 400 mV compared to a bias of 150 mV. For the other noble metals and in part Pt this assumption also holds. For Ni and Pd, the first break occurs at the bias voltage and we can not use this simplification for these two platinum metals (cf. Fig. 8.8a).

### 8.7.2 Solution to model

With the above assumptions and simplifications we now get the break rate as a function of voltage:

$$R(V) = \nu e^{-U(V)/kT(V)}. \quad (8.6)$$

We find the probability  $P$  for breaking by solving

$$\frac{dP}{dt} = R(V) (1 - P(V)), \quad (8.7)$$

and get the full solution:

$$P(V) = 1 - \exp\left(-\left(\frac{dV}{dt}\right)^{-1} \int_0^V R(V') dV'\right) \quad (8.8)$$

### Analytic solution to model

We cannot solve Eq. (8.8) easily because  $R$  has a complicated time dependence. Instead we Taylor-expand the exponent in  $R(V)$  to first order in time (or voltage),

$$-\frac{U(V)}{kT(V)} \approx -\frac{U_0}{kT_0} + \Lambda \frac{e(V - V_0)}{kT_0} \quad (8.9)$$

where we have introduced the dimensionless

$$\Lambda = \gamma + \frac{U_0}{kT_0} \alpha, \quad (8.10)$$

which describes the combined effect of barrier lowering and heating with voltage. We expand around a voltage, where the break rate is within the experimental window of the order  $R \sim 1000 \text{ s}^{-1}$ . With the prefactor  $\nu$  of the order  $10^{12} \text{ s}^{-1}$ , the fraction  $U_0/kT_0 \simeq 30$ . Finally we obtain the solution,

$$P(V) = 1 - e^{-f(V)} \quad (8.11)$$

$$f(V) = \frac{\nu kT_0}{(dV/dt) \Lambda e} e^{-\frac{U_0 + \Lambda e V_0}{kT_0}} \left( e^{\Lambda e V/kT_0} - 1 \right) \quad (8.12)$$

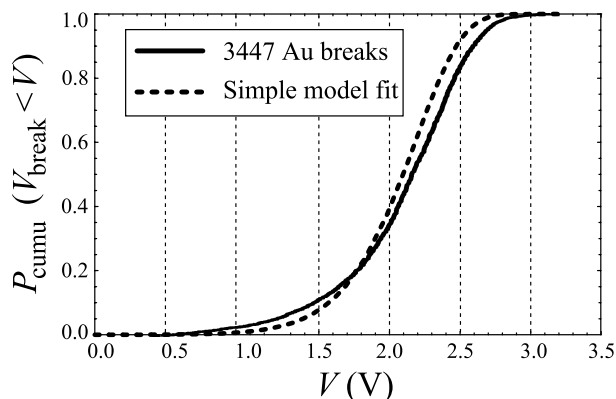


Figure 8.10: Fitting the full solution of the simple model Eq. (8.8) to the CBV obtained from 3447 Au breaks (see Fig. 8.8a). The fitting parameters are stated in Table 8.3. (Adapted from figure provided by Mads Brandbyge).

$\nu$ ( $s^{-1}$ )	$\frac{dV}{dt}$ ( $\frac{kV}{s}$ )	$kT_0$ (eV)	$U_0$ (eV)	$\alpha$	$\gamma$	$\Lambda$
$10^{12}$	1.6	0.032	0.92	0.0055	0.030	0.19

Table 8.3: Fitting parameters for the fit shown in Fig. 8.10, of the full solution of the simple model Eq. (8.8) to the CBV for Au (Fig. 8.8a). The first two are fixed, the next four are free, and finally  $\Lambda$  is found from Eq. (8.10).

### 8.7.3 Fitting to real data

We have in Fig. 8.10 used the full solution to the simple model Eq. (8.8) to obtain a fairly successful fit to the CBV with all the Au data from Fig. 8.8a, but without taking the different  $dV/dt$  into account.

There is, however, a serious problem with the model as it stands. There are too many free parameters (all fitting parameters are shown in Table 8.3), and it is possible to obtain good fits with many different values of the fitting parameters since they are not independent. We are still working on a method to test the model in greater detail. In this way we hope to find out what to expect from these parameters. Next step will be a more complicated model with less dependence on the parameters, and even more important, a model that takes the large ensemble of different contact geometries into account.

## 8.8 Discussion

From our experiments we can rule out that the break is caused by integrated effects, like the dissipation of energy during the entire burst. Especially because we did not find any  $dV/dt$  dependence on the CBP. The power is proportional to the rate of energy dissipation, and the total amount of dissipated energy would seem to be an important parameter for the break. The slower the voltage rate the more energy will be dissipated before the burst reaches a given current, and this energy would increase the temperature considerably in the entire ballistic contact area, if the rate is slow. The voltage rate spanned at least three orders of magnitude, so why did we then not see any clear effect on the CBP?

Here we should note that the contacts seem unaffected by the constant bias applied before the burst. Although the temperature rises a little due to the bias, it must settle at an equilibrium value where the contact is still very stable. It is hence not the total dissipated energy, but the total extra energy available for increasing the temperature that is important. This is not possible to find directly, but since there is no dependence on the voltage rate, it seems that the equilibrium is reached on a time scale much faster than the burst time. This implies that the temperature does not depend on the history of the voltage, but only on the instantaneous voltage. This means that the contact is in quasi-thermal equilibrium as we indeed assumed in our simple model.

The model disregards one of the most important findings from our disruption experiments: The discovery of a huge dependence on the contact geometry.

As we showed in Fig. 8.4b the CBC can change considerably even for the exact same experiment, and in Fig. 8.6 we show how much the CBC can change from day to day on the same sample.

For a given contact geometry there must be a certain energy barrier that has to be overcome in order for the break to occur. When the voltage rises, there will be more energy available from the increasing temperature. The barrier may also be lowered due to the electric field and electron wind forces. As described in the model, there is an attempt frequency, with which the contact tries to break. As this is very high ( $10^{12} \text{ s}^{-1}$ ), the contact will break immediately when a certain voltage limit is reached. This will then be independent of the voltage rate, but highly dependent on the contact geometry. If, however, the contact is *not* in quasi-thermal equilibrium this may not hold, as a huge effect on the voltage rate could then exist. This is possibly what we observe in the Pd and Ni data (Fig. 8.6).

There may also be some dependence on the ambient temperature, as this will contribute to the available energy. This is in accordance with our STM

experiments which we performed at 140–240 K [18]. Here the median break-voltage for Au was around 1.5 V much lower than the 2.2 V we find at 4.2 K. It would be interesting to make experiments at elevated temperature in the MCBJ (i.e. 10–100 K), but care should be taken regarding possible impurities released by increasing the temperature.

Although these observations are very important the comparison of the noble metals with the platinum metals is even more interesting. For the neighbor atoms from each group,<sup>12</sup> we find that  $I_m$  for the noble metal is double or even triple that of the platinum metals<sup>13</sup> (see Table 8.2). This is most likely related to the difference in electronic structure. The simple electronic structure of the noble metals resulted in linear  $I$ - $V$  curves as presented in Chapter 7. The single almost completely open transmission eigenchannel is mainly of  $s$  character, and the conductance is independent of the voltage. For Pt the  $d$  electrons also contributed to several partially open and voltage dependent channels. As the voltage increases the contribution to the conductance from the  $d$  channels decreases. This may result in a less stable bonding, explaining why the platinum metals break at lower conductances than their noble metal neighbor.<sup>12</sup>

Especially Au is able to sustain large currents, even when compared to the other noble metals. It is, however, very interesting that Pt also sustains much higher currents than the remaining platinum metals. Pt is actually more stable compared to Pd and Ni (2.6 times higher  $I_m$ ) than Au compared to Ag and Cu (1.7 and 1.9 times higher  $I_m$ , respectively). It seems that within their own groups<sup>12</sup> Au and Pt behave similarly compared to the other group members.

This is not the only thing that Au and Pt have in common. Both metals can form monatomic chains and their surfaces reconstruct in the same way. [See an example of the Au(111) “herringbone” reconstruction in Fig. 3.4 on page 34]. These two effects have been related [21] (see discussion on page 99 in Sec. 6.7.2), and none of the other metals form either chains or display surface reconstructions [21]. The ability to form chains should in general also indicate a higher stability of the monatomic contact.

A final feature to discuss is the shape of the cumulated break probability distributions. In Fig. 8.7 it is clear that the shape of the Pt CBC is not the same as for Cu and Ag. This is most clearly seen when comparing with Ag. At the median, the Ag probability distribution is at highest current, but below  $P_{\text{cumu}} = 0.1$  and above  $P_{\text{cumu}} = 0.9$ , it is the Pt probability distribution which is at the highest current.

<sup>12</sup>See Fig. 1.1 on page 5 for the definitions of these relations.

<sup>13</sup>We are aware that the break-current for Pt is of the same order as Ag and Cu. These should instead be compared to Pd and Ni, respectively.

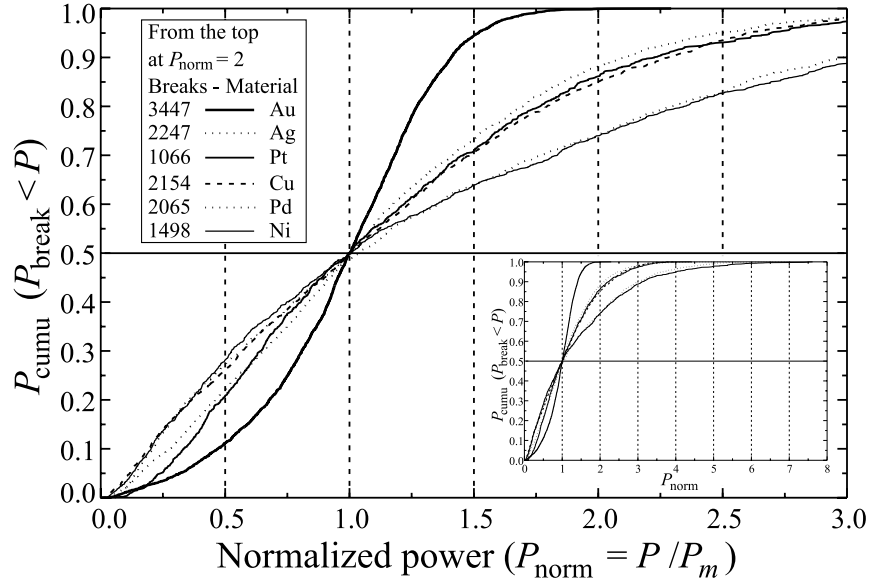


Figure 8.11: Cumulated break-power for all metals vs the normalized power  $P_{\text{norm}}$  given by Eq. (8.13). All curves will by definition go through the point  $(1.0, 0.5)$ . The number of broken contacts are quoted next to the legend representing the different materials. Note that the same legends have been used more than once, but the metals are cited in decreasing order of  $P_{\text{cumu}}$  at  $P_{\text{norm}} = 2$ . The inset zooms out to where the last curve for Ni reaches  $P_{\text{cumu}} = 1$  (at  $P_{\text{norm}} = 7.7$ ). All data are measured on monatomic contacts formed at 4.2 K under cryogenic vacuum with the MCBJ.

In an effort to investigate the shape further we have tried to normalize the break-power from the CBPs in Fig. 8.8b. The CBP is chosen over the other two, due to the huge differences observed between the metals, especially with regard to the huge break-powers for Au. We obtain the normalized power  $P_{\text{norm}}$  by dividing the power  $P$  with the median value of the break-power  $P_m$ :

$$P_{\text{norm}} \equiv P/P_m. \quad (8.13)$$

From this definition the CBP will always reach 0.5 at  $P_{\text{norm}} = 1$ . This can be seen from the graph in Fig. 8.11, where the cumulated break-power probability distribution vs  $P_{\text{norm}}$  is plotted for the six metals. Again Au stands out;

this time as the only metal where  $P_{\text{cumu}}$  reaches 1.0 already at  $P_{\text{norm}} \simeq 2$ . This means that the median break-power lies halfway between the maximum and the minimum break-power of the Au contacts. The other noble metals and Pt only reaches  $P_{\text{cumu}} = 1$  at four times the value of  $P_m$ , and for Pd and Ni, the highest break-power is almost eight times higher than  $P_m$  as seen from the inset of Fig. 8.11, where a zoom-out is presented.

Having a CBP distribution, where  $P_{\text{cumu}} = 1$  is not reached until powers many times higher than the median value, indicates that most contacts are unstable, and will break at a low power compared to a few very stable contacts sustaining much higher powers before breaking. For Au there is almost no unstable contacts, so even the most stable contacts are, relatively seen, not so much different from the others. This is not the case for Ag, Cu and Pt, and especially not for Pd and Ni.

In passing we mention that whereas the normalized Ag and Pt CBP follow each other both below and above  $P_{\text{cumu}} = 0.5$ , the Cu CBP first follows Pd and Ni below, and then switches to follow the other two above. This is a very interesting and yet unexplained feature.

## 8.9 Conclusion

In general, we have reached several interesting conclusions from our experiments with current-induced disruptions of monatomic contacts.

Firstly we found that the cumulated break-current probability distribution for Au is almost independent of the voltage rate, and the same is more or less seen for the other noble metals as well as for Pt. For the two remaining noble metals, there seems to be some  $dV/dt$  dependence but it is uncertain whether the results are actually caused by the changing  $dV/dt$ .

Secondly we found that the most important parameter regarding the influence on the measured cumulated break probability distributions is the atomic configuration. We have seen this both from sample to sample, day to day, and even between individual cycles in the measurement. Most often the effect of these changes is much stronger than a possible voltage rate dependence, except for some cases with Pd and Ni.

Thirdly we found that there are huge differences between the stability towards current between the individual metals. Au sustains by far the highest current densities, amongst other leading to the record described in Fig. 8.9. Especially when the CBPs are compared, will the increased stability of Au stand out. But also the shape of the CBP is clearly different for Au compared

to the other metals. Au is the only metal for which an equal amount of contacts break at currents above and below the median values. In the case of the least stable metals Pd and especially Ni the highest break values are almost eight times higher than the median, indicating very skew CBPs.

Last but not least we have approached the experimental results with a simple “toy” model. The model fits the CBV for Au nicely, but it needs several improvements before we can obtain useful information from the obtained fitting parameters.

There are, however, still many loose ends and it will be difficult to obtain much more information from this type of experiments as long as we have no control over the contact geometry. Right now the most likely method to reach a better understanding of the breaks will come from an extended model which include a full ensemble of different atomic configurations as a parameter in the fit.

The stability of ASCs will continue to be a very important issue to address and understand before we can use them successfully as interconnects in electrical devices.

## References

- [1] A. I. Yanson, G. R. Bollinger, H. E. van den Brom, N. Agraït, and J. M. van Ruitenbeek, "Formation and manipulation of a metallic wire of single gold atoms," *Nature* **395**, 783–785 (1998).
- [2] H. Yasuda and A. Sakai, "Conductance of atomic-scale gold contacts under high-bias voltages," *Phys. Rev. B* **56**, 1069–1072 (1997).
- [3] K. Itakura, K. Yuki, S. Kurokawa, H. Yasuda, and A. Sakai, "Bias dependence of the conductance of Au nanocontacts," *Phys. Rev. B* **60**, 11163–11170 (1999).
- [4] K. Yuki, A. Enomoto, and A. Sakai, "Bias-dependence of the conductance of Au nanocontacts at 4 K," *Appl. Surf. Sci.* **169–170**, 489–492 (2001).
- [5] K. Yuki, S. Kurokawa, and A. Sakai, "Quantized Conductance in Pt Nanocontacts," *Jpn. J. of Appl. Phys.* **39**, 4593–4595 (2000).
- [6] T. N. Todorov, J. Hoekstra, and A. P. Sutton, "Current-Induced Embrittlement of Atomic Wires," *Phys. Rev. Lett.* **86**, 3606–3609 (2001).
- [7] T. N. Todorov, J. Hoekstra, and A. P. Sutton, "Current-induced forces in atomic-scale conductors," *Philos. Mag. B* **80**, 421–455 (2000).
- [8] T. N. Todorov, "Tight-binding simulation of current-carrying nanostructures," *J. Phys. Cond. Matt.* **14**, 3049–30842 (2002).
- [9] M. Rokni and Y. Levinson, "Joule heat in point contacts," *Phys. Rev. B* **52**, 1882–1889 (1995).
- [10] T. N. Todorov, "Local heating in ballistic atomic-scale contacts," *Philos. Mag. B* **77**, 965–973 (1998).
- [11] N. Agraït, C. Untiedt, G. Rubio-Bollinger, and S. Vieira, "Onset of Energy Dissipation in Ballistic Atomic Wires," *Phys. Rev. Lett.* **88**, 216803 (2002).
- [12] R. de Picciotto, H. L. Stormer, L. N. Pfeiffer, K. W. Baldwin, and K. W. West, "Four-terminal resistance of ballistic quantum wire," *Nature* **411**, 51–54 (2001).
- [13] G. Rubio, N. Agraït, and S. Vieira, "Atomic-Sized Metallic Contacts: Mechanical Properties and Electronic Transport," *Phys. Rev. Lett.* **76**, 2302–2305 (1996).

- 
- [14] G. Rubio-Bollinger, S. R. Bahn, N. Agraït, K. W. Jacobsen, and S. Vieira, “Mechanical Properties and Formation Mechanisms of a Wire of Single Gold Atoms,” *Phys. Rev. Lett.* **87**, 026101 (2001).
- [15] T. N. Todorov, “Calculation of the residual resistivity of three-dimensional quantum wires,” *Phys. Rev. B* **54**, 5801–5813 (1996).
- [16] H. Mehrez and S. Ciraci, “Yielding and fracture mechanisms of nanowires,” *Phys. Rev. B* **56**, 12632–12642 (1997).
- [17] O. Y. Kolesnychenko, A. J. Toonen, O. I. Shklyarevskii, and H. van Kempen, “Millisecond dynamics of thermal expansion of mechanically controllable break junction electrodes studied in the tunneling regime,” *Appl. Phys. Lett.* **79**, 2707–2709 (2001).
- [18] K. Hansen, “Electrical Properties of Atomic-Sized Metal Contacts,” PhD thesis, University of Aarhus, 2000. (Can be downloaded from <http://www.ifa.au.dk/~kimh/pdf/thesis.pdf>).
- [19] W. H. Press, B. P. Flannery, S. A. Teukolsky, and W. T. Vetterling, *Numerical Recipes in Pascal* (Cambridge University Press, Cambridge, 1989).
- [20] S. R. Bahn and K. W. Jacobsen, “Chain Formation of Metal Atoms,” *Phys. Rev. Lett.* **87**, 266101 (2001).
- [21] R. H. M. Smit, C. Untiedt, A. I. Yanson, and J. M. van Ruitenbeek, “Common Origin for Surface Reconstruction and the Formation of Chains of Metal Atoms,” *Phys. Rev. Lett.* **87**, 266102 (2001).

## Chapter 9

# Bias Dependence of Platinum Histograms

We have previously only focused on current-voltage ( $I$ - $V$ ) curves of atomic sized contacts (ASCs) where fast changing currents are used to obtain the results. The first experiments on ASCs were, however, performed while applying a constant bias. The interest in ASCs began with the observation of quantized conductance of gold (Au) [1, 2] which is best observed in *conductance histograms* [3]. In Chapter 4, general examples of conductance histograms for the noble and the platinum metals can be found together with a description of the concept of conductance histograms. (From now on we will write histograms, if there is no risk of confusion, see later sections). The bias is constant while measuring individual histograms, but the effect of measuring at different bias has been investigated [4–9]. For platinum (Pt) the position of the first peak in the histogram is bias-dependent [7–9].

In this chapter, based on paper [VI], we will use the mechanically controllable break-junction (MCBJ) (see Sec. 3.3) to investigate the bias dependence of Pt histograms, measured on thousands of ASCs formed at liquid helium (He) temperature (4.2 K) in a ultra-clean cryogenic vacuum environment. A small but significant shift in the position of the first histogram peak from 1.5 to 1.8  $G_0$ <sup>1</sup> is observed when the bias increases past 300 mV. The shift is surprisingly in the opposite direction of what would have been expected from the Pt  $I$ - $V$  curves presented in Chapter 7. This indicates that the shift is not caused by

---

<sup>1</sup>The fundamental unit of conductance  $G_0$  is defined in Eq. (2.3) on page 15.

an electronic effect. We will present evidence that the shift marks a geometric transition point where monatomic chains are replaced by monatomic contacts.

## 9.1 Introduction

Several reports of the bias dependence of histograms have been published [4–9]; both Au [4–7], Pt [7–9] and other transition metals [9] have been investigated. In the individual Pt experiment, the maximum applied bias voltage ranges from below 300 mV [7] to above 1 V [8]. We begin, in Fig. 9.1, from the other end of the voltage-scale, by presenting a Pt histogram obtained at a low bias of 10 mV. This particular histogram is compiled from 3000 conductance traces of *breaking* ASCs obtained with the MCBJ at 4.2 K under cryogenic vacuum.

In [8], the maximum bias used was 1.2 V. Increasing the bias to 1.4 V resulted in the complete disappearance of the remaining structure of the histogram; a peak at  $1.7 G_0$ . This is in agreement with our current-induced disruptions in Chapter 8. Here we found that half of the monatomic Pt contacts had broken already at 0.7 V, and out of the total 1066 measured breaks of monatomic Pt contacts, only the most stable reached a voltage close to 1.4 V before breaking (see Table 8.2 on page 166). The missing peaks indicate that at these high biases the ASCs will break faster than the relaxation time of the experimental setup, but even with our fast changing currents and at 4.2 K vs RT did we not observe ASC of Pt surviving more than 1.4 V!

In Chapter 6, we described how the controversy between bias-independent peak positions in Au histograms [4–6] and non-linear current-voltage curves observed for Au [10–15] encouraged us to measure  $I$ - $V$  curves, confirming the bias-independent peak positions by showing that  $I$ - $V$  curves of Au ASCs indeed are linear.

For Pt, on the other hand, some controversy regarding the bias dependence has arisen. In experiments where the ASCs were encapsulated in an atmosphere of nitrogen ( $N_2$ ) with 5% hydrogen ( $H_2$ ) at room temperature (RT), a peak at  $1 G_0$  were observed at low bias [8, 9]. At higher bias (600 mV) this peak was replaced with a new peak centered around  $1.7 G_0$  [8, 9] (see footnote 7 on page 101). As described in Sec. 6.7.3, the presence of hydrogen changes the position of the first peak from around  $1.5 G_0$  to  $1 G_0$  [16]. For experiments performed with the MCBJ at 4.2 K under cryogenic vacuum the first peak was centered at conductances above  $1.4 G_0$  for all biases [7]. Here a clear shift in the position of the first histogram peak towards higher conductances, was observed when the bias increased above 200 mV [7].

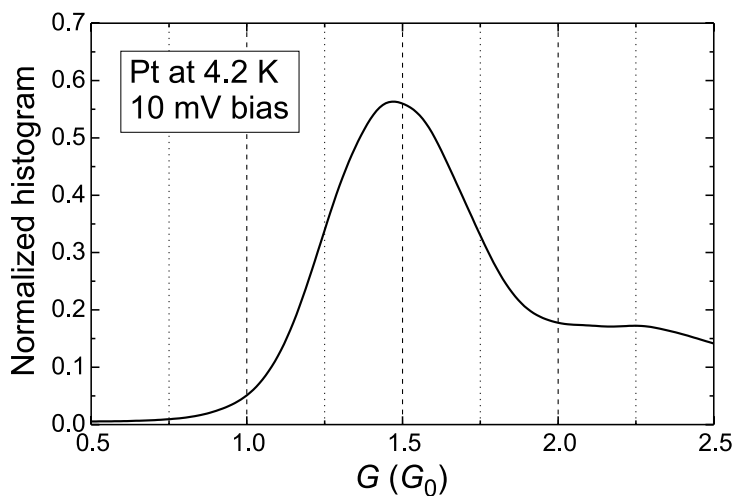


Figure 9.1: Pt conductance histogram recorded at a low bias of 10 mV, from 3000 conductance traces of *breaking* ASCs, obtained with the MCBJ at 4.2 K under cryogenic vacuum.

## 9.2 Bias-dependent histograms

We only focus on the first peak in the histograms, as can be seen from the 10 mV bias Pt histogram in Fig. 9.1. The peak is very broad and centered close to a conductance  $G = 1.5 G_0$ . When increasing the bias above 10 mV the peak remains at  $1.5 G_0$  up to 200 mV. However, when the bias increases even further, the shape of the histogram clearly changes, as seen in Fig. 9.2a where we show four histograms measured while the bias increases from 100–400 mV.

Whereas the 100 and 200 mV histograms are similar to the 10 mV histogram from Fig. 9.1, we find that the main part of the histogram peak at 300 mV is now centered at  $1.8 G_0$  although a broad shoulder is seen around  $1.5 G_0$ . At 400 mV, the shoulder has disappeared and the peak center has completely moved from  $1.5$  to  $1.8 G_0$ . At the same time the peak intensity decreases considerably relative to the that of the 100 and 200 mV histogram peaks. In the 200 mV histogram, the peak is slightly smaller than the 100 mV histogram peak, but this effect is much less pronounced than the shift seen in the higher bias histograms. The first peak

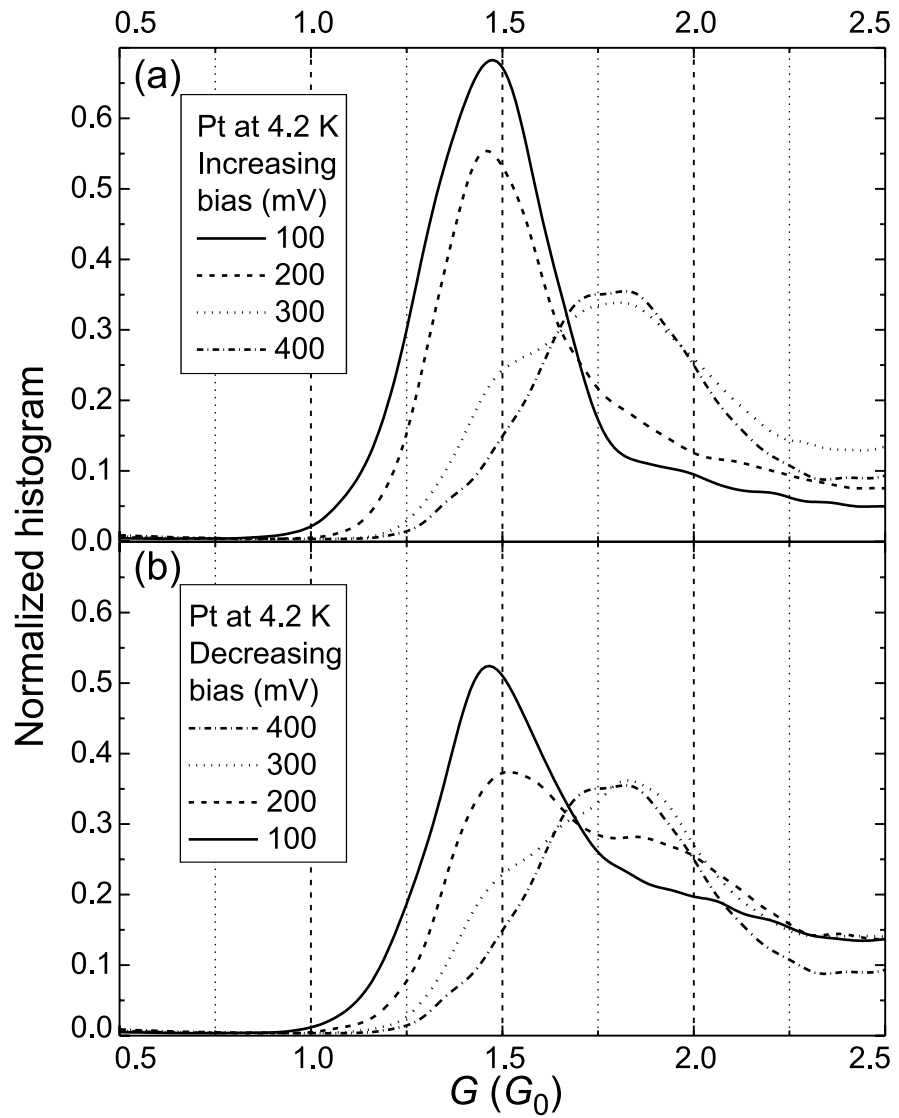


Figure 9.2: Bias dependence of Pt conductance histograms measured in succession on the same sample. Each of these are compiled from 2000 conductance traces of *breaking* ASCs obtained with the MCBJ under cryogenic vacuum at 4.2 K. The bias increases from 100 to 400 mV (a) and decreases back again (b) in 100 mV steps. The same 400 mV histogram is repeated in both graphs.

for these two histograms has, on the other hand, approximately the same size

By lowering the bias back to 100 mV we test if the process is reversible. The resulting histograms are shown in Fig. 9.2b and should be directly comparable to those in Fig. 9.2a, since all seven histograms (the 400 mV histogram is repeated in both figures) are measured in succession under the exact same experimental conditions, except for the bias. It is, however, not always possible to compare the size of the peaks directly due to the normalization of the histograms (see discussion at the end of Sec. 4.1).

The 300 mV histograms are very similar, but at 200 mV some differences are observed between the two histograms. The peak at  $1.5 G_0$  has reappeared, but it is now relatively smaller and there is still a broad shoulder around  $1.8 G_0$ . At 100 mV the shoulder disappears, but there is an increased intensity at higher conductances, and the peak is lower than before the 400 mV bias was applied. This indicates some kind of hysteresis, as the histograms return to the original shape when measured again after about an hour at low bias.

Most of the time, the measured histograms look similar to those in Fig. 9.2, although the exact peak position before and after the high bias changes a few per cent between experiments.<sup>2</sup> We do, however, on a few occasions encounter ASCs with a different behavior. For these contacts the first histogram peak is centered close to  $2 G_0$ , independent of the bias. After measuring several histograms on such contacts, they can suddenly change and again produce histograms with the “normal” shape like in Fig. 9.2. All of the above-mentioned observations will be treated further in the discussion.

### 9.3 Comparison with current-voltage curves

We took up the investigation of  $I$ - $V$  curves on ASCs of Pt because we were familiar with the bias dependence of Pt histograms [7], as it is presented in Fig. 9.2. We intended to test whether an electronic effect could explain the observed shift, and did indeed find non-linear  $I$ - $V$  curves on Pt (see Fig. 7.1b on page 117). The  $I$ - $V$  behavior for ASCs of Pt were compared to that of Au contacts, and these results were published in paper [III], which forms the basis for Sec. 7.2.

The non-linearity of the  $I$ - $V$  curves is described by fitting the curves to a third-order polynomial in the voltage [see Appendix A]:

$$I(V) = GV + G'V^2 + G''V^3. \quad (9.1)$$

Here  $G$  is the low bias conductance,  $G'$  is a constant describing the polarity-dependence of the current due to asymmetries in the contact region and  $G''$  is the non-linear term. From hundreds of  $I$ - $V$  curves on ASCs of Pt we obtain the

<sup>2</sup>The bias at which the shift occurs can change between experiments. We mostly find the shift at 300 mV, but sometimes 400 mV is needed. A shift at 200 mV was observed earlier [7].

mean value of the non-linear term  $\langle G'''(G) \rangle$  as a function of low bias conductance  $G$  (see the plot in Fig. 7.3b on page 121). We can now find the average behavior of the conductance with voltage  $G(V)$  for an  $I$ - $V$  curve measured on a contact having a given low bias conductance  $G$ . With the mean value of  $G'''$  corresponding to the selected  $G$ , we find the evolution of the conductance by dividing Eq. (9.1) with  $V$ :

$$G(V) = G + \langle G'''(G) \rangle V^2. \quad (9.2)$$

We have disregarded the second term in the third-order polynomial  $G'$ , and this is a good approximation since we remove clearly asymmetric contact configurations from the data anyway by setting an upper limit on the value of  $|G'|$  (see Appendix B).

With the shift from 1.5 to 1.8  $G_0$  for the histogram peaks (Fig. 9.2), we have chosen these two values for  $G$  to calculate  $G(V)$ . The resulting curves are shown in Fig. 9.3 where we also plot the position of the first Pt histogram peak vs bias as found from Fig. 9.1 and 9.2a.

When measuring  $I$ - $V$  curves, we surprisingly find that  $G(V)$  decreases with voltage, the exact opposite effect of what we expected from the observed 0.3  $G_0$  peak shift towards higher conductances in the histograms. With  $\langle G'''(G) \rangle$  negative at all conductances (cf. Fig. 7.3 on page 121) this will be the general  $I$ - $V$  behavior for Pt ASCs and not only of the monatomic contacts responsible for the first histogram peak.

In Fig. 9.3 we can see that the average contact with  $G = 1.5 G_0$ , only experiences a small decrease in the conductance when the bias rises up to 400 mV, whereas for the 1.8  $G_0$  contact  $G(V)$  clearly falls below the original value at this bias. At even higher voltages, the down bending becomes much more clear, since the non-linearity is proportional to the voltage squared [Eq. (9.2)]. The two conductance curves cross each other at a voltage of 1100 mV (at  $G = 1.25 G_0$ ). This implies that the contact with the highest  $G$  (at low bias), would actually have the smallest  $G(V)$  above this voltage. The  $I$ - $V$  curves of Pt, presented in Chapter 7, were measured with a maximum amplitude of 1 V (see Table 7.1 on page 114), and in the disruption experiments of Chapter 8 we found that only about 10% of the contacts are stable enough to sustain the current resulting from a voltage of 1100 mV (cf. Fig. 8.8a on page 165).

Finally we note, that in general it is very difficult to obtain  $I$ - $V$  curves at a low bias conductance  $G$  close to 1.5  $G_0$ . We even had to extrapolate  $\langle G'''(G) \rangle$  down to 1.5  $G_0$  due to the few data acquired at  $G \simeq 1.5 G_0$  (see Fig. 7.3a on page 121). It was possible to stabilize ASCs at this conductance, but they would be unstable towards voltages above a few hundred mV. We needed to

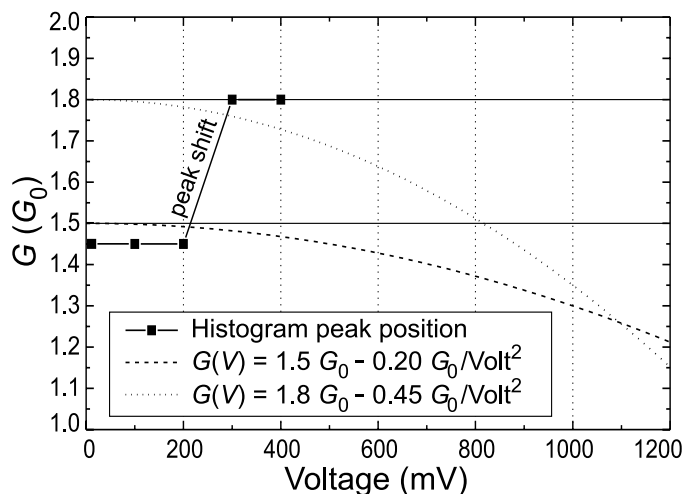


Figure 9.3: Comparing the voltage dependence of the conductance for monatomic Pt contacts, when their conductance is obtained either from the position of the first peak in conductance histograms or from the average behavior of several  $I$ - $V$  curves. The black squares show the approximate position of the center for the first peak in the conductance histograms from Fig. 9.1 and 9.2a (e.g.  $G \approx 1.45$  or  $1.8 G_0$ ). The evolution of the conductance  $G(V)$  for an  $I$ - $V$  curve is calculated from Eq. (9.2) using the average value of the non-linear term  $\langle G''(G) \rangle$  for contacts with a low bias conductance  $G$  of  $1.5 G_0$  (dashed curve) or  $1.8 G_0$  (dotted curve). The average value is extracted from Fig. 7.3b on page 121 and we obtain  $\langle G''(1.5 G_0) \rangle \approx -0.20 G_0/\text{Volt}^2$  and  $\langle G''(1.8 G_0) \rangle \approx -0.45 G_0/\text{Volt}^2$ . The two horizontal lines indicate the chosen values of  $G$  as a guide to the eye.

use a burst amplitude of at least 500 mV to ensure a decent fit to the  $I$ - $V$  curves (see Appendix C) and this explains the limited amount of data obtained around this conductance. First when  $G \geq 1.8 G_0$ , will ASCs in general be stable enough to measure  $I$ - $V$  curves with amplitudes higher than 500 mV.

The  $I$ - $V$  curves show, that the bias-dependent shift in the histograms is not an electronic effect. When the voltage increases very fast up to 500 mV (1–10 ms for the  $I$ - $V$  curves) on a given ASC formed at low bias, the conductance decreases slightly. When, however, the ASCs are formed at a bias above 300 mV, the position of the first histogram peak is shifted  $0.3 G_0$  towards higher conductance. The  $I$ - $V$  curves also indicate that low-conductance ASCs ( $G < 1.8 G_0$ ) are unstable towards high bias. Could this be the reason for the peak shift?

## 9.4 Plateau-length histograms

It has long been known that Au forms monatomic chains [17, 18] (see Sec. 6.7.2). Recently, it was proven that also Pt forms these characteristic chains [19, 20].

An example of the conductance trace for a *breaking* Pt ASC displaying chain formation is shown in Fig. 9.4. When the piezo voltage increases (lower axis) the electrodes are displaced accordingly (upper axis). Although the conductance decreases in uneven jumps from below  $30 G_0$  down to  $2.5 G_0$ , the overall behavior is a continuous decrease of  $G$ . This changes when the conductance drops below  $2.5 G_0$ , (indicated by a mark on the upper horizontal bar). This is the maximum conductance of a monatomic Pt contact according to Smit *et al.* [20] (see also Sec. 7.2.4). From then on the conductance remains close to  $1.5 G_0$  while the contact is elongated almost  $15 \text{ \AA}$  before finally breaking (second mark). After this, the electrodes must be returned  $20 \text{ \AA}$  (from  $15$  to  $-5 \text{ \AA}$ ) before a new contact is obtained, as indicated on the lower horizontal bar at  $0.5 G_0$ . No (clean) Pt chain or contact will ever exist, with a conductance below this value.

When the chain breaks the atoms will not only fall back onto the electrodes, but also the electrodes themselves will relax when the strain in the chain is released, explaining the longer return distance observed [18, 21]. Since the bulk bond length of Pt is only  $2.77 \text{ \AA}$ , a chain with up to six atoms is needed to explain the trace in Fig. 9.4. Monatomic chains of up to four Pt atoms have been observed [20], but the bond length in these chains is shorter than the bulk bond length [20], so even more atoms (8) would actually be needed to explain this extraordinary long plateau (see discussion on page 99 in Sec. 6.7.2 and also footnote 6 on page 98).

Statistically, large amounts of traces with long plateaus are, however, required in order to prove a general formation of monatomic chains. This can be obtained with the *plateau-length histograms* [18, 20] used by Smit *et al.* to show that not only Au but also Pt and iridium (Ir) can form these chains [20]. It is here very important to emphasize the fundamental difference between a plateau-length histogram and the conductance histograms we have used so far.

The *conductance* histogram is compiled by projecting all the measured conductance traces onto the conductance axis as described in Sec. 4.1. With this procedure, histogram peaks reveal the most probable *conductance values* obtained when the ASCs break.

A *plateau-length* histogram is constructed by measuring the last plateau-length from thousands of conductance traces of *breaking* ASCs like the one in Fig. 9.4. By plotting the number of times a given length occurs, a histogram with

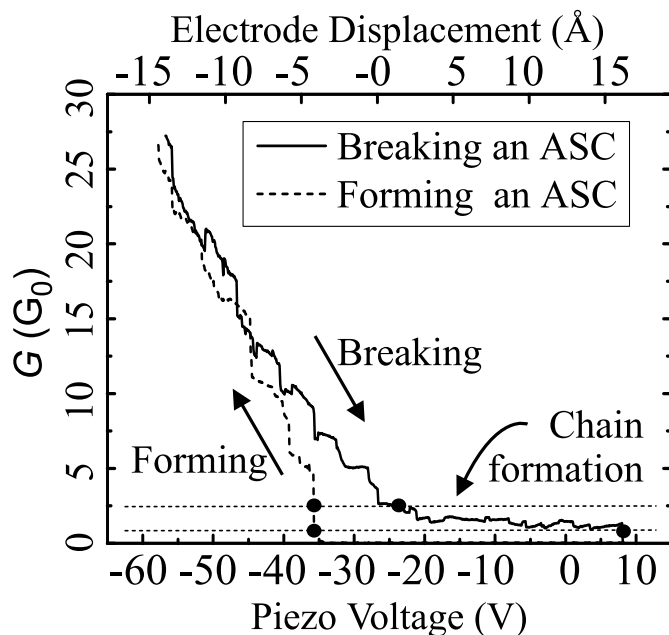


Figure 9.4: Conductance trace for the breaking and subsequent formation of a Pt ASC, as indicated by the arrows. When the piezo voltage increases (lower scale) the electrodes will be displaced a known distance (upper scale). Horizontal lines at  $2.5$  and  $0.5 G_0$  indicate the conductance region for monatomic chains and contacts [20]; crossings with these are marked ( $\bullet$ ). The  $15 \text{ \AA}$  long final plateau between the two lines is the result of chain formation. (Adapted from a figure provided by Roel Smit).

peaks revealing the typical *disruption lengths* at which the monatomic chains or contacts break, will result. The first peak shows the length of the monatomic contact and more than one peak indicates the formation of monatomic chains.

In Fig. 9.5a, we show an example of a plateau-length histogram for Pt, displaying clear chain formation by the appearance of three peaks. Each time a new atom is added to the chain during the elongation process, the whole contact configuration can relax. It will then be possible to stretch the chain even further before a critical strain level is reached, and the chain must either incorporate another atom (i.e. increase its length again), or finally subdue to the stretching,

and break. Peaks are realized because the critical strain levels of the individual chains in general correspond to certain more or less fixed lengths.

Smit *et al.* used the conductance window from  $0.5$ – $2.5 G_0$ , indicated by the two horizontal lines in Fig. 9.4, to define when the Pt contact consisted of a monatomic contact or chain [20]. This interval is extracted from the region covered by the first peak in the Pt conductance histograms (cf. Fig. 9.2). The length of these last conductance plateaus is a measure of the chain length. In this way it was shown that at least four peaks occurred in the Pt plateau-length histogram with  $2.3 \text{ \AA}$  intervals, proving that monatomic Pt chains do form [20]. Whereas similar results were obtained for Au and Ir, only one peak was observed for palladium (Pd), silver (Ag) and rhodium (Rh) indicating that these metals do not form chains [20].<sup>3</sup>

The measurements were performed at a low bias ( $10$ – $25 \text{ mV}$ ) [20] and cannot give us any information on the behavior of the ASCs at a bias of  $300 \text{ mV}$ , where the peak shift in the conductance histogram occurs (see Fig. 9.2). Instead Roel Smit presented us with the data for the plateau-length histograms in Fig. 9.5 measured at biases of (a)  $200$  and (b)  $400 \text{ mV}$ , respectively. At  $200 \text{ mV}$  bias, the plateau-length histogram is very similar to the one presented in [20]. Three clear peaks are visible, the first corresponding to a monatomic contact, a “one atom chain”, and the next peaks represent chains with two and three atoms, respectively. Thus, we conclude that monatomic chains still form at a bias as high as  $200 \text{ mV}$ .

The three peaks in Fig. 9.5a are centered at  $2.7$ ,  $4.8$  and  $7.0 \text{ \AA}$ , respectively. The distance between them are thus  $2.1$ – $2.2 \text{ \AA}$ , similar to the  $2.3 \text{ \AA}$  found in [20]. The first peak is, however, found at  $2.7 \text{ \AA}$ , a value close to the bulk bond length of Pt ( $2.8 \text{ \AA}$ ). A similar difference between the first and subsequent peaks did not appear at low bias [20]. The calibration was not adjusted for the high bias used, and this may, as well as high bias effects, explain the discrepancy.

The exact length is anyway not that important for our purpose, which is to reveal at which bias the monatomic chains cease to exist. This can be seen from the number of peaks, not from their individual position. The presence of only one single peak in the  $400 \text{ mV}$  plateau-length histogram (Fig. 9.5b), centered at  $1.9 \text{ \AA}$ , proves that chains no longer form at this high bias. The peak do not coincide with the corresponding first peak in the  $200 \text{ mV}$  plateau-length histogram. This difference is most likely due to the higher bias causing the monatomic contact to break at a smaller strain than at low bias (see the discussion).

<sup>3</sup>A discussion of the relation between the ability to form monatomic chains and surface reconstructions [20] can be found on page 99 in Sec. 6.7.2.

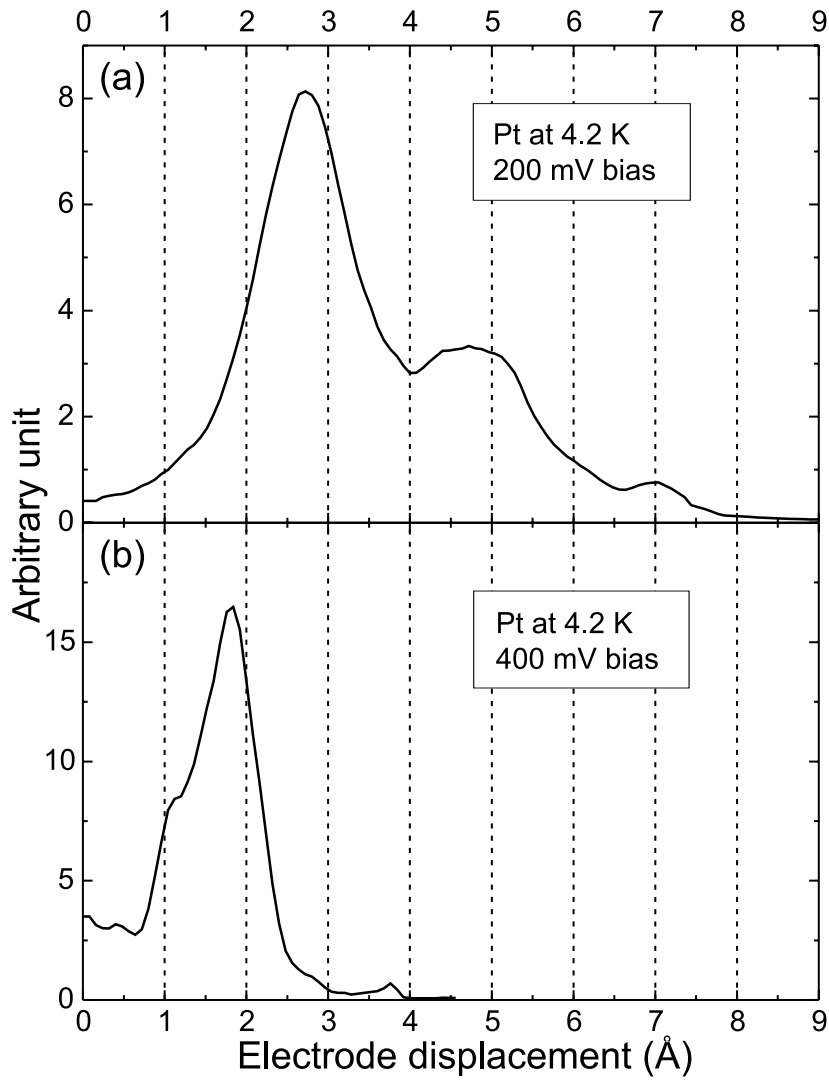


Figure 9.5: Plateau-length histograms [18, 20] of Pt each compiled from 2000 *breaking* ASCs obtained with the MCBJ at 4.2 K under cryogenic vacuum. A bias of (a) 200 mV and (b) 400 mV is applied. The arbitrary unit on the horizontal axis is a measure for the frequency with which a given chain length occurs. (Data provided by Roel Smit).

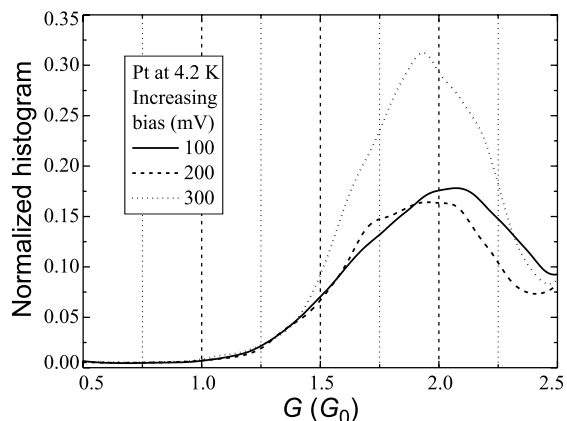


Figure 9.6: Return conductance histograms of Pt. Each histogram is compiled from 2000 conductance traces and are measured in succession on the same sample while the bias increases from 100 to 300 mV in 100 mV steps. The measurements are performed by *forming* the ASCs with the MCBJ under cryogenic vacuum at 4.2 K.

## 9.5 Return histograms

From the plateau-length histograms we found that the formation of atomic chains is inhibited at the higher bias where the shift in the conductance histogram occurs. We needed a method to test whether the chain formation affected the peak position or not. The solution came in what we have called the *return conductance histogram*<sup>4</sup> (return histogram from now on).

The conductance histograms presented previously in this chapter are all obtained from the conductance traces of *breaking* ASCs. This was also the case for all histograms shown in Chapter 4. When breaking the contacts, atomic chain formation can occur. If we instead obtain the ASCs by returning the electrodes back into contact, chains cannot form, as illustrated by Fig. 9.4. Measuring the conductance traces while *forming* ASCs, resulted in the return histograms presented in Fig. 9.6.

From these return histograms it is clear that the first peak is centered close to  $2 G_0$ , independent of bias, although the shape and size of the peak changes (see the discussion). It thus seems that the peak shift happens when the chain formation is inhibited, since the peak is located at an even higher conductance independent of bias when no chains at all forms.

<sup>4</sup>Note that this is again a type of conductance histogram, *not* a plateau-length histogram.

## 9.6 Discussion

The conductance of monatomic chains and contacts is, however, not expected to be very different from each other, so why does the peak position shift to higher conductances due to the removal of chains?

A theoretical calculation showing that the conductance of a monatomic Pt contact decreases with increasing bond length was presented earlier.<sup>5</sup> When we stretch the monatomic contact, the conductance decreases until the break occurs. A strained contact will be more sensible to the heating caused by an applied bias, so increasing the bias should result in contact rupture at a lower strain level. Since the strain level determines the conductance of the monatomic contact, a higher bias will force the contact to disrupt at a higher conductance, resulting in a shift of the histogram peak to higher  $G$ . This effect will even be amplified by the fact that monatomic chains no longer form at high bias, as seen from Fig. 9.5b. When the bias is low enough for monatomic chain formation to occur, the contact will be stretched to the limit, reaching the lowest conductances before the next atom enters the chain. In this way, chain-forming contacts will be under strain for a longer time and on average have a lower conductance than monatomic contacts breaking directly. These considerations can be used to explain all types of histograms presented above.

When *breaking* ASCs at low bias (Fig. 9.1), monatomic chains form, and the conductance histogram peak will be centered at  $\sim 1.5 G_0$  due to the long periods with increased strain. With the long plateaus caused by the chains, the conductance histogram is also likely to have a bigger peak than when no chains form. This agrees with the relatively smaller peak for the conductance histograms at high bias (300–400 mV) in Fig. 9.2 and all the return histograms (100–300 mV) in Fig. 9.6 when they are compared with the low bias (100–200 mV) conductance histograms in Fig. 9.2. It can be difficult, though, to compare the peak size from different conductance histograms directly as mentioned previously.

The observed peak shift from  $1.5 G_0$  to  $1.8 G_0$  can be explained using the above mentioned calculation, together with the plateau-length histograms in Fig. 9.5. At high bias most contacts simply break before they reach a strain level where they obtain a conductance much below  $1.8 G_0$ . At low bias, the chains often experience strain, resulting in conductances below  $1.5 G_0$ .

The first peak of the return histograms in Fig. 9.6 is situated at an even higher conductance than those of the high bias conductance histograms in Fig. 9.2. When pushing the electrodes together, the contacts are compressed

---

<sup>5</sup>The result was plotted in Fig. 7.5 on page 123 and shows that the conductance decrease from 2.1 to 1.1  $G_0$  when the bond length of the Pt contact is stretched from 2.65 to 3.45 Å.

and never strained, resulting in a conductance around  $2 G_0$  for the monatomic contact and the corresponding peak.

The return histograms resemble the rarely occurring histograms mentioned at the end of Sec. 9.2, where the first histogram peak was situated at  $2 G_0$ , even though the ASCs were breaking not forming. This could be explained by exotic geometric structures which would break as soon as the monatomic contact was ever so slightly strained. After some time these structures changes again allowing the formation of monatomic chains, and the peak moves back to  $1.5 G_0$ .

If the monatomic contacts in general are more stable than the higher conductance few-atom contacts, this may explain the difference in peak height between the 300 mV bias return histogram and the other two measured at a lower bias (Fig. 9.6). At low bias the least stable atomic configuration will survive for a relatively longer period than expected, when comparing to the lifetime of the most stable configuration. At higher biases, the unstable geometries may in some cases not even form, as visualized by the lack of chain formation at biases above 300 mV. Since the return histograms are normalized [see Eq. (4.1) on page 45] the peak at  $2 G_0$  becomes lower if there are an increased intensity in the return histogram at higher conductances. At 300 mV the relative intensity at high conductance may have dropped, because the conductance traces of the forming ASCs will jump faster to higher conductances when the initially formed monatomic contact ( $G \sim 2 G_0$ ) is squeezed. This would cause the 300 mV return histogram peak to be bigger than for the lower bias return histograms.

Comparing the size of peaks between conductance histograms can be very difficult if these are not measured in succession. This is due to the normalization, which depends, amongst other things, on the highest conductances which have been included in the conductance traces used to compile the conductance histograms (i.e.  $30 G_0$  for a trace as in Fig. 9.4 vs  $5 G_0$  for the traces in Fig. 4.2 on page 43). However, the conductance histograms in Fig. 9.2 and the return histograms in Fig. 9.6 are measured under similar conditions. We hence try to compare the two 300 mV bias histograms in Fig. 9.2a and Fig. 9.6, and find that they have almost the same size. For the breaking histogram the chain formation causes the larger peaks at low bias (Fig. 9.2). This is prevented in return histograms, and here it is the high bias peak which is the biggest (see Fig. 9.6).

Finally the hysteresis of the conductance histograms in Fig. 9.2, observed when the bias is decreased, can be understood as if the high bias has forced the contacts to obtain a certain atomic configuration, preventing the formation of chains. This will result in a considerably lower peak height, and hence, relatively more intensity at higher conductances. If the contact has time to relax at low bias, the conductance histogram changes back to its original shape.

## 9.7 Conclusion

We have found that the bias-dependent shift of the first peak in the Pt conductance histograms is related indirectly to the formation of monatomic chains, since the conductance depends on the maximum strain that the ASCs can sustain before breaking. The conductance of the monatomic contact decreases when the strain increases. Formation of monatomic chains will amplify this effect, since the period during which the strain is high, will be much longer than when the monoatomic contacts (“one atom chains”) break directly. This will always happen at high bias as inferred from the plateau-length histograms.

If the contacts are formed by pushing the electrodes together, like in the return histograms, chains cannot form. This is the same we expect to happen at high bias, but for the return histograms the peak is located at an even higher conductance, because the monatomic contact is compressed rather than strained.

By measuring current-voltage curves we have seen that the electronic effect of increasing the voltage is a decrease in the conductance, but this turned out to result in a much smaller change in the conductance than for the geometrical effect presented here.

We arrive at the following conclusion: The shift of the first peak in the Pt conductance histogram from 1.5 to 1.8  $G_0$  when the bias increases past 300 mV, marks a geometric transition point where monatomic chains are replaced by monatomic contacts.

## References

- [1] N. Agraït, J. G. Rodrigo, and S. Vieira, “Conductance steps and quantization in atomic-size contacts,” *Phys. Rev. B* **47**, 12345–12348 (1993).
- [2] J. I. Pascual, J. Méndez, J. Gómez-Herrero, A. M. Baró, N. García, and V. T. Binh, “Quantum Contact in Gold Nanostructures by Scanning Tunneling Microscopy,” *Phys. Rev. Lett.* **71**, 1852–1855 (1993).
- [3] M. Brandbyge, J. Schiøtz, M. R. Sørensen, P. Stoltze, K. W. Jacobsen, J. K. Nørskov, L. Olesen, E. Lægsgaard, I. Stensgaard, and F. Besenbacher, “Quantized conductance in atom-sized wires between two metals,” *Phys. Rev. B* **52**, 8499–8514 (1995).
- [4] H. Yasuda and A. Sakai, “Conductance of atomic-scale gold contacts under high-bias voltages,” *Phys. Rev. B* **56**, 1069–1072 (1997).
- [5] K. Itakura, K. Yuki, S. Kurokawa, H. Yasuda, and A. Sakai, “Bias dependence of the conductance of Au nanocontacts,” *Phys. Rev. B* **60**, 11163–11170 (1999).
- [6] K. Yuki, A. Enomoto, and A. Sakai, “Bias-dependence of the conductance of Au nanocontacts at 4 K,” *Appl. Surf. Sci.* **169–170**, 489–492 (2001).
- [7] A. I. Yanson, “Atomic Chains and Electronic Shells: Quantum Mechanisms for the Formation of Nanowires,” PhD thesis, Rijksuniversiteit Leiden, 2001. (Can be downloaded from <http://lions1.leidenuniv.nl/wwwhome/ruitenbe/ThesisAlex.pdf>).
- [8] K. Yuki, S. Kurokawa, and A. Sakai, “Quantized Conductance in Pt Nanocontacts,” *Jpn. J. of Appl. Phys.* **39**, 4593–4595 (2000).
- [9] K. Yuki, S. Kurokawa, and A. Sakai, “Conductance in Breaking Nanocontacts of Some Transition Metals,” *Jpn. J. of Appl. Phys.* **40**, 803–808 (2001).
- [10] J. I. Pascual, J. Méndez, J. Gómez-Herrero, A. M. Baró, N. García, U. Landman, W. D. Luedtke, E. N. Bogachev, and H.-P. Cheng, “Properties of Metallic Nanowires: From Conductance Quantization to Localization,” *Science* **267**, 1793–1795 (1995).

- 
- [11] V. V. Dremov and S. Y. Shapoval, "Quantization of the conductance of metal nanocontacts at room temperature," *Pis'ma Zh. Eksp. Teor. Fiz.* **61**, 321–324 (1995), [JEPT Lett. **61**, 336 (1995)].
- [12] B. Rodell, V. Korenivski, J. Costa, and K. V. Rao, "Quantized conductivity in STM drawn 100Å nanowires of Au and Ni," *Nanostruct. Mater.* **7**, 229–235 (1996).
- [13] J. L. Costa-Krämer, N. García, P. García-Mochales, P. A. Serena, M. I. Marqués, and A. Correia, "Conductance quantization in nanowires formed between micro and macroscopic metallic electrodes," *Phys. Rev. B* **55**, 5416–5424 (1997).
- [14] J. Abellán, R. Chicón, and A. Arenas, "Properties of nanowires in air. Controlled values of the conductance," *Surf. Sci.* **418**, 493–501 (1998).
- [15] A. Correia, J.-L. Costa-Krämer, Y. W. Zhao, and N. García, "Non-linear contribution to intensity-voltage characteristics of gold nanowires," *Nanostruct. Mater.* **12**, 1015–1020 (1999).
- [16] R. H. M. Smit, Y. Noat, C. Untiedt, N. D. Lang, M. van Hemert, and J. M. van Ruitenbeek, "Measurement of the conductance of a hydrogen molecule," accepted for publication in *Nature*, (2002), <http://xxx.lanl.gov/pdf/cond-mat/0208407>, (unpublished).
- [17] H. Ohnishi, Y. Kondo, and K. Takayanagi, "Quantized conductance through individual rows of suspended gold atoms," *Nature* **395**, 780–783 (1998).
- [18] A. I. Yanson, G. R. Bollinger, H. E. van den Brom, N. Agraït, and J. M. van Ruitenbeek, "Formation and manipulation of a metallic wire of single gold atoms," *Nature* **395**, 783–785 (1998).
- [19] S. R. Bahn and K. W. Jacobsen, "Chain Formation of Metal Atoms," *Phys. Rev. Lett.* **87**, 266101 (2001).
- [20] R. H. M. Smit, C. Untiedt, A. I. Yanson, and J. M. van Ruitenbeek, "Common Origin for Surface Reconstruction and the Formation of Chains of Metal Atoms," *Phys. Rev. Lett.* **87**, 266102 (2001).
- [21] G. Rubio-Bollinger, S. R. Bahn, N. Agraït, K. W. Jacobsen, and S. Vieira, "Mechanical Properties and Formation Mechanisms of a Wire of Single Gold Atoms," *Phys. Rev. Lett.* **87**, 026101 (2001).



## Chapter 10

# Outlook

Although many experimental papers regarding atomic-sized contacts (ASCs) will be published in the years to come, the most interesting properties have already been investigated in great detail. Now the theoreticians need to put forward models explaining the experimental results, and in this way increase our understanding of the many interesting phenomena observed. In this thesis we presented a few calculated current-voltage ( $I$ - $V$ ) curves of gold (Au) and platinum (Pt), but we have still barely scratched the surface.<sup>1</sup>

In the introduction I based the discussion of why it would be interesting to investigate ASCs on the ever decreasing size of microchips. Both transistors and interconnects are being miniaturized and from Feynman's famous talk [1], was it extracted that the smallest possible wire between two components is a chain of single atoms (Sec. 1.2). We have now examined this system in great detail and it is time to take the next step and find the smallest possible transistor. Since transistors are electrical components, they can never be realized by a single atom but likely candidates will be single functional molecules [2, 3].

With our fast experimental setup and the mechanically controllable break junction (MCBJ) we may just have the right tools at our disposal for the investigation of such molecules.

---

<sup>1</sup>Only made atomic-sized contact, so to say!

## Conduction through molecules

Molecular electronics or moletronics [4] is a research field in rapid growth and the successful connection of several molecular devices have been accomplished [5]. The concept of moletronics is the use of single molecules as functional units in electronic circuits. Recently, there have been examples of single-molecule transistors [2, 3] and this may eventually realize the dream of “computing with molecules” [6] (see Fig. 10.1).

Although it may be possible to investigate single molecules as in Fig. 10.1, serious problems will arise with the mass production of the components needed in the design of a useful computer. Here nature comes to our assistance with the possibility of forming self-assembled monolayers (SAMs) of similar molecules [7]. This may provide a template for the fabrication of an enormous amount of functional molecules.

We intend to rebuild our MCBJ in order to enable the investigation of the conduction through molecules [6, 8–11]. In spite of the entire discussion of the importance of ultra-clean experimental conditions (see Sec. 6.7), we need to move the MCBJ to a less clean environment, since it is impossible to work with large organic molecules under cryogenic vacuum. There may, however, be a way of avoiding the impurity problem using the method of Reed *et al.* [8]: By placing a drop with a solution of the interesting molecule above the notch in the sample wire (cf. Fig. 3.5 on page 35), the two freshly exposed electrodes will be in direct contact with the molecules of the solution as soon as the wire is broken.

Still, we must keep the very serious risk of contamination in mind. A possible way to circumvent some of these problems could be the use of a molecule which binds very strongly to our electrode material. A realizable experiment could be the use of Au electrodes to investigate organic molecules with mercapto groups (HS) included in their structure (e.g. thiols [6, 7], see Fig. 10.1). When the wire is broken the electrodes will instantly be covered with SAMs and by moving them back together, the first contact will occur between the protruding molecules. In this way we hope to continue the ongoing investigation of the conductance through molecules, and measure  $I$ - $V$  curves [6, 8–10] on these with our fast and accurate experimental setup.

One may hope that the contributions from such experiments will take us yet another step closer to the ultimate nano-technology: *Feynman's bottom* [1], where functional molecules and atomic-sized wires will be used as the building blocks for electrical devices in general and for the design of computers in particular.

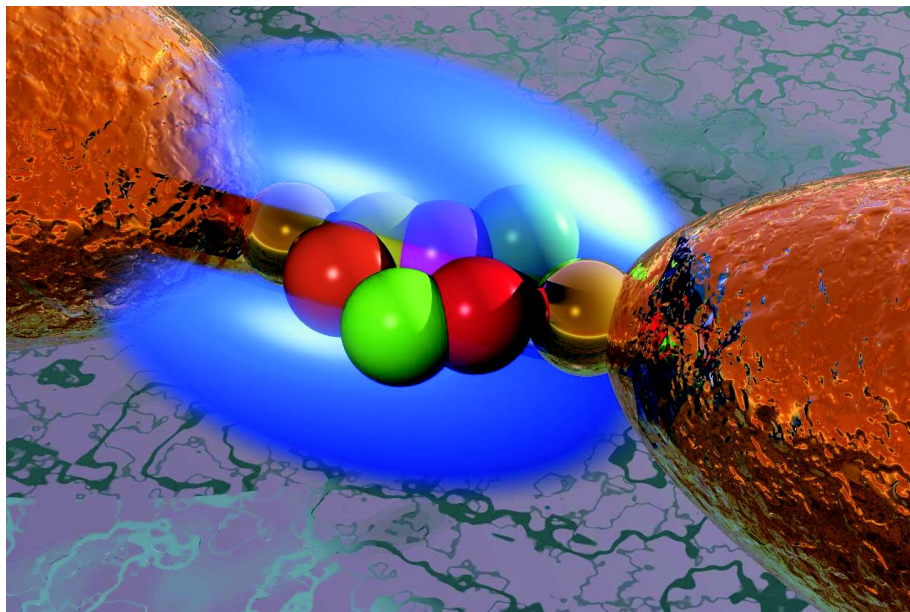


Figure 10.1: Artistic expression by Mark A. Reed of a single benzenedithiol molecule connecting two Au electrodes [6]. Benzenedithiol is a thiol with two mercapto groups (HS) and when the hexagonal benzene ring connects with the Au electrodes it occurs at the sulphur (S) atoms on the expense of the hydrogen (H) atoms, which disappear. The cloud along the molecule illustrates the free electrons in the conjugated pi-electron system, which is a characteristic feature for all molecules containing benzene rings. This electron system explains the very interesting chemical properties of benzene molecules. It is also through this that the electrons are allowed to pass from one electrode to the other. Experiments in which such connections were realized in order to measure the  $I$ - $V$  behavior of benzenedithiol, were presented in the visionary paper: “Computing with molecules” by M. A. Reed and J. M. Tour [6]. (Reprinted from: [6] by permission from Scientific American and with the authors’ consent).

## References

- [1] R. P. Feynman, "There's Plenty of Room at the Bottom," 1959, talk at the Annual Meeting of The American Physical Society at California Institute of Technology. Available on the web at <http://www.zyvex.com/nanotech/feynman.html>.
- [2] J. Park, A. N. Pasupathy, J. I. Goldsmith, C. Chang, Y. Yaish, J. R. Petta, M. Rinkoski, J. P. Sethna, H. D. Abruña, P. L. McEuen and D. C. Ralph, "Coulomb blockade and the Kondo effect in single-atom transistors," *Nature* **417**, 722–725 (2002).
- [3] W. Liang, M. P. Shores, M. Bockrath, J. R. Long, and H. Park, "Kondo resonance in a single-molecule transistor," *Nature* **417**, 725–729 (2002).
- [4] R. Dagani, "Taking baby steps to 'moletronics'," *Chemical and Engineering News* **January 3**, 22–26 (2000).
- [5] Breakthrough of the year: Nanocircuits, *Science* **294**, issue 5551, (2001). See R. F. Service, "Molecules Get Wired," 2442–2443.
- [6] M. A. Reed and J. M. Tour, "Computing with Molecules," *Sci. Am.* **June**, 68–75 (2000).
- [7] For a recent review see F. Schreiber, "Structure and growth of self-assembling monolayers," *Prog. Surf. Sci.* **50**, 151–256 (2000).
- [8] M. A. Reed, C. Zhou, C. J. Muller, T. P. Burgin, and J. M. Tour, "Conductance of a Molecular Junction," *Science* **278**, 252–254 (1997).
- [9] J. M. Tour, A. M. Rawlett, M. Kozaki, Y. Yao, R. C. Jagessar, S. M. Dirk, D. W. Price, M. A. Reed, C.-W. Zhou, J. Chen, W. Wang and I. Campbell, "Synthesis and Preliminary Testing of Molecular Wires and Devices," *Chem. Eur. J.* **7**, 5118–5134 (2001).
- [10] J. Reichert, R. Ochs, D. Beckmann, H. B. Weber, M. Mayor, and H. v. Löhneysen, "Driving Current through Single Organic Molecules," *Phys. Rev. Lett.* **88**, 176804 (2002).
- [11] H. He and N. Tao, "Interactions of Molecules with Metallic Quantum Wires," *Adv. Mater.* **14**, 161–164 (2002).

# Kapitel 11

## Dansk resumé

Nanoteknologien er i dag et felt i rivende udvikling. Mens man inden for kemi, biologi og medicin stort set altid har opereret i nanoverdenen med molekyler, amøber og bakterier, er det først inden for de sidste 10–20 år, at fysikken også er nået ned på denne længdeskala. Forskningen vender sig i dag mod nanovidenskaberne og tilbyder en ny og forbedret indsigt i mange af de processer, som man før benyttede, men ikke helt havde forstået.<sup>1</sup> Det faktum, at stort set alle naturvidenskaber nu er nået ned på samme længdeskala betyder, at deres fælles interesser mødes i nanoverdenen og nye interdisciplinære samarbejder opstår.<sup>2</sup>

Nano kommer fra det græske ord *nanos*, der meget passende betyder *dværg*, da det henviser til størrelsen af de systemer, som bliver undersøgt. (Se figuren på side 1). Længdeskalaen er netop *nanometer*, hvor en enkelt nanometer svarer til en milliardtedel af en meter ( $1 \text{ nm} = 0.000\,000\,001 \text{ m}$ ). Beskrivelsen *nanoteknologi*, dækker alle systemer med en udstrækning fra få tiendedele og helt op til flere hundrede nanometer. Den typiske afstand mellem atomerne i et metal, som guld (Au), er 0.3 nm eller 3 Å, hvor Å står for Ångström. Én Ångström er en tiendedel af en nanometer, og det er den længdeenhed man normalt benytter til beskrivelsen af atomare systemers udstrækning.

---

<sup>1</sup>Katalyse er et glimrende eksempel, hvor man først med udviklingen inden for nanofysikken har fået en mere fundamental forståelse for, hvordan en katalysator egentligt virker.

<sup>2</sup>Meget aktuelt er det nye Interdisciplinært Nanoscience Center (*iNano*) ved Aarhus Universitet, der åbnede den 28. januar 2002. Her samarbejder forskere fra fysik med kemikere, biologer og molekylærbiologer. Centeret har desuden forskere fra medicin som associerede medlemmer og har en stærk tilknytning til erhvervslivet. Besøg hjemmesiden på: <http://www.inano.dk/>

## Makroskopiske analogier til den atomare verden

*Jylland mellem tvende have som en runesten er lagt,  
fortid mæle dine grave, fremtid folder ud din magt;  
havet af sit fulde bryst synger højt om Jyllands —  
højt om Jyllands kyst.*

Sidste strofe af “Jylland mellem tvende have”,  
H. C. Andersen, 1859.

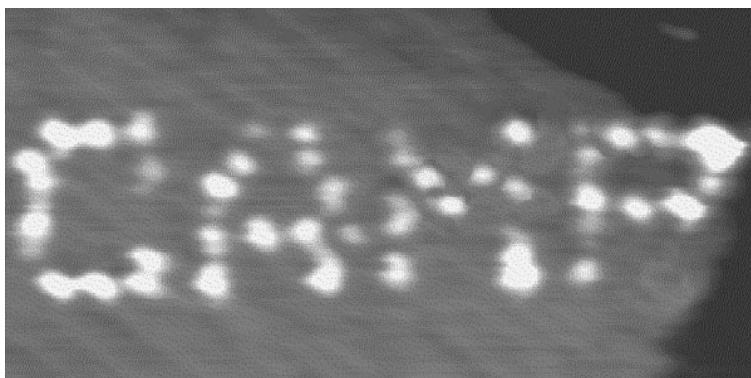
Atomer er så ufatteligt små, at det praktisk talt er umuligt at forholde sig til det. I et forsøg på at visualiserer, hvor små de egentlig er, vil jeg lave forskellige analogier til den makroskopiske verden. F.eks. vil der langs diameteren i punktet for enden af denne sætning ligge ca. én million atomer.

Som en mere folkelig analogi benytter jeg fodbolde samt H. C. Andersens runesten, som udgør den største del af dette *yndige* land. Man kan beregne, at der ligger lige så mange atomer hen over tværsnittets diameteren på et enkelt hår ( $d \approx 0.1$  mm), som der kan ligge fodbolde hen over Jylland mellem Esbjerg havn og Kolding Fjord! Hvem der så kunne få lyst til at afprøve dette ved at placere 333 333 bolde side om side på denne 70 km lange strækning?

### En ekstra dimension: CAMP-logoet

Jeg tager nu to dimensioner i brug og benytter logoet fra Center for Atomic-scale Materials Physics (CAMP). Logoet findes på forsiden af denne afhandling og er endvidere forstørret op i Fig. 11.1. Frembringelsen af dette logo vha. et *skanning-tunnellerings-mikroskop* (STM) vil blive beskrevet i detalje i næste afsnit. Logoet er 1000 Å bredt og 500 Å højt og består af fire bogstaver hver skrevet med omkring 12 individuelle pletter bestående af en klump atomer hævet over selve overfladen. Generelt kan man skrive et vilkårligt bogstav ud fra et rektangel bestående af  $5 \times 5$  pletter (kun M og W har dog brug for hele 5 pletter i bredden), men skal der være mellemrum mellem bogstaverne og ordentligt linjeafstand, skal man nok beregne  $6 \times 7 = 42$  pletter<sup>3</sup> pr. tegn. Benyttes denne skriftstørrelse kan man skrive ikke mindre end 10 millioner bogstaver på tværsnittet af det førømtalte hår. Da denne *lille* pamflet indeholder næsten en halv million tegn (234 sider, ca. 40 linjer pr. side og omkring 50 tegn pr. linje), vil man kunne nedfælde mere end 20 ph.d.-afhandlinger på tværsnittet af et enkelt hår! Og min afhandling hører vist nok ikke engang til blandt de kortere. . .

<sup>3</sup>Ifølge afdøde Douglas Adams’ “Håndbog for vakse galakseblaffere” (“The Hitchhikers Guide to the Galaxy”), er netop *toogfyrré* (42) svaret på det ultimative spørgsmål om livet, universet og alt det der!



Figur 11.1: Logoet for Center for Atomic-scale Materials Physics (CAMP) er kun 1000 Å bredt og 500 Å højt. Det er “skrevet” på en nikkel overflade [Ni(110)], hvorpå der er lagt et tyndt lag guld. De enkelte bogstaver er dannet af ca. tolv lyse pletter, som hver for sig består af knapt 300 atomer, hævet op over selve overfladen. Antallet af atomer i en plet kan udledes fra diameteren, der er omkring 50 Å. Dette fås fra, at der er plads til ca. 20 pletter på tværs af billedet. Generelt set kan et bogstav skrives med et rektangel bestående af  $5 \times 5$  pletter men for at skrive tekst, skal der regnes med mindst  $6 \times 7 = 42$  pletter,<sup>3</sup> så der også er plads til mellemrum.

## STM’et og CAMP-logoet

For at kunne skrive et logo som “CAMP” har man benyttet et STM. STM’et bliver beskrevet detaljeret i sektion 3.2, men især to dele er vigtige for at kunne forstå selve skanneprocessen. Den ene er prøven (en meget flad metaloverflade) og den anden er en yderst spids metalnål, der bruges til at skanne overfladen.

Når man benytter et STM som *mikroskop* til at *skanne* billeder som CAMP-logoet (Fig. 11.1), føres nålen hen over prøvens overflade i atomar afstand (under 1 nm). Ved at påtrykke en spændingsforskel kan man måle den såkaldte *tunnelleringsstrøm* mellem nål og prøve. Nålen rører ikke overfladen, og da der kun er få atomers afstand op til prøven,<sup>4</sup> vil der altid være vakuum mellem disse mens der skannes. Klassisk set er det forbudt for elektronerne at bevæge sig gennem et vakuum, men kvantemekanisk viser det sig, at det kan lade sig gøre. Dette skyldes, at det faktisk ikke er muligt at bestemme elektronernes eksakte position og impuls samtidigt, og man kan kun beregne sandsynligheden

<sup>4</sup>I vores terminologi nærmer nålen sig prøven nedefra, se Fig. 3.3 på side 32.

for at en elektron befinder sig inden for et bestemt område.<sup>5</sup> Da området også strækker sig ud i vakuumet, er der derfor en mulighed for, at en elektron kan hoppe (tunnellerer) over vakuumbaret fra nål til prøve. Sandsynligheden for at dette sker, og dermed også størrelsen af tunnelleringsstrømmen, aftager eksponentielt med afstanden. Hvis bare et enkelt atom yderst på nålens spids sidder et par Ångström længere fremme end alle de andre atomer, vil 90% af strømmen blive trukket over dette atom alene. Det betyder, at nålen principielt ender i et enkelt atom og den kan dermed beskrives som værende atomart spids!

På grund af den ekstreme afstandafhængighed kan man via strømmen måle nålens højde i forhold til overfladen med subatomar præcision. Hvis man nu skanner nålen hen over prøven, mens man flytter den op og ned for at holde størrelsen af strømmen konstant, kan man opnå en tredimensional afbildning af overfladens konturer. Dette kan gøres så præcist, at man kan opnå atomar opløsning, som illustreret i Fig. 3.4a på side 34, hvor et billede der kun er  $30 \times 30 \text{ \AA}^2$  viser ca. 100 atomer på en guldoverflade [Au(111)].

CAMP-logoet er blevet taget på samme måde, men det er langt fra atomart opløst, da de enkelte pletter er omkring 50 Å i diameteren og er dannet af små 300 atomer<sup>6</sup> (Fig. 11.1). Pletterne er dannet ved at fører STM-nålen “dybt” ind i overfladen (50–100 Å), og når den efterfølgende trækkes ud igen, vil atomer fra forbindelsen mellem nål og overflade afsættes som en lille forhøjning, der afbildes lysere, når der skannes billeder. Det svarer lidt til det, der sker, når man f.eks. trækker en ske ud af tykt flødeskum (se også Fig. 3.2 på side 31). Udføres denne proces i det rigtige mønster, kan man danne de fire bogstaver C A M P, hvorefter et billede som i Fig. 11.1 kan skannes.

## STM-nålen contra Eiffel-tårnet

For at alt dette overhovedet kan lade sig gøre, skal man først løse den formidable opgave det er, at føre STM-nålen fra makroskopisk afstand (1 mm) til atomar afstand (1 nm). At dette i det hele taget er muligt, skyldes anvendelsen af de såkaldte piezo-elektriske krystaller, hvis udstrækning kan kontrolleres på en sub-Ångström længdeskala vha. en påtrykt spænding (se fodnote 11 på side 210).

<sup>5</sup>Dette er kendt som Heisenbergs usikkerhedsrelation:  $\Delta x \Delta p \gtrsim h$ , hvor  $h$  er Plancks konstant,  $\Delta x$  er usikkerheden i elektronens position og  $\Delta p$  er usikkerheden på impulsen  $p = mv$ . Her er  $m$  massen og  $v$  hastigheden af elektronen.

<sup>6</sup>Det er også muligt at skrive med enkelte atomer, hvilket bl.a. blev gjort med IBMs logo. Dette kan ses på <http://www.almaden.ibm.com/vis/stm/images/stm10.jpg>. På denne måde behøver man kun 42 atomer pr. tegn. Da der er 300 atomer i hver af de pletter, der udgør et enkelt CAMP-logobogstav, vil der altså være plads til at skrive over  $300 \times 20 = 6000$  ph.d.-afhandlinger på et enkelt hårs tværsnit!

Nålen er ca. 3 mm lang og føres på under to minutter fra 1 mm til 1 nm uden at "brase" ind i overfladen. Dermed undgår man, at lave en makroskopisk fordybning i det der skal undersøges. Derefter skannes nålens yderste atom (ca. 3 Å i diameter) hurtigt og præcist hen over prøvens overflade og tager billeder som CAMP-logoet ( $1000 \times 500 \text{ \AA}^2$ ). Lad os sammenligne denne opgave med en tilsvarende, hvor nålen i stedet erstattes med Eiffel-tårnet. Eiffel-tårnet er 300 m højt ud til den yderste spids af antennen, som sikkert er en lille centimeter tyk, men jeg antager for sammenlægningsens skyld, at den alleryderste flig af antennen kun er 0.3 mm tyk. Eiffel-tårnet skal nu føres fra en afstand af 100 m ind til kun 0.1 mm på under to minutter uden at ramme imod overfladen! Antennen skannes derefter hurtigt men så præcist, at de enkelte prikker kan skelnes i et CAMP-logo med dimensionerne  $10 \times 5 \text{ cm}^2$ , præcist samme størrelse som logoet i Fig. 11.1. Hele Eiffel-tårns analogien er illustreret i Fig. 11.2.

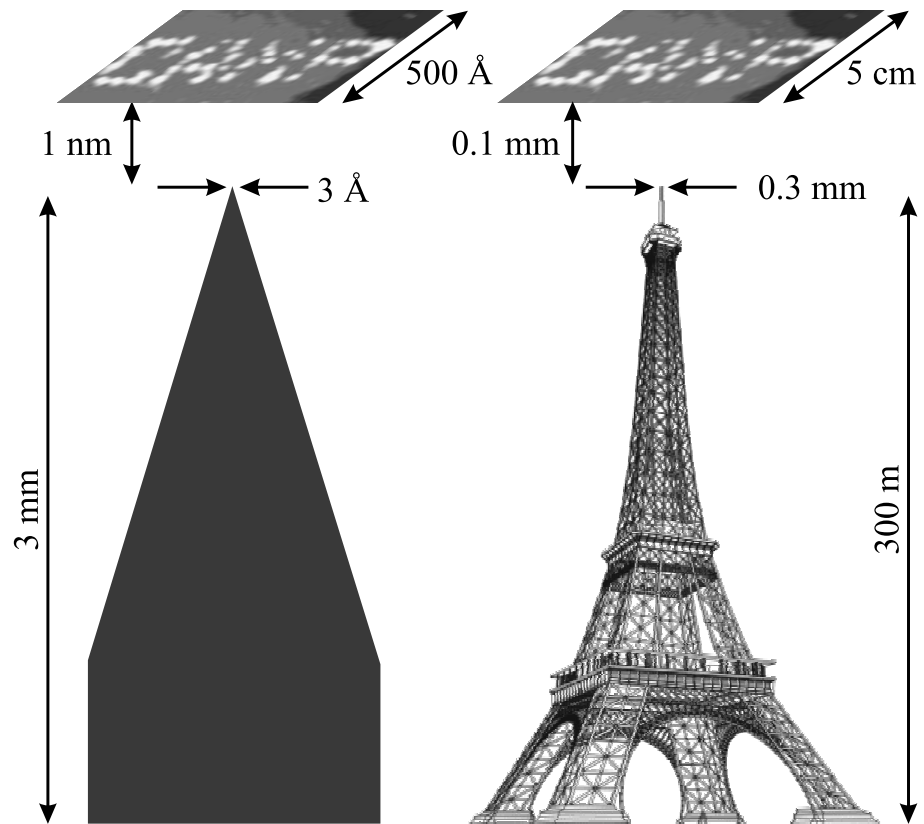
## Den øjeblikkelige formåen

I dag er man stadig langt fra at beherske en teknik, der kan skrive noget permanent ned i CAMP-logo format, så det også kan læses igen senere.<sup>7</sup> På de mikrochips, der benyttes i dagens computere, er man dog ved at bevæge sig ned i nanoverdenen. Da den første chip blev konstrueret i 1971, bestod den kun af ganske få komponenter, men i dag kan man presse 42 millioner transistorer ned på en enkelt chip (se fodnote 3 på side 204). De elektriske ledninger mellem disse komponenter er også blevet submikroskopiske (ca. 130 nm i diameter).

Jeg kommer lige med endnu en makroskopisk sammenligning: Det vil kræve mere end en halv million af disse ledninger, før bundtet opnår en tykkelse svarende til det nu så berømte hår! Alligevel er der næsten 200 000 atomer i tværsnittet af en enkelt ledning. Med miniaturiseringen af computere vil næste generation af mikrochips have endnu tyndere ledninger, og fortsætter udviklingen uden hindringer, vil man nå ned på den atomare skala allerede om godt 50 år.<sup>8</sup>

<sup>7</sup>IBM er dog på vej med en ny teknik, der gør det muligt at overføre informationen fra ikke mindre end 25 DVD'er til en overflade på størrelse med et frimærke! På denne måde vil de kunne skrive denne afhandling mere end 100 000 gange på dette frimærke. Men selv med en sådan informationstæthed vil der kun være plads til halvdelen af afhandlingen på tværsnittet af det famøse hår, altså 50 gange mindre end med CAMP skrift. Læs mere (på engelsk) her [http://www.research.ibm.com/resources/news/20020611\\_millipede.shtml](http://www.research.ibm.com/resources/news/20020611_millipede.shtml).

<sup>8</sup>Faktisk forventer man *ikke*, at udviklingen bare kan fortsætte ufortrødent. Allerede inden for de næste 10 år vil man nå nogle fundamentale fysiske grænser for silicium (Si) teknologien. Det er dog langt fra første gang at man har regnet med at ville løbe panden mod en mur i forsøget på at forbedre mikrochipene. I alle tidligere tilfælde er nye metoder og idéer dog dukket op i tide til at forhindre det frygtede stop i udviklingen.



Figur 11.2: STM-nålen contra Eiffel-tårnet. Hvad nu hvis STM-nålen ikke kun var 3 mm lang men 300 meter høj ligesom Eiffel-tårnet? Hvorledes ville de tilsvarende dimensioner så forholde sig? Til venstre i figuren har jeg skitseret nålens dimensioner og størrelsen af det CAMP-logo, som den skal skanne fra en afstand af ca. 1 nm. Til højre ses de tilsvarende mål, hvis det var Eiffel-tårnet, der skulle udføre en lignende bedrift. Til at starte med bliver nålen ført ind fra 1 mm til 1 nm på under to minutter; med tilsvarende hastighed skal Eiffel-tårnet derfor føres fra 100 m ind til bare 0.1 mm! Dette skal vel at mærke ske uden at antennen banker ind i selve overfladen, da det ville ødelægge det område, som skal skannes. Endelig skal man huske, at STM'et også kan skanne helt ned til atomar størrelse, hvilket betyder, at når CAMP-logoet er afbilledet, skal Eiffel-tårnet derefter kunne føres endnu tættere på, så det kan skanne i en sådan detalje grad at selv de mindste detaljer i hver enkelt plet kommer med. Prøv at fundere lidt over dette, mens figuren betragtes i stilhed. (Billedet af Eiffel-tårnet er fundet på den officielle hjemmeside: <http://www.tour-eiffel.fr/>). [If any English readers should be interested, this shows the task of an STM tip if it had the size of the Eiffel tower].

## Opbygning af afhandling

I denne afhandling har vi allerede taget skridtet fuldt ud ved at vælge en undersøgelse af de absolut mindste forbindelser man kan forestille sig mellem to metalelektroder: En tråd der kun består af en enkelt række atomer. Mere præcist har vi udforsket atomare metalkontakter (AMK'er).<sup>9</sup>

I princippet kan de fleste af vores eksperimenter beskrives ganske enkelt som en måling af modstanden  $R$  for disse kontakter, men vi har forsøgt at gøre dette på forskellige sofistikerede måder for at øge vores viden om de basale elektriske egenskaber for disse *ekstremt* små systemer.

I kapitel 2 beskriver jeg hvorfor ledningsevnen  $G$ , der er det reciprokke af modstanden ( $G = 1/R$ ), er en mere naturlig størrelse til beskrivelse af elektrontransport i AMK'er. Her indføres også begreber som *kvantiseret ledningsevne* og *eigenkanaler*. Kvantiseringen af ledningsevnen for guld i enheder af den fundamentale ledningsevneenhed  $G_0$ <sup>10</sup> blev en opdagelse, som var med til at starte den store interesse, der har været for netop atomare guldkontakter. Guld er da også et af de metaller, hvorpå vi har udført de mest detaljerede undersøgelser.

Kvantiseringen opstår pga. fuldstændigt åbne og/eller lukkede *eigenkanaler*. En eigenkanal svarer til en forbindelse mellem de to makroskopiske metalelektroder gennem den atomare kontakt. Når sådan en kanal åbnes fuldstændigt vil det øge kontaktens ledningsevne med præcist  $1 G_0$ . For nogle metaller, f.eks. guld og de andre *ædelmetaller* sølv (Ag) og kobber (Cu), vil disse kanaler enten være næsten helt åbne eller fuldstændigt lukkede så længe kontakterne kun består af op til tre atomer. Det betyder, at ledningsevnen altid vil antage en værdi, der er et helt kvanta af  $G_0$ ; heraf betegnelsen *kvantiseret ledningsevne*. Specielt finder man, at ledningsevne er eksakt  $1 G_0$  for én-atomare ædelmetalkontakter. Det er dog ikke for alle metaller at disse eigenkanaler altid er fuldstændigt åbne, og for f.eks. *platinmetallerne* [platin (Pt), palladium (Pd) og nikkel (Ni)] bliver ledningsevnen af den én-atomare kontakt kun ca.  $1.5 G_0$ , selvom f.eks. ikke mindre end fire eigenkanaler er delvist åbne for platin. Alle forsøg i afhandlingen er udført på atomare ædel- og platinmetalkontakter (se Fig. 1.1 på side 5).

I kapitel 3 beskrives de eksperimentelle opstillinger, som vi har anvendt for overhovedet at kunne danne AMK'er. Den ene metode benytter samme princip til dannelse af kontakten, som den der blev brugt, til at danne de pletter der udgør bogstaverne i CAMP-logoet. STM-nålen føres ind i overfladen og danner en "stor" metalkontakt. Når nålen efterfølgende trækkes ud af overfladen, kan man danne kontakter bestående af helt ned til ét enkelt atom. Dette vil forekomme lige inden kontakten brydes (se Fig. 3.2 på side 31).

<sup>9</sup>I selve afhandlingen svarer atomic-sized contacts (ASCs) til det, som her kaldes AMK'er.

<sup>10</sup> $G_0$  blev defineret i ligning (2.3) på side 15.

Vi har på tilsvarende måde fremstillet AMK'er ved at benytte den *mekanisk kontrollerbare brud-junktion* (MCBJ) (se Fig. 3.5 på side 35). Her er nål og prøve skiftet ud med en metaltråd, som brækkes midt over. Mellem metaltrådens brudflader kan der nu danne AMK'er, når brudfladerne føres tilbage i kontakt med hinanden igen. Som med STM'et benyttes de piezo-elektriske krystaller til at kontrollere størrelsen af de dannede kontakter på atomart niveau.<sup>11</sup>

Begge metoder har fordele og ulemper, men de har dog den egenskab til fælles, at kontakterne bliver dannet under yderst rene betingelser. STM'et er placeret i et ultrahøjt vakuum (UHV) kammer, hvor trykket er ekstremt lavt ( $10^{-13}$  atmosfære) og prøverne kan endvidere rengøres inde i selve kammeret.

Med MCBJ-teknikken sænker man en lille beholder med prøven ned i flydende helium (He). Temperaturen er her 4.2 K ( $-269^{\circ}\text{C}$ ), og alle gasser, undtagen helium der jo er flydende, fortætter på indersiden af beholderen. På denne måde opnår man et tryk, der er endnu lavere end UHV for alle andre gasser end helium og evt. hydrogen ( $\text{H}_2$ ). Først under disse betingelser brydes metaltråden, og nye rene metaloverflader dannes direkte i vakuumet.

Vi har bl.a. benyttet AMK'er dannet under disse ultrarene forhold til at måle såkaldte *ledningsevnehistogrammer* (kapitel 4) for alle seks metaller benyttet i afhandlingen (se Fig. 1.1 på side 5). I ledningsevnehistogrammer viser toppe de typiske ledningsevneværdier, som de atomare kontakter antager, når de forlænges indtil de endeligt brydes. Den første top svarer til ledningsevnen for den én-atomare kontakt, og for blandt andre ædelmetallerne kan man observere kvantiseret ledningsevne som toppe ved heltallige værdier af  $G_0$ .

Når vi benytter STM'et ved stuetemperatur er de dannede AMK'er meget ustabile og brydes på få milisekunder. I kapitel 5 beskrives konstruktionen af vores meget hurtige og præcise eksperimentelle opstilling, som vi benytter til måling af *strøm-spændings* ( $I$ - $V$ ) *kurver*.

Måler man  $I$ - $V$  kurver meget hurtigt (mikrosekunder), forventer man makroskopisk, at disse kurver bliver lineære. Fra Ohms lov:  $I = GV$  får man forholdet mellem strømmen  $I$  og spændingen  $V$  henover en kontakt, hvor dennes ledningsevne  $G$  er proportionalitetskonstant. For en makroskopisk kontakt vil  $G$  forblive konstant når spændingen øges hurtigt, som under vores forsøgsbetingelser, og forholdet mellem  $I$  og  $V$  vil være lineært (Ohmisk). Hvis spændingen i stedet ændres langsomt, får strømmen temperaturen til at stige. Dette vil medføre, at  $R$  og dermed  $G$  bliver afhængige af spændingen og resultatet bliver ikke-lineære  $I$ - $V$  kurver.

<sup>11</sup>Piezo-elektriske krystaller er kendt fra hverdagens engangslightere (dem der tændes med et enkelt tryk på en knap). Det er dog den omvendte proces af den, der benyttes i STM'et. Krystallen placeres under knappen og udsættes her for et kraftigt tryk så dens dimensioner ændres. Dette medfører en høj spændingsforskel over krystallen, der straks aflades med en statisk gnist, som antænder den gas, der samtidigt bliver lukket ud, mens knappen er trykket ned.

Der er dog umiddelbart ingen grund til at forvente at ledningsevnen for en atomar kontakt skulle forblive konstant når spændingen øges. Man kunne f.eks. forestille sig, at en delvist åben egenkanal ville blive påvirket og lukke mere til. Vi blev interesserede i at måle  $I$ - $V$  kurver, da der allerede var flere rapporter om ikke-lineære  $I$ - $V$  kurver målt på atomare guldkontakter. I disse tilfælde var en forøgelse af  $G$  med spændingen blevet observeret, men modstridende eksperimenter gjorde yderligere undersøgelser både interessante og nødvendige.

Vigtigheden af at danne AMK'erne under rene forsøgsbetingelser, hvis man skal gøre sig håb om at undersøge deres finere elektriske egenskaber, udgør hovedtemaet i kapitel 6. Her benytter vi de ultrarene betingelser i STM'et sammen med den hurtige eksperimentelle opstilling til at vise, at  $I$ - $V$  karakteristikker på atomare guldkontakter faktisk er næsten Ohmske. Ikke-lineære  $I$ - $V$  kurver kan til gengæld forklares med et lag af urenheder, der har samlet sig på guldoverfladen og dermed forhindrer en direkte kontakt mellem de to elektroder. Disse observationer bekræftiges med forskellige teoretiske beregninger. Urenhederne kommer fra luften, og det er derfor uhyre vigtigt, at man kan rengøre sin prøve eller danne den direkte under rene forhold, hvis man skal arbejde med AMK'er.

I kapitel 7 beskrives den fortsatte undersøgelse af  $I$ - $V$  kurver målt ved at benytte MCBJ-teknikken til at danne AMK'er og vi udvider nu undersøgelsen til at omfatte alle seks metaller. Specielt finder vi, at modsat guld, der stadigt opfører sig Ohmsk under disse anderledes betingelser (lav temperatur og ny metode til dannelse af kontakterne), er  $I$ - $V$  kurver for platin klart ikke-lineære. Ledningsevnen for platinkontakterne aftager med spændingen, hvilket er den modsatte effekt af hvad vi observerer for de ikke-lineære  $I$ - $V$  kurver vi målte på en "snavset" guldoverflade. Da vi nu benytter MCBJ-teknikken, skulle det til gengæld være helt sikkert, at der ikke er nogen urenheder til stede.

Forskellen mellem guld og platin bekræftes med teoretiske udregninger, og forklares via den fundamentalt forskellige ydre elektronstruktur for de to metaller. Guld har en enkelt fri  $s$ -elektron i sin ydre skal, hvilket resulterer i kun én åben egenkanal for den én-atomare kontakt. Platin har derimod også frie  $d$ -elektroner, der pga. deres komplicerede orbitalstruktur er årsag til de ikke-lineære  $I$ - $V$  kurver. De andre ædelmetaller har samme elektronstruktur som guld og opfører sig tilsvarende med næsten lineære  $I$ - $V$  kurver, mens palladium og nikkel  $I$ - $V$  kurver, skønt klart ikke-lineære, afviger en del fra platins opførsel.

I kapitel 8 måler vi igen  $I$ - $V$  kurver, men ikke længere for at observere deres opførsel. I stedet øger vi nu spændingen over kontakterne så meget, at de bliver brudt pga. den store strøm der løber i gennem dem. Vi har undersøgt disse *strøminducerede brud* på tusinder af én-atomare kontakter og benyttet alle seks metaller i undersøgelsen. Den én-atomare kontakt er bevidst valgt, fordi den repræsenterer den enkleste atomare konfiguration, hvilket gør en sammenligning

med teoretiske modeller nemmere. Det viser sig, at guld danner de klart mest stabile atomare kontakter, mens også de andre ædelmetaller har mere stabile kontakter end deres umiddelbare nabo blandt platinmetallerne (jfr. Fig. 1.1 på side 5). Den større stabilitet for guld-, sølv- og kobberkontakter i forhold til kontakter dannet af platinmetaller, kan meget vel skyldes den simple ædelmetal-elektronstruktur, som også er årsag til, at  $I$ - $V$  kurver bliver næsten lineære for netop atomare kontakter fra disse metaller.

Ofte bryder én-atomare guldkontakter ikke før en utrolig høj strømtæthed af størrelsen  $1\,000\,000\,000\text{ A/mm}^2$  er opnået. Sammenlignes det med strømtætheden i glødetråden på en elektrisk pære (ca.  $1\text{ A/mm}^2$ ), finder man, at atomare guldkontakter i korte øjeblikke opretholder op til en milliard gange højere strømtæthed, før de brydes. Noget af forklaringen på dette er bl.a., at elektronerne spreder og afsætter deres energi som varme på urenheder og fejl i metallet. For én-atomare kontakter kan der pr. definition ikke være fejl eller urenheder. Desuden vil elektroner, der farer gennem kontakten (op til en million pr. nanosekund), nå langt forbi før de endeligt spredes og dermed øger temperaturen.<sup>12</sup>

Til sidst i kapitel 9 ses der på spændingsafhængigheden af ledningsevne-histogrammer for platin. Vi har observeret, at positionen af den første top i histogrammet flytter sig fra omkring  $1.5$  til  $1.8 G_0$ , når spændingen øges forbi  $300\text{ mV}$ . Det viser sig, at dette kan sammenholdes med at platin har en egenskab, der gør én-atomar-kædedannelse mulig. Denne egenskab deles kun med guld og iridium (Ir), som er naboer til platin i det periodiske system (jfr. Fig. 1.1 på side 5). Ved høje spændinger bliver kæderne dog så ustabile, at de ikke længere kan dannes. Da det bl.a. var kæderne, der holdt ledningsevnen nede på  $1.5 G_0$ , forklarer dette, at histogramtoppen flytter sig til  $1.8 G_0$ , når spændingen øges.

Vores studier af atomare metalkontakter har ført os vidt omkring i nanoverdenen. Jeg forsøger i kapitel 10 at forudsige udviklingen inden for feltet i den nærmeste fremtid. Den såkaldte molekylelektronik (moletronic) vil være en af de muligheder, som vi regner med at vende os mod fremover. Her vil enkelte molekyler overtage funktionen af elektriske komponenter som transistorer på en computerchip. Selvom dagens transistorer på en makroskopisk skala er meget små, er de, på samme måde som ledningerne, stadig kæmpestore, når de sammenlignes selv med komplekse organiske molekyler. Det er vores hensigt at ombygge vores MCBJ, så den kan bruges til at undersøge de elektriske egenskaber af funktionelle molekyler. Ved at gå denne vej håber vi på at man engang i fremtiden kan opnå den ultimative nanoteknologi, hvor atomare kontakter og individuelle molekyler bruges til opbygningen af computere samt anden elektronik.

<sup>12</sup>Elektrontransporten i AMK'er kaldes ballistisk, fordi elektroner der bevæger sig gennem kontakten, kun spredes på dennes ydre grænser. Der sker ingen spredning af elektronerne på selve atomerne inde i kontakten. Denne form for elektrontransport er beskrevet i kapitel 2.

## Appendix A

# Interpretation of Polynomial Fits to Current-Voltage Curves

In Chapters 6 and 7, current-voltage ( $I$ - $V$ ) curves on atomic-sized contacts (ASCs) have been fitted with a third order polynomial to check for non-linearities. In this and the next two appendixes, some important aspects of the fitting procedure will be described in detail.

All relevant  $I$ - $V$  curves have been fitted with the following equation:

$$I(V) = GV + G'V^2 + G''V^3, \quad (\text{A.1})$$

where  $G$  is the low bias conductance measured in units of  $G_0$ ,<sup>1</sup>  $G'$  is a constant describing the polarity-dependence of the current due to asymmetries in the contact region and  $G''$  is the non-linear term. This equation was first used in Chapter 6 as Eq. (6.1) on page 88 and also in the next chapter as Eq. (7.1) on page 116. In Eq. (5.15) on page 76 of Chapter 5 a similar equation was used for fitting  $I$ - $V$  curves on resistors. Here a constant offset current  $I_0$  was included, but it is an artifact of the experimental setup, e.g. from thermal drift (see Sec. 5.5).  $I_0$  is always smaller than a  $\mu\text{A}$  and we do not mention it in later chapters, since the current  $I$  through the ASCs is typically of the order 100  $\mu\text{A}$ .

---

<sup>1</sup>The fundamental unit of conductance  $G_0$  is defined in Eq. (2.3) on page 15.

It is very important to realize that Eq. (A.1) is not based on a physical model describing the  $I$ - $V$  behavior for ASCs of metals. We use the equation because it fits all the simplest types of smooth curves very well. This method has furthermore been applied previously [1–3] to obtain information on the magnitude of the non-linearity of the curves.

An example of a physical model developed to fit  $I$ - $V$  curves was mentioned in Sec. 6.5. This was the parabolic barrier model describing tunneling through a thin insulating film [4]. The model fitted very well the non-linear  $I$ - $V$  curves obtained on a gold (Au) sample which had not been cleaned after exposure to air (see Fig. 6.5 on page 94). In the model the curves are fitted with an equation involving the hyperbolic sinus function [4]. Taylor expanding to third order will, however, result in a polynomial like Eq. (A.1) with zero  $G'$  term, as expected for the symmetric contact geometry, described in the model.

Although not a physical model, we do obtain interesting information on the general behavior of the  $I$ - $V$  curves from the fitting to Eq. (A.1):

1.  $G$  gives the low bias conductance, before the burst begins.
2.  $G'$  reveals the degree of asymmetry of the ASCs.
3.  $G''$  is the non-linear term which can sort the curves into three fundamentally different types:
  - (a) Linear  $I$ - $V$  curves with  $G'' \simeq 0$ .
  - (b) Non-linear  $I$ - $V$  curves with  $G'' > 0$  (up-bending).
  - (c) Non-linear  $I$ - $V$  curves with  $G'' < 0$  (down-bending).

An example of each type of curve is displayed in Fig. A.1. The term up/down-bending refers to the behavior of the  $I$ - $V$  curve when the burst rises towards positive voltage (see figure). An example of a linear curve (a) is given by an  $I$ - $V$  curve on Au.<sup>2</sup> In general, all the noble metals display very linear  $I$ - $V$  curves, see Sec. 7.3. For the up-bending curve (b) we have chosen an  $I$ - $V$  curve on a Au sample that was only rinsed in air and not in the ultra-high vacuum (UHV) of the scanning tunneling microscope (STM) (see Sec. 6.2 and curve (c) in Fig. 6.1 on page 89). In this case, the current tunnels through an insulating layer of contamination between the two Au electrodes and the conductance increases with applied voltage. This is the type of curve that can also be fitted with the above-mentioned parabolic barrier model.

<sup>2</sup>This is the 4.2  $G_0$  curve from Fig. 7.1a on page 117

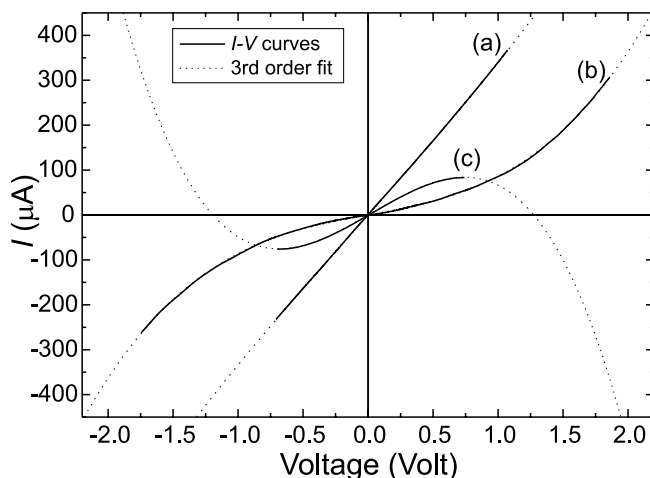


Figure A.1: Examples of the three fundamentally different types of  $I$ - $V$  curves. (a) linear  $I$ - $V$  curve with  $G'' \simeq 0$  measured on a clean Au sample at 4.2 K under cryogenic vacuum using the mechanically controllable break-junction (MCBJ). (b) Non-linear  $I$ - $V$  curve with  $G'' > 0$  measured on a Au sample, not cleaned after exposure to air, using the scanning tunneling microscope (STM) at room temperature (RT) under ultra-high vacuum (UHV). (c) Non-linear  $I$ - $V$  curve with  $G'' < 0$  measured on a clean platinum (Pt) sample at 4.2 K under cryogenic vacuum using the MCBJ. All curves are fitted to the third-order polynomial from Eq. (A.1) and fits are plotted as dotted lines. The fitting parameters ( $G, G''$ ) for these three curves are given in units of ( $G_0, G_0/\text{Volt}^2$ ): (a) (4.2, 0.12); (b) (0.5, 0.46); (c) (2.1, -1.36). All curves have very small  $G'$  and different  $G$  were selected for clarity.

The magnitude of the non-linear term  $G''$  is given in the figure caption. Compared to the linear curve (a),  $G''$  is only four times larger for the non-linear curve (b). The conductance is, however, eight times smaller for curve (b), and the non-linearity is relatively at least one order of magnitude higher for curve (b) than for curve (a).

The final curve (c) is a typical example of one of the down-bending curves of platinum (Pt) measured at 4.2 K under cryogenic vacuum using the MCBJ. Other curves can be seen in Fig. 7.1b on page 117. This is the general behavior of all the platinum metals, with palladium (Pd) by far the most non-linear (see Sec. 7.4). For curves of this type a breakdown of the simple polynomial fit be-

comes directly visible in the figure. Whereas the plotted fit for curves (a) and (b) behaved realistically on this voltage-scale this is not the case for curve (c). It can be seen in the figure, that the fitted curve for (c) crosses zero before 1.5 V, indicating that the conductance becomes negative at higher voltages. This is of course unphysical. Half of the Pt ASCs can, however, not withstand voltages of more than 0.7 V and they all break before the voltage reaches 1.4 V (see Fig. 8.8 on page 165), i.e. before the conductance of the fit becomes negative. The process responsible for the lowering of the conductance is also likely to cause the low stability towards higher voltages (see the discussion in Chapter 8).

Although Eq. (A.1) is not a physical model, we obtain information from the fits which allows us to sort the  $I$ - $V$  curves of metals into three different types. Furthermore, we also have a measure of the magnitude of the non-linearity. In the next appendix we will discuss how we use  $G'$  as a selection criteria to avoid clearly asymmetric contact geometries.

## References

- [1] J. L. Costa-Krämer, N. García, P. García-Mochales, P. A. Serena, M. I. Marqués, and A. Correia, “Conductance quantization in nanowires formed between micro and macroscopic metallic electrodes,” *Phys. Rev. B* **55**, 5416–5424 (1997).
- [2] J. Abellán, R. Chicón, and A. Arenas, “Properties of nanowires in air. Controlled values of the conductance,” *Surf. Sci.* **418**, 493–501 (1998).
- [3] A. Correia, J.-L. Costa-Krämer, Y. W. Zhao, and N. García, “Non-linear contribution to intensity-voltage characteristics of gold nanowires,” *Nanostruct. Mater.* **12**, 1015–1020 (1999).
- [4] K. Hansen, “Electrical Properties of Atomic-Sized Metal Contacts,” PhD thesis, University of Aarhus, 2000. (Can be downloaded from <http://www.ifa.au.dk/~kimh/pdf/thesis.pdf>).

## Appendix B

# Applying Selection Criteria to Current-Voltage Curves

Before individual current-voltage ( $I$ - $V$ ) curves are accepted, we apply different selection criteria. With the scanning tunneling microscope (STM) experiments the amount of  $I$ - $V$  curves were limited, and it was manageable to go through all curves manually. In this way we removed data where the contacts were unstable resulting in jumps between different conductance values during the burst. For the mechanically controllable break-junction (MCBJ) experiments, where large amounts of data were acquired, this would have been almost impossible. Instead we needed a parameter telling us when an  $I$ - $V$  curve was measured on an unstable contact. For this we used chi-square fitting.

We also wished to remove asymmetric contact geometries from both the STM and the MCBJ data. The degree of asymmetry is described by the second term  $G'$  in Eq. (A.1) of Appendix A. If this is not zero the  $I$ - $V$  curve is not symmetric and the magnitude of the interesting non-linear term will be affected. Hence, we use  $G'$  to set an upper limit to the asymmetry.

Finally, we also set a limit to the uncertainty of the cubic term  $\sigma_{G''}$ . In the STM experiments only  $I$ - $V$  curves with  $\sigma_{G''} < 0.01 G_0/\text{Volt}^2$  were accepted.<sup>1</sup> With the MCBJ experiment we found that the two other criteria already remove traces with large  $\sigma_{G''}$  and no further sorting was needed. These other two selection criteria will be described in detail below.

---

<sup>1</sup>The fundamental unit of conductance  $G_0$  is defined in Eq. (2.3) on page 15.

## Chi-square fitting

To test the stability of the contacts and in general how well a given  $I$ - $V$  curve can be fitted to Eq. (A.1), we have used a special version of chi-square ( $\chi^2$ ) fitting [1]. The goodness of fit (GOF) is a function of  $\chi^2$  and the number of degrees of freedom  $N$ . Since  $N$  is given by the number of fitting points and parameters, it is of the order of thousands. When  $N$  is that large, it turns out that the GOF is almost a step function of  $\chi^2$ , rising from zero to one in a very narrow interval around  $\chi^2 = N$ . The value of  $\chi^2$  is amongst other things determined by the standard deviation on the individual data points in the fit, i.e. the standard deviation of the calculated current  $\sigma_I$ . All data points are assigned with the same value of  $\sigma_I$  whereas the actual value is used as a free parameter in the fitting procedure. We then force the GOF to be close to 50%, meaning  $\chi^2 \simeq N$ . In this way  $\sigma_I$  turns into a measure of the average deviation between model and experimental data. The smaller  $\sigma_I$  the better the model fits the data.

If an  $I$ - $V$  curve is discontinuous due to jumps in the conductance,  $\sigma_I$  will be very large, and it is easy to locate and remove these traces from the data. Even for traces with smooth  $I$ - $V$  curves,  $\sigma_I$  can take on values anywhere between 0.1–10  $\mu\text{A}$ . The curves with the highest values of  $\sigma_I$  can clearly not be fitted well with Eq. (A.1). By visual inspection the maximum limit for  $\sigma_I$ , under which all curves look smooth, is found and used as a selection criteria. The limit changes between individual experiments and depends on the parameters used. Typically, low conductance and high burst amplitude will give the smallest  $\sigma_I$ . Regardless of the experimental settings the limiting value of  $\sigma_I$  has always been chosen close to 1  $\mu\text{A}$ .

## Asymmetric curves

To avoid data from atomic-sized contacts (ASCs) with asymmetric atomic configurations, we remove clearly asymmetric  $I$ - $V$  curves by using  $|G'/G|$  as a selection criterion. In this way we set an upper limit for the percentage of asymmetry. If an ASC is completely symmetric, the current will by definition be polarity independent and  $G' \equiv 0$ . Only asymmetric contacts can have large values of  $G'$ , the opposite can, however, not be stated since an asymmetric contact may have  $G'$  close to zero. The use of the selection criteria allows a more reliable comparison with the theoretical calculations, because these are performed on symmetric contact configurations ( $G' \equiv 0$ ).

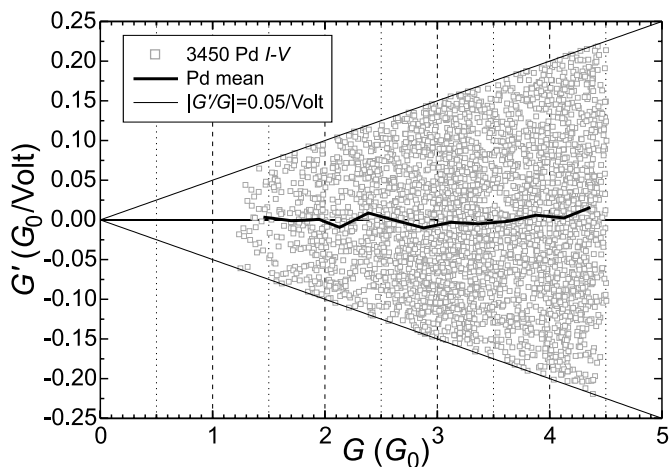


Figure B.1: Asymmetric term  $G'$  vs low bias conductance  $G$  for Pd. Each point represents a fit to Eq. (A.1) of one  $I$ - $V$  curve on one ASC. In Fig. 7.9a on page 135 the non-linear term  $G''$  is plotted for the same 3450  $I$ - $V$  curves. The solid curve represents the mean value of  $G'$  drawn through points found by averaging over at least 50 successive data points (see footnote 6 on page 119). The selection criterion  $|G'/G| < 0.05/\text{Volt}$  is indicated by the thin solid lines.

When deciding the limit we have to take the stability of the ASCs into account. A higher burst amplitude will result in a more precise fitting (see the next appendix). This means that for the most stable contacts it is possible to use a lower limit without excluding all the data. For all metals the selection criterion remove about 50% of the acquired  $I$ - $V$  curves.

The lowest limit is used for the stable gold (Au) contacts at 4.2 K in the MCBJ experiments of Chapter 7. Here curves with  $|G'/G| > 0.025/\text{Volt}$  are excluded. For the room temperature (RT) STM experiments on Au presented in Chapter 6 the limit is  $|G'/G| < 0.05/\text{Volt}$ . This limit is also used for the MCBJ experiments on the remaining metals silver (Ag), copper (Cu), platinum (Pt) and palladium (Pd). Only for the very unstable ASCs of nickel (Ni) did we use a higher limit of  $|G'/G| < 0.1/\text{Volt}$ .

In Fig. B.1 the selection criterion is illustrated for Pd with a scatter plot of  $(G, G')$  for fits to Eq. (A.1). As in the corresponding  $(G, G'')$  scatter plot only

points with  $G < 4.5 G_0$  are shown (cf. Fig. 7.9a on page 135). The selection criterion has been applied and all points are hence located between the two lines representing  $|G'/G| = 0.05/\text{Volt}$ . It is clear from the figure that the  $G'$  values spread evenly between the two limits. This is confirmed by the calculated mean value of  $G'$  (solid line), which remains close to zero at all conductances, the general behavior of  $G'$  for all data presented in Chapters 6 and 7.

## References

- [1] W. H. Press, B. P. Flannery, S. A. Teukolsky, and W. T. Vetterling, *Numerical Recipes in Pascal* (Cambridge University Press, Cambridge, 1989).

## Appendix C

# Reliability of the Fitting Procedure

Since we are fitting a third order polynomial [Eq. (A.1) of Appendix A] to the short segment of a current-voltage ( $I$ - $V$ ) curve, it is important to consider how much the fitted terms depend on the burst parameters. If the burst amplitude  $A$  is too low even a fit to a straight  $I$ - $V$  curve can result in a large non-linear term  $G''$  as discussed in Sec. 5.8.

Measuring with the mechanically controllable break-junction (MCBJ) on gold (Au), the metal with the most stable atomic-sized contacts (ASCs), we used bursts with  $A$  between 1 and 2 V, and for the monatomic contacts ( $G \simeq 1 G_0$ )<sup>1</sup> the amplitude was never below 1.5 V. While this may be enough to ensure a reliable fit, the case could be very different for the other metals; especially for the platinum metals where burst amplitudes below 0.5 V are often necessary in order not to disrupt the ASCs (cf. Table 7.1 and Fig. 8.8a on page 114 and 165, respectively).

In order to test the reliability of the parameters obtained from fitting  $I$ - $V$  curves we have performed the relevant experiments on our calibrated resistors (see Sec. 5.2).  $I$ - $V$  curves on Ohmic resistors are linear, so the value of any non-zero higher order fitting parameters gives a measure of the fitting uncertainty. For a comparison with the experimental results of Au and platinum (Pt), we used two different types of calibrations. Since Au is more stable than Pt, the highest burst amplitudes are used when measuring  $I$ - $V$  curves

---

<sup>1</sup>The fundamental unit of conductance  $G_0$  is defined in Eq. (2.3) on page 15.

on Au. The calibration settings determine the voltage scale on the oscilloscope ( $V/\text{div}$ ). For Au, the scale must not saturate even if a 1 V burst is applied to an ASC with  $G = 4 G_0$ , whereas for Pt, 0.6 V is usually the maximum voltage applied (cf. Table 7.1 on page 114). The use of a lower voltage scale results in an increased precision of the measurements, and this becomes even more important when using low amplitude as with the platinum metals. It is not possible to change the voltage setting on the oscilloscope during an experiment (see Sec. 5.5). With these considerations in mind we decided to compare a Au-like and a Pt-like calibration.

By acquiring  $I$ - $V$  curves on several calibrated resistors with conductances in the typical range of ASCs, we tested the spread of the fitting parameters  $G$ ,  $G'$  and  $G''$  using many different settings. The parameters we tested included conductance as well as burst amplitude and frequency. For each setting we obtained 50  $I$ - $V$  curves in order to compare the spread in the fitted parameters between different settings.

In Fig. C.1 we show typical results of these tests for the non-linear term  $G''$  vs burst amplitude or conductance, comparing Au and Pt-like calibrations. In (a) and (b)  $G''$  vs burst amplitude is shown for a Au and a Pt-like calibration, respectively. Here the same resistor with  $G = 2 G_0$  is used, since it is a typical conductance of ASCs for both metals. The Au-like data are measured at higher voltages than the Pt-like data as in the experiments on the real metals. From the two graphs it is now clear that the spread is much smaller for the Au-like than for the Pt-like calibrations, since the  $G''$  scale is a factor ten smaller for (a) the Au-like than for (b) the Pt-like calibrations. It is also clear that the spread in  $G''$  increases rapidly when the voltage decreases for both calibrations. It should be noted that the smallest voltages used in (a) and (b) is below the lower limits of the experiments: 1 V for Au and 0.5 V for Pt.

In Fig. C.1c,  $G''$  is compared to the low bias conductance  $G$  in the same way that we have presented all our  $I$ - $V$  data in Chapters 6 and 7, and the spread in  $G''$  for the Au and Pt-like calibration is compared. The Pt data have been shifted to higher conductance for clarity. The higher burst amplitude for the Au-like data results in a smaller spread compared to Pt, but the spread increases with conductance for both types of calibrations. It is clear that a non-zero spread exist which is not always centered around zero. The spread depends on the amplitude and the conductance but there is almost no dependence on the frequency.

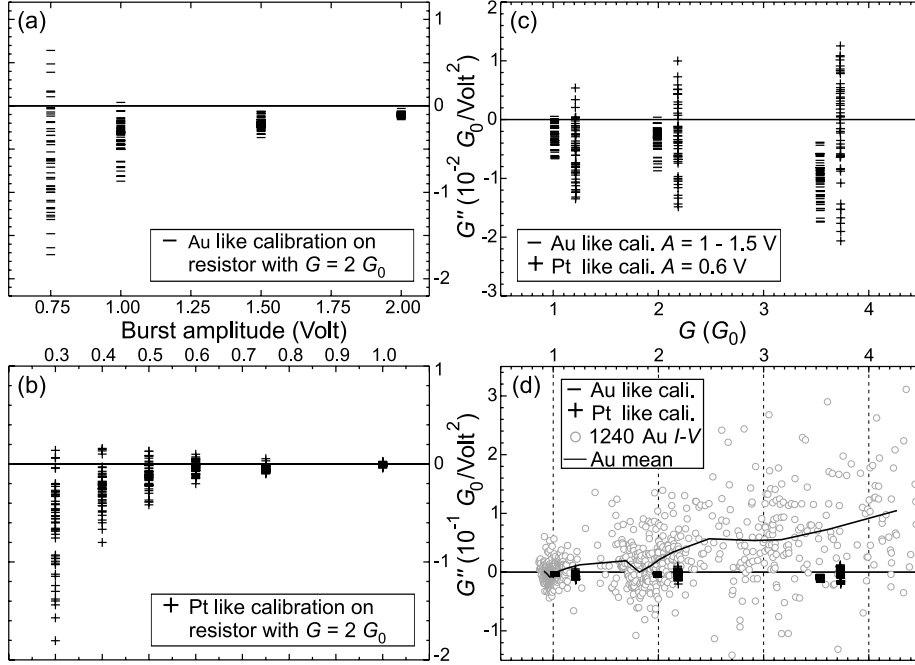


Figure C.1: Testing the reliability of the fitting procedure. (a) Dependence of the spread in the non-linear term  $G''$  vs burst amplitude measured on a resistor with  $G = 2 G_0$  while using a Au-like calibration (see text). There are 50 points for each setting. (b) Same as (a) but for a Pt-like calibration. (Note that the voltage scale is different in the two panels and that the  $G''$  scale for both the top panels is a factor 10 smaller than for the bottom panels). (c) Comparing the Au and Pt-like calibrations by plotting the spread in  $G''$  vs low bias conductance  $G$ . For the Au-like calibration the burst amplitude is 1.5 V when  $G = 1 G_0$  and 1 V at higher  $G$ . For the Pt-like calibration  $A = 0.6$  V at all conductances. The data have been measured on the same three resistors with conductances of 1, 2 and  $3.5 G_0$ , respectively. The Pt data are shifted  $+0.2 G_0$  for clarity. (d) Comparing the spread in the  $G''$  data from (c) with the Au data from 1240  $I$ - $V$  curves and the calculated mean from Fig. 7.2 on page 119.

We now have to answer the question: “Is the fitting procedure reliable?” From the comparison in Fig. C.1d, we find that the answer is yes. Here the data in (c) is compared with the  $I$ - $V$  curve data from Fig. 7.2 on page 119 measured on ASCs of Au formed under cryogenic vacuum at 4.2 K with the MCBJ. It is clear that the spread in the Au data point is much larger than the spread resulting from fitting  $I$ - $V$  curves to a resistor. The spread of the black points, representing the 50  $I$ - $V$  curves measured on resistors from Fig. C.1c, are very small compared to the spread of the data points in the corresponding conductance region. Even the spread of the Pt-like calibration data is much smaller than the spread in the real Au data. The Pt-like calibration data should, however, be compared with the much larger spread in  $G''$  observed for the real Pt data, as presented in Fig. 7.3a on page 121.

The spread in  $G'$  is relatively of the same order as in  $G''$  when compared with real data, whereas the spread of the low bias conductance  $G$  is much smaller. This is expected since the fit always has to be close to the slope around zero voltage resulting in a good estimate of the low bias conductance, even when small burst amplitudes are used.

The conclusion we can draw is that the fluctuations in the fitting parameters are much smaller than the actual spread of the real data and do not affect the obtained results.